In situ groundwater remediation treatments:

Natural denitrification study and nano Zero Valent Iron production

Ph. D. thesis

David Ribas Fargas

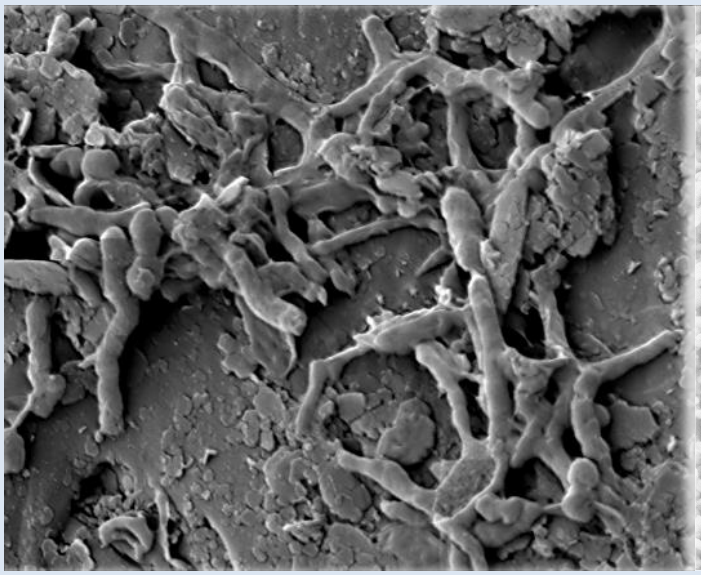

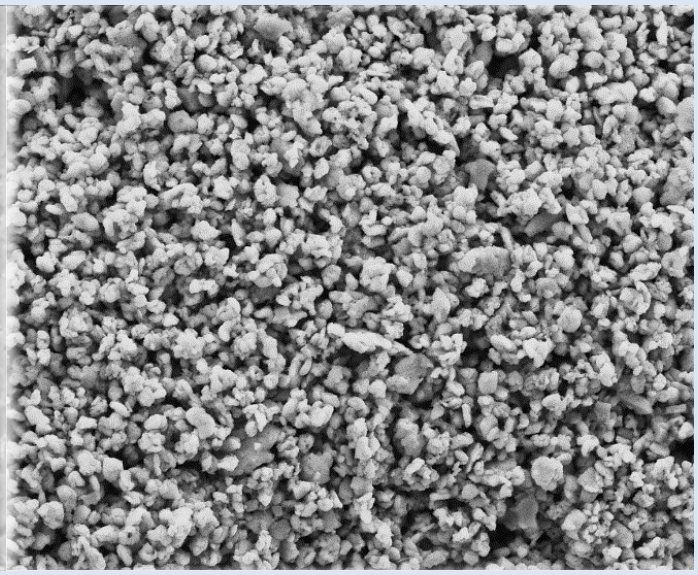

UNIVERSITAT POLITÈCNICA DE CATALUNYA

Natural Resources and Environment Doctorate Programme

IN SITU GROUNDWATER REMEDIATION TREATMENTS:

NATURAL DENITRIFICATION STUDY AND NANO ZERO-VALENT IRON PRODUCTION

Ph. D. thesis

David Ribas Fargas

Advisors:

Ph. D. Vicenç Martí Gregorio

Ph. D. José Antonio Benito Páramo

January 23th 2017, Manresa

“Look again at that dot. That's here. That's home. That's us. On it everyone you love, everyone you know, everyone you ever heard of, every human being who ever was, lived out their lives. The aggregate of our joy and suffering, thousands of confident religions, ideologies, and economic doctrines, every hunter and forager, every hero and coward, every creator and destroyer of civilization, every king and peasant, every young couple in love, every mother and father, hopeful child, inventor and explorer, every teacher of morals, every corrupt politician, every "superstar," every "supreme leader," every saint and sinner in the history of our species lived there – on a mote of dust suspended in a sunbeam.

The Earth is a very small stage in a vast cosmic arena. Think of the endless cruelties visited by the inhabitants of one corner of this pixel on the scarcely distinguishable inhabitants of some other corner, how frequent their misunderstandings, how eager they are to kill one another, how fervent their hatreds. Think of the rivers of blood spilled by all those generals and emperors so that, in glory and triumph, they could become the momentary masters of a fraction of a dot.

Our posturings, our imagined self-importance, the delusion that we have some privileged position in the Universe, are challenged by this point of pale light.

Our planet is a lonely speck in the great enveloping cosmic dark. In our obscurity, in all this vastness, there is no hint that help will come from elsewhere to save us from ourselves.

The Earth is the only world known so far to harbor life. There is nowhere else, at least in the near future, to which our species could migrate. Visit, yes. Settle, not yet. Like it or not, for the moment the Earth is where we make our stand.

It has been said that astronomy is a humbling and character-building experience. There is perhaps no better demonstration of the folly of human conceits than this distant image of our tiny world. To me, it underscores our responsibility to deal more kindly with one another, and to preserve and cherish the pale blue dot, the only home we've ever known.”

— Carl Sagan (1994), Pale Blue Dot: A Vision of the Human Future in Space

Acknowledgements

I would like to give my warmest thanks to the following people for their inspiration, guidance and support:

First and foremost my advisors,

Vicenç Martí for taking a chance and for believing in me when he gave me the opportunity to work on his projects through a Ph. D. grant, also for being a cornerstone during all the thesis and caring on a personal level.

Toni Benito for his guidance, supervision, humour and humanity during the most tedious moments of this thesis and for his invaluable expertise in milling.

My workmates in both CTM and ETSEIB where I found a sincere support and help, sometimes in unknown fields for me such as materials science. So, many thanks to CTM where I would like to thank Montse Calderer, Irene Jubany and Miquel Rovira as the counterparts of AquaRehab and NanoRem in CTM and also to Neus Bahí for being a very patient lab supervisor, and of course all my CTM colleagues, it would be impossible to name all of them; labmates, officemates and technicians. From ETSEIB to Casimir Cases and Kim Albo for helping me with the milling experimental part.

I feel very lucky to have met such nice people during my studentships in Czech Republic who made me feel part of the group and opened their culture to me. Miroslav Černík, Lucie Cádrová, Eva Kakosova, Kristýna Pešková, Zuzana Masopustová, Jíťa Krýstina, Vojtěch Antoš and Stanislaw Waclawek. Also I wouldn't forget my advisor in the USA Sibel Pamukcu and my colleagues: Zhiyi Yin and Alberto Colombo.

And finally, I am grateful to my family and friends, who during these four years have been encouraging, supporting and showing belief in me and in my work, as also sharing beers and mountains, of course.

Institutional acknowledgements

The present research has been co-funded by:

The European Union project FP7 AQUAREHAB (Development of rehabilitation technologies and approaches for multipressured degraded waters and the integration of their impact on river basin management) FP7 ENV 2008.3.1.1.1. Grant agreement Nr. 226565. 2009-2013.

The European Union project FP7 NANOREM (Taking nanotechnological Remediation Processes from Lab Scale to End User Applications for the Restoration of a Clean Environment) FP7 NMP.2012.1.2-1. Grant agreement Nr. 309517. 2013-2017.

The Spain Ministry of Science and Innovation project ATTENUATION (Natural and Induced Attenuation of groundwater pollution from agricultural and industrial sources). Grant agreement Nr. CGL2011-29975-C04-0. 2012-2015.

The Spain Ministry of Science and Innovation project NANOATTENUATION (Study of metals and inorganic compounds attenuation processes in groundwater by using of mineral nanoparticles). Grant agreement Nr. CGL2014-57215-C4-4-R. 2015-2017.

The Czech Republic “National Programme for Sustainability I”. Project LO1201.

The Czech Republic OPR&DI Centre for nanomaterials, Advanced Technologies and Innovation. Project CZ.1.05/2.1.00/01.0005.

The Czech Republic Ministry of Education, Youth and Sports of the Czech Republic. Project LO1305.

The author of this thesis has been supported by Spanish Ministry of Economy and Competitiveness, under the project (CGL2011-29975-C04-03) and FPI grant (BES-2012-052327).

Abstract

Freshwater is a scarce resource, threatened by constant pollution, global climate change and industrialization. Among other freshwater sources, groundwater is by far the most important source of usable freshwater. However, attempts to remove contaminants are more complex and slow due to the intrinsic nature of aquifers, low flow rates and a complex matrix in comparison with superficial waters.

The aim of this thesis is to investigate two remediation technologies: first, nitrate and nitrite removal based on natural occurring bioremediation and second, the production, reactivity and agglomeration of nano Zero Valent Iron (nZVI) particles.

Natural occurring denitrification is a partially implemented and promising remediation approach but concerns about its performance out of the lab are justified. The following studies were carried out: evaluation of denitrification potential of wetlands from two sites in Denmark, soil characteristics and composition impact on denitrification highlighting the role and vertical distribution of organic matter, assessment of the Dissimilatory Nitrate Reduction to Ammonium (DNRA) importance as a denitrification competitor and effect of the seasonal variations.

Regarding seasonal fluctuations, results showed that Heterotrophic Denitrification (HD) is an Arrhenius temperature dependant process and it can be influenced by mass transfer limitations. However, observing that HD is a very resilient process, being dominant under all tested conditions, the importance of DNRA arose in dried and frozen soils In addition, a nitrite increase was observed.

Concerning organic matter studies, heterotrophic denitrification was only present in a very narrow superficial zone where Organic Matter (OM) was abundant. DOC and LOI could not express by themselves an absolute correlation with HD, however high amounts of DOC ensured enough quantity and quality of OM. DNRA was important only in the very superficial samples where an excessive content of OM could trigger it.

On the other hand, nZVI is a very promising in situ new technology which can achieve the degradation of a broad range of contaminants, some being reluctant to previous remediation and bioremediation approaches. The purpose is to help overcome some of the challenges that limit a widespread implementation of this technique, such as: the lack of a cost – effective – straightforward production method, uncertainness on the reactivity governing factors including the passivating oxide shell in commercial particles and the agglomeration driving factors.

After replicating the previous milling methods in literature (where the iron ductility if using inert media was an insurmountable barrier to reach a nanoscale size), the need to break the iron flakes was stated. Several approaches were tested, finally the addition of micronized alumina produced nanoscale particles. Abrasion of the grinding media and breakage of flakes were the main mechanisms for the nZVI production. The physicochemical properties of the obtained particles were: a mean particle diameter of 0.16 µm (by SEM) and a specific surface area of 29.6 $m^2 \cdot g^{-1}$ and a reactivity toward Cr (VI), trichloroethylene and tetrachloroethylene higher than commercial nZVIs.

In reference to the assessment of the effect of a passivation oxide layer on a commercial nZVI (NANOFER STAR, NANORION s.r.o.), it was concluded that the oxide shield of surface-passivated nZVI particles significantly decrease performance. A process to weaken the oxide shield was tested, it consisted in exposing the passivated nZVI to water for 36 hours at w iron / w water concentration of 0.2, just before the reaction with the pollutants. The results show that this activation process increases the effectiveness of the remediation and simplifies the overall handling of the nZVI.

Research on ζ-potential and magnetic attraction of nZVI particles were also studied to detect possible effects on agglomeration.

Publications

Ribas, D., Calderer, M., Martí, V., & Rovira, M. (2015). Effect of different seasonal conditions on the potential of wetland soils for groundwater denitrification. Desalination and Water Treatment, 53(4), 994-1000. DOI: 10.1080/19443994.2013.871344.

Impact factor: 1.173

Ribas, D., Calderer, M., Marti, V., Johnsen, A.R., Aamand, J., Nilsson, B., Jensen, J.K., Engesgaard, P. & Morici, C. Subsurface nitrate reduction under riparian lands takes place in narrow superficial zones. Environmental Technology. DOI: 10.1080/09593330.2016.1276220

Impact factor: 1.760

Ribas, D., Cernik, M., Martí, V., & Benito, J. A. (2016). Improvements in nanoscale zero-valent iron production by milling through the addition of alumina. Journal of nanoparticle Research, 18(7), 1-11. DOI: 10.1007/s11051-016-3490-2.

Impact factor: 2.101

Ribas, D., Černík, M., Benito, J., Filip, J. & Marti, V. Activation process of air stable nanoscale zero-valent iron particles.

Submitted

Ribas, D., Cernik, M., Martí, V., & Benito, J. A. High performance and quality nanoscale zero-valent iron production by milling through the addition of alumina on particles.

In progress

Nguyen, N. H., **Ribas, D.**, Řeháková, H., Vlková, D., Kejzlar, P., & Ševců, A. The impact of micro and nano-iron particles on microorganism community of Harcov lake water.

In progress

Contributions to conferences

Ribas, D., Calderer, M., Martí, V., & Rovira, M. (2013). Effect of different seasonal conditions on the potential of wetland soils for groundwater denitrification. International Joint CB-WE-MED Conference, Tunis (Tunisia). Oral presentation.

Martí, V., Royo, N., Gibert, O., Valderrama, C., Martínez, M.R. **Ribas, D**., & Jubany, I. (2015). Denitrification capacity of leachates from wetland soils and vegetal biomass in the Llobregat river basin. AquaConSoil, Copenhagen (Denmark). Poster presentation.

Ribas D., Benito J. A., Martí V., Jubany I., & Černík M. (2015). Lab scale fabrication of nano Zero Valent Iron (nZVI) particles for groundwater remediation by milling. AquaConSoil, Copenhagen (Denmark). Poster presentation.

Pešková, K., Jaroslav, N., **Ribas, D.,** & Černík, M. (2015). Methodology of laboratory test for the description and comparison of the reactive and migration properties of new types of iron nanoparticles. AquaConSoil, Copenhagen (Denmark). Poster presentation.

Ribas D., Masopustova Z., Benito J. A., Martí V., Jubany I., & Černík, M. (2015). Study of the cryomilling technique for the production of nano Zero Valent Iron (nZVI) particles. AquaConSoil, Copenhagen (Denmark). Poster presentation.

Pešková, K., Černík, M., **Ribas D.**, Benito J. A., Martí V., Parma, P., Lacinová, L., Zbořil, R. & Filip, J. (2015). Oxidic shield and its influence on the reactivity and migration of air stable iron nanoparticles. NANOCON, Brno (Czech Republic). Oral presentation.

Benito J.A., **Ribas D.,** & Martí, V. (2015). Manufacturing of iron nanopowders by mechanical milling. Euro PM2015 proceedings: powder manufacturing, Reims (France). Oral presentation.

Ribas, D., Cernik, M., Martí, V., & Benito, J. A. (2016). Improvements in nZVI production by wet milling through the use of alumina. nanoRem 3rd annual meeting, Manchester (United Kingdom). Oral presentation.

Martí, V., Jubany, I., **Ribas, D.**, Tortosa, A., Gibert, O., Valderrama, C., & Martínez M. R. (2016). Lab scale study of continuous nitrate reduction with leachates from reed biomass. 10 th ISEB conference 2016, Barcelona. Poster presentation.

Ribas, D., Cernik, M., Martí, V., & Benito, J. A. (2016). nZVI Production by Wet Milling through the Addition of Alumina. NANOCON, Brno (Czech Republic). Oral presentation.

Martí, V., Benito, J. A., Martínez, M. R., Navalón, M., Solé, J., & **Ribas, D.**, (2016). Adsorption of Arsenic from groundwater onto nanoparticles obtained by hematite milling. NANOCON, Brno (Czech Republic). Poster presentation.

Nguyen, N. H., **Ribas, D.**, Řeháková, H., Vlková, D., Kejzlar, P., & Ševců, A., (2016). The impact of micro- and nano-iron particles on microorganism community of HARCOV lake water. NANOCON, Brno (Czech Republic). Oral presentation.

Ribas, D., Pešková, K., Cernik, M., Filip, J., Benito, J. A., & Martí, V., (2016). Production of abrasive milling nZVI and activation of air stable nZVI as methods to improve groundwater remediation. Nanoremediation for Soil and Groundwater Clean-up - Possibilities and Future Trends - Final

Conference EU-FP7 NanoRem, within DECHEMA. Frankfurt am Main (Germany). Accepted poster presentation.

Martí, V., Benito, J. A., **Ribas, D.**, Martínez, M. R., Cernik, M., & Jubany, I. (2017). Study of iron and hematite nanoparticles production by top to down approach and its reactivity for groundwater remediation. AquaConSoil Lyon (France). Accepted oral presentation.

Internships

Under the Ph. D. programme three fruitful internships were completed:

Technical University of Liberec, Institute for nanomaterials, Advanced Technologies and Innovation. Advisor: Professor Miroslav Černík. From: 04/05/2014 - To: 03/08/2014 (92 days). Grand: EEBB-I-14-08874.

Topics: Characterization of the oxide shell of nano Zero Valent Iron (nZVI) particles, including its chemical composition and thickness. Development of methods to remove to oxide shell, leading particle reactivation and assessment of a reactivation method effectiveness.

Technical University of Liberec, Institute for nanomaterials, Advanced Technologies and Innovation. Advisor: Professor Miroslav Černík. From: 01/02/2015 - To: 22/02/2015 (22 days).

Topics: Reactivity quantification through nZVI reactivity against Cr (VI) and chlorinated aliphatic hydrocarbons (Trichloroethylene and Tetrachloroethylene) of different commercial nZVI and nZVI produced by milling at CTM-UPC.

LeHigh University, Civil and Environmental Engineering, PA, USA. Advisor: Sibel Pamukcu. From: 20/04/2015 - To: 14/08/2015 (117 days). Grand: EEBB-C-15-00669.

Topics: ζ-potential – pH titration and isoelectric point determination of commercial nZVI particles and other developed by milling in CTM-UPC. Exploration of nZVI mobility assisted by electric fields. Characterization of hydrophobic – hydrophilic proprieties and transitions of a thermoresponsive polymer Poly(N-isopropylacrylamide).

Table of Contents

Main abbreviations

(n)	Number of replicates.
ANAMMOX	ANaerobic AMMonium OXidation
BET-SSA	Brunauer–Emmett–Teller Specific Surface Area
BH	BoroHydride
BPR	Ball to Powder Ratio
CAH	Chlorinated Aliphatic Hydrocarbons
CIP	Carbonyl Iron Powder
cis-DCE	*cis*-1,2-Dichloroethene
d	Mean particle diameter
DNAPL	Dense Non-Aqueous Phase Liquids
DNRA	Dissimilatory Nitrate Reduction to Ammonium
DOC	Dissolved Organic Carbon
EC	Electrical Conductivity
EDX	Energy-Dispersive X-ray spectroscopy elemental analyser
GC-MS	Gas Chromatography – Mass Spectrometry
HD	Heterotrophic Denitrification
HEPA	High Efficiency Particulate Arrestance
HR-XPS	High-resolution X-ray photoelectron spectroscopy
k	Reaction Rate constant
LD	Laser Diffraction particle size analysis
LNAPL	Light Non-Aqueous Phase Liquid
LOI	Loss On Ignition
M	Moisture
MEG	Mono Ethylene Glycol
mZVI	micro Zero Valent Iron
NR	Nitrate Reduction
NRP	Nitrate Reduction Potential
nZVI	nano Zero Valent Iron
OM	Organic Matter
ORP	Oxidation Reduction Potential
P_B	Percentage of particles below 1 µm
PCA	Principal Component Analysis
PCE	Perchloroethylene or Tetrachloroethylene
PCM	Perchlorometane, Carbon Tetrachloride or Tetrachloromethane

PEG	PolyEthylene Glycol
PRB	Permeable Reactive Barriers
SEM	Scanning Electron Microscopy
SHE	Standard Hydrogen Electrode
SSA	Specific Surface Area
TCE	Trichloroethylene
TCM	Trichloromethane
TEM	Transmission Electron Microscopy
TOC	Total Organic Carbon
XRPD	X-Ray Powder Diffraction
ZVI	Zero Valent Iron
ζ-potential	Zeta-Potential

1 Introduction

1.1 General overview

Freshwater is a very scarce resource. Despite the common perception of the Earth as a blue planet, of the total existing water ($1.39 \cdot 10^9$ km^3), freshwater only represents 2.5% ($1.06 \cdot 10^7$ km^3). Freshwater must be considered as a limited resource. Moreover, from this total percentage of freshwater: 68.7% of it is in permanent solid state trapped in ice caps, glaciers and permanent snow, 30.1% ($1.05 \cdot 10^7$ km^3) is groundwater and the easily accessible superficial freshwater represents just a 0.26% ($9.31 \cdot 10^4$ km^3), *Fig. 1.1 and Table 1.1*, *(Gleick, 1996)*. Decisively, freshwater is not a widespread unlimited resource, it should be viewed as a strategic asset in the modern human civilization.

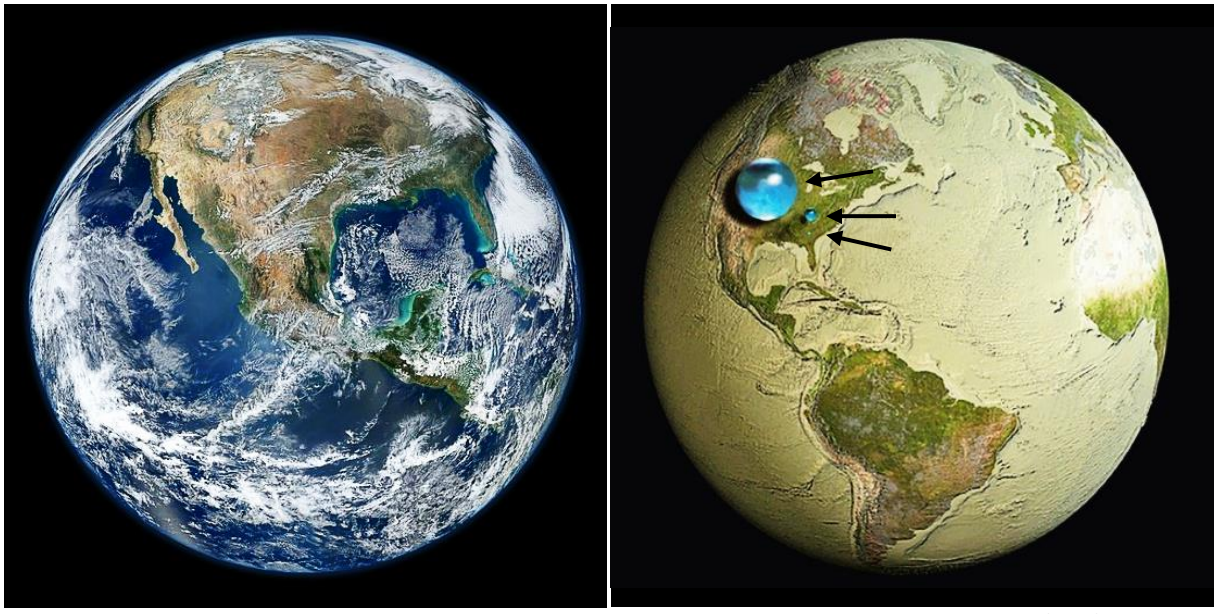

Fig. 1.1 (Left) The Blue Marble, *(NASA et al., 2012)*. (Right) globe illustration: big sphere ($1.39 \cdot 10^9$ km^3 – Ø: 1384 km) all earth's water, medium sphere ($1.06 \cdot 10^7$ km^3 – Ø: 273 km) all liquid freshwater, small sphere ($9.31 \cdot 10^4$ km^3 – Ø: 56 km) superficial liquid freshwater, *(Perlman, 2012)*.

Management of water resources and water availability is a global challenge which is threatened by advancing/constant pollution *(Water, 2012)*, global climate change *(Field et al., 2014)*, human overpopulation *(Steinfeld et al., 2006; Thornton, 2010)*, non-sustainable industrialization and regional conflicts *(Griffiths and Lambert, 2013)* as stated by intergovernmental organizations and scientific community.

> "*Water is at the core of sustainable development. Water resources, and the range of services they provide, underpin poverty reduction, economic growth and environmental sustainability. From food and energy security to human and environmental health, water contributes to improvements in social wellbeing and inclusive growth, affecting the livelihoods of billions*" *(WWAP, 2015)*.

Table 1.1 Water resources, its total amount and its relative abundance over the total and the fresh water, *(Gleick, 1993)*. Percentages may not sum to 100 percent due to rounding.

Water source	Water volume km^3	Total water %	Fresh water %
Oceans, Seas, & Bays	$1.34 \cdot 10^9$	96.54	---
Ice caps, Glaciers & Permanent Snow	$2.41 \cdot 10^7$	91.74	68.6
Groundwater	$2.34 \cdot 10^7$	91.69	---
Fresh	$1.05 \cdot 10^7$	90.76	30.1
Saline	$1.29 \cdot 10^7$	90.93	---
Soil Moisture	$1.65 \cdot 10^5$	90.001	90.05
Ground Ice & Permafrost	$3.00 \cdot 10^5$	90.022	90.86
Lakes	$1.76 \cdot 10^5$	90.013	---
Fresh	$9.10 \cdot 10^4$	90.007	90.26
Saline	$8.54 \cdot 10^4$	90.007	---
Atmosphere	$1.29 \cdot 10^4$	90.001	90.04
Swamp Water	$1.15 \cdot 10^4$	90.0008	90.03
Rivers	$2.12 \cdot 10^3$	90.0002	90.006
Biological Water	$1.12 \cdot 10^3$	90.0001	90.003

1.1.1 Groundwater pollution challenge

Groundwater accounts for 30.1% of the total freshwater or the 96.0% of the total liquid freshwater, excluding ice caps, glaciers and permanent snow *Table. 1.1 (Gleick, 1996). Therefore, it constitutes* the most important source of usable water. Groundwater is widely spread, for example, following river basins where sediment deposits created a permeable media that forms aquifers *(Anderson, 1989; Vidon and Hill, 2004a; Dahl et al., 2007)*. The underground water body in river basins are formed by the wetted channel, the parafluvial and floodplain hyporheic zones and the groundwater. Interestingly, groundwater usually represents the most important contributor to the baseflow of the rivers *(Sophocleous, 2002),* where an important exchange between superficial water and groundwater bodies is produced. This system is considered as a continuum by some authors and regulations *(Brunke and Gonser, 1997)*.

Nowadays, anthropic pollution is threatening groundwater quality. Pollution sources are present across all systems of modern civilization, from all sectors of economy: farming, cropping, mining, heavy and light industry, services, etc. to city infrastructures, such as: wastewater and landfilling. *(Zaporozec et al., 2002)*, *Fig. 1.2*.

Due to the intrinsic nature of aquifers; low flow rates *(Vidon and Hill, 2004b)* and a complex matrix compared to superficial water (i.e.: rivers), natural dilution and attempts to eliminate the pollution are more complex and slow. Consequently, aquifers are a long term source of pollution to the river baseflow.

Fig. 1.2 Surface and groundwater sources pollution sources *(Foundation for Water Research, 2016)*

1.1.2 European Union legal framework

Under this context, the European Union has developed a consequent legal framework. This is articulated by the following three main directives:

- The European Union Water Framework Directive - integrated river basin management for Europe *(EU Directive 2000/60/CE)*. It is the most significant piece of European water legislation and it is updating most of the existing regulations. The keystone of this directive is to consider all the connected waterbodies a continuum under the river basin denomination. It is an important advance in groundwater protection that dictates assessment of quantitative status (stock monitoring) and chemical status (pollution monitoring) of this reservoir. Particularly, groundwater is defined as:

  > *"All the water which is below the surface of the ground in the saturation zone and in direct contact with the ground or subsoil. In addition, aquifer is defined as a subsurface layer or layers of rock or other geological strata of sufficient porosity and permeability to allow either a significant flow of groundwater or the extraction of significant quantities of groundwater."*

- The Nitrates Directive *(EU Directive 91/676/EEC)* was developed to protect water quality across the European Union by preventing nitrates from: agricultural sources, polluted ground and surface waters by promoting the use of good farming practices. The Nitrates Directive forms an integral part of the Water Framework Directive. The implementation of this directive is divided in the following measures:

- Identification of polluted water bodies, or at risk of pollution, such as: surface freshwater, groundwater, estuaries, coastal waters and marine waters.

- Designation as "Nitrate Vulnerable Zones"(NVZs) of: eutrophic river areas or the whole territory of the country.

- Establishment of “Codes of Good Agricultural Practice” (CGAP) to be implemented by farmers on a voluntary basis. Codes should include: limitation of the periods when nitrogen fertilizers can be applied, prevention of nutrients leaching into waters, limitation of the conditions for fertilizer application.

- Establishment of action programmes to be implemented by farmers within NVZs on a compulsory basis.

- National monitoring and reporting.

- The Groundwater Directive *(EU Directive 2006/118/CE)*. Concerning the protection against pollution and deterioration of groundwater, this directive is ruled by the following principles:

  - Groundwater is the most sensitive and the largest body of freshwater in the European Union and, in particular, also a main source of public drinking water supply in many regions.

  - Groundwater bodies used for abstraction of drinking water or intended for such future use must be protected to avoid deterioration of the water quality. This is aimed to reduce the level of the present and future purification treatment required in the production of drinking water.

  - In order to protect the environment as a whole, and human health in particular, detrimental concentrations of harmful pollutants in groundwater must be avoided, prevented or reduced. Particularly, nitrate threshold where groundwater fails quality status is ≥ 50 $mg \cdot l^{-1}$.

  - Chemical status of groundwater bodies should be reported so as to prevent and control groundwater pollution, including criteria to assess good chemical status and criteria to identify significant sustained upward trends.

  - Chemical status of the contact between groundwater and surface water. In order to protect the groundwater dependent ecosystems along rivers, lakes, wetlands and coastal areas.

  - Research should be conducted in order to provide better criteria for ensuring groundwater ecosystem quality and protection.

1.1.3 European Union 7th Framework Programme

7th Framework Programme (FP7) was the EU's main instrument for funding research in Europe and it ran from 2007-2013. FP7 was designed to respond to Europe's employment needs, competitiveness and quality of life. It lasted for seven years from 2007 to 2013. The programme had a total budget of over 50,000 M€.

Indeed, FP7 was a key tool to respond to Europe's needs in terms of jobs and competitiveness, and to maintain leadership in the global knowledge economy contributing to the development of a knowledge-based economy and society *(EU Decision No 1982/2006/EC)*. These fundings were spent on grants to research actors all over Europe and beyond, in order to co-finance research, technological development and demonstrative projects. Grants were determined on the basis of calls for proposals and a peer review process, which were highly competitive.

In the light of the strong need to preserve and clean the groundwater sources, the developed EU legal framework and the FP7 programme, this thesis found a key source of motivation, driving force, resources and acceptance. For this reason this thesis is focused on new research approaches for groundwater remediation, specifically to:

- Promote and understand remediation mechanisms naturally present in the groundwater – river interface. Denitrification has a huge potential as a remediation mechanism but factors affecting the process performance remain largely unknown.

- Improve remediation solutions based on nanomaterials. New techniques have arisen thanks to the appearance of these new kind of materials. nano Zero Valent Iron (nZVI) is a paradigmatic example showing a high reactivity against pollutants and mobility into aquifers. It is then important to study and boost this technology.

1.2 Remediation based on natural systems, denitrification

Natural remediation consists of using the self-resources of the environment to eliminate or immobilize a particular pollutant. In this thesis, denitrification was studied as a case of natural remediation, specially the factors governing its performance in wetlands.

Wetlands and floodplains play key roles in the environment serving human interests with an economic value that is estimated in the range of several thousand dollars per hectare and year *(Groot et al., 2012)*. These services include, among others: climate stability due to carbon sequestration, coastal protection, water flow and flood regulation and water quality improvement through pollution control and detoxification *(Flight et al., 2012),* where the latter is one of the main contributors to wetland antrophic value *(Groot et al., 2012)*.

Wetlands are increasingly recognized and restored as critical water quality improvement zones, for example nitrate removal can easily achieve an efficiency >90% in natural wetlands, *(Mayer et al., 2005)*. In the last three decades, natural wetland principles have been implemented in waste water treatment plants to meet the increasing restrictive nitrogen, phosphorus and organic matter emission limits *(Wu et al., 2014)*. Lastly, these principles are being applied to restore and build new wetlands as a buffer zones for mitigating pollution of surface water bodies due to runoff from adjacent agricultural fields *(Gumiero et al., 2013)*.

1.2.1 The nitrogen pathways

The nitrogen cycle is divided principally in four active pools: atmosphere, hydrosphere, pedosphere and biosphere. The transformations between them are governed through several mechanisms: fixation, ammonification, nitrification, denitrification, assimilation, ANaerobic AMMonium OXidation (ANAMMOX), Dissimilatory Nitrate Reduction to Ammonium (DNRA) and the Haber – Bosch process *Fig. 1.3*. Human impact on the nitrogen cycle is significant, it is produced by the overload of the hydrosphere and pedosphere with nitrogenous nutrients *(Galloway et al., 2008)*.

Nitrogen is an essential and scarce element for vegetal growth. Therefore, it is a very limiting nutrient in the biosphere and consequently, it must be supplied regularly to the crops. Nitrogen is obtained from three main sources:

- Synthetic. This is the main origin of nitrogen for anthropic uses since geologic or biologic usable pools are very limited. Atmospheric nitrogen is industrially fixed to ammonia through the Haber - Bosch process (energy reaction: *Eq. 1.1*) *(Gruber and Galloway, 2008)*. Afterwards, ammonia is converted to fertilizers commonly based on urea, ammonium nitrate or nitrate and applied to crops. This process is so prevalent that over 80% of the nitrogen in the protein of an average human is derived from this source, *(Howarth et al., 2008)*.

$$N_{2\,(g)} + 3\,H_2 \rightarrow 2\,NH_{3\,(g)} \qquad \textbf{Eq. 1.1}$$

- Waste by-products. Such as manure, as an important fraction of the agricultural output is used to feed livestock, nitrogen goes through the trophic chain and ends up in the manure. Finally, in some degree, it is reapplied onto the crops.

- Nitrogen fixing plants. This is the natural alternative to Haber - Bosch process. It is driven by the plants of Legume family, *Fabaceae*. They contain symbiotic bacteria, commonly from *Rhizobium* genus, within nodules in the root systems. These bacteria produce organic nitrogenated compounds that are absorbed by the host plant and spread across tropic system and soil.

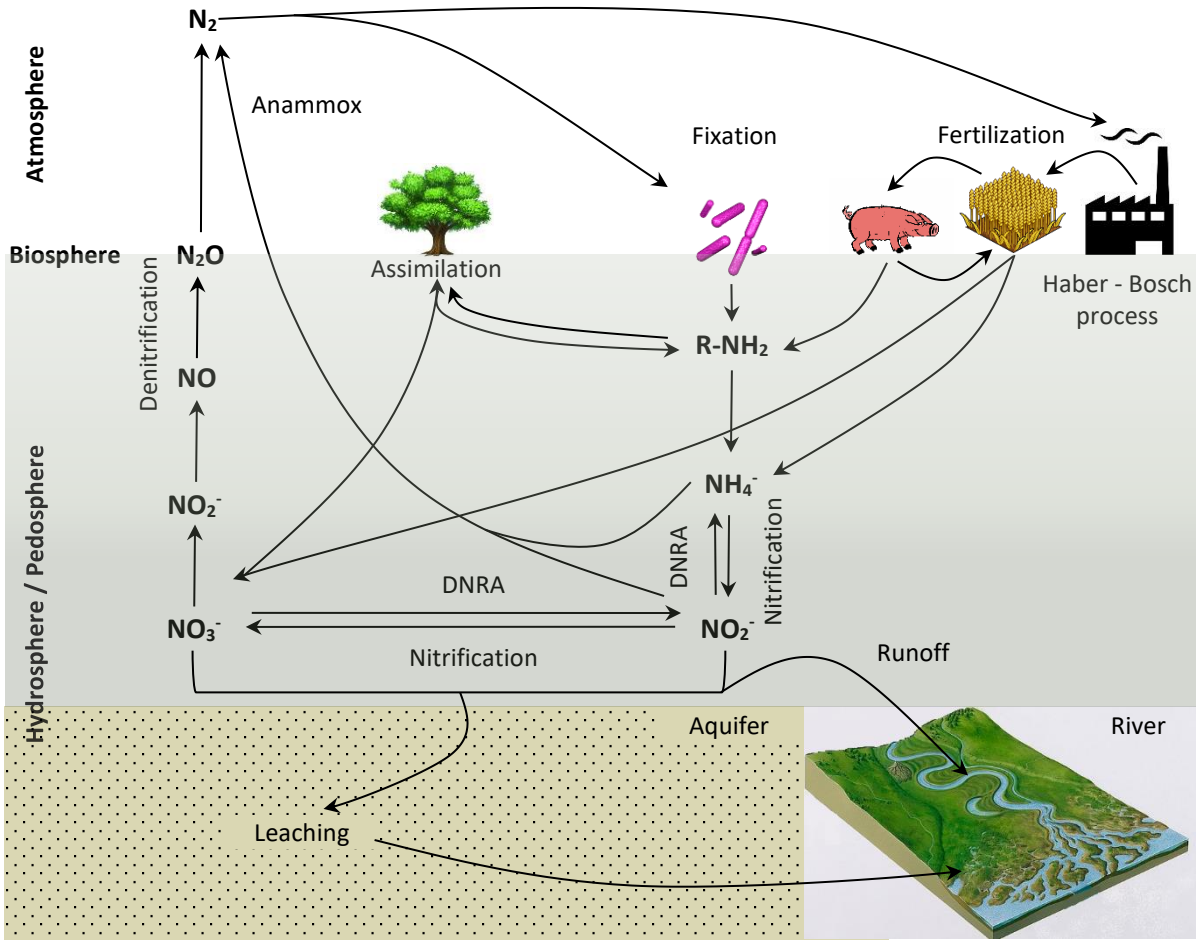

Fig. 1.3 The nitrogen cycle.

Nitrogen overload emerges because synthetic fertilizers and manure are applied in excess and washed out from the agricultural fields into the groundwater, wetlands and rivers *(Stein et al., 2016)*. Manure is not usually seen as a valuable product but as a residue, because crop zones are decoupled from livestock zones, being costly to transport it to crops. Hence, there is a manure surplus which is applied to the fields near the manure-producing farms, therefore exceeding soil needs. The widespread and indiscriminate application of nitrogen into the environment leads to what is called diffuse pollution.

New approaches and techniques to reduce this pollution are required because, alongside the justified environmental concerns, a very restrictive legislation *(EU Directives 91/676/EEC and 2000/60/CE)* is being applied. Pollution and legislation are increasing the pressure to find new solutions.

A close view into the nitrogen transformation steps between the different nitrogen pools and the involved microorganism reveals some interesting processes, some of them usable for remediation:

- Oxidation of ammonium to nitrite. If nitrogen fertilizers are composed of ammonium ($NH_4^+{}_{(aq)}$) or generate it, which is common, then it is easily immobilized into the soil (due to its positive charge). Hereafter, it is oxidized by two different groups of organisms and ammonia-oxidizing archaea. Oxidation of ammonium to nitrite is the limiting steps of nitrification. Redox half-reaction *Eq. 1.2* and scheme *Fig. 1.4*, *(Hatzenpichler, 2012)*.

$$NH_4^+{}_{(aq)} + O_2 \rightarrow NO_2^-{}_{(aq)} + 4\,H^+ + 2\,e^- \qquad \textbf{Eq. 1.2}$$

- Oxidation of nitrite to nitrate. Nitrite is easily oxidized to nitrate ($NO_3^-{}_{(aq)}$) completing the nitrification process, which is mainly done by bacteria of the genus *Nitrobacter* and *Nitrospira*. Redox half-reaction *Eq. 1.3* and scheme *Fig. 1.4*, *(Cebron and Garnier, 2005)*.

$$NO_2^-{}_{(aq)} + H_2O \rightarrow NO_3^-{}_{(aq)} + 2\ H^+ + 2\ e^- \qquad \textbf{Eq. 1.3}$$

Both nitrate and nitrite are very soluble in water and negatively charged, thus they are not retained in the soil (contrary to NH_4^+). This fact brings a great mobility to these anions which spread across runoff and groundwater, moving effortlessly through the river basin. The main concerns of nitrate and nitrite pollution are: eutrophication and, regarding human health, methemoglobinemia disease caused mainly by nitrite. Methemoglobinemia is characterized by the presence of a higher concentration of methemoglobin rather than haemoglobin which has a lower affinity to oxygen. Methemoglobin increases the oxygen blinding stretch of to the remaining heme sites, leading to an overall reduction of the ability of the red blood cells to release oxygen to the tissues *(Wright et al., 1999)*. Consequently, the drinking water legislation *(EU Directive 2006/118/CE and 98/83/CE)* sets a maximum level of 50 $mg{\cdot}l^{-1}$ of nitrate and 0.5 $mg{\cdot}l^{-1}$ of NO_2, respectively.

- Reduction of nitrate to nitrogen and nitrous oxide. Denitrification is the key step of remediation which allows the conversion of nitrate to nitrogen (N_2) or to the intermediate compound nitrous oxide (N_2O). Both are gas species pumping out nitrogen compounds of the hydrosphere and pedosphere. It is accomplished by a very diverse group of facultative anaerobic bacteria, redox half reactions: *Eq. 1.4, 1.5, 1.6, 1.7* and scheme *Fig. 1.4*.

$$NO_3^-{}_{(aq)} + 2e^- + 2H^+ \rightarrow NO_2^-{}_{(aq)} + H_2O \qquad \textbf{Eq. 1.4}$$

$$NO_2^-{}_{(aq)} + e^- + 2H^+ \rightarrow NO_{(aq)} + H_2O \qquad \textbf{Eq. 1.5}$$

$$2NO_{(aq)} + 2e^- + 2H^+ \rightarrow N_2O_{(g)} + H_2O \qquad \textbf{Eq. 1.6}$$

$$N_2O_{(g)} + 2e^- + 2H^+ \rightarrow N_{2\,(g)} + H_2O \qquad \textbf{Eq. 1.7}$$

Other secondary processes which are important for being competitive or collaborative with denitrification:

- Anammox, (ANaerobic AMMonium OXidation). In this an autotroph process where nitrite and ammonium are converted directly to nitrogen, this pathway is a relatively new discovery and is a promising technique for wastewater treatment. However, the long replication times of these bacteria limits its wide usage. The energy reaction *Eq. 1.8* and scheme *Fig. 1.4, (Mulder et al., 1995)*.

$$NH_4^+{}_{(aq)} + NO_2^-{}_{(aq)} \rightarrow N_{2\,(g)} + 2\ H_2O \qquad \textbf{Eq. 1.8}$$

- DNRA, (Dissimilatory Nitrate Reduction to Ammonium). This is a competing mechanism for denitrification, it occurs when an excess of organic matter is present reconverting nitrate to ammonium. There are many bacteria capable of performing this pathway including: *Alcaligenes faecalis*, *Alcaligenes xylosoxidans*, *Bradyrhizobium japonica*, *Blastobacter denitrificans* and numerous from the genus *Pseudomonas, (Rütting et al., 2011)*. The overall reaction was first presented by *(Robertson et al., 1996), Eq. 1.9* and *Fig. 1.4*

$$2CH_2O + NO_3^-{}_{(aq)} + 2H^+ \rightarrow NH_4^+{}_{(aq)} + 2CO_2 + H_2O \qquad \textbf{Eq. 1.9}$$

- In heterotrophic and autotrophic denitrification part of the nitrate is used in anabolic pathways, increasing the bacterial biomass. The energy and biomass (empirically simplified to $C_5H_7O_2N$) reaction differs among the electron donor used, i.e.: *Eq. 1.10* shows autotrophic

denitrification using hydrogen meanwhile *Eq. 1.11* is the heterotrophic denitrification with methanol and *Eq. 1.12* with acetate, *(Bruce and Perry, 2001)*.

$$0.5H_2 + 0.1773NO_3^-{}_{(aq)} + 0.0246CO_2 + 0.1773H^+ \rightarrow 0.00493C_5H_7O_2N + 0.0862N_{2\,(g)} + 0.5714H_2O$$

Eq. 1.10

$$0.1667CH_3OH + 0.1561NO_3^-{}_{(aq)} + 0.1561H^+ \rightarrow 0.00954C_5H_7O_2N + 0.0733N_{2\,(g)} + 0.3781H_2O + 0.119CO_2$$

Eq. 1.11

$$0.125CH_3COO^- + 0.1438NO_3^-{}_{(aq)} + 0.1438H^+ \rightarrow 0.0122C_5H_7O_2N + 0.0658N_{2\,(g)} + 0.125HCO_3^- + 0.0639CO_2 + 0.1542H_2O$$

Eq. 1.12

The amount of immobilized nitrogen as biomass depends on the electron donor used. It represents an small amount compared to the expelled dinitrogen, for example the immobilized nitrogen is 6.1% using methanol as electron donor and 8.5% for acetate. In natural media similar electron donors composed by short alcohols and volatile fatty acids would be expected as products of anaerobic digestion. In the present thesis, where heterotrophic denitrification is studied, nitrate and nitrite depletion and ammonium generation (to weigh the DNRA) are analysed and used to assess denitrification. This method assumes that nitrogen is not used into the biomass synthesis, but because of the small amount used in this way and of the difficulty to scale up more precise methods (i.e.: acetylene procedure *(Yoshinari et al., 1977)* up to the amount of samples studied, it was chosen.

1.2.2 Riparian zones / Wetlands

Transition from the river to the land is known as a riparian zone, it is a very particular zone joining characteristics of both dry land and the river. Depending on the hydric regime, these can be classified as: wetlands or floodplains although the borders between them are unclear *(Cole, 2016)*.

Wetlands are lands that are saturated with water either permanently or seasonally, being the water table very close to the surface *(Cole, 2016)*. It has a characteristic ecology, considered as one of the most biodiverse of all ecosystems. Aquatic plants are adapted to the particular hydric soil regime, some examples are: hydrophytes and reeds from the: *Poaceae*, *Cyperaceae*, *Sparganiaceae* and *Restionaceae* families. There is a close link between the flora and the first organic horizon of the soil, which can be submerged and hence become anaerobic, called peat layer. An important flux of fresh organic matter is deposited constantly on the peat layer, then this organic matter undergoes an anaerobic biodegradation, leaching labile organic matter through the deeper horizons of the soil *(Hill and Cardaci, 2004).*

Floodplains are areas of land adjacent to the active channel of the river. These zones are not permanently saturated with water since water regime is governed by flooding during periods of high discharge. However, the water table is almost always close to the surface due to the proximity of the active channel of the river *(Dahl et al., 2007; Cole, 2016)*. The floodplain ecosystem is dominated by deciduous forests with a very high productivity because of the broad availability of water and essential nutrients. This high production rate supplies, as in the case of the wetlands, a constant flux of organic matter to the soil, *(Arora et al., 2016)*.

Both wetlands and floodplains connect the water table, seepage and the run off with a rich organic matter soil, being a very suitable interface for denitrification. Denitrification is produced either as an autotrophic and heterotrophic process. However, autotrophic pathway requires non common electron acceptors in the soil, such as: sulphur *(Komor and Fox, 2002)* and hydrogen *(Smith et al., 1994)*. On the

other hand, heterotrophic denitrification uses organic matter, simplified here as CH_2O in the overall reaction *Eq. 1.13, (Jørgensen et al., 2004; Appelo et al., 2007)*. Heterotrophic denitrification is performed by i.e. bacteria genus: *Pseudomonas*, *Cytophaga-Flavobacter-Bacteroides* and *Hyphomicrobi, (Madigan et al., 2000)*.

$$5CH_2O_{(aq)} + 4NO_3^-{}_{(aq)} \rightarrow 2N_{2(g)} + 4HCO_3^-{}_{(aq)} + 3H_2O_{(aq)} + CO_{2(g)} \qquad \textbf{Eq. 1.13}$$

As previously exposed, organic matter is widely available in upper layers of the wetlands and floodplains soils, moreover, these zones intercept polluted water coming from the nitrogen sources i.e.: crops and farms making them very suitable for nitrate interception and elimination.

One very interesting approach to the problem of reducing leached nitrogen from agricultural diffuse sources is the establishment of buffer zones between the pollutant source areas and the receiving waters. Being a very promising low-cost, sustainable and ecologically-friendly approach for mitigating the diffuse pollutants such as nitrate *(Tournebize et al., 2015)* and pesticides *(Krutz et al 2005; Reichenberger et al., 2007)*. Recently, several wetlands have been used as a restoration technology in many countries. Some wetlands have been re-established, other have been approved for restoration and some have been considered for further investigation, *(Funen County, 2003; Hoffmann and Baatrup-pedersen, 2007)*. Moreover, recent work indicates that such zones also might be successful in decreasing the transport of pesticide residues into the river, *(Krutz et al., 2005; Reichenberger et al., 2007)*.

Despite these very promising perspectives, there is insufficient information on the importance of: deep subsurface flow, the global effectiveness of the system, its performance in the deep layers of the soil and the negative effects of seasonal disturbances (winter period, a drought period and a flood periods).

Denitrification research in this thesis is focused on providing new information that would help to decipher these uncertainties.

1.2.3 AQUAREHAB Project

AQUAREHAB (Development of rehabilitation technologies and approaches for multipressured degraded waters and the integration of their impact on river basin management) (FP7 ENV 2008.3.1.1.1.) was a large-scale EU financed research project under the 7th Framework Programme of the European Union in rehabilitation technologies for degraded water systems presenting quality and quantity problems. The project developed innovative rehabilitation technologies for soil, groundwater and surface water to cope with a number of different priority contaminants (nitrates, pesticides, chlorinated compounds, aromatic compounds and mixed pollution, among others) within heavily degraded water systems. Developed methods were focused on determining the long-term impact of the innovative rehabilitation technologies to reduce river and groundwater pollution. Lastly, the project promotes the uptake of successful technologies for use in river basin management measures.

It was coordinated by VITO (Belgium) involving a consortium of 19 partners. The project started 1st May 2009 and lasted until the end of 2013 (56 months).

The present thesis shows part of the results of Work Package 1 which is dedicated to the study of the role of wetlands in nitrogen discharge reduction from groundwater to rivers.

1.3 nano Zero Valent Iron remediation

Frequently, natural occurring mechanisms in soil and aquifers are insufficient to decompose or immobilize pollutants. This can be the result of: lack of a feasible biological pathway, a low performance because the process is not thermodynamically very favourable or some nutrients or co-substrates are not present. Where natural remediation does not work, assisted or artificial remediation should be provided. A very diverse range of techniques have been applied, however, these are limited depending on the properties of the contaminant and the aquifer. Some examples include: surfactant flushing, in situ chemical oxidation, gas, steam and thermal treatments, reactive permeable barriers, bioremediation, excavation, pump and tread and nano Zero Valent Iron (nZVI) injection, *(Yao et al., 2012; Mao et al., 2015)*.

1.3.1 Pollutants in aquifers

Owing to the intrinsic nature of the aquifer matrix and the slow hydrogeological regime of these systems, pollutants find a natural enclosure where remediation becomes very challenging. The obstacles for a successful remediation can be classified according to the properties of the contaminants and hereafter, contaminant behaviour and remediation strategies can be addressed. Common cases are:

Low solubility organic compounds

These pollutants have low water solubility, usually in the range of milligrams per litre. Consequently, they form a new and insoluble liquid phase in the aquifer. The properties of these phases are basically determined by the density of the constituent compounds, because following the solubility, the governing factors in the aquifer are buoyancy and capillarity forces.

- Light Non-Aqueous Phase Liquid (LNAPL), the pollutant phase has a lower density than water. It causes of the phase to spread over the water table. This is, for example, the case of some hydrocarbons, such as: gasoline, benzene, toluene and xylene.

- Dense Non-Aqueous Phase Liquid (DNAPL), the pollutant phase has a larger density than water. The pollutant phase tends to mobilize downwards only stopping when reaching an impermeable bedrock, *(Vrba and Adams, 2008)*. During the immersion it forms multiple horizontal layers or lenses, connected by vertical trails of residual saturation, *Fig. 1.6*. Examples of these pollutants are: chlorinated aliphatic hydrocarbons (chlorinated ethenes, ethanes, methanes and benzenes), creosote and polychlorinated biphenyl (PCBs).

DNAPL are considered more difficult and expensive to remediate because their penetration into the aquifer makes it difficult to locate and remediate. On the other hand, LNAPLs float on top of the underground water table, where pump and treat strategies can be easily implemented.

Heavy metals

Solubility of heavy metals is governed by the pH. If pH conditions are favourable, some heavy metals become highly soluble, having a great mobility in the aquifer waterbody, due to the groundwater flux and diffusion. Common examples include harmful metal ions, such as: Cr(VI), Cd(II), As(III), As(V) and Pb(II) *(O'Caroll et al., 2013)*.

Remarkably, Zero Valent Iron (ZVI) has the capability to be useful in both types of pollutants, organic hydrophobic and heavy metals, being able to eliminate some organic compounds and immobilize a vast number of harmful ions.

Traditionally, ZVI has been used in millimetric or micrometric form in hundreds of Permeable Reactive Barriers (PRBs) since the early 1990s, *(Gillham and O'Hannesin, 1994)*. PRB is a static in-situ treatment, which intercepts contaminant plume, despite the success of PRBs, they have some important limitations: technical difficulties and associated costs of excavation restrict the depth of the barrier to 30 - 40 m and finally, no direct treatment of the contaminant source is provided, *Fig. 1.4*, *(Tosco et al., 2014)*.

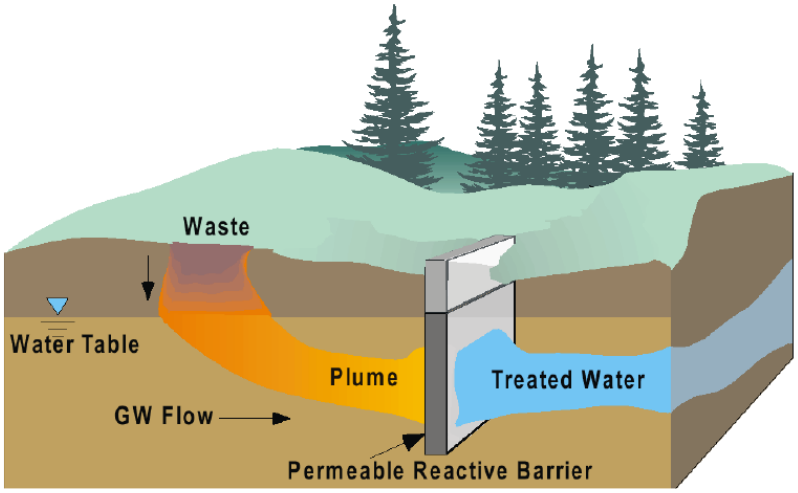

Fig. 1.4 Conceptual schematic of a permeable reactive barrier, *(Mountjoy et al., 2003)*.

The irruption of nanoscale ZVI (nZVI) can overcome most of these problems due to the nanoscale size, allowing its direct release into the underground plume or source (i.e.: DNAPL). nZVI can travel across the aquifer matrix, therefore increasing contact with contaminants, *Fig. 1.5*. Moreover, an important new feature is its high superficial surface area, boosting ZVI reactivity several orders of magnitude, which means faster degradation rates, *(Zhang, 2003).* This increased reactivity of nanoscale iron presents new challenges such as: possible toxicity *(Grieger et al., 2010)* and the pyrophoricity (spontaneous ignition in air) exhibited by nanoscale iron in free atmosphere.

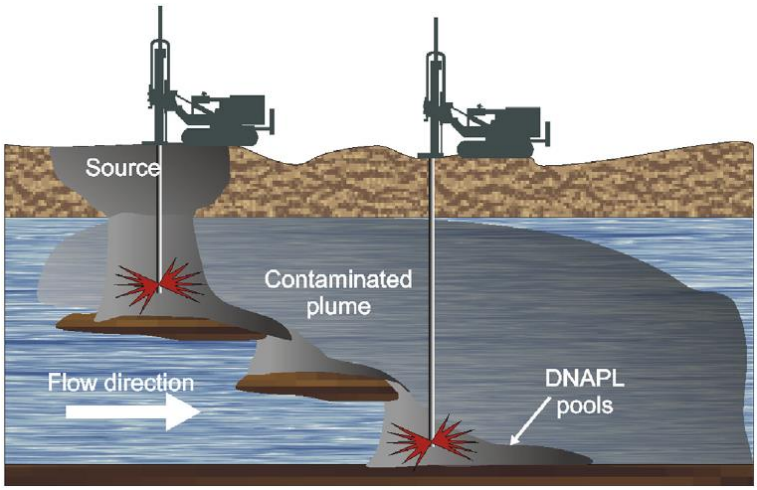

Fig. 1.5 Conceptual schematic of an injection treatment with nZVI, *(Tosco et al., 2014)*.

The most basic form of nZVI consists of spherical zero valent iron (Fe^0) nanoparticles with individual particle dimensions of less than 100 nm, *(Grieger et al., 2010)*. A homologated definition of the boundary between micrometric and nanometric ZVI is not clear, among others, it is challenging due to

the large aggregation / welding of the discrete particles during application and production in most of the present manufacturing methodologies, i.e.: *Fig. 1.6*.

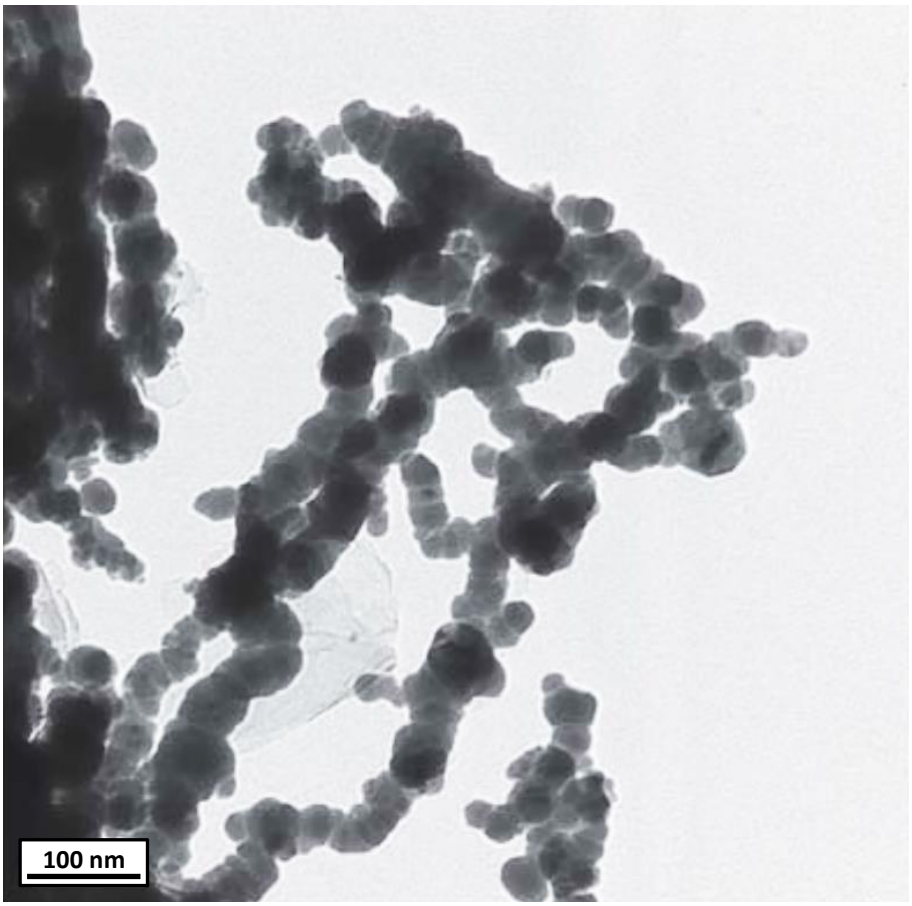

Fig. 1.6 TEM image of fresh nZVI produced by borohydride reduction, *(Zhang and Elliott, 2006)*.

1.3.2 nZVI production methods

In spite of being a very promising technology, nZVI is not yet a widespread commercial technology. This can be attributed to a set of factors: including a precautionary attitude towards nanomaterials, performance concerns regarding mobility and passivation, the fact that the technology is unknown to consultants, governments and site owners and finally the costs, *(Mueller et al., 2012; O'Carroll et al., 2013; Fu et al., 2014)*. Since nZVI particles represent an important fraction of the application cost *(Li, et al., 2006)* and physicochemical characteristics and performance are partially ruled by the production method, it is mandatory to study and improve the present production methods.

The introduction of a straightforward method of nZVI production for remediation research in lab scale was published in 1997, *(Wang and Zhang, 1997).* This marked the appearance of the nZVI field, bringing the introduction of nZVI to many research institutions, thus developing the field and assessing the potentials and limitations. The method consisting in the reduction of iron(III) chloride hexahydrate by sodium borohydride precipitating metallic iron spheres with a diameter between 1-100nm, simplified *Eq. 1.14*.

$$Fe(H_2O)_6^{3+} + 3BH_4^- + 3H_2O \rightarrow Fe^0 \downarrow + 3B(OH)_3 + 10.5H_2 \qquad \textbf{Eq. 1.14}$$

The sodium borohydride reduction method is difficult to scale up for commercial applications due to the cost of sodium borohydride, health and safety considerations involving the synthesis and to the concern that residual boron in iron nanoparticles could leach into the aquifer, *(Sigmund et al., 2008)*.

As of this first process, a collection of new methods have been proposed. These methods can be classified as bottom up or top down. Bottom up entails the production of nanostructures atom by atom, whereas top down starts with large size, granular or microscale materials which are divided up to the nanometric range.

- Bottom up:

  - Thermal reduction. The method is based on the reduction of iron oxide nanoparticles, pentacarbonyl or aqueous Fe^{2+} by thermal energy (350–600 °C) and gaseous reducing agents (H_2, CO_2, CO, etc.), *(Uegami et al., 2006; Crane and Scott, 2012)*.

  - Green synthesis. This method is similar to sodium borohydride reduction but replacing the sodium borohydride for a polyphenolic reducing agents extracted from vegetal sources such as: coffee, green tea, lemon balm and sorghum bran, *(Shahwan et al., 2011)*.

  - Electrolysis. This consists of the electrochemical reduction of a Fe^{2+} salt solution. The attachment of the produced particles into the cathode is a concern, it seems that it can be mitigated using ultrasounds, *(Chen et al., 2004)*.

  - And other: thermal *(Farrell et al., 2003)* and sonochemical *(Koltypin et al., 2004)* decomposition of iron-containing complexes, chemical vapour condensation process using the pyrolysis of iron pentacarbonyl *(Choi et al., 2002)*, sequential synthesis offered by reverse micelles *(Carpenter, 2001)* and ultrasounds *(Tiehm et al., 2009)*.

- Top down:

  - Precision milling, using high energetic ball mills in water *(Li et al. 2009)* or using an inert grinding media, *(Köber et al. 2014)*.

  - And others: electro-exploding wires *(Siwach and Sen, 2008)* and arc discharge *(Kassaee et al., 2011)*.

From all the methods presented, only two have been scaled up and commercialized for remediation. On *Table 1.2*, main features from two nZVI European producers are exposed.

Table 1.2 Production process used in available commercial nZVI.

Production Process	Size & morphology	SSA $m^2 \cdot g^{-1}$	ZVI %	Shipping	Cost €·kg^{-1}
Thermal reduction[1]	≈50 nm spheres (rounded morphology) forming aggregates of few micrometres	25	≈90	- water slurry - oxide shell stabilized - pyrophoric in inert atmosphere	≈100*
Milling[2]	Flakes with a lateral size of several micrometres and a thickness <200 nm	18	>70	- suspended in an inert solvent, ethylene glycol	≈30*

SSA: Superficial Surface Area; [1] *(Soukupova et al. 2015);* [2]*(Köber et al. 2014);* *costs are based on the 2016 feedback from companies: NANORION s.r.o. and UVR-FIA GmbH.

As one can see in *Table 1.2*, the nanoparticles with the best size and morphology properties are the most expensive ones. New and reliable methods for large-scale and cost-effective production are crucial for the success of nZVI remediation method, *(Müller and Nowack, 2010)*. In addition, besides the high costs, the present commercial particles have important limitations concerning: reactivity, mobility and long term storage. There is a crucial need to find new methods able to lower production costs and improve the present properties of the nZVI regarding: size, specific superficial area, mobility, reactivity and Fe(0) content.

1.3.3 Remediation mechanisms, nZVI reactivity

ZVI is being used and studied to remediate a wide range of contaminants, such as: chlorinated organic compounds, nitroaromatic compounds, reduction *(Fu et al., 2014)*, reduce and immobilize harmful metal ions: *(Blowes et al., 2000)* and other ions *(Lin et al., 2016)* also, it is studied for the remediation of emergent pollutants *(Machado et al., 2013)*. Depending on the nature of the contaminant, there are many mechanisms and pathways proposed for iron and its oxides action: reduction, precipitation, co-precipitation and adsorption may be involved, *Fig. 1.7*, *(Tang and Lo, 2013; Ji, 2014)*. It is important to notice that not only the Zero Valent iron is involved in the pollutant remediation, generated oxides such as: magnetite, hematite – maghemite and hydroxides also play an important role in adsorption and in some degree with reduction for iron (II) oxides*, (Tang and Lo., 2013)*.

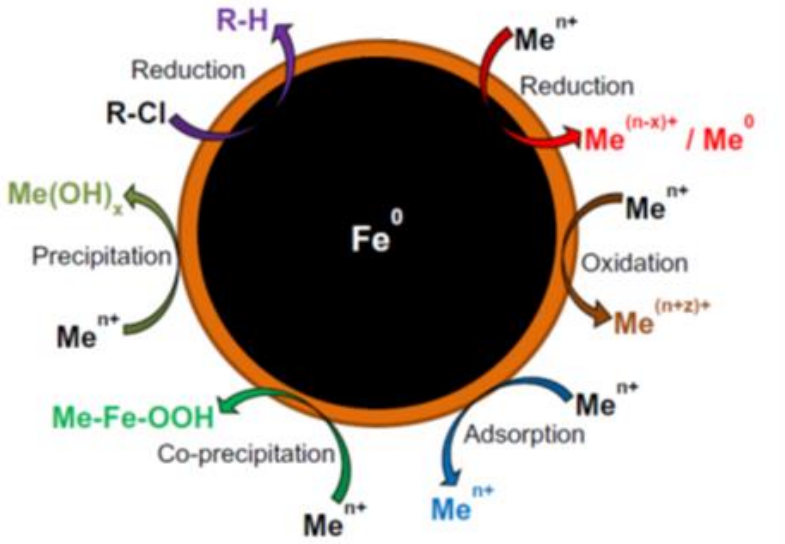

Fig. 1.7 All know ZVI and oxides acting mechanisms, *(O'Caroll et al., 2013)*.

The chemical energy is supplied by iron corrosion. In absence of oxygen, iron oxidation could be described by the semi reactions *Eq. 1.15* and *Eq. 1.16.* As observed below, hydrogen and an alkali media are generated by iron corrosion, *(Crane and Scott, 2012)*.

$$2Fe^{0}_{(s)} + 2H_2O \rightarrow 2Fe^{2+}{}_{(aq)} + H_{2\,(g)} + 2OH^{-}_{(aq)} \quad E^0 = -0.39\,V \qquad \textbf{Eq. 1.15}$$

$$2Fe^{2+}_{(s)} + 2H_2O \rightarrow 2Fe^{3+}{}_{(aq)} + H_{2\,(g)} + 2OH^{-}_{(aq)} \quad E^0 = -1.60\,V \qquad \textbf{Eq. 1.16}$$

During the experiments with nZVI, iron reactivity against some common pollutants was used as a performance test to evaluate and compare commercial and new developed particles.

The pollutants used were: Cr(VI), trichloroethylene (TCE), tetrachloroethylene (PCE) and other chlorinated aliphatic compounds. All of them are suitable to be remediated through nZVI and are

among the most studied ones, *(Fu et al., 2014; Stefaniuk et al., 2016).* Metals and chlorinated aliphatic compounds differ in the pollutant degradation mechanism strengthening the results if these concur.

Metal immobilization

The mechanisms involved in metal remediation rely on the permanent immobilization, and not elimination, thanks to one of or the combination of the following processes, *(O'Carroll et al., 2013)*:

- Reduction: **Cr**, As, Cu, U, Pb, Ni, Se, Co, Pd, Pt, Hg, Ag.
- Adsorption: **Cr**, As, U, Pb, Ni, Se, Co, Cd, Zn, Ba.
- Oxidation/reoxidation: As, U, Se, Pb.
- Co-precipitation: **Cr**, As, Ni, Se.
- Precipitation: Cu, Pb, Cd, Co, Zn.

In the studied case with Cr(VI), the exact degradation mechanism is not completely understood but what seems clear is that it involves different steps, including: adsorption, reduction and co-precipitation *(Neubactep, 2010)*. Cr(VI) reduction to Cr(III) is the most representative step since chromium compounds are generally insoluble, consequently, they do not have the capacity to cross the cell membrane leading to a toxicity estimated to be 1000 times less toxic than Cr(VI) compounds, *Eq. 1.17, (Gheju., 2011)*. Moreover, Cr(VI) may also be reduced by hydrogen ions adsorbed onto iron surfaces, by Fe(II) in solution, or in mineral phases, or by dissolved organic compounds, *(Melitas et al., 2001)*.

$$Fe^{0}_{(s)} + CrO^{2-}_{4\,(aq)} + 4H_2O \rightarrow Cr(OH)_{3\,(s)} + Fe(OH)_{3\,(s)} + 2OH^{-}_{(aq)} \qquad \textbf{Eq. 1.17}$$

In addition to the reduction to $Cr(OH)_3$, Cr(III) may also form Cr_2O_3 or solid solutions with Fe(III), *Eq. 1.18,* improving its immobilization. There is a negative side effect of adsorption; new compounds of Cr-Fe and solid solutions of both Cr(VI) and Cr(III) have a passivating effect on the iron particle surface, *Eq. 1.18, (Mitra et al., 2011)*. Chromium is a well-known and widely used anticorrosion additive in steels thanks to the build-up of a chromium passivated oxide layer. This phenomenon decreases the reactivity progressively, thus the performance of ZVI while the Cr – Fe interaction is produced, *(Kerkar et al., 1990; Melitas et al., 2001; Mitra et al., 2011*).

Chlorinated Aliphatic Hydrocarbons

On the other hand, trichloroethylene and tetrachloroethylene degradation mechanisms only involve reduction. The reduction up to ethane is not performed directly, it involves intermediates. Depending on the pathway, some intermediates like vinyl chloride have a toxicity higher than its precursors, *(Roberts et al., 1996)*. Different pathways for trichloroethylene and tetrachloroethylene dechlorination have been proposed: hydrogenolysis, reductive β-elimination and hydrogen addition, *Fig. 1.8. (Arnold and Roberts, 2000; Hara et al., 2005)*. Hydrogenolysis is prevalent in anaerobic biotic mediated systems, which entails the accumulation of undesired intermediates such as vinyl chloride *(Carucci et al., 2007)*. Fortunately, in ZVI application β-elimination prevails being 10 – 100 faster than α-elimination *(Hara et al., 2005)* accumulation of vinyl chloride using nZVI in significant levels is seldom reported in the literature.

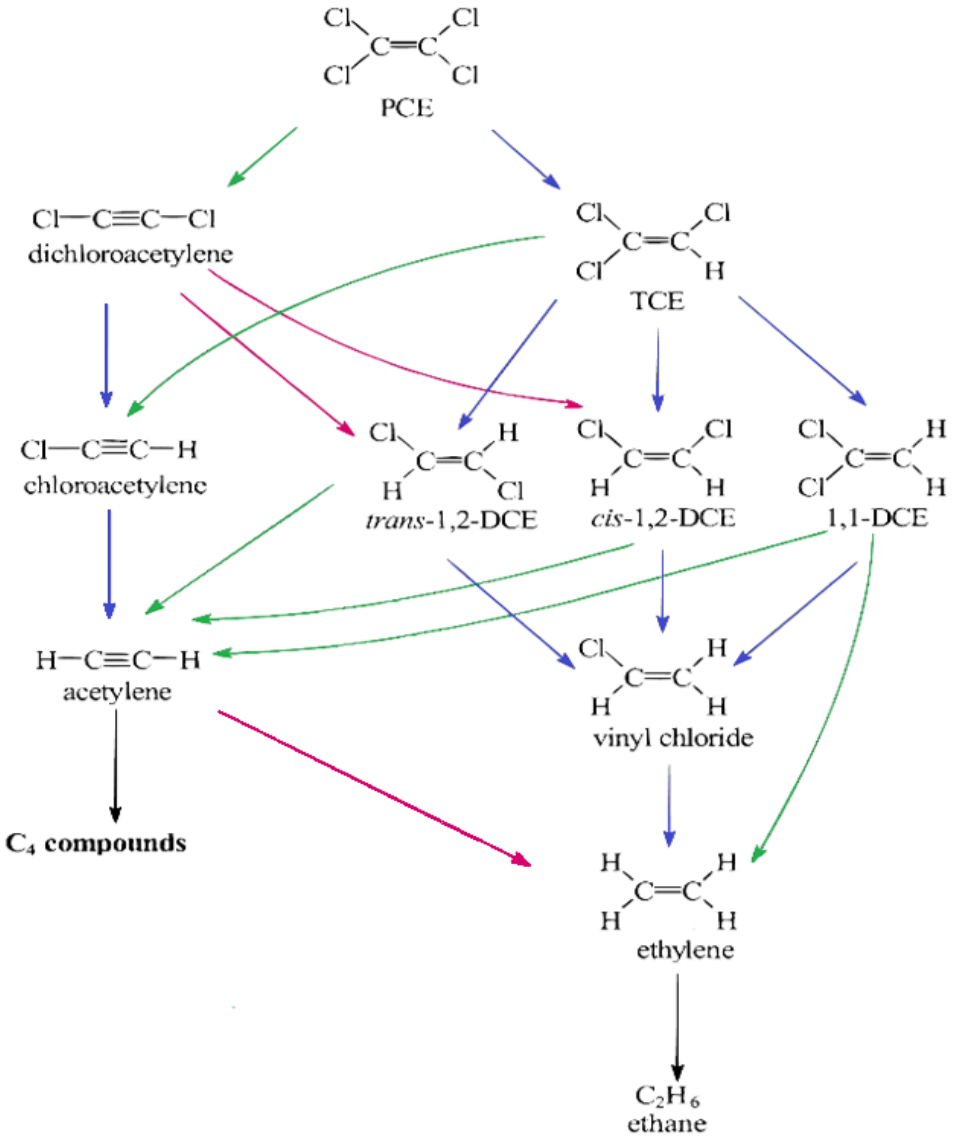

Fig. 1.8 Trichloroethylene and tetrachloroethylene reduction pathways: hydrogenolysis (blue), reductive β-elimination (green), hydrogen addition (magenta), final products (black). Adapted from, *(Arnold and Roberts, 2000)*.

1.3.5 Suspension stability and mobility

Besides nZVI reactivity, suspension stability and mobility in the aquifer matrix have a dramatic effect on the remediation performance at field scale. An important problem arises once nZVI is put into suspension, since nZVI tends to aglomerate, producing large flocs of several micrometres, thus clogging the pore media. Consequently, this phenomena produces a poor mobility of nZVI in the aquifer usually limited within few meters of the injection borehole *(Johnson et al., 2013)*.

The governing aggregation forces of nZVI and some of its oxides are: Van der Waals attraction, the electrostatic double layer repulsion (ζ-potential) and attractive magnetic forces *(Dalla Vecchia et al., 2009)*. Extensive research has been made in order to increase suspension stability and ultimately he nZVI mobility. Usually, it is accomplished thanks to the use of dispersants *(Comba and Sethi, 2009)*. Although dispersants improves significantly this proble, mobility is still limited within few meters and, in addition, these reduce nZVI reactivity *(Dong et al., 2016)*.

In relation to magnetism, few studies have been carried out addressing the magnetism problem of nZVI, thus any exploratory approach could be important. In this thesis, exploratory approaches trying to overcome this problem are presented.

1.3.6 Natural and nZVI remediation combined

Merging natural bioremediation and nZVI remediation is a new topic, this is being studied for some specific contaminants such as organohalide compounds.

At the moment, the effect of the nZVI on the aquifer microflora is not clear, seeming toxic to some species but not to others. Some studies suggest physical damage and biochemical destruction as a result of intracellular oxidative stress *(Sacca et al., 2014).* This damage could be driven by reactive oxygen compounds that can interact directly with membrane lipids, proteins and DNA. These highly reactive oxygen compounds are produced by Fenton reactions where nZVI is involved. On the other hand, stimulative effects on the growth of some microbe species are reported *(Xie et al., 2017)*. These effects of nZVI on certain bacteria are associated with the formation of an appropriate living environment through providing electron donor such as H_2 *(Xiu et al., 2010; Jugder et al., 2016)*.

The combination of nZVI and some microbes shows synergistic effect on contaminant removal. Organohalide compounds seems very suitable for this approach thanks to the hydrogen provided by nZVI, *(Wang et al., 2016)*, because hydrogen is the primary electron donor for organohalide-respiring bacteria *(Adrian et al., 2016; Jugder et al., 2016), Fig. 1.9*.

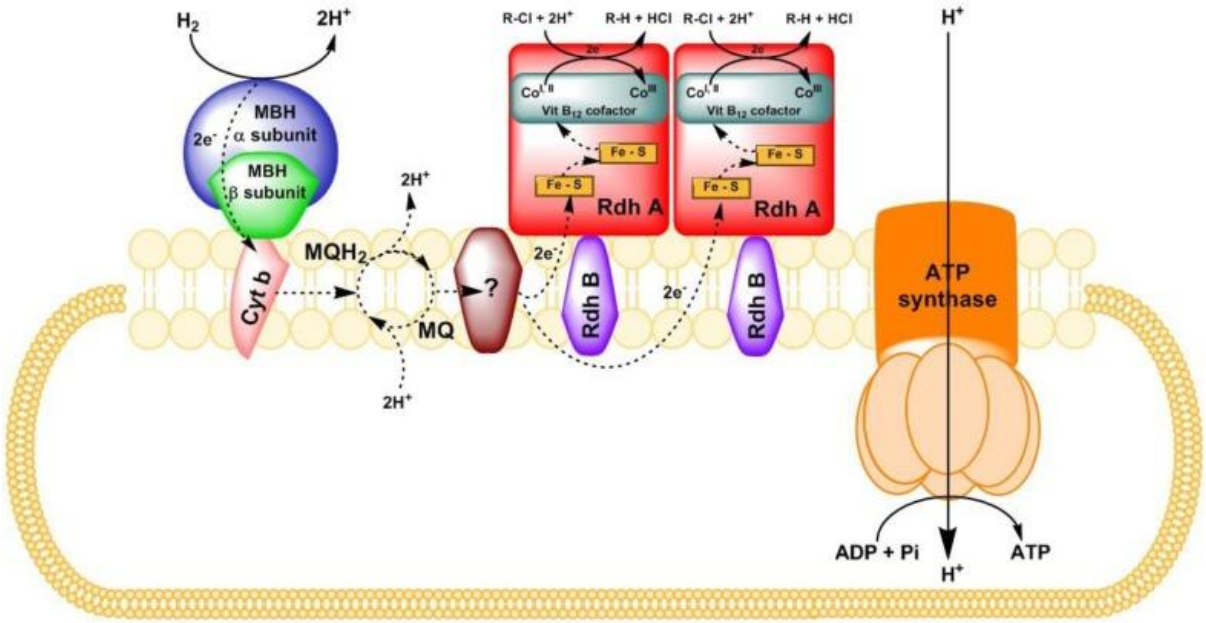

Fig. 1.9 representation of electron transfer chain with H_2 as electron donor, and organohalide as electron acceptor in *S. multivorans (Jugder et al., 2016)*.

Lastly, the aged NZVI can be utilized by some iron-reducing bacteria, resulting in the transformation of Fe(III) to Fe(II), which can further contribute to the contaminant reduction, *(Němeček et al., 2016).*

1.3.7 NANOREM Project

nanoRem (taking nanotechnological Remediation Processes from lab scale to end user applications for the restoration of a clean environment) (NMP.2012.1.2-1) was a research project, funded under 7th Framework Programme of the European Union. It was focused on the facilitation of practical, safe, economic and exploitable nanotechnology for in situ remediation. A holistic approach has been taken to disclose whether the potential for nanoremediation can be developed and applied in practice to enhance a stronger development of nanoremediation markets and applications in the EU. This was done in parallel to developing a comprehensive understanding of the environmental risk-benefit for the use of nanoparticles (NPs), market demand, overall sustainability, and stakeholder perceptions. Ultimately, the project was designed to unlock the potential of nanoremediation processes from laboratory scale to end user applications.

The nanoRem consortium was multidisciplinary, cross-sectoral and transnational. It included 28 partners from 12 countries organized in 11 work packages. The consortium included 18 of the leading nanoremediation research groups in the EU, 10 industry and service providers (8 SMEs) and one organisation with policy and regulatory interest. The project lasted form 1st February 2013 until January 2017 (48 months).

Regarding this thesis, the work done on nZVI in Work Package 2 was focused on:

- Development of techniques with lower manufacturing cost, producing nZVI particles with satisfactory properties regarding: reactivity, mobility and safety.

- The study of nZVI surface properties, including: the development of a method to increase the reactivity of present commercial nZVI products and ζ-potential determination of different nZVI particles and nZVI aging products.

1.4 References

Adrian, L., & Löffler, F. (2016). Organohalide Respiring Bacteria. Ch. Electron Acceptor Interactions Between Organohalide-Respiring Bacteria: Cross-Feeding, Competition, and Inhibition. Springer.

Anderson, M. P. (1989). Hydrogeologic facies models to delineate large-scale spatial trends in glacial and glaciofluvial sediments. Geological Society of America Bulletin, 101(4), 501-511.

Appelo, C. A. J., & Postma, D. (2007). Geochemistry, groundwater and pollution. 2on ed., A,.A. Balkema Publishers, Leiden The Nederlands, pp. 649.

Arnold, W. A., & Roberts, A. L. (2000). Pathways and kinetics of chlorinated ethylene and chlorinated acetylene reaction with Fe(0) particles. Environmental Science & Technology, 34(9), 1794-1805.

Arora, B., Spycher, N. F., Steefel, C. I., Molins, S., Bill, M., Conrad, M. E., ... & Williams, K. H. (2016). Influence of hydrological, biogeochemical and temperature transients on subsurface carbon fluxes in a flood plain environment. Biogeochemistry, 127(2-3), 367-396.

Blowes, D. W., Ptacek, C. J., Benner, S. G., McRae, C. W., Bennett, T. A., & Puls, R. W. (2000). Treatment of inorganic contaminants using permeable reactive barriers. Journal of Contaminant Hydrology, 45(1), 123-137.

Bruce, E. R., & Perry, L. M. (2001). Environmental biotechnology: principles and applications. New York: McGrawHill, 400. pp 503.

Brunke, M., & Gonser, T. O. M. (1997). The ecological significance of exchange processes between rivers and groundwater. Freshwater Biology, 37(1), 1-33.

Carpenter, E. E. (2001). Iron nanoparticles as potential magnetic carriers. Journal of Magnetism and Magnetic Materials, 225(1), 17-20.

Carucci, A., Manconi, I., & Manigas, L. (2007). Use of membrane bioreactors for the bioremediation of chlorinated compounds polluted groundwater. Water Science & Technology, 55(10).

Cebron, A., & Garnier, J. (2005). Nitrobacter and Nitrospira genera as representatives of nitrite-oxidizing bacteria: detection, quantification and growth along the lower Seine River (France). Water Research, 39(20), 4979-4992.

Chen, S. S., Hsu, H. D., & Li, C. W. (2004). A new method to produce nanoscale iron for nitrate removal. Journal of nanoparticle Research, 6(6), 639-647.

Choi, C. J., Tolochko, O., & Kim, B. K. (2002). Preparation of iron nanoparticles by chemical vapor condensation. Materials Letters, 56(3), 289-294.

Cole, C. A. (2016). Assessment of a judgment-based hydrogeomorphic wetland classification using long-term hydrologic data. Ecohydrology.

Comba, S., & Sethi, R. (2009). Stabilization of highly concentrated suspensions of iron nanoparticles using shear-thinning gels of xanthan gum. Water Research, 43(15), 3717-3726.

Crane, R. A., & Scott, T. B. (2012). nanoscale zero-valent iron: future prospects for an emerging water treatment technology. Journal of Hazardous Materials, 211, 112-125.

Dahl, M., Nilsson, B., Langhoff, J. H., & Refsgaard, J. C. (2007). Review of classification systems and new multi-scale typology of groundwater–surface water interaction. Journal of Hydrology, 344(1), 1-16.

Dalla Vecchia, E., Coisson, M., Appino, C., Vinai, F., & Sethi, R. (2009). Magnetic characterization and interaction modeling of zerovalent iron nanoparticles for the remediation of contaminated aquifers. Journal of nanoscience and nanotechnology, 9(5), 3210-3218.

De Groot, R., Brander, L., Van Der Ploeg, S., Costanza, R., Bernard, F., Braat, L., ... & Hussain, S. (2012). Global estimates of the value of ecosystems and their services in monetary units. Ecosystem services, 1(1), 50-61.

Dong, H., He, Q., Zeng, G., Tang, L., Zhang, C., Xie, Y., ... & Wu, Y. (2016). Chromate removal by surface-modified nanoscale zero-valent iron: Effect of different surface coatings and water chemistry. Journal of Colloid and Interface Science, 471, 7-13.

EU Decision No. 1982/2006/EC of 18 December 2006 concerning the Seventh Framework Programme of the European Community for research, technological development and demonstration activities (2007-2013), Council of the European Union, Official Journal L412/1, 30.12.2006. pp 1-41.

EU Directive 2000/60/CE of 30 October 2000 establishing a framework for community action in the field of water policy, European Parliament and the Council of the European Union, Official Journal L327, 22/12/2000. pp 1-72.

EU Directive 2006/118/CE of 12 December 2006 on the protection of groundwater against pollution and deterioration, Council of the European Union, Official Journal L372/19, 27.12.2006. pp 1-13.

EU Directive 91/676/EEC of 12 December 1991 concerning the protection of waters against pollution caused by nitrates from agricultural sources, Council of the European Union, Offical Journal L375, 31/12/1991. pp 1-12.

EU Directive 98/83/CE of 3 November 1998 on the quality of water intended for human consumption, Council of the European Union, Official Journal L330 05/12/1998. pp 32-54.

Farrell, D., Majetich, S. A., & Wilcoxon, J. P. (2003). Preparation and characterization of monodisperse Fe nanoparticles. The Journal of Physical Chemistry B, 107(40), 11022-11030.

Field, C.B., V.R. Barros, D.J. Dokken, K.J. Mach, M.D. Mastrandrea, T.E. Bilir, M. Chatterjee, K.L. Ebi, Y.O. Estrada, R.C. Genova, B. Girma, E.S. Kissel, A.N. LEvi, S. MacCracken, P.R. Mastrandrea, & L.L.White. (2014). Summary for policymakers. In: Climate Change 2014: Impacts, Adaptation, and Vulnerability. Part A: Global and Sectoral Aspects. Contribution of Working Group II to the Fifth Assessment Report of the Intergovernmental Panel on Climate Change. Cambridge University Press, Cambridge, United Kingdom and New York, NY, USA, pp. 1-32.

Flight, M. J., Paterson, R., Doiron, K., & Polasky, S. (2012). Valuing Wetland Ecosystem Services: A Case Study of Delaware. National Wetlands Newsletter, 34(5).

Foundation for Water Research. (accessed 2016). FWR: Groundwater. http://www.euwfd.com/html/groundwater.html.

Fu, F., Dionysiou, D. D., & Liu, H. (2014). The use of zero-valent iron for groundwater remediation and wastewater treatment: a review. Journal of Hazardous Materials, 267, 194-205.

Funen County (2003). Odense River basin. Provisional Article 5 report pursuant to the Water Framework Directive. Fyn County, Denmark.

Galloway, J. N., Townsend, A. R., Erisman, J. W., Bekunda, M., Cai, Z., Freney, J. R., ... & Sutton, M. A. (2008). Transformation of the nitrogen cycle: recent trends, questions, and potential solutions. Science, 320(5878), 889-892.

Gheju, M. (2011). Hexavalent chromium reduction with zero-valent iron (ZVI) in aquatic systems. Water, Air, & Soil Pollution, 222(1-4), 103-148.

Gillham, R. W., & O'Hannesin, S. F. (1994). Enhanced degradation of halogenated aliphatics by zero-valent iron. Ground water, 32(6), 958-967.

Gleick, P. H. (1996). Water resources. Encyclopedia of climate and weather. Ed. by S. H. Schneider, Oxford University Press, New York, vol. 2, pp.817-823.

Grieger, K. D., Fjordbøge, A., Hartmann, N. B., Eriksson, E., Bjerg, P. L., & Baun, A. (2010). Environmental benefits and risks of zero-valent iron nanoparticles (nZVI) for in situ remediation: risk mitigation or trade-off?. Journal of Contaminant Hydrology, 118(3), 165-183.

Griffiths, J., & Lambert, R. (2013). Free Flow: Reaching Water Security Through Cooperation. UNESCO. Ch. Transboundary water management, 40-96.

Gruber, N., & Galloway, J. N. (2008). An Earth-system perspective of the global nitrogen cycle. Nature, 451(7176), 293-296.

Gumiero, B., Mant, J., Hein, T., Elso, J., & Boz, B. (2013). Linking the restoration of rivers and riparian zones/wetlands in Europe: sharing knowledge through case studies. Ecological Engineering, 56, 36-50.

Hara, J., Ito, H., Suto, K., Inoue, C., & Chida, T. (2005). Kinetics of trichloroethene dechlorination with iron powder. Water Research, 39(6), 1165-1173.

Hatzenpichler, R. (2012). Diversity, physiology, and niche differentiation of ammonia-oxidizing archaea. Applied and Environmental Microbiology, 78(21), 7501-7510.

Hill, A. R., & Cardaci, M. (2004). Denitrification and organic carbon availability in riparian wetland soils and subsurface sediments. Soil Science Society of America Journal, 68(1), 320-325.

Hoffmann, C.C. & A. Baatrup-pedersen. (2007). Re-establishing freshwater wetlands in Denmark. Ecological Engineering. 30: 157-166.

Howarth, R. W. (2008). Coastal nitrogen pollution: a review of sources and trends globally and regionally. Harmful Algae, 8(1), 14-20.

Ji, Y. (2014). Ions removal by iron nanoparticles: a study on solid–water interface with zeta potential. Colloids and Surfaces A: Physicochemical and Engineering Aspects, 444, 1-8.

Johnson, R. L., Nurmi, J. T., O'Brien Johnson, G. S., Fan, D., O'Brien Johnson, R. L., Shi, Z., ... & Lowry, G. V. (2013). Field-scale transport and transformation of carboxymethylcellulose-stabilized nano zero-valent iron. Environmental Science & Technology, 47(3), 1573-1580.

Jørgensen, P. R., Urup, J., Helstrup, T., Jensen, M. B., Eiland, F., & Vinther, F. P. (2004). Transport and reduction of nitrate in clayey till underneath forest and arable land. Journal of Contaminant Hydrology, 73(1), 207-226.

Jugder, B. E., Ertan, H., Bohl, S., Lee, M., Marquis, C. P., & Manefield, M. (2016). Organohalide Respiring Bacteria and Reductive Dehalogenases: Key Tools in Organohalide Bioremediation. Frontiers in microbiology, 7.

Kassaee, M. Z., Motamedi, E., Mikhak, A., & Rahnemaie, R. (2011). Nitrate removal from water using iron nanoparticles produced by arc discharge vs. reduction. Chemical Engineering Journal, 166(2), 490-495.

Kerkar, M., Robinson, J., & Forty, A. J. (1990). In situ structural studies of the passive film on iron and iron/chromium alloys using X-ray absorption spectroscopy. Faraday Discuss. Chem. Soc, 89(P001), 1-20.

Köber, R., Hollert, H., Hornbruch, G., Jekel, M., Kamptner, A., Klaas, N., ... & Braun, J. (2014). nanoscale zero-valent iron flakes for groundwater treatment. Environmental Earth Sciences, 72(9), 3339-3352.

Koltypin, Y., Perkas, N., & Gedanken, A. (2004). Commercial edible oils as new solvents for ultrasonic synthesis of nanoparticles: the preparation of air stable nanocrystalline iron particles. Journal of Materials Chemistry, 14(20), 2975-2977.

Komor, A., & Fox, P. (2002). Evaluation of denitrification rates and mechanisms in microcosm experiments with sediments and plants. Proceedings of the Water Environment Federation, 2002(16), 496-514.

Krutz, L. J., Senseman, S. A., Zablotowicz, R. M., & Matocha, M. A. (2005). Reducing herbicide runoff from agricultural fields with vegetative filter strips: a review. Weed Science, 53(3), 353-367.

Li, S., Yan, W., & Zhang, W. X. (2009). Solvent-free production of nanoscale zero-valent iron (nZVI) with precision milling. Green Chemistry, 11(10), 1618-1626.

Machado, S., Stawiński, W., Slonina, P., Pinto, A. R., Grosso, J. P., Nouws, H. P. A., ... & Delerue-Matos, C. (2013). Application of green zero-valent iron nanoparticles to the remediation of soils contaminated with ibuprofen. Science of the Total Environment, 461, 323-329.

Madigan, M. M., Martinko, J., & Parker, J. (2000). J. Brock Biología de los Microorganismos (Octava edición revisada).

Mao, X., Jiang, R., Xiao, W., & Yu, J. (2015). Use of surfactants for the remediation of contaminated soils: a review. Journal of Hazardous Materials, 285, 419-435.

Mayer, P. M., Reynolds, S. K., McCutchen, M. D., & Canfield, T. J. (2007). Meta-analysis of nitrogen removal in riparian buffers. Journal of environmental quality, 36(4), 1172-1180.

Melitas, N., Chuffe-Moscoso, O., & Farrell, J. (2001). Kinetics of soluble chromium removal from contaminated water by zerovalent iron media: corrosion inhibition and passive oxide effects. Environmental Science & Technology, 35(19), 3948-3953.

Mitra, P., Sarkar, D., Chakrabarti, S., & Dutta, B. K. (2011). Reduction of hexa-valent chromium with zero-valent iron: batch kinetic studies and rate model. Chemical Engineering Journal, 171(1), 54-60.

Mountjoy, K. J., Pringle, E. K., Choi, M., & Gowdy, W. (2003). The use of permeable reactive barriers for in-situ remediation of groundwater contaminants. Remediation Technology Symposium, Alberta (Vol. 15, p. 17).

Mueller, N. C., Braun, J., Bruns, J., Černík, M., Rissing, P., Rickerby, D., & Nowack, B. (2012). Application of nanoscale Zero Valent iron (NZVI) for groundwater remediation in Europe. Environmental Science and Pollution Research, 19(2), 550-558.

Mulder, A., Graaf, A., Robertson, L. A., & Kuenen, J. G. (1995). Anaerobic ammonium oxidation discovered in a denitrifying fluidized bed reactor. FEMS Microbiology Ecology, 16(3), 177-184.

Müller, N. C., & Nowack, B. (2010). nano Zero Valent iron—The solution for water and soil remediation. Report of the ObservatoryNANO, 1-34.

NASA, NOAA, GSFC, Suomi NPP, VIIRS & Kuring N. (2012). North America from low orbiting satellite Suomi.

Němeček, J., Pokorný, P., Lhotský, O., Knytl, V., Najmanová, P., Steinová, J., ... & Cajthaml, T. (2016). Combined nano-biotechnology for in-situ remediation of mixed contamination of groundwater by hexavalent chromium and chlorinated solvents. Science of The Total Environment, 563, 822-834.

Noubactep, C. (2010). The fundamental mechanism of aqueous contaminant removal by metallic iron. Water Sa, 36(5), 663-670.

O'Carroll, D., Sleep, B., Krol, M., Boparai, H., & Kocur, C. (2013). nanoscale Zero Valent iron and bimetallic particles for contaminated site remediation. Advances in Water Resources, 51, 104-122.

Perlman, H., (2012). U.S. Geological Survey; globe illustration. Woods Hole Oceanographic Institution.

Reichenberger, S., Bach, M., Skitschak, A., & Frede, H. G. (2007). Mitigation strategies to reduce pesticide inputs into ground-and surface water and their effectiveness; A review. Science of the Total Environment, 384(1), 1-35.

Roberts, A. L., Totten, L. A., Arnold, W. A., Burris, D. R., & Campbell, T. J. (1996). Reductive elimination of chlorinated ethylenes by zero-valent metals. Environmental Science & Technology, 30(8), 2654-2659.

Robertson, W. D., Russell, B. M., & Cherry, J. A. (1996). Attenuation of nitrate in aquitard sediments of southern Ontario. Journal of Hydrology, 180(1), 267-281.

Rütting, T., Boeckx, P., Müller, C., & Klemedtsson, L. (2011). Assessment of the importance of dissimilatory nitrate reduction to ammonium for the terrestrial nitrogen cycle. Biogeosciences, 8(7), 1779-1791.

Sacca, M. L., Fajardo, C., Martinez-Gomariz, M., Costa, G., Nande, M., & Martin, M. (2014). Molecular stress responses to nano-sized zero-valent iron (nZVI) particles in the soil bacterium Pseudomonas stutzeri. PloS one, 9(2), e89677.

Shahwan, T., Sirriah, S. A., Nairat, M., Boyacı, E., Eroğlu, A. E., Scott, T. B., & Hallam, K. R. (2011). Green synthesis of iron nanoparticles and their application as a Fenton-like catalyst for the degradation of aqueous cationic and anionic dyes. Chemical Engineering Journal, 172(1), 258-266.

Sigmund, W., El-Shall, H., Shah, D. O., & Moudgil, B. M. (Eds.). (2008). Particulate systems in nano-and biotechnologies. CRC Press. 313-314

Siwach, O. P., & Sen, P. (2008). Fluorescence properties of Fe nanoparticles prepared by electro-explosion of wires. Materials Science and Engineering: B, 149(1), 99-104.

Smith, R. L., Ceazan, M. L., & Brooks, M. H. (1994). Autotrophic, hydrogen-oxidizing, denitrifying bacteria in groundwater, potential agents for bioremediation of nitrate contamination. Applied and Environmental Microbiology, 60(6), 1949-1955.

Sophocleous, M. (2002). Interactions between groundwater and surface water: the state of the science. Hydrogeology Journal, 10(1), 52-67.

Soukupova, J., Zboril, R., Medrik, I., Filip, J., Safarova, K., Ledl, R., ... & Cernik, M. (2015). Highly concentrated, reactive and stable dispersion of zero-valent iron nanoparticles: Direct surface modification and site application. Chemical Engineering Journal, 262, 813-822.

Stefaniuk, M., Oleszczuk, P., & Ok, Y. S. (2016). Review on nano zerovalent iron (nZVI): From synthesis to environmental applications. Chemical Engineering Journal, 287, 618-632.

Stein, L. Y., & Klotz, M. G. (2016). The nitrogen cycle. Current Biology, 26(3), R94-R98.

Steinfeld, H., Gerber, P., Wassenaar, T. D., Castel, V., & de Haan, C. (2006). Livestock's long shadow: environmental issues and options. Food & Agriculture Org.

Tang, S. C., & Lo, I. M. (2013). Magnetic nanoparticles: essential factors for sustainable environmental applications. Water Research, 47(8), 2613-2632.

Thornton, P. K. (2010). Livestock production: recent trends, future prospects. Philosophical Transactions of the Royal Society of London B: Biological Sciences, 365(1554), 2853-2867.

Tiehm, A., Kraßnitzer, S., Koltypin, Y., & Gedanken, A. (2009). Chloroethene dehalogenation with ultrasonically produced air-stable nano iron. Ultrasonics Sonochemistry, 16(5), 617-621.

Tosco, T., Papini, M. P., Viggi, C. C., & Sethi, R. (2014). nanoscale zerovalent iron particles for groundwater remediation: A review. Journal of Cleaner Production, 77, 10-21.

Tournebize, J., Chaumont, C., Fesneau, C., Guenne, A., Vincent, B., Garnier, J., & Mander, Ü. (2015). Long-term nitrate removal in a buffering pond-reservoir system receiving water from an agricultural drained catchment. Ecological Engineering, 80, 32-45.

Uegami, M., Kawano, J., Okita, T., Fujii, Y., Okinaka, K., Kakuya, K., & Yatagi, S. (2006). U.S. Patent No. 7,022,256. Washington, DC: U.S. Patent and Trademark Office.

Vidon, P. G., & Hill, A. R. (2004a). Landscape controls on the hydrology of stream riparian zones. Journal of Hydrology, 292(1), 210-228.

Vidon, P. G., & Hill, A. R. (2004b). Landscape controls on nitrate removal in stream riparian zones. Water Resources Research, 40(3).

Vrba, J. & Adams, B. (2008). Groundwater Early Warning Monitoring Strategy, A Methodological Guide. UNESCO, United Nations Educational Scientific and Cultural Organization.

Wang, C. B., & Zhang, W. X. (1997). Synthesizing nanoscale iron particles for rapid and complete dechlorination of TCE and PCBs. Environmental Science & Technology, 31(7), 2154-2156.

Wang, S., Chen, S., Wang, Y., Low, A., Lu, Q., & Qiu, R. (2016). Integration of organohalide-respiring bacteria and nanoscale zero-valent iron (Bio-nZVI-RD): A perfect marriage for the remediation of organohalide pollutants?. Biotechnology Advances, 34(8), 1384-1395.

Water, U. N. (2012). Managing water under uncertainty and risk, The United Nations world water development report 4, UN Water Reports, World Water Assessment Programme.

Wright, R. O., Lewander, W. J., & Woolf, A. D. (1999). Methemoglobinemia: etiology, pharmacology, and clinical management. Annals of Emergency Medicine, 34(5), 646-656.

Wu, S., Kuschk, P., Brix, H., Vymazal, J., & Dong, R. (2014). Development of constructed wetlands in performance intensifications for wastewater treatment: a nitrogen and organic matter targeted review. Water research, 57, 40-55.

WWAP, (2015). The United Nations World Water Development Report 2015: Water for a Sustainable World. Paris, UNESCO.

Xie, Y., Dong, H., Zeng, G., Tang, L., Jiang, Z., Zhang, C., ... & Zhang, Y. (2017). The interactions between nanoscale zero-valent iron and microbes in the subsurface environment: A review. Journal of Hazardous Materials, 321, 390-407.

Xiu, Z. M., Jin, Z. H., Li, T. L., Mahendra, S., Lowry, G. V., & Alvarez, P. J. (2010). Effects of nano-scale zero-valent iron particles on a mixed culture dechlorinating trichloroethylene. Bioresource Technology, 101(4), 1141-1146.

Yao, Z., Li, J., Xie, H., & Yu, C. (2012). Review on remediation technologies of soil contaminated by heavy metals. Procedia Environmental Sciences, 16, 722-729.

Yoshinari, T., Hynes, R., & Knowles, R. (1977). Acetylene inhibition of nitrous oxide reduction and measurement of denitrification and nitrogen fixation in soil. Soil Biology and Biochemistry, 9(3), 177-183.

Zaporozec, A., Conrad, J. E., Hirata, R., Johansson, P. O., Nonner, J. C., & Romijn, E. (2002). Groundwater contamination inventory: a methodological guide. IHP-VI, Series on groundwater No. 2.

Zhang, W. X. (2003). nanoscale iron particles for environmental remediation: an overview. Journal of nanoparticle Research, 5(3-4), 323-332.

Zhang, W. X., & Elliott, D. W. (2006). Applications of iron nanoparticles for groundwater remediation. Remediation Journal, 16(2), 7-21.

2 General objectives

Taking into account the huge challenge that the remediation of thousands of contaminated sites with a huge variety of pollutants implies, the aim of this thesis is to study new methods, to increase the understanding of the optimal parameters of the present technologies and investigate groundwater remediation processes.

Two main techniques were studied: natural occurring bioremediation in wetlands and chemical degradation by using nano Zero Valent Iron (nZVI) particles.

Regarding natural based remediation of nitrate and nitrite, though being a working technology, lack of knowledge of its performance in real field conditions is an issue. In order to elucidate these concerns, the following goals were stablished:

- Evaluation of restored wetlands as buffer zones for nitrate remediation. Comparison of restored wetlands with natural ones and determination of the main factors affecting denitrification performance.

- Soil characteristics and composition impact on denitrification and DNRA, highlighting the role of organic matter and the distribution over the depth of the soil.

- Effect of the seasonal variations including temperature changes and different hydric regimes on denitrification performance in wetlands.

nZVI is a relatively new and very promising remediation technique. Remarkably, nZVI is capable of degrading a wide range of contaminants, some being very difficult to treat with previous remediation approaches. Some important challenges and drawbacks to overcome remain; the aim of this thesis is to bring new insight and methods to improve the nZVI performance. The aims are to:

- Develop a cost-effective and straightforward production method through milling (top down approach) with the purpose to obtain nZVI particles with high reactivity, mobility and long term storage capacity.

- Study the role of the passivating oxide shell in commercial particles, surface and crystallographic characteristics. Development of methods to improve reactivity by eliminating the passivating oxide shell.

- Investigation of nZVI agglomeration affecting aspects such as ζ-potential and magnetism.

Chapter 3 shows the thesis workflow to reach these objectives.

3 Thesis Workflow

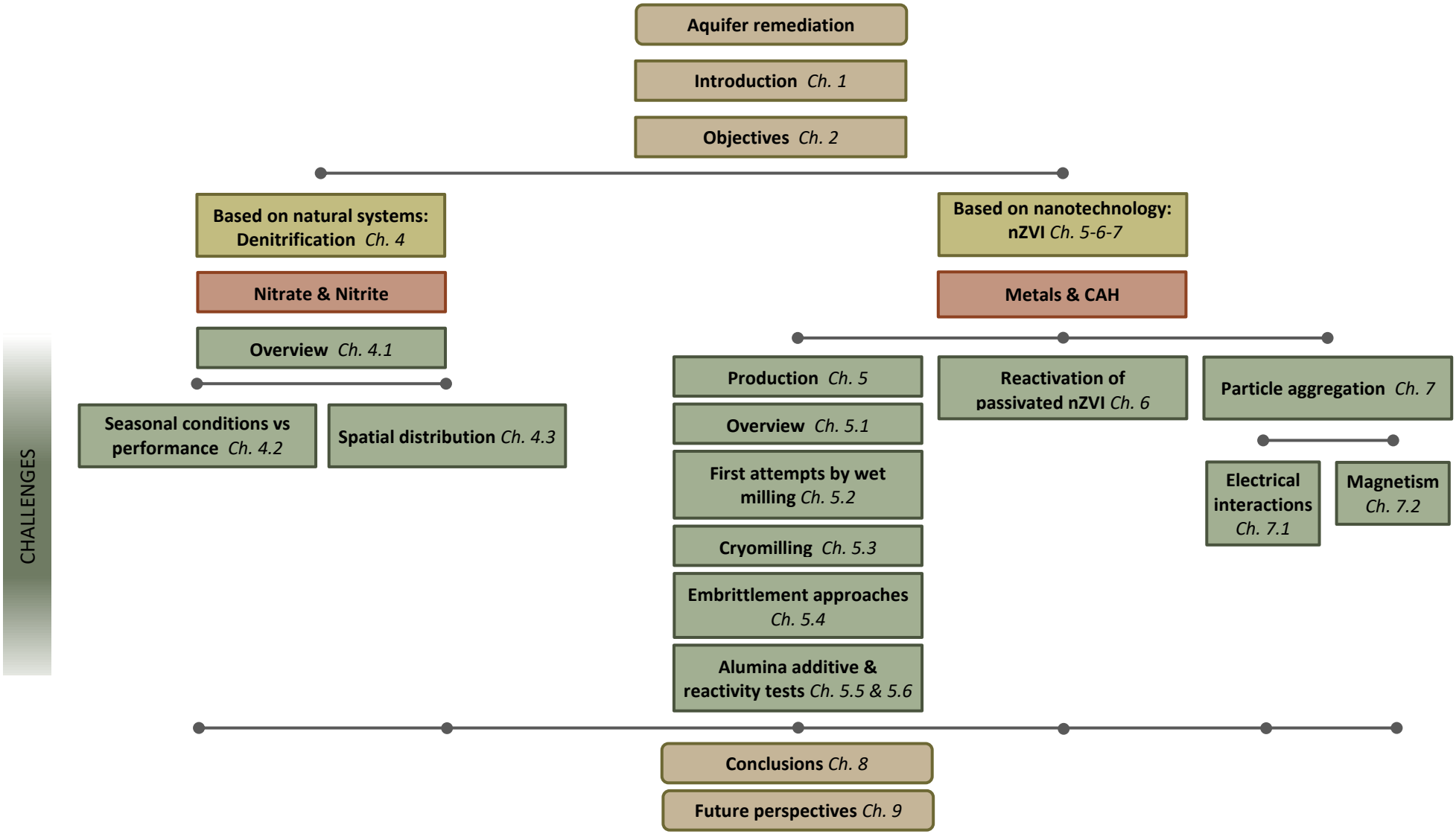

4 Denitrification

4.1 Research in denitrification overview

The main scope of this thesis regarding denitrification studies is to deep in the natural denitrification driving forces. It is vitally important to unveil what causes denitrification work and what factors stops or drops its performance, especially the less known ones. This task was divided in two main specific strands of work:

- The assessment of the influence of the seasonal perturbations such as: changes in the soil temperature, drought periods and freeze-thaw cycles. Usually, lab studies on denitrification performance uses ideal temperature and humidity parameters which leaks the real field environments. Since the wetland or floodplain are among the most dynamic natural systems it is critical to know how denitrification works out of its ideal and steady conditions. In this thesis, the effect of different environmental perturbations on denitrification is studied.

- The link between: the organic matter, soils depth and denitrification. It is known that denitrification in certain circumstances is not observed, for example in deep aquifers due to the leak of a suitable organic matter that enables the heterotrophic denitrification. The minimum amount of organic matter, its composition and other side factor remains large unknown and it is considered a keystone for nitrate remediation. In the following study, cores from different sites were studied to stablish some initial correlations between the main driving factors in denitrification and environmental factors.

4.1.1 Identification of key seasonal conditions and sites selection

The following seasonal variations were targeted to be studied due to its possible influence in the denitrification performance:

- Temperature variations. In northern European countries where low temperatures (below 10 ºC) are common in groundwater, denitrification performance could be affected *(Brüsch et al., 1993; Rivett et al. 2008).* Therefore studding the denitrification at these temperatures is crucial.

- Likewise, Freeze-thaw cycles are a common situation in northern European countries, they are produced in two different timeframes: seasonally between winter and spring and daily where the most upper part of the wetland soil suffers freeze-thaw events due to temperature oscillation between day and night *(Philippot et al., 2007)*. It is reported that the superficial zones of the wetlands are the most important contributors to the denitrification *(Clément et al., 2002; Hayakawa et al., 2012)* which highlights the importance of this phenomenon.

- Periods of drought are frequent because related to seasonal or weather alterations some wetlands have important water table fluctuations. These fluctuations can lead to the drought of the upper part of the wetland soil, which as discussed before, plays a key role in the denitrification *(Clément et al., 2002; Hayakawa et al., 2012)*.

Following the identified perturbations, the Brynemade site (Odense river basin, Denmark) was selected to study the effect of different seasonal conditions on the denitrification potential as an ideal location due to: its northern location and its fluctuating water table *(Jensen, 2014).* Concerning the study of the spatial denitrification distribution and the performance of restored compared to natural wetlands, Brynemade (restored) and Evi (natural), these sites were chosen. Both sites were previously characterized, having similar geology and climatic conditions *(Kronvang et al., 2009; Jensen, 2014, Poulsen et al., 2015; Sebok et al., 2015)*.

4.1.2 Sites studied

Within the AQUAREAB project two sites in Denmark were selected. From these, soils and their intrinsic bacteria populations were sampled. These two sites were named as Brynemade and Evi and they are extensively characterised in the following sections, it can be highlighted that they only differed in the time when they were settled. Brynemade is a well re-established wetland, *Fig. 4.1 (Left); Fig. 4.2*, and the Evi site (Holtum river basin in Jutland, Western Denmark) is a model of a natural wetland-river system, *Fig. 4.1 (Right)*. It enables the assessment of the effectiveness of the re-established wetlands intended to be used as a buffer zone in remediation.

Fig. 4.1 (Left) Brynemade site: river Odense, between Brobyværk and Hillerslev, Fyn Island, Denmark. (Right) Evi site: located close to Lake Ejstrup and the city of Ejstrupholm, Jutland, Denmark.

Fig. 4.2 Brynemade site, sampling field.

4.1.3 Sampling campaign, storage and management

Two soil cores from Brynemade up to 3 m depth were sampled in May 2012 and next year two additional soil cores were sampled at the Evi site in May 2013. Sampling campaigns were performed by Manresa Technological Centre (CTM) and Geological Survey of Denmark and Greenland (GEUS) technicians. These cores were used to perform all the experiments described in this chapter.

Since heterotrophic denitrifying bacteria requires an anaerobic atmosphere in order to perform they catabolism, it is imperative to work in a free oxygen atmosphere. It adds a new precaution to be considered in the soil transport, experiment setting, incubation and sampling.

Concerning core extraction, transport and soil context characterization, the following procedures were applied. After the extraction of the cores, they were sliced in 10 cm sections, three sections at a time. These three sections were capped immediately and brought to the anaerobic glove box where they were flushed with nitrogen three times before being transferred to the glovebox. 50-60 g of sediment from the centre of each section were placed in 50-ml plastic screw-cap tubes. These subsamples were intended for denitrification assays and were sent to Manresa in air-tight hinged Kilner jars with an anaerobic nitrogen atmosphere. 40 g of the remaining sample was transferred to other screw-cap tubes and frozen for later analyses of nitrate, nitrite and Dissolved Organic Carbon (DOC). The exact amount of sediment and the weight of the tubes was determined. To the thawed samples 10 ml of MilliQ water were added and shaken briefly. The tubes were centrifuged at approximately 1000 g for 10 min, water from the supernatant was filtered and analysed for the groundwater characterization. The tubes with sediment were dried to determine the amount of pore-water that was present in the sediment, and the pore-water concentrations of nitrate, nitrite and DOC were also calculated. Hereafter in Barcelona, anaerobic conditions were achieved thanks to the combination of two techniques: caring out all the operations inside a glove box and the usage of hermetic vials during the cultures previously set into the glove box.

The glove box (2P, Jacomex) has an internal volume constantly fluxed with nitrogen gas and also it is filtered eliminating the remaining oxygen. This system allows an atmosphere with an oxygen content below 5 ppm. Material input and output is carried out through a pre-chamber where the external atmosphere is eliminated thanks to several cycles of vacuum and nitrogen flushing, *Fig. 4.3*.

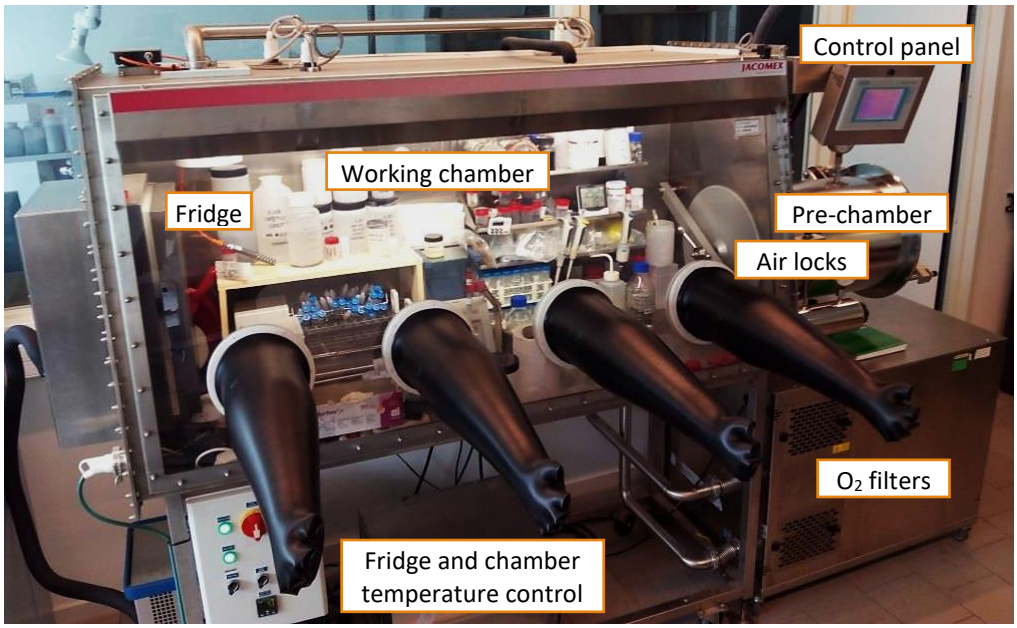

Fig. 4.3 Glovebox (2P, Jacomex) parts.

Cultures were set in the glove box and sealed in hermetic vials with crimp seals. Seals were made of PTFE and red rubber being airtight and chemically inert, these were replaced after each sample extraction because after needle puncture the hermeticity of the septum can be compromised. The use of hermetic vials enabled the incubation outside the glove box, meaning a close control of temperature and light conditions.

4.2 References

Brüsch, W., & Nilsson, B., (1993). Nitrate transformation and water movement in a wetland area. In Nutrient Dynamics and Retention in Land/Water Ecotones of Lowland, Temperate Lakes and Rivers (pp. 103-111). Springer Netherlands.

Clément, J. C., Pinay, G., & Marmonier, P. (2002). Seasonal dynamics of denitrification along topohydrosequences in three different riparian wetlands. Journal of Environmental Quality, 31(3), 1025-1037.

Hayakawa, A., Nakata, M., Jiang, R., Kuramochi, K., & Hatano, R. (2012). Spatial variation of denitrification potential of grassland, windbreak forest, and riparian forest soils in an agricultural catchment in eastern Hokkaido, Japan. Ecological Engineering, 47, 92-100.

Jensen, J.K., (2014). Flow and transport in riparian zones. Ph. D. Thesis. University of Copenhaguen.

Kronvang, B., Hoffmann, C. C., & Dröge, R. (2009). Sediment deposition and net phosphorus retention in a hydraulically restored lowland river floodplain in Denmark: combining field and laboratory experiments. Marine and Freshwater Research, 60(7), 638-646.

Philippot, L., Hallin, S., & Schloter, M. (2007). Ecology of denitrifying prokaryotes in agricultural soil. Advances in Agronomy, 96, 249-305.

Poulsen, J. B., Sebok, E., Duque, C., Tetzlaff, D., & Engesgaard, P. K., (2014). Detecting groundwater discharge dynamics from point to catchment scale in a lowland stream: combining hydraulic and tracer methods. Hydrology and Earth System Sciences Discussions, 11(12), 13101-13143.

Rivett, M. O., Buss, S. R., Morgan, P., Smith, J. W., & Bemment, C. D., (2008). Nitrate attenuation in groundwater: a review of biogeochemical controlling processes. Water research, 42(16), 4215-4232.

Sebok, E., Duque, C., Engesgaard, P., & Boegh, E., (2015). Application of Distributed Temperature Sensing for coupled mapping of sedimentation processes and spatio-temporal variability of groundwater discharge in soft-bedded streams. Hydrological Processes, 29(15), 3408-3422.

4.2 Effect of different seasonal conditions on the potential of wetland soils for groundwater denitrification

Wetlands, as active riparian areas in denitrification processes, are largely dependent on the environment. The main objective of this paper is to evaluate changes in the denitrification potential of wetland soils at lab scale promoted by climatic and seasonal influences.

Several batch denitrification tests were performed with fresh superficial wetland soil (peat) from Brynemade (Denmark) under: three different temperatures (20, 10 and 5°C), drought period and freeze-thaw event.

Results show that nitrate was eliminated in all the experiments in percentages over 90%. However, not all the nitrate removed was reduced to nitrogen gas via the denitrification process, Dissimilatory Nitrate Reduction to Ammonium (DNRA) was also present. In fact, the percentage of total nitrogen eliminated at the end of the tests was: 79.7% at 20°C, 84.1% at 10°C, 82.9% at 5°C, 41.0% in the dried soil and 57.0% in the frozen soil. Thus, it can be concluded that the drying and freezing of the soil favour the DNRA process. Furthermore, in these conditions nitrite increased sharply and was also accumulated possibly, as a DNRA or denitrification intermediate.

Nitrate removal was fitted to a zero order model, and an increase of the denitrification rates with the temperature was observed (3.8 mg $NO_3^-{\cdot}l^{-1}{\cdot}d^{-1}$ at 20°C, 3.0 mg $NO_3^-{\cdot}l^{-1}{\cdot}d^{-1}$ at 10ºC and 2.9 mg $NO_3^-{\cdot}l^{-1}{\cdot}d^{-1}$ at 5°C). These overall rates were modelled as a function of temperature by the Arrhenius equation and activation energy of 12.88 $kJ{\cdot}mol^{-1}$ was determined.

The fact that the activation energy is low in this work (unstirred batches) compared to previous publications (stirred batches) could be the result of a strong restriction on the nitrate mass transfer in the soil versus reaction kinetics, which masks kinetic regulating factors of the denitrification rate. Thus, the variation of the denitrification rate with temperature is possibly the result of a combination of changes in mass transfer (diffusive transport) and kinetic constant variation, successfully modelled by the Arrhenius equation.

The work described in this chapter has been published in:

Ribas, D., Calderer, M., Martí, V., & Rovira, M. (2015). Effect of different seasonal conditions on the potential of wetland soils for groundwater denitrification. Desalination and Water Treatment, 53(4), 994-1000.

4.2.1 Introduction

Basin waters are exposed to higher nitrogen inputs as a result of an increase in organic and chemical fertilizer usage in agriculture. This situation implies a risk of eutrophication and public health concerns resulting from nitrate and nitrite exposal. In order to counter this problem, natural wetlands, in the same way as riparian zones, play an important role in nitrogen remediation from nonpoint source pollution.

In spite of high theoretical performance of the wetlands, its denitrification potential shows an important variation with regards to many factors such as oxygen, organic carbon, temperature, nitrate concentration and soil texture, *(Song et al., 2012)*. The relative importance of each one in limiting denitrification potential depends on its magnitude, finding in different cases, different principal limitation factors, that include: temperature *(Hernandez et al., 2007)*, water table elevation *(Hefting et al., 2004)*, organic carbon *(Pfenning et al., 1997)* and nitrogen input, *(Song et al., 2012)*.

Groundwater temperature is one of the most important factors controlling denitrification *(Kadlec et al., 2001; Kuroda et al., 2010)*. Like many others enzyme mediated biological reactions, denitrification shows a direct dependence with temperature, which could be modelled by employing the Arrhenius equation. Activation energy is positively related with the denitrification susceptibility to temperature. In addition to biologic aspects, dissolved oxygen is strongly negative depending on the temperature, *(Veraart et al., 2011)*.

Periods of drought (seasonal or weather episodes) with the resulting loss of soil humidity have a deep impact on soil bacteria, nutrients and texture. Due to the dry conditions air enters into the soil and thus, soil becomes aerobic. Soil desiccation leads to larger bacterial mortality, which is reflected in the increase in dissolved carbon and exchangeable ammonium as a result of cell lysis and mineralization *(Mitchell et al., 1998)*, the resulting ammonium could be transformed to nitrate enhancing in some cases the denitrification *(Akatsuka et al., 2011)*. Once the soil is rehydrated denitrifying communities gradually recover. A relation between the period of soil dehumidification and the period of the recovery of denitrification levels was found, *(Austin et al., 2011)*. Additionally, there is a growing interest in this phenomenon because of the increase in N_2O emissions as a result of incomplete denitrification, *(Prieme et al., 2001)*.

Freeze-thaw events release Dissolved Organic Carbon (DOC) and nitrogen due to disruption of soil aggregates, plant residues and lysis of microorganisms, *(Philippot et al., 2007)*. There is a so-called partial sterilization of denitrifying communities which causes an initial decrease in the denitrification rate but an increase in the growth of denitrifying bacteria that survived the freeze-thaw cycle, *(Yanai et al., 2007)*. Similarly to drought periods, freeze-thaw cycles increase the production of N_2O by denitrification, a process which is currently the object of numerous studies concerning climatic change, *(Mørkved et al., 2006)*.

Dissimilatory Nitrate Reduction to Ammonium (DNRA) is a respiratory or fermentative pathway where nitrate is reduced steps by steps to ammonium competing with denitrification for the nitrate *(Calderer et al., 2010)*, *Eq. 4.1*. Ammonium is immobilized in the soil until nitrification, plant uptake or Anammox occurs. Conditions favouring DNRA are less understood than denitrification although it can be a significant or even a dominant process in some ecosystems, *(Rütting et al., 2011)*. It is believed, however, that heterotrophic denitrification supplies more free energy than DNRA. Under nitrate limiting conditions DNRA could be favoured because more electrons can be transferred per mole of nitrate, *(Krafta et al., 2011)*. Notice that in both pathways nitrite is an intermediate.

$$NO_3^- \rightarrow NO_2^- \begin{cases} \rightarrow NH_4^+ & \text{DNRA} \\ \rightarrow NO \rightarrow N_2O \rightarrow N_2 & \text{Denitrification} \end{cases} \qquad \textbf{Eq. 4.1.}$$

It is imperative to undertake further research into denitrification limiting factors because of its importance in the nitrogen cycle and nitrate bioremediation.

4.2.2 Methods

Site description

The site is a wetland of the Odense River basin near Brynemade, Denmark (55º13'12''N, 10º17'35''E; WGS84) selected as a model of a well-established wetland. The "Brynemade" site has been carefully studied regarding geology, geochemistry and geophysics in the framework of AQUAREHAB project. The climate of the site is temperate and humid, characterized by windy winters and cool summers, an annual mean temperature of 8.9ºC and an annual accumulated precipitation of 733 mm (Years: 2001 to 2010, grid 20x20 km for temperature and 10x10 km for precipitation), *(Riddersholm, 2013)*. The site is used as pasture for livestock, such as horses.

Soil sampling and characterization

Peat soil (0–10 cm) was collected from a core extraction in May, 2012. The soil was for 4 months at field moisture and at 10ºC in plastic bags. Soil samples were thoroughly homogenized under inert atmosphere and a small fraction was separated to perform an initial characterization: pH, Electrical Conductivity (EC), Moisture (M), Loss Of Ignition (LOI), and lixiviation test of nitrate (NO_3^-), nitrite (NO_2^-), ammonium (NH_4^+) and DOC were performed and repeated in further characterizations.

Extractions with $CaCl_2$ (0.01 M) and de-ionized water (Milli-Q system, Merck Millipore) were prepared to measure pH and the conductivity of soil samples, respectively, according to the method UNE 77308:2001.Water content was determined as the loss of mass after drying at 105ºC overnight according to the method ISO 11465:1993. LOI was calculated as the fraction of dry matter that was removed after 16 hours at 400ºC employing the standard method, *(Nelson et al., 1996)*. Nitrate, nitrite and ammonium were extracted from soil samples with deionized water (dry soil: water ratio of 1:10 in weight) and further analysed by ion chromatography (Dionex ICS-2100, Dionex). The same lixiviate was also analysed by TOC analyser (Multi N/C 3100, Analytik Jena AG) to determine DOC content after being filtered through 0.2 µm nylon filter, acidified with concentrated sulfuric acid and purged with synthetic air. All results are given in relation to dry weight.

Experimental set up

Three seasonal scenarios were identified as common environmental conditions in wetlands and were reproduced experimentally, as follows: temperature change, drought period and a phase of freeze-thaw.

Temperature change was tested culturing three identical batch lines spiked with 25 $mg \cdot l^{-1}$ of nitrate at three different temperatures at 5, 10 and 20ºC respectively.

The drought period was created in the laboratory by maintaining the soils at 30ºC for one week, during which it lost most of the moisture. Meanwhile an aerobic condition as a result of atmospheric inlet, was observed. Following that, the batches were set up, spiked with 25 $mg \cdot l^{-1}$ of nitrate and maintained at 10ºC for the duration of the experiment.

The freeze-thaw phase was studied by maintaining hydrated batch tests at -20ºC for one week and then thawed at room temperature (20ºC). Following that, batches were spiked with 25 mg·l^{-1} of nitrate and maintained at 10ºC for the duration of the experiment.

All conditions were tested three times, 10ºC was chosen as a reference temperature to compare between different conditions and periodically, batch tests were sampled for nitrate, nitrite, ammonium and DOC analyses. Additionally, abiotic controls and negative controls without nitrate were performed.

Batch incubations

The equivalent of 2.92 g of dry soil and 100 ml of de-ionized water was placed in 115 ml vials (97 mm in height, 48 mm in diameter), in which settled soil a fine texture accounted for 10 mm. Vials were sealed with butyl rubber septums. The culture was enriched with 25 mg·l^{-1} of nitrate supplied by sodium nitrate stock solution. All procedure was performed in a globe box in a nitrogen atmosphere. Vials were stored in thermostatic cabinets at target temperatures of 5, 10 and 20ºC under non-stirred conditions to simulate field conditions. All experiments were monitored until nitrate depletion fell to the minimum level of detection.

Analytical monitoring

Batches were analysed periodically in approximately at 24 hour intervals in order to follow the evolution of the aqueous substrates and intermediates of the denitrification pathways.

Concentrations of nitrate, nitrite and ammonium in the aqueous phase of the batches were determined by Ion chromatography (Dionex ICS-2100, Dionex). The concentration of DOC was determined with a total organic carbon analyser (Multi N/C 3100, Analytik Jena AG) following the same procedure used for soil lixiviates.

Denitrification rate calculations

Denitrification rate could be calculated thanks to nitrate consumption when nitrite remains below the level of detection. Results were tested in order to fit these models: first order, *Monod (Calderer et al., 2010)* and zero order, finally the best fitting was obtained with zero order model, *Eq. 4.2*.

$$[A]_t = [A]_0 - k \cdot t \qquad \textbf{Eq. 4.2}$$

Where:

$[A]_t$ = concentration of the nitrate at a particular time.
$[A]_0$ = initial nitrate concentration.
k = zero order rate constant.
t = reaction time.

Arrhenius modelling

Nine zero order rate constants at three different temperatures (20, 10 and 5ºC respectively) were used to obtain activation energy and the frequency factor of the Arrhenius expression, *Eq. 4.3,* to model the zero order rate constant dependence on temperatures.

$$k_{(T)} = A \cdot e^{-\frac{E_A}{R \cdot T}} \qquad \textbf{Eq. 4.3}$$

Where:

$k_{(T)}$ = overall zero order rate constant at given Temperature (T), (mol·l^{-1}·s^{-1}(T))
A = frequency factor, zero order (mol·l^{-1}·s^{-1})
E_A = activation energy (J·mol^{-1})
R = universal gas constant (8.31 J·mol^{-1}·K^{-1})
T = absolute temperature (K)

Moreover, the Arrhenius equation was used to model the diffusion constants with temperature founding Arrhenius-type dependence *(Bastarrachea et al., 2010)*, it is feasible because higher temperature leads to a higher average kinetic energy of molecules and higher collision rate.

4.2.3 Results

Soils characterization and lixiviates

Table 4.1, presents the results of the characterization of fresh soil, soil after a drought period and soil after a freeze-thaw phase.

Table 4.1 Main physicochemical soil parameters and lixiviates concentration.

Batch	pH	EC $_{25ºC}$ µS·cm^{-1}	M %	LOI %	[NO_3^-] mg·kg^{-1} d.m.	[NO_2^-] mg·kg^{-1} d.m.	[NH_4^+] mg·kg^{-1} d.m.	[DOC] mg·kg^{-1} d.m.
Fresh soil	6.9	68.9	68.8	35.5	20.5	13.7	< Q.L	571.9
Dried soil	6.6	85.5	9.4	36.9	68.5	10.3	3.4	719.2
Frozen soil	6.6	74.2	--	--	27.4	30.8	< Q.L	547.9

d.m: dry matter, <Q.L. below Quantification Level

Fresh soil was characterized by an important organic fraction and a high water and slightly acidic content. Fresh soil lixiviated enough DOC to not be limited in heterotrophic denitrification pathway. As it is shown, dried peat can reach a higher amount of DOC, ammonium and nitrate due to the cellular lysis as stated by some authors, *(Austin et al., 2011)*. This table also shows that nitrate has increased as a result of preliminary aerobic mineralization.

In the case of frozen soil results shows few difference in DOC, contrarily to references *(Philippot et al., 2007)* that found an increase of DOC owing to the cellular lysis and the disruption of soil aggregates.

Denitrification at different temperatures

Nitrate consumption could be fitted in a zero order model at all temperatures, *Fig. 4.4*, obtaining the rate constants given in *Table 4.2*. As can be observed, nitrate consumption rates increased at a temperature of 20ºC when the process can be observed be quicker.

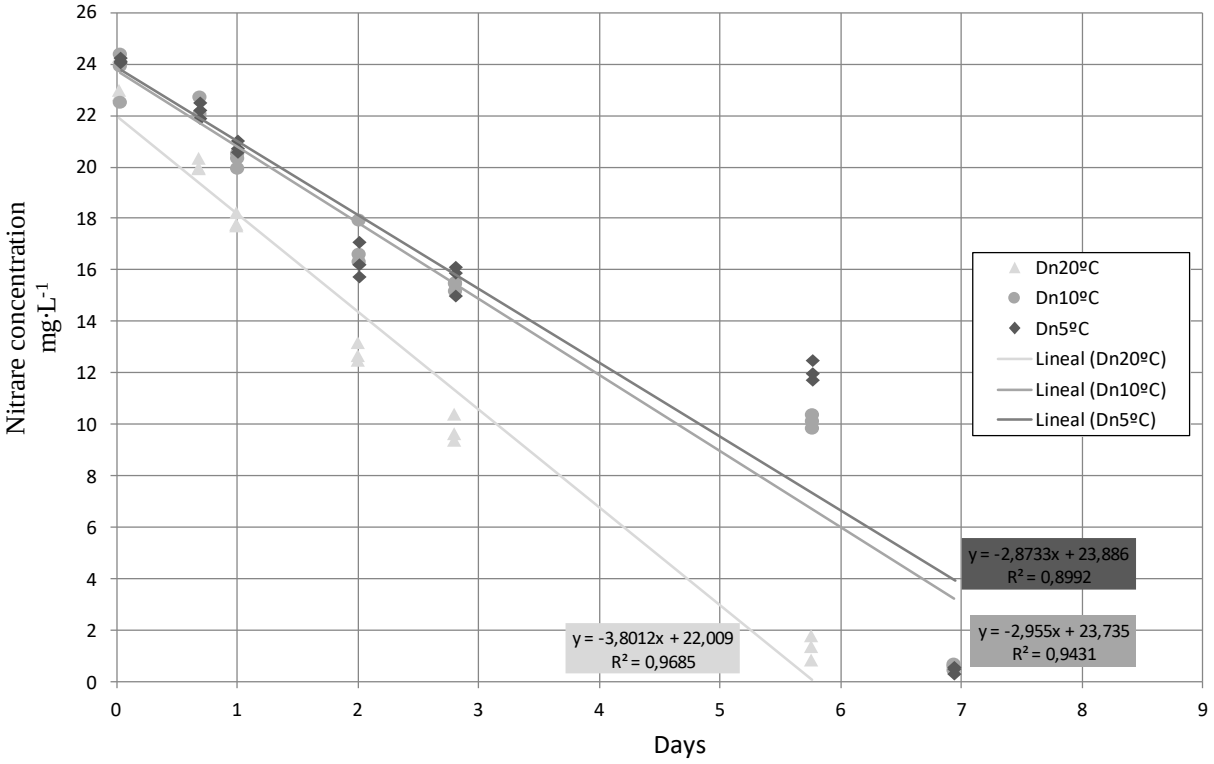

Fig. 4.4 Nitrate consumptions in batch at different temperatures and zero order model fits. Dn = Denitrification.

Table 4.2 Observed rates at different temperatures.

Temperature	**Average rates**	**R^2 (n)**
ºC	$mgNO_3^- \cdot l^{-1} \cdot d^{-1}$	
20	3.8 (± 0.10)*	0.97 (17)
10	3.0 (± 0.06)*	0.94 (20)
5	2.9 (± 0.01)*	0.90 (21)

* ± 95% Confidence Interval

Rate constants were used to obtain the activation energy and frequency factor from the Arrhenius equation, see *Table 4.3*. With the determined constants of the Arrhenius equation, the overall rate of denitrification could be predicted in function of the temperature, *Fig. 4.5*.

Table 4.3 Obtained Arrhenius equation constants.

E_A	**A**
$Kj \cdot mol^{-1}$	$mol \cdot l^{-1} \cdot s^{-1}$
12.88 (±1.07)	6.12 (+3.48; -2.22)·10^4

* ± 95% Confidence Interval

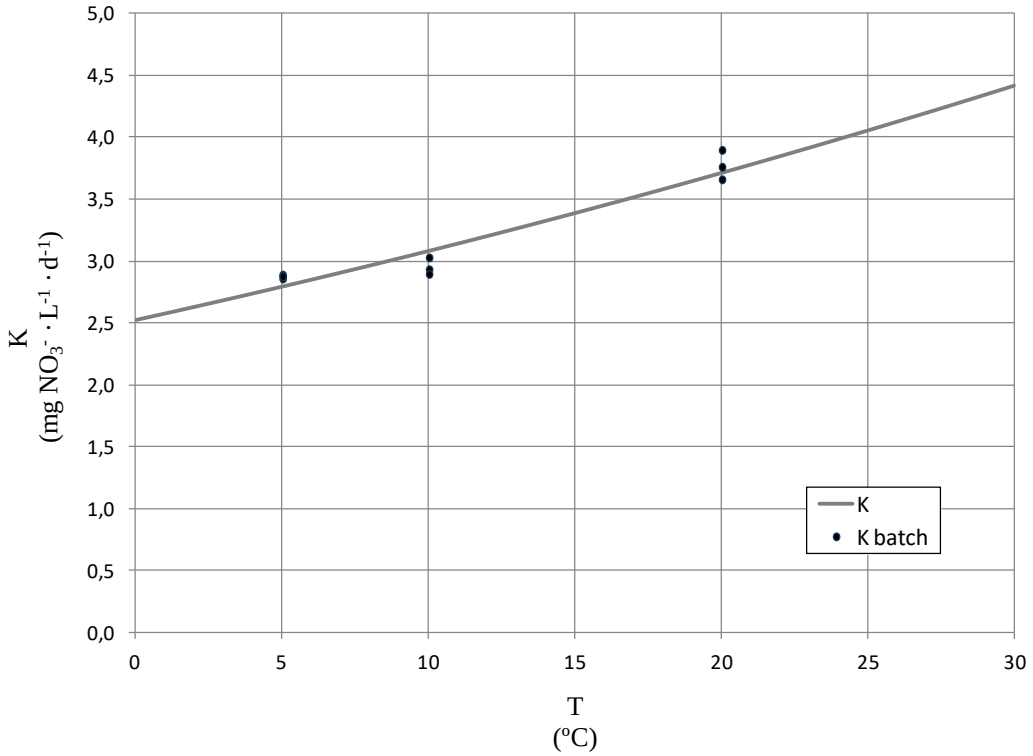

Fig. 4.5 Experimental overall rate constants found and extrapolation with Arrhenius.

The fact that the activation energy is low in this work (unstirred batches) compared to that which appears in published papers (stirred, column forced flow or shaken), *Table 4.4*, could be the result of a restriction on the nitrate transfer in the soil, which masks other regulating factors of the denitrification rate. Thus, the variation of the denitrification rate according to the temperature is suspected to be due to a combination of variation of mass transfer (diffusive transport) and kinetic constant variation, with a predominance of the transfer effect. Finally, despite the mix of both effects, its shared Arrhenius behaviour could explain the observation of the expected match. *Fig. 4.5.*

Table 4.4 Activation energies and transference regimes found in published papers.

Bacterial context	Transference regime	References	E_A KJ·mol^{-1}
Surface water	Stirred	Folgar et al., 2010	46
Deutschland soil	Stirred	Hartwing et al., 2002	62
Finland soil	Stirred	Hartwing et al., 2002	50
Sweden soil	Stirred	Hartwing et al., 2002	57
Clay soils	Column	McKenney et al., 1984	50
Sandy loam soil	Column	Hartwing et al., 2002	55
Lake sediments	Shaken	Messer et al., 1983	77
Hyporheic sediments	Column	Sheibley et al., 2003	82

Denitrification was the main cause of nitrate consumption as can be seen in the total nitrogen depletion: 79.7% at 20ºC, 84.1% at 10ºC and 82.9% at 5ºC with respect to the initial levels, *Fig. 4.6.* Ammonium and nitrite remained at lower concentrations, accounting for less than 20% of the total nitrogen at the conclusion of the experiments.

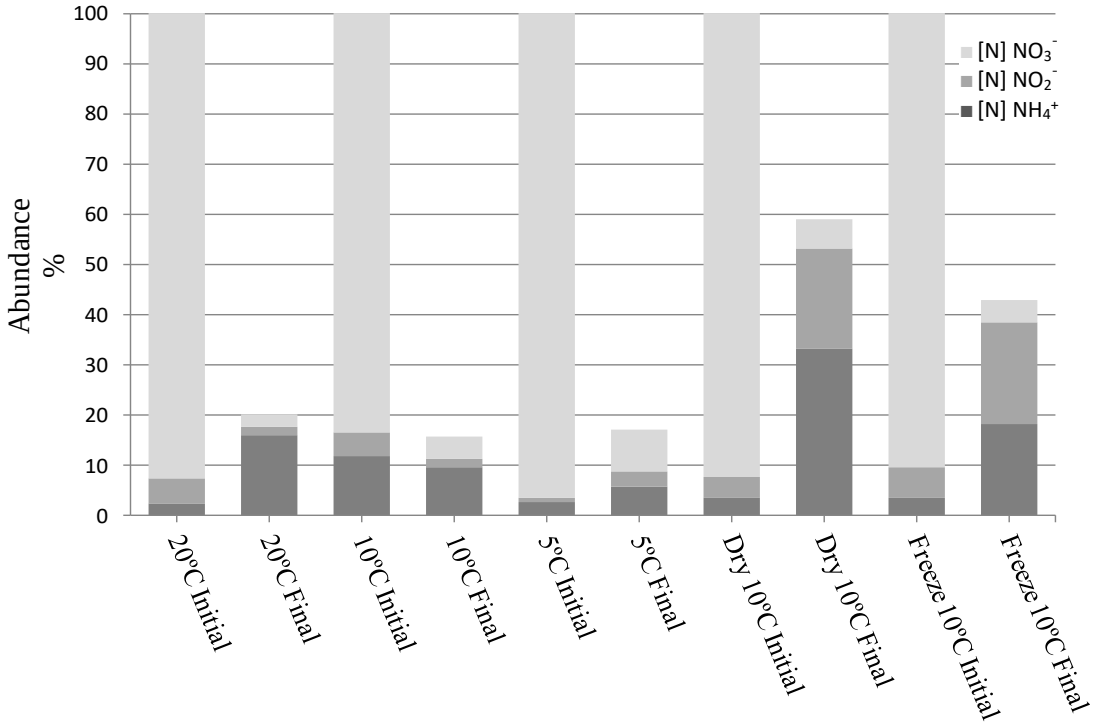

Fig. 4.6 Relative aqueous nitrogen abundances at initial and final point of the experiments, all species were normalized to nitrogen.

Drought period

This phase caused variations in the final nitrogen distribution compared to temperature variation experimental lines, *Fig. 4.6*. Remarkably, a higher nitrate conversion to nitrite with a final nitrogen fraction of 20.0% and ammonium of 33.2% was detected instead of a predominant denitrification process observed in experiments at different temperatures. Only 41.0% of the total nitrogen was eliminated. In addition the nitrate depletion ratio was sharply increased.

Ammonium generation was attributed to Dissimilatory Nitrate Reduction to Ammonium (DNRA) that was presumably favoured by the drought conditions. The increase in the final nitrite concentration could be either the result of an intermediate product of denitrification or DNRA processes.

Freeze-thaw cycle

Nitrogen in the form of nitrate was efficiently consumed reaching a residual level of 4.4% but similarly, to the drought period, this event decreased the conversion of nitrate to nitrogen gas; increasing nitrite until there was a final nitrogen fraction of 18.2% and 20.4% of ammonium. Again, DNRA is the most feasible process for ammonium production and nitrite accumulation that could be indistinctly denitrification or DNRA, *Fig. 4.6.* In the same way, that during the drought period, nitrate depletion ratio increased.

4.2.4 Conclusions

- Nitrate has been eliminated in all experiments; with high percentages of above 90%, being mainly as a result of heterotrophic denitrification but shared with DNRA in dried soil and frosted soil. It is reflected in a total nitrogen depletion of over 80% for the experiments at different temperatures and only under 60% in dried soil and frosted soil.

- In the study of the variation of the denitrification potential at 20ºC, 10ºC and 5°C, the denitrification rate was directly correlated to the temperature. Activation energy was lower in these experiments than in stirred, column or shaken systems, this behaviour is suspected to be due to a predominant restriction in mass transfer (diffusive transport) instead of denitrification kinetic.

- Drying and freezing of the soil favours DNRA. Furthermore, in both conditions nitrite increased sharply and was also accumulated possibly as a DNRA or denitrification intermediate. As a consequence wetlands permanently flooded with low freezing periods are supposed to exhibit better denitrification potential.

4.2.5 References

Akatsuka, T., & Mitamura, O. (2011). Response of denitrification rate associated with wetting and drying cycles in a littoral wetland area of Lake Biwa, Japan. Limnology, 12(2), 127-135.

Austin, B. J., & Strauss, E. A. (2011). Nitrification and denitrification response to varying periods of desiccation and inundation in a western Kansas stream. Hydrobiologia, 658(1), 183-195.

Bastarrachea, L., Dhawan, S., Sablani, S. S., & Powers, J. (2010). Release kinetics of nisin from biodegradable poly (butylene adipate-co-terephthalate) films into water. Journal of Food Engineering, 100(1), 93-101.

Calderer, M., Gibert, O., Martí, V., Rovira, M., de Pablo, J., Jordana, S., ... & Bruno, J. (2010). Denitrification in presence of acetate and glucose for bioremediation of nitrate-contaminated groundwater. Environmental Technology, 31(7), 799-814.

Calderer, M., Jubany, I., Pérez, R., Martí, V., & De Pablo, J. (2010). Modelling enhanced groundwater denitrification in batch micrococosm tests. Chemical Engineering Journal, 165(1), 2-9.

Foglar, L., Bolf, N., & Lukić, M. (2010). Kinetic modelling of surface water biodenitrification. WSEAS Transactions on Environment and Development, 6(5), 375-384.

Hefting, M., Clement, J. C., Dowrick, D., Cosandey, A. C., Bernal, S., Cimpian, C., ... & Pinay, G. (2004). Water table elevation controls on soil nitrogen cycling in riparian wetlands along a European climatic gradient. Biogeochemistry, 67(1), 113-134.

Hernandez, M. E., & Mitsch, W. J. (2007). Denitrification in created riverine wetlands: Influence of hydrology and season. Ecological Engineering, 30(1), 78-88.

Holtan-Hartwig, L., Dörsch, P., & Bakken, L. R. (2002). Low temperature control of soil denitrifying communities: kinetics of N 2 O production and reduction. Soil Biology and Biochemistry, 34(11), 1797-1806.

Kadlec, R. H., & Reddy, K. R. (2001). Temperature effects in treatment wetlands. Water Environment Research, 543-557.

Kraft, B., Strous, M., & Tegetmeyer, H. E. (2011). Microbial nitrate respiration–genes, enzymes and environmental distribution. Journal of Biotechnology, 155(1), 104-117.

Kuroda, H., Kato, T., Koshigoe, Y., Yaegashi, D., Horaguti, S., Inubushi, K., ... & Suwa, Y. (2010). The improvement of the nitrogen removal capacity in wetlands. Desalination and Water Treatment, 19(1-3), 146-148.

McKenney, D. J., Johnson, G. P., & Findlay, W. I. (1984). Effect of temperature on consecutive denitrification reactions in Brookston clay and Fox sandy loam. Applied and Environmental Microbiology, 47(5), 919-926.

Messer, J. J., & Brezonik, P. L. (1984). Laboratory evaluation of kinetic parameters for lake sediment denitrification models. Ecological Modelling, 21(4), 277-286.

Mitchell, A., & Baldwin, D. S. (1998). Effects of desiccation/oxidation on the potential for bacterially mediated P release from sediments. Limnology and Oceanography, 43(3), 481-487.

Mørkved, P. T., Dörsch, P., Henriksen, T. M., & Bakken, L. R. (2006). N 2 O emissions and product ratios of nitrification and denitrification as affected by freezing and thawing. Soil Biology and Biochemistry, 38(12), 3411-3420.

Nelson, D. W., Sommers, L. E., Sparks, D. L., Page, A. L., Helmke, P. A., Loeppert, R. H., ... & Sumner, M. E. (1996). Total carbon, organic carbon, and organic matter. Methods of soil analysis. Part 3-chemical methods., 961-1010.

Pfenning, K. S., & McMahon, P. B. (1997). Effect of nitrate, organic carbon, and temperature on potential denitrification rates in nitrate-rich riverbed sediments. Journal of Hydrology, 187(3), 283-295.

Philippot, L., Hallin, S., & Schloter, M. (2007). Ecology of denitrifying prokaryotes in agricultural soil. Advances in Agronomy, 96, 249-305.

Priemé, A., & Christensen, S. (2001). Natural perturbations, drying–wetting and freezing–thawing cycles, and the emission of nitrous oxide, carbon dioxide and methane from farmed organic soils. Soil Biology and Biochemistry, 33(15), 2083-2091.

Riddersholm, W.P. (2013). Teknisk Rapport 13-09, Klimagrid Danmark, Referenceværdier 2001-2010. Danish Meteorological Institute.

Rütting, T., Boeckx, P., Müller, C., & Klemedtsson, L. (2011). Assessment of the importance of dissimilatory nitrate reduction to ammonium for the terrestrial nitrogen cycle. Biogeosciences, 8(7), 1779-1791.

Sheibley, R. W., Jackman, A. P., Duff, J. H., & Triska, F. J. (2003). Numerical modeling of coupled nitrification–denitrification in sediment perfusion cores from the hyporheic zone of the Shingobee River, MN. Advances in Water Resources, 26(9), 977-987.

Song, K., Kang, H., Zhang, L., & Mitsch, W. J. (2012). Seasonal and spatial variations of denitrification and denitrifying bacterial community structure in created riverine wetlands. Ecological Engineering, 38(1), 130-134.

Veraart, A. J., De Klein, J. J., & Scheffer, M. (2011). Warming can boost denitrification disproportionately due to altered oxygen dynamics. PLoS One, 6(3), e18508.

Yanai, Y., Toyota, K., & Okazaki, M. (2007). Response of denitrifying communities to successive soil freeze–thaw cycles. Biology and Fertility of Soils, 44(1), 113-119.

4.3 Subsurface nitrate reduction under riparian lands takes place in narrow superficial zones

The aim of the present study is to investigate the vertical distribution of the Nitrate Reduction Potential (NRP) at different depths on a natural (Evi site) and a re-stablished (Brynemade) wetlands. It is how that the obtained NRP together with other environmental parameters provides a valuable data of the main driving factors affecting denitrification, including the competitive process DNRA and the performance of a re-stablished wetland. To perform this objective, intact soil cores (0-3 m) were collected and were divided in 10 cm slices for the determination of Organic Matter (OM) trough Loss of Ignition (LOI) as well as Dissolved Organic Carbon (DOC), Moisture (M) and Nitrate Reduction Potential (NRP) spiking nitrate in batch tests.

Brynemade had a 1 m peat layer with high amount of LOI, DOC and M that decreased with depth and Evi had a low content of DOC and M, but high content of LOI at some depths. The nitrate reduction was fitted as a pseudo-first order rate constant (k) from where NRPs were obtained. In addition NRPs showed a decreasing natural logarithmic trend with depth. Brynemade showed high NRPs potentials while Evi had a lower performance demonstrating the functionality of the re-established wetland. NRP took place in a very narrow superficial zone for all cores, in deeper samples, nitrate reduction decreased to undetectable levels. The main driving factor besides depth was OM. Although DOC and LOI could not express by themselves and absolute correlation with NRP, high amounts of DOC in Brynemade ensured enough quantity and quality of organic matter for nitrate reduction. Contrarily, Evi site presents high concentration of LOI but a scarce abundance of DOC.

Finally, Dissimilatory Reduction of Nitrate to Ammonium (DNRA) by analysing initial and final nitrate, nitrite and ammonium abundance in some samples was assessed, showing it to be important in very superficial samples of Brynemade with high contents of OM.

The work described in this chapter is intended to be published as:

Ribas, D., Calderer, M., Marti, V., Johnsen, A.R., Aamand, J., Nilsson, B., Jensen, J.K., Engesgaard, P. & Morici, C. Subsurface nitrate reduction under riparian lands takes place in narrow superficial zones.

4.3.1 Introduction

Wetlands and riparian zones are examples of habitats that can be used directly to decrease nutrient loading of surface waters and to improve its water quality. Nitrate Reduction (NR) in a riparian area is commonly attributed to denitrification, immobilization and plant uptake *(Haycock et al. 1993; Mayer et al. 2005)*.

Specifically, denitrification is a biological process based on the biochemical reduction of nitrate and nitrite in groundwater due to the presence of anaerobe facultative bacteria in the site which can be autotrophic (if sulphur *(Komor and Fox, 2002)* or hydrogen *(Smith et al., 1994)* are present) or heterotrophic. In the latter case, electrons needed for nitrate reduction are originated from the oxidation of organic matter that also acts as a source of cellular carbon (heterotrophism). Illustrative, a stoichiometric reaction of a complete heterotrophic denitrification to nitrogen gas is presented in *Eq. 4.4 (Jørgensen et al. 2004; Appelo et al., 2007)*.

$$5CH_2O + 4NO_3^- \rightarrow 2N_2 + 4HCO_3^- + 3H_2O + CO_2 \qquad \textbf{Eq. 4.4}$$

Riparian soils are rich in organic carbon substrate in top layers (Horizon O, e.g. Peat layer), that leaches dissolved Organic Matter (OM) which provides a carbon source to the heterotrophic denitrification pathway. In this way the age of the OM and the constant input of fresh OM from decayed vegetation is a key point for the process performance. The aging of (OM) has an important influence on the denitrification through soil depth because the disappearance of labile fraction against horizons and time, limits the labile leachate that reaches deeper horizons *(Choi and Wang, 2004; Strosser, 2010).*

In addition, microorganisms are strongly influenced by environmental conditions: dissolved oxygen, mineralizable carbon, pH, nutrients (e.g. phosphorus) *(Pfenning and McMahon, 1997; Song et al., 2012)*, water table elevation *(Hefting et al., 2004; Hernandez and Mitsch 2007)*, temperature and other seasonal conditions *(Ribas et al., 2013)*. All these conditions are critical for the denitrification process.

Reported nitrate reduction rates ranged from 0.004 to 26.5 mg nitrate·l^{-1}·day^{-1} *(Gibert et al., 2008)* and first order constants were in the range $3 \cdot 10^{-5}$ to 1.4 day^{-1} *(Leverentz et al. 2010)* for different types of vegetal-based materials and under different conditions.

Due to high environment heterogeneity in riparian soils, past studies of spatial distribution of the denitrification potential in these systems showed high variations in width and depth *(Cosandey et al., 2003; Curie et al., 2011; Hayakawa et al., 2012; Kjellin et al., 2007; Oehler et al., 2007).* In addition to previously exposed factors in riparian zones, variability can be caused by the great diversity of minerals and organic materials that can be found in different stratigraphic positions, due to sediment transport and settling mechanisms. These mechanisms are affected by frequency and duration of floods, flow patterns, stream velocity and distance from the main channel and eventually sediments could be flushed at one place and filled at another *(Asselman and Middelkoop, 1995)*.

Dissimilatory Nitrate Reduction to Ammonium (DNRA) could also be present. DNRA is a respiratory or fermentative pathway where nitrate is reduced step by step to ammonium competing with denitrification for the nitrate in groundwater *(Calderer et al., 2010)* and in riparian zones *(Sgouridis et al., 2011)*, *Eq. 4.5*.

$$2CH_2O_{(aq)} + NO_3^-{}_{(aq)} + 2H^+ \rightarrow NH_4^+{}_{(aq)} + 2CO_{2\,(g)} + H_2O \qquad \textbf{Eq. 4.5}$$

Ammonium is retained in the soil until nitrification, plant uptake or anaerobic ammonium oxidation process occurs (Anammox). DNRA are less understood than denitrification although it can be a significant or even a dominant process in some ecosystems, *(Rütting et al., 2011)*. Conditions favouring DNRA may include high temperature *(Chen et al., 2015)* and high C/N ratio *(Kraft et al., 2014).* It is

believed, that heterotrophic denitrification supplies more free energy than DNRA, but under nitrate limiting conditions or high OM concentrations DNRA could be favoured because more electrons can be transferred per mole of nitrate, *(Krafta et al., 2011)*. Notice that in both pathways nitrite is an intermediate.

In this work a lab-based methodology for the measurement of the Nitrate Reduction Potentials (NRP) on a natural and re-stablished wetlands at different depths is performed, it is hypothesized that biochemical differences could exist. The obtained NRP together with other environmental parameters provides a valuable data of the main factors affecting denitrification and the competitive process DNRA. It will validate the feasibility to restore wetlands with a working remediation role and assist the design of future re-stablished wetlands taking into account the key parameters affecting the denitrification performance.

4.3.2 Materials and methods

Description of the sites

Two Danish wetland field sites with similar quaternary geology and climate were selected for the present study. The Brynemade site (Odense river basin in Odense Island) has been chosen as a model of a well re-established wetland and the Evi site (Holtum river basin in Jutland, Western Denmark) as a model natural wetland-river system.

The two sites present a very similar geology, both are glacial flood plains composed by a first layer of freshwater deposits such as peat, organic silt, clay and sand followed by a deeper layer of sand and gravel deposited by glacial streams from the Weichsel glacial period. Sites were previously characterized in terms of geology by means of drilling and borehole logging. Several monitoring campaigns were performed after the sampling of the cores in order to compose their respective hydrogeological models and to acquire information about the groundwater chemistry, *(Kronvang et al., 2009; Jensen, 2014, Poulsen et al., 2015; Sebok et al., 2015)*.

Brynemade wetland at the Odense river Basin (Denmark) (55º13’12’’N, 10º17’35’’E; WGS84) was restored in 2003 and was used to document seasonal changes in flow dynamics and nitrate/pesticide degradation performance in a re-established wetland-river system. The restoration included re-raising the riverbed and re-meandering the river to the position it had prior to the 1958 channelization. The site is bordered by a Christmas tree plantation and crop land in the northern part.

The seasonal flow and transport of water and nitrates in this wetland was extensively modelled using hydrogeological characterization with wells, slug and infiltration tests, geophysical image of the subsurface using multi electrode profiling and measurements of the discharge to the river by seepage -meter and river bed temperature studies *(Jensen, 2014)*. From this modelling it was found that in non-flooding periods groundwater flow was horizontal from wetland to river. During flooding periods (75% of the year) flow was upward through the peat layer. It was estimated that between 25 and 37% of the total groundwater was discharged through the peat. The main climate parameters were an annual mean temperature of 8.9ºC and an annual accumulated precipitation of 733 mm (Years: 2001 to 2010, grid 20x20 km for temperature and 10x10 km for precipitation), *(Riddersholm, 2013).*

Evi site is a natural wetland located close to Lake Ejstrup and the city of Ejstrupholm, in Jutland, (55º59’28’’N, 9º19’43’’E; WGS84). The catchment area is at the border of the maximum extension of the Weichselian glaciers corresponding to the last glacial advance. Unlike the Brynemade site, the Evi site is never flooded. Groundwater flow is strongly dependent on precipitations and no reverse flow from streambed to aquifer was observed, *(Poulsen et al., 2015; Sebok et al., 2015)*. The main climate parameters were an annual mean temperature of 8.4ºC and an annual accumulated precipitation of

860 mm (years: 2001 to 2010, grid 20x20 km for temperature and 10x10 km for precipitation), *(Riddersholm, 2013)*.

Sampling of soil cores and characterization

Two intact soil cores from Brynemade (B C.1 and B C.2, up to 3 m) and Evi site (E C.1 up to 3 m and E C.2 up to 2 m) were collected in May 2012 and May 2013, respectively. The soil cores were divided in slices of 10 cm in the laboratory and these subsamples were handled under anaerobic (nitrogen glove box) conditions for determination of NRP.

Moisture (M) was determined gravimetrically as the loss of mass after drying at 105ºC overnight according to the method ISO 11465:1993 values were expressed in wet basis. Loss of Ignition (LOI) was calculated as the fraction of dry matter that was removed after 16 hours at 400ºC employing the standard method, *(Nelson et al., 1996)*.

Dissolved Organic Carbon (DOC) was determined at 1 hour batch experimental time and at the final of the test, the analyses were performed using a TOC analyzer (Multi N/C 3100, Analytik Jena AG) after being filtered through 0.2 µm nylon filter, acidified with concentrated sulfuric acid and purged with synthetic air. These DOC values were used to estimate the initial concentration of DOC that could take part in nitrate reduction.

NRP and DNRA of the soil cores

Batch tests were used to study the kinetics of NRP in subsamples. 10 g of soil from each subsample was mixed with deionised water (100 ml) and placed in 115 ml vials (97 mm in height, 48 mm in diameter). Vials were sealed with butyl rubber septums. The culture was enriched up to 25 $mg \cdot l^{-1}$ of nitrate supplied by sodium nitrate stock solution. All procedure was performed in a globe box in a nitrogen atmosphere. Tests were incubated at 10ºC in a non-stirred system until nitrate depletion or up to 42 days. During incubation, water samples were withdrawn periodically through the septum and inside the globe box to analyse inorganic nitrogen species (nitrate, nitrite and ammonium).

Concentration of nitrogen species in batches were determined by ion chromatography (Dionex ICS-2100, Dionex). In particular, nitrate and nitrite were analysed by using the column Ion pack AS19 4x250 mm (quantification limit for both analytes of 1 $mg \cdot l^{-1}$) and ammonium with the Ion pack CS16 4x250 mm column (quantification limit of 0.2 $mg \cdot l^{-1}$). Concentration of DOC was determined by high temperature catalytic combustion – CO_2 NDIR-Detector. (Multi N/C 3100, Analytik Jena AG) (quantification limit of 0.2 $mg \cdot l^{-1}$).

First-order nitrate reduction rate constants (*k*) were determined by fitting the concentration results to *Eq. 4.6.* Although the batches were analysed up to one month only the first days were considered in order to avoid side effects such as changes or contamination in microbial populations. Quantification limit of k=0.01 d^{-1} was considered by using this method.

$$ln\,[C]_t = ln\,[C]_0 - k \cdot t \qquad \textbf{Eq. 4.6}$$

Where:

$[C]_t$: Concentration of nitrate at time t ($mg \cdot l^{-1}$)
$[C]_0$: Concentration of nitrate at time 0 ($mg \cdot l^{-1}$)
k: nitrate reduction rate constant (d^{-1})
t: reaction time (d)

Ammonium and nitrite were analysed in some depths in order to assess DNRA importance. Both, denitrification and DNRA have a first parallel steps where nitrate is reduced to nitrite, but the

important difference to determine DNRA is if finally nitrogen is present as ammonium or as gaseous nitrogen, *Eq. 4.4 and 4.5*.

All experimental data and *k* have been treated using a statistical software (XLSTAT 2015.1.01, Addinsoft) to obtain Pearson Matrices and PCA analysis in order to determine the main correlations between the parameters.

4.3.3 Results and Discussion

Characterization of the cores

Brynemade site
At Brynemade site, based on the measurements of multi electrode profiling *(Jensen, 2014)*, the wetland hydrogeology could be characterized by a three-layer system, i.e., an upper 1-2 m thick peat layer followed by an approximately 8-18 m thick heterogeneous sand aquifer, and a lower more silty/clayey layer of an undetermined thickness. This conceptual model has been confirmed by the following core characterization.

The LOI content of the cores showed a top (0-100 cm) rich peat layer, with values close to 90% in B C.1 and 70% in B C.2., *Fig. 4.7*. The deeper layers in B C.1 and B C.2 were inorganic, whereas in B C.2, the top peat was succeeded by a second layer (100-140 cm) of increased LOI content, averaging 13.8% (n=4).

Initial DOC, *Fig. 4.7*, from lixiviates of B C.1 and B C.2 at 1 hour of running experiment presented high values in the upper part (0-100 cm) averaging 43.2 and 23.1 $mg \cdot l^{-1}$ (n=10, each core) respectively following a decreasing in a saw-tooth trend.

Final DOC from lixiviates (results not shown) were higher than initial ones for upper layers and were lower for deeper layers in B C.1, pointing to the peat as an important and constant dissolving source of DOC. Probably, an excess of DOC was present in upper layers and denitrification was not limited by the substrate, completing all the reduction of the spiked nitrate. In the case of B C.2, the DOC concentration did not change during the experiment in any of the depths.

Moisture showed similar behaviour with a very humid peat layer (70-80%) and deeper layers ranging between 10-20%, *Fig. 4.7*. In this case there was a more progressive transition than was the case of LOI which could be due to capillary effects.

Evi site
The LOI content of the cores from the Evi site *(Fig. 4.8)* was very high. E C.1 had a relatively low concentration in the top layer (first 10 cm) with 17.1% followed by high organic content layer from 40 to 160 cm in depth averaging 76.9% (n=13) then a saw-tooth trend to extinction was observed. In E C.2 transitions between organic layers and mineral layers were very marked with a very rich top layer 0-30 cm averaging 73.7% (n=3) and other layer at 70-80 cm with 25.1% (n=1).

Interestingly, initial DOC concentrations in both cores were very low in contrast to its LOI content, *Fig. 4.8*. In E C.1 lixiviates were constant without a trend to extinction with depth, averaging 14.7 $mg \cdot l^{-1}$ in all samples (n=29), contrarily E C.2 showed very low concentrations with a fast transition in the upper 20 cm from a 18.3 $mg \cdot l^{-1}$ to a base level of 3 $mg \cdot l^{-1}$. These values were appreciably lower than in the Brynemade site. No significant DOC evolution was observed at the end of the experiment.

Moisture values, such as those observed in Brynemade, were in accordance to LOI values, but in Evi the moisture was much lower than in Brynemade with an organic layer (more than 10%) and deeper

layers less than 10% moisture, *Fig. 4.8*. As in Brynemade, the different materials suppose different moisture that could be linked to field capacity as deep levels were saturated with water.

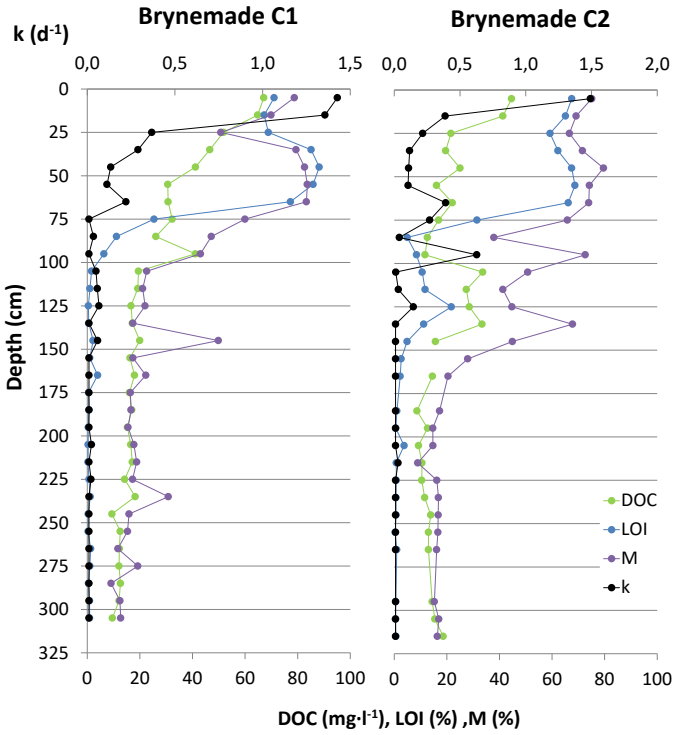

Fig. 4.7 Depth-dependence of soil organic matter determined as DOC and LOI, soil moisture (M) and first-order nitrate reduction rate constants (*k*) at the Brynemade cores.

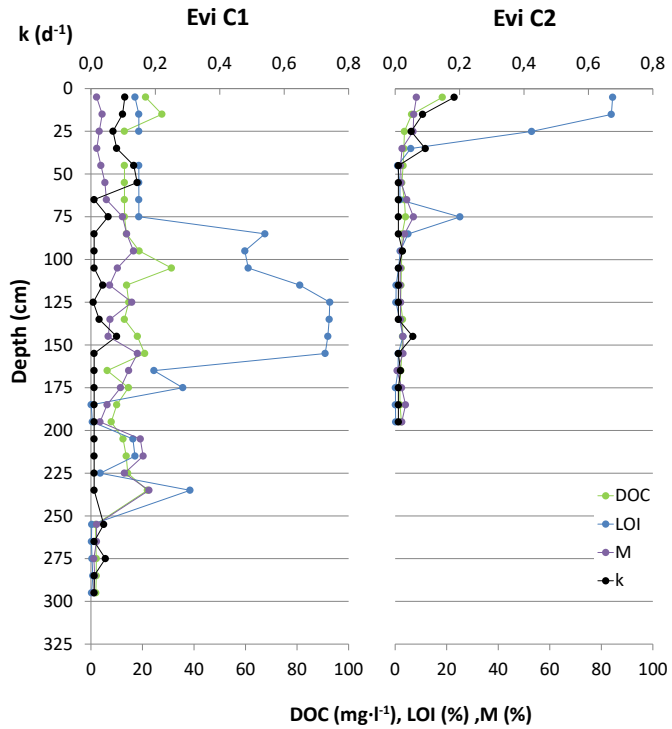

Fig. 4.8 Depth-dependence of soil organic matter determined as DOC, LOI, soil moisture (M) and first-order nitrate reduction rate constants (*k*) at Evi Cores.

Nitrate reduction potential results

The nitrate concentration data in NRP experiments were fitted to *Eq. 4.6* model. Examples of the fitting are shown in *Fig. 4.9*. As it can be observed, nitrate reduction was explained as a pseudo first-order constant in the first days which is in agreement with the literature *(Heinen, 2006)*. Finally the lack of proper DOC for the nitrate reduction or the kinetic quantification limit of the technique restricted the application of the first-order model. Despite the low incubation temperature (10 ºC) used in order to simulate field conditions, high NRP were observed.

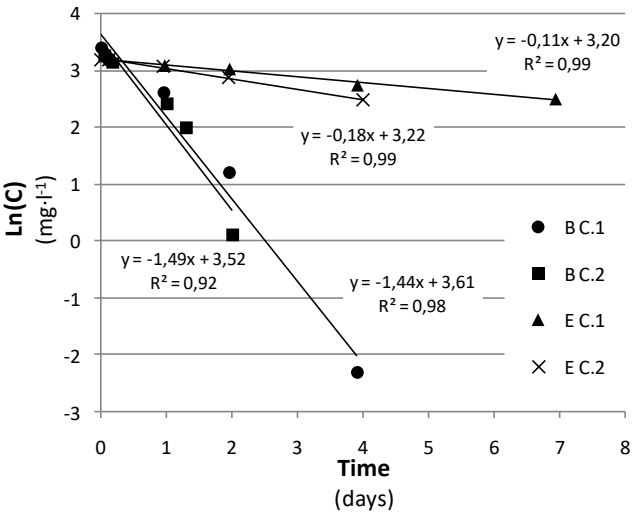

Fig. 4.9 Kinetics fittings of first-order kinetics for 0-10 cm depth of Brynemade C.1 and C.2, Evi C1 and C.2.

At Brynemade site, high NRPs were found in the upper part of the cores <30 cm *(Fig. 4.7)* that also showed high concentrations of LOI and DOC <70 cm. In this zone high first-order rate constants were achieved, reaching 1.43 d^{-1} B C.1 and 1.49 d^{-1} B C.2 in the top (0-10 cm), then kinetics decreased exponentially with depth. Into these first 30 cm of soil NRP averaged 1.05 d^{-1} (n=3) B C.1 and 0.70 (n=3) d^{-1} B C.2. The high NRPs and rich OM zone was succeeded by a lower NRP and OM zone, nitrate reduction was undetectable, considered as 0.01 d^{-1}, in many samples under 70 cm depth and in most samples under 130 cm depth giving an overall mean of 0.14 d^{-1} (n=31) 0 to 310 cm B C.1 and 0.14 d^{-1} (n=31) 0 to 320 cm B C.2. A remarkably exception in B C.2 at 130-140 cm depth with 0.63 d^{-1} was found. Samples from below 315 cm would probably also be below the detection limit of 0.01 d^{-1}. In addition, DOC was probably recalcitrant compared to the top layers because rate constants were negligible. The origin of this recalcitrant DOC in the cores was unlikely to come from the sand and possible came from upper layers where the labile OM for nitrate reduction has been consumed.

The Evi site showed a poor nitrate reduction potential in both cores in spite of high LOI content, even in the top zone of the soil (0-10 cm) being 0.11 d^{-1} E C.1 and 0.18 d^{-1} E C.2, respectively. The averages for the first 30 cm were: 0.09 d^{-1} (n=3) in E C.1 and 0.11 (n=3) d^{-1} in E C.2. Then NRP followed a quickly trend to extinction also in E C.1 which presented a very high LOI content from 30 to 170 cm. Global means were 0.04 d^{-1} (n=29) 0 to 300 cm in E C.1 and 0.03 d^{-1} (n=20) 0 to 200 cm in E C.2, *Fig. 4.8*.

Link of NRP to environmental parameters

Cores from the same sites had a similar behaviour in NRP and had similar environmental parameters. Statistical analysis was performed merging the data from both cores of each site in order to determine the main parameters involved in the NRP.

The Pearson Matrix (PM) *Table 4.5 (Brynemade) and 4.6 (Evi)* produces the correlation coefficients between all the couples of variables. This matrix has been extended by adding the natural logarithm

of the measured variables to test linear, exponential and potential fitting models. For all these correlation studies, significance levels of 5% and 1% were calculated.

From *Table 4.5*, all correlations in Brynemade exceeded 1% of significance level and showed a strong correlation between parameters. The most important correlations were the anticorrelations of soil depth (z) vs: ln *k*, ln LOI, ln DOC and M demonstrating a natural logarithmic extinction through soil depth. It was also observed that *k*, LOI, DOC and M were positive and strongly correlated.

The most important correlation found in Evi's PM, *Table 4.6*, were *k* vs ln z. As in Brynemade all the measured parameters decrease with z. In parallel, only DOC-LOI, *k*-DOC, DOC-LOI and LOI-M correlations were significant.

Table 4.5 Matrix of Pearson correlation coefficients of Brynemade site Core 1 and 2 processed jointly, a statistical significance at the level of 5% is indicated in* and at the level of 1% in**. n = 60.

Variables	z	k	LOI	DOC	M	ln z	Ln k	ln LOI	ln DOC	Ln M
z	1,00									
k	-0,55**	1,00								
LOI	-0,78**	0,57**	1,00							
DOC	-0,70**	0,71**	0,71**	1,00						
M	-0,86**	0,55**	0,88**	0,68**	1,00					
ln z		-0,80**	-0,83**	-0,82**	-0,81**	1,00				
ln k	-0,80**		0,81**	0,67**	0,80**	-0,87**	1,00			
ln LOI	-0,87**	0,54**		0,71**	0,94**	-0,84**	0,79**	1,00		
ln DOC	-0,75**	0,60**	0,71**		0,73**	-0,79**	0,65**	0,74**	1,00	
ln M	-0,88**	0,51**	0,81**	0,69**		-0,80**	0,76**	0,92**	0,75**	1,00

Table 4.6 Matrix of Pearson correlation coefficients of Evi site Core 1 and 2 processed jointly, a statistical significance at the level of 5% is indicated in* and at the level of 1% in**. n = 49.

Variables	z	k	LOI	DOC	M	lnz	Ln k	lnLOI	lnDOC	Ln M
z	1,00									
k	-0,53**	1,00								
LOI	-0,28	0,24	1,00							
DOC	-0,26	0,31*	0,60**	1,00						
M	0,10	-0,15**	0,53**	0,60**	1,00					
ln z		-0,72**	-0,26	-0,31*	0,14	1,00				
ln k	-0,50**		0,23	0,25	-0,21	-0,66**	1,00			
ln LOI	-0,49**	0,36*		0,70**	0,62**	-0,43**	0,35*	1,00		
ln DOC	-0,31*	0,33*	0,64**		0,67**	-0,33*	0,27	0,79**	1,00	
ln M	-0,10	-0,02	0,62**	0,65**		-0,02	-0,09	0,71**	0,75**	1,00

From statistical analysis, it was concluded that the most important driving factors for *k* in Brynemade were ln z and OM and in Evi ln z.

The link between NRP and OM (LOI and DOC) was only significant in the Brynemade site. In the Evi site NRP was lower than in Brynemade with high amounts of LOI but low DOC. This means that in this case the quality of the OM is more important than the quantity as stated in previous cases *(Bastviken et al., 2005; Dodla et al., 2008; Hill and Cardaci, 2004; Hume et al., 2002)*.

Complementarily, due to the high number of correlations established between measured parameters, a PCA analysis was performed with z, *k*, LOI, DOC and M for all the samples grouping Brynemade and Evi cores. Eigenvalues analysis showed that in the case of Brynemade first principal component (F1) described 76.1% of total variation between soil samples. By adding a second principal component (F2) 88.5% was explained and adding a third principal component (F3) the explanation reached 93.6%. In the case of Evi site F1 explained 45.9% of total variation and F1 and F2 reached 77.3%. These three

factors explained 86.9%. Two main factors were chosen for both cases because they already reached >75% of explanation.

Loadings diagrams show the relationship between the two main factors (F1 and F2) and original variables *Fig. 4.10 and 4.11*. For a given factor, the variables are better represented if they are closer to the outer circle and the angle between the projections of the variables reveals the correlation between these projections. If this angle is close to 0º then the factors are correlated, if they are close to 180º then they are anticorrelated, finally those factors close to 90º are not correlated (independent).

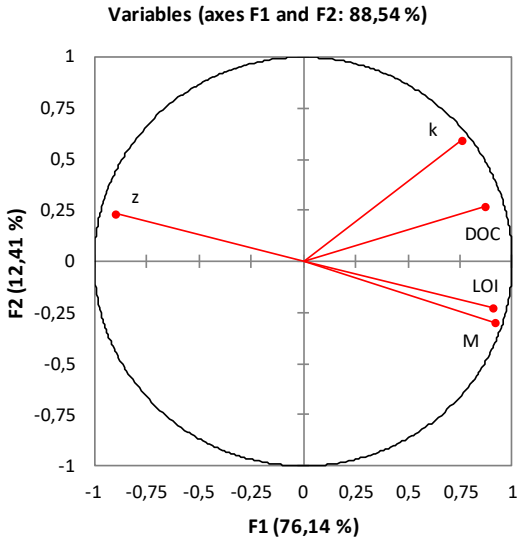

Fig. 4.10 Loading graph analysis of Brynemade site Core 1 and 2.

Fig. 4.10, shows Brynemade F1 and F2, it could be concluded that all the variables *k*, LOI, DOC and M contributed strongly to F1 and were anticorrelated with z. These results matched with the correlation matrix where high and negative correlations were observed. On the other side, *k* value was the variable that more contributes to F2. These results pointed to attribute F1 to the composition of the soil with depth and F2 to complementary explain the reduction capacity. Thus NRP could be explained partially by composition and was less correlated with depth that the other variables.

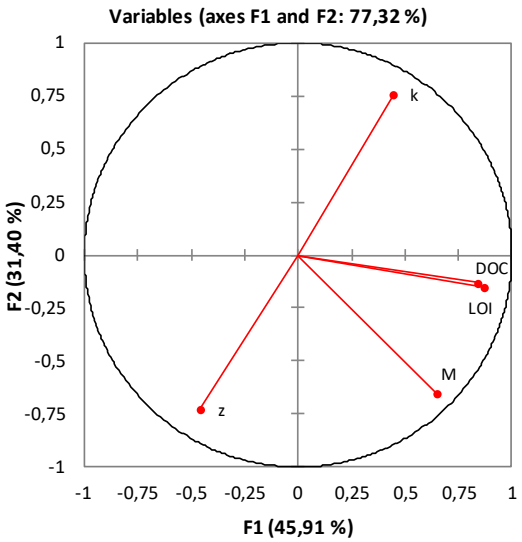

Fig. 4.11 Loading graph analysis of Evi site Core 1 and 2 processed jointly.

In the case of Evi site, analysis of the two first factors, *Fig. 4.11,* showed that F1 was strongly influenced by DOC, LOI and M whereas F2 showed that *k* and z were close to be independent of LOI, DOC and M. In contrast to Brynemade, in Evi LOI and DOC were much correlated and *k* has a stronger dependence of z.

In order to compare the trends of *k* values with z, *Table 4.7* shows the fitting of *k* vs ln z that was the best empirical correlation that fitted the trend of *k* measurements with z. As it can be seen, Brynemade showed much higher initial values of *k* (intercept is *k* value for 1 cm) with higher decreasing trend compared to Evi values.

Table 4.7 Nitrate reduction potential first-order kinetic constants (*k*) along depth fitted in natural logarithmic regressions. B (Brynemade), E (Evi), C (Core) and (n). z in cm.

Brynemade wetland			**Evi wetland**	
k B.C1 d^{-1}	*k* B.C2 d^{-1}		*k* E.C1 d^{-1}	*k* E.C2 d^{-1}
-0.30·ln(z) + 1.570 R^2 = 0.71 (31)	-0.23·ln(z) + 1.241 R^2 = 0.58 (29)	**d**	-0.02·ln(z) + 0.174 R^2 = 0.48 (29)	-0.03·ln(z) + 0.198 R^2 = 0.69 (20)

Re-established or natural condition of the Brynemade and Evi sites had minor impact on the NRP performance. Other effects of local conditions had major influence, such as the availability of labile OM had a higher impact on NRP than the re-stablishing condition, these results are completely in agreement with similar studies in restored and unrestored Danish steams, *(Veraart et at., 2014)*.

DNRA Evaluation

DNRA evaluation was performed from the measurement of the increment of ammonium that is shown in *Table 4.8*.

Table 4.8 Measurements of ammonium ($mg \cdot l^{-1}$) at the beginning (1h) and at the end of nitrate reduction experiments.

	B C1		**B C2**		**E C1**		**E C2**	
Depth	Initial	Final	Initial	Final	Initial	Final	Initial	Final
0-10	1.8	6.0	3.0	6.2	0.6	0.9	0.5	0.8
20-30	0.6	1.0	0.6	1.0	0.3	0.7	< 0.2	< 0.2
40-50	0.4	0.2	0.2	0.2	0.3	0.4	< 0.2	< 0.2
180-190	<0.2	<0.2	< 0.2	<0.2	n.a.	n.a.	n.a.	n.a.

n.a. not available

As it is seen in *Table 4.8*, B C.1 and B C.2 between 0-10 cm depth accumulated an important amount of ammonium. Nitrite in the same samples was negligible, with maximum increasing values of 1 mg nitrite·l^{-1} in core B C.2 at 25 cm and without increase for cores B C.1, E C.1 and E C.2.

Taking into account that the nitrogen contained in an ammonium concentration of 7.2 mg·l^{-1} is equal to 25 mg·l^{-1} of nitrate (spiked initial concentration), the following expression could be used to evaluate the fraction of DNRA, *Eq. 4.7*. *Table 4.9* shows the results of DNRA fraction.

$$f_{DNRA} = -3{,}472 \frac{\Delta[NH_4^+]}{\Delta C} \qquad \textbf{Eq. 4.7}$$

Where:

f_{DNRA}, DNRA fraction
$\Delta[NH_4^+]$ is the increment with time of ammonium concentration ($mg \cdot l^{-1}$)
ΔC is the variation in time of nitrate ($mg \cdot l^{-1}$) measured in the same points.

Table 4.9 Measurement of f_{DNRA} in reduction experiments.

Depth	B C.1	B C.2	E C.1	E C.2
0-10	0.50	0.43	0.04	0.04
20-30	0.05	0.06	0.12	<0.01
40-50	<0.01	<0.01	0.01	<0.01
180-190	n.a.*	<0.01	n.a.	n.a.

*n.a.: not available

As it is seen in *Table 4.9* the fraction of DNRA was only significant in the first 10 cm of Brynemade cores (between 43 and 50% in B C.2 and B C.1, respectively). Contrarily, at the Evi site, the DNRA activity was only important between 20 and 30 cm at E C.1, other samples always showed a DNRA fraction below 1%. These results could be explained by the high superficial concentration of organic matter that favours DNRA pathway.

4.3.4 Conclusions

- Nitrate reduction followed a pseudo first-order constant and showed a falling natural logarithmic trend with depth. Consequently, subsurface nitrate reduction under these riparian zones took place in a very narrow superficial zone. In deeper samples, nitrate reduction decreased to undetectable levels.

- DOC and LOI cannot express by themselves an absolute correlation with NRP, but high amounts of DOC in Brynemade during the experiment ensured enough quantity and quality of organic matter for NR. The opposite situation was observed in Evi site where low DOC and NRP values were observed. DNRA was important only in the very superficial samples of Brynemade, where an excessive content of labile OM could produce favourable conditions for DNRA.

- Evi site presented low NRP and a high concentration of LOI but a scarce abundance of DOC, showing organic matter not usable for NR, strengthening the idea that labile OM (quality) is more important that quantity.

- Comparing a natural wetland (Evi) to the re-stablished Brynemade with a similar geology and climate and taking into consideration the high NRPs observed, it is clear that wetlands can be restored satisfactorily. Other factors such as the availability of labile OM had a higher impact on NRP than the re-stablishing condition.

4.3.5 References

Appelo, C. A. J., & Postma, D. (2007). Geochemistry, groundwater and pollution. 2on ed., A,.A. Balkema Publishers, Leiden The Nederlands, pp. 649.

Asselman, N. E., & Middelkoop, H., (1995). Floodplain sedimentation: quantities, patterns and processes. Earth Surface Processes and Landforms, 20(6), 481-499.

Bastviken, S. K., Eriksson, P. G., Premrov, A., & Tonderski, K., (2005). Potential denitrification in wetland sediments with different plant species detritus. Ecological Engineering, 25(2), 183-190.

Calderer, M., Gibert, O., Martí, V., Rovira, M., de Pablo, J., Jordana, S., Duro, L., Guimerà, J. & Bruno, J., (2010). Denitrification in presence of acetate and glucose for bioremediation of nitrate-contaminated groundwater. Environmental Technology, 31 799-814.

Choi, Y., & Wang, Y., (2004). Dynamics of carbon sequestration in a coastal wetland using radiocarbon measurements. Global Biogeochemical Cycles, 18(4).

Cosandey, A. C., Guenat, C., Bouzelboudjen, M., Maıtre, V., & Bovier, R., (2003). The modelling of soil-process functional units based on three-dimensional soil horizon cartography, with an example of denitrification in a riparian zone. Geoderma, 112(1), 111-129.

Curie, F., Ducharne, A., Bendjoudi, H., & Billen, G., (2011). Spatialization of denitrification by river corridors in regional-scale watersheds: Case study of the Seine river basin. Physics and Chemistry of the Earth, Parts A/B/C, 36(12), 530-538.

Dodla, S. K., Wang, J. J., DeLaune, R. D., & Cook, R. L., (2008). Denitrification potential and its relation to organic carbon quality in three coastal wetland soils. Science of the Total Environment, 407(1), 471-480.

Gibert, O., Pomierny, S., Rowe, I. & Kalin, R.M., (2008). Selection of Organic Substrates as Potential Reactive Materials for use in a Denitrification Permeable Reactive Barrier (PRB). Bioresource Technology, 99(16), 7587-7596.

Hayakawa, A., Nakata, M., Jiang, R., Kuramochi, K., & Hatano, R., (2012). Spatial variation of denitrification potential of grassland, windbreak forest, and riparian forest soils in an agricultural catchment in eastern Hokkaido, Japan. Ecological Engineering, 47, 92-100.

Haycock, N. E., Pinay, G., & Walker, C., (1992). Nitrogen retention in river corridors: European perspective. Ambio,21(8), 340-6.

Hefting, M., Clement, J. C., Dowrick, D., Cosandey, A. C., Bernal, S., Cimpian, C., ...& Pinay, G., (2004). Water table elevation controls on soil nitrogen cycling in riparian wetlands along a European climatic gradient. Biogeochemistry, 67(1), 113-134.

Heinen, M., (2006). Simplified denitrification models: overview and properties. Geoderma, 133(3), 444-463.

Hernandez, M. E., & Mitsch, W. J., (2007). Denitrification in created riverine wetlands: Influence of hydrology and season. Ecological Engineering, 30(1), 78-88.

Hill, A. R., & Cardaci, M., (2004). Denitrification and organic carbon availability in riparian wetland soils and subsurface sediments. Soil Science Society of America Journal, 68(1), 320-325.

Hume, N. P., Fleming, M. S., & Horne, A. J., (2002). Plant carbohydrate limitation on nitrate reduction in wetland microcosms. Water Research, 36(3), 577-584.

Jensen, J.K., (2014). Flow and transport in riparian zones. Ph. D. Thesis. University of Copenhaguen.

Jørgensen, P. R., Urup, J., Helstrup, T., Jensen, M. B., Eiland, F., & Vinther, F. P., (2004). Transport and reduction of nitrate in clayey till underneath forest and arable land. Journal of Contaminant Hydrology, 73(1), 207-226.

Kjellin, J., Hallin, S., & Wörman, A., (2007). Spatial variations in denitrification activity in wetland sediments explained by hydrology and denitrifying community structure. Water Research, 41(20), 4710-4720.

Kraft, B., Strous, M., & Tegetmeyer, H. E., (2011). Microbial nitrate respiration–genes, enzymes and environmental distribution. Journal of Biotechnology, 155(1), 104-117.

Kronvang, B., Hoffmann, C. C., & Dröge, R. (2009). Sediment deposition and net phosphorus retention in a hydraulically restored lowland river floodplain in Denmark: combining field and laboratory experiments. Marine and Freshwater Research, 60(7), 638-646.

Leverenz, H. L., Haunschild, K., Hopes, G., Tchobanoglous, G., & Darby, J. L., (2010). Anoxic treatment wetlands for denitrification. Ecological Engineering, 36(11), 1544-1551.

Mayer, P. M., Reynolds, S. K., McCutchen, M. D., & Canfield, T. J., (2007). Meta-analysis of nitrogen reduction in riparian buffers. Journal of Environmental Quality, 36(4), 1172-1180.

Nelson, D.W., & Sommers, L.E., (1996). Total carbon, organic carbon, and organic matter. In: Methods of Soil Analysis, Part 2, 2nd ed., A.L. Page et al., Ed. Agronomy. 9:961-1010. American Society of Agronomy., Inc. Madison, WI.

Oehler, F., Bordenave, P., & Durand, P., (2007). Variations of denitrification in a farming catchment area. Agriculture, Ecosystems & Environment, 120(2), 313-324.

Pfenning, K. S., & McMahon, P. B., (1997). Effect of nitrate, organic carbon, and temperature on potential denitrification rates in nitrate-rich riverbed sediments. Journal of Hydrology, 187(3), 283-295.

Poulsen, J. B., Sebok, E., Duque, C., Tetzlaff, D., & Engesgaard, P. K., (2014). Detecting groundwater discharge dynamics from point to catchment scale in a lowland stream: combining hydraulic and tracer methods. Hydrology and Earth System Sciences Discussions, 11(12), 13101-13143.

Ribas, D., Calderer, M., Martí, V., & Rovira, M., (2015). Effect of different seasonal conditions on the potential of wetland soils for groundwater denitrification. Desalination and Water Treatment, 53(4), 994-1000.

Riddersholm W.P., (2013). Teknisk Rapport 13-09, Klimagrid Danmark, Referenceværdier 2001-2010. Danish Meteorological Institute.

Robertson, W. D., Russell, B. M., & Cherry, J. A. (1996). Attenuation of nitrate in aquitard sediments of southern Ontario. Journal of Hydrology, 180(1), 267-281.

Rütting, T., Boeckx, P., Müller, C., & Klemedtsson, L., (2011). Assessment of the importance of dissimilatory nitrate reduction to ammonium for the terrestrial nitrogen cycle. Biogeosciences, 8(7), 1779-1791.

Sebok, E., Duque, C., Engesgaard, P., & Boegh, E., (2015). Application of Distributed Temperature Sensing for coupled mapping of sedimentation processes and spatio-temporal variability of groundwater discharge in soft-bedded streams. Hydrological Processes, 29(15), 3408-3422.

Sgouridis, F., Heppell, C. M., Wharton, G., Lansdown, K., & Trimmer, M., (2011). Denitrification and dissimilatory nitrate reduction to ammonium (DNRA) in a temperate re-connected floodplain. Water research, 45(16), 4909-4922.

Song, K., Kang, H., Zhang, L., & Mitsch, W. J., (2012). Seasonal and spatial variations of denitrification and denitrifying bacterial community structure in created riverine wetlands. Ecological Engineering, 38(1), 130-134.

Strosser, E., (2010). Methods for determination of labile soil organic matter: an overview. Journal of Agrobiology, 27(2), 49-60.

Veraart, A. J., Audet, J., Dimitrov, M. R., Hoffmann, C. C., Gillissen, F., & de Klein, J. J. (2014). Denitrification in restored and unrestored Danish streams. Ecological Engineering, 66, 129-140.

5 nano Zero Valent Iron: production approaches and reactivity

The following chapter exposes the experimental processes and the results obtained through the research for a new method to produce nano Zero Valent Iron (nZVI) by milling and the extensive characterization of these new produced particles.

Previously to the lab work, first task was to consider safe requirements, designing and implementing safety measures and protocols.

5.1 Research with nano Zero Valent Iron overview

In the production and manipulation of new nanoscale materials a precautionary attitude must be taken. Some of these materials exhibit carcinogenesis and in the specific case of the nano Zero Valent Iron (nZVI) toxicity research is just being assessed *(Sun et al., 2016)*. Besides to toxicity, most fine divided metals present pyrophoricity, this fact adds an extra issue to consider when designing the safety and working protocols.

5.1.1 Working with pyrophoric and nanomaterials: procedures and safety considerations

High aspect ratio nanomaterials are often defined (but not limited) to have one of the following characteristics: thinner than 3 µm, fibres longer than 10 – 20 µm, biopersistent and not soluble, *(Health and Safety Executive, 2013)*. These presents a health concern, besides the chemical composition of the bulk material an extra danger emerges due to the nanoscale size. Two main exposition pathways can be defined:

Firstly, nanoscale materials may penetrate the cell wall and disrupt the DNA working mechanisms, ultimately, causing carcinogenesis. This can be produced over the skin contact or by an internal contact.

Secondly, due to the high capacity of the dry nanoscale materials to produce aerosols thus to be airborne, respiratory exposure is very likely and at nanoscale sizes alveolar deposition is expected, *Fig. 5.1*.

Pyrophoricity is a danger that should be seriously considered, during this thesis it was accidentally observed. In a non-aerosol form nZVI burns in a slowly and non-explosive form but reaching high temperatures, *Fig. 5.2*. It was experimentally determine that spontaneous ignition was not produced if oxygen content was <1%, the use of a tight controlled anaerobic atmosphere is mandatory.

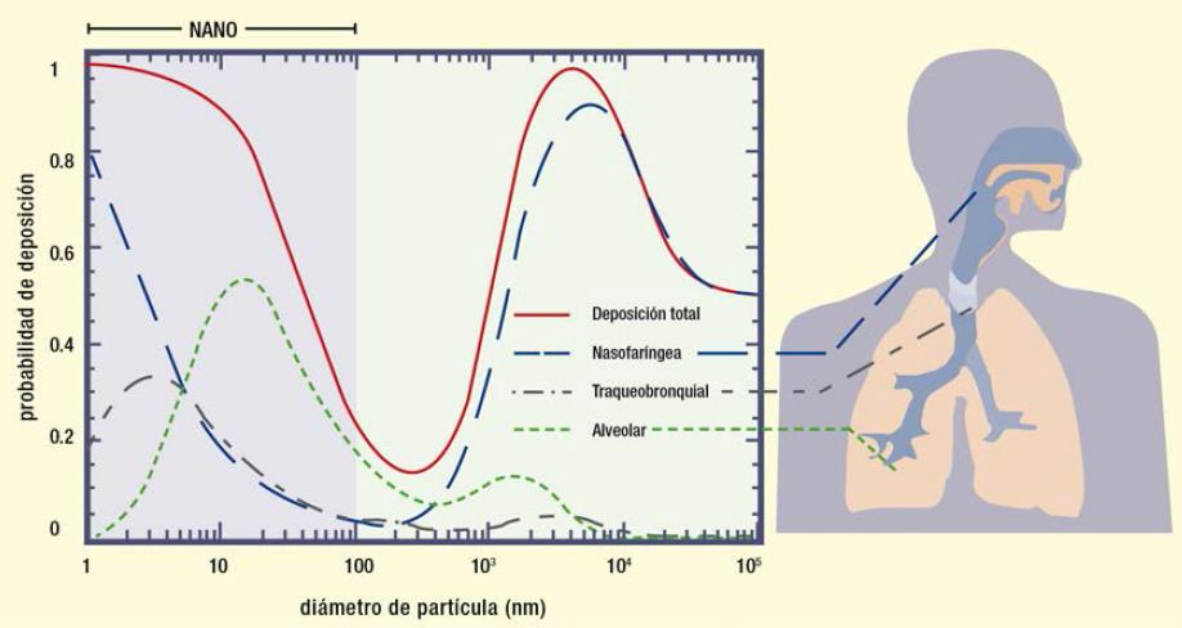

Fig. 5.1 Deposition probability for different particle diameters on different parts of the respiratory system, *(Quintana et al., 2013)*.

Fig. 5.2 nZVI pyrophoricity tests.

Safety protocols states that the first measure to adopt is to reduce the accident provability. Suspending the nZVI in a viscous and non-flammable liquid is an excellent method to avoid the release of free particles into the air, removing respiratory exposure pathway. In addition, it stops the explosion and flammability risk because liquid acts as an oxygen barrier. However, for certain analysis and some commercial samples, particles in dry form were handled thus forcing the adoption of additional measures and leading to the implementation of protocols to operate with pyrophoric materials. The adapted safety flow chart and the consequent adopted safety measures are exposed in *Fig. 5.3 and Table 5.1*.

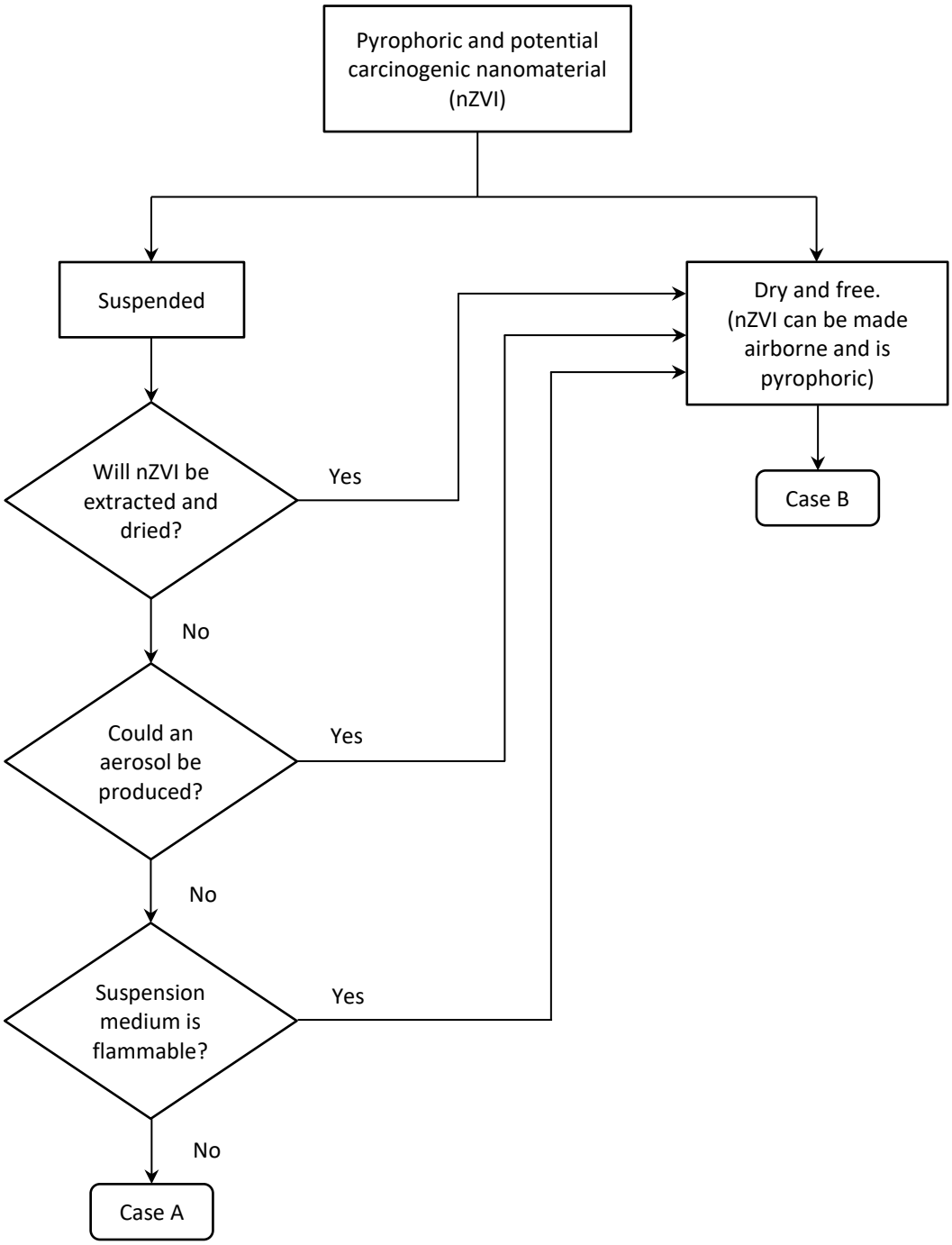

Fig. 5.3 Safety protocol flow chart, adapted from *(Health and Safety Executive, 2013)*.

Table 5.1 Safety measures adopted depending on the identified case.

Case	Safety measures
A	• FFP3 mask homologation or higher. • Use of double gloves: latex + long sleeve nitrile. • Laboratory googles. • All generated absorbents and other cleaning material residues discarded submersing and storing it under water.
B	• Full enclosure with HEPA 14 filtration, anaerobic glove box and flushing to a safe place. • Storage in a double anaerobic containment in anaerobic glove box. • Residues suspended in water within the glovebox.

5.1.2 References

Health and Safety Executive. (2013). Using nanomaterials at work Including carbon nanotubes (CNTs) and other biopersistent high aspect ratio nanomaterials (HARNs). HSG272.

Quintana, M.J., Agurtzane, M., Uribe, M.C., Uribe, B., Jiménez, R., Cohen, E., Gálvez, V., Sousa, M.E., Sánchez, M.T., Colorado, M. & Aguilar, J. (2015). Seguridad y salud en el trabajo con nanomaterials. Instituto Nacional de Seguridad e Higiene en el Trabajo (INSHT).

Sun, Z., Yang, L., Chen, K. F., Chen, G. W., Peng, Y. P., Chen, J. K., ... & Lin, C. H. (2016). Nano zerovalent iron particles induce pulmonary and cardiovascular toxicity in an in vitro human co-culture model. Nanotoxicology, 1-10.

5.2 First attempts in nano Zero Valent Iron production by wet milling

First steps were aimed to replicate the previous nano Zero Valent Iron production methods through milling found in the literature, all based in wet ball milling in water medium. Although in the first tests the final particle size reached was ≈ 20 nm, the Zero Valent iron recovered after the milling procedure was minimal. All produced particles were mainly composed by iron oxides due to the reactivity of iron in water.

Several attempts to replace the water using inert organic solvents were performed. The requirements for the new wet medium were: high water solubility, high flash point, low dynamic viscosity, environmentally friendly and low cost. The following wet media were tested: ethanol, Mono Ethylene Glycol (MEG), propylene glycol and polyethylene glycol MW200.

Ethanol showed to be a suitable milling medium but flammability and its low boiling point generated a large pressure build up into the milling vials. Propylene glycol and polyethylene glycol MW200 had a very poor performance due to the shock energy diminution as a result of the high viscosity. Finally, MEG was selected since it has the lower viscosity among all the media which fitted most of the requirements.

Accidental chromium and nickel alloying from a stainless steel grinding media lead to the first tests using conventional ball milling that produced smaller particles than the feed iron. However, it would be environmentally unacceptable in field applications in consequence cross contamination was avoided in the following tests.

The obtained particles using non-aqueous media and chromium – nickel free grinding balls were large flakes of several micrometres in diameter but only 100-50 nm in thickness. The ductility of iron arose when the oxidation was avoided thanks to the non-aqueous media and particle size reduction was stopped regardless of milling time. New strategies to

The work described in this chapter has been published in:

Ribas, D., Cernik, M., Martí, V., & Benito, J. A. (2016). Improvements in nanoscale zero-valent iron production by milling through the addition of alumina. Journal of Nanoparticle Research, 18(7), 1-11.

5.2.1 Introduction

The use of iron nanoparticles, more commonly known as nano zero-valent iron (nZVI), for groundwater remediation has been investigated for the last 10-15 years because of its great potential to reduce subsurface contaminants such as halogenated organic compounds *(Wang et al. 1997)*, transition metals, including chromium *(Klimkova et al. 2011)* and a wide range of other chemical pollutants *(Crane et al. 2012)*. Even though there are more than 50 pilot or full-scale applications of nZVI for in-situ applications worldwide *(Mueller et al. 2012; Yan et al. 2013)*, there are certain critical points that require improvement so as to make possible large-scale commercialization of this technology.

One of the problems is nZVI´s low mobility in porous media given that iron nanoparticles (20-150 nm in diameter) have a strong tendency to aggregate forming a network of micrometer-sized particles *(Phenrat et al. 2007; O'Carroll et al. 2013)*. On the other hand, there are several uncertainties concerning the use of nanotechnology as regards environmental toxicity, meaning that its use is limited by a number of countries through strict regulations *(Yan et al. 2013)*. Finally, current production methods produce only limited quantities of nZVI at a relatively high cost, which may be the main reason why its use is not more widespread *(Crane et al. 2012; Mueller et al. 2012)*.

There are many methods for producing iron nanoparticles, but only a few of them are commercially available *(Crane et al. 2012; Yan et al. 2013)*. The use of nZVI obtained from borohydride reduction of dissolved Fe (III) in an aqueous solution *(Wang et al. 1997)* is common in controlled laboratory studies. At a commercial scale, nZVI is currently produced by gas phase reduction of iron oxides at elevated temperatures *(Uegami et al. 2006; nanoIron 2016)*. Finally, nZVI can also be produced by wet milling of conventional iron powder. In the latter case, stable dispersions of iron nanoparticles in an aqueous solution with an average size of 100 nm and good oxidation-reduction potential (ORP) have been reported *(Zhang et al. 2006)*. However, the use of an aqueous solution may lead to a large decrease of Fe(0) content due to the known reactivity of iron with water *(Crane et al. 2012)*.

First tests were aimed to replicate the research found in the available information about top-down production. In all reviewed literature, the most successful methods in which a nanoscale is reached, were based on high energetic ball milling in water medium *(Zhang, 2006; Li et al., 2009)*.

- *(Zhang, 2006)*. In this patent the production of nano Zero Valent iron particles with a mean diameter <100nm is claimed. The grinding was carried under a high energetic ball milling, specifically in an attritor mill (LabStar, Netzsch), filling a 0.6 l vial up to 80-85% of the volume with steel grinding media beds (ø = 150 µm). The milling time lasted for 45 – 240 min at 2200 – 2400 rpm providing an energy density of 1.5 – 1.8 kW per litre of suspension. During all the process, the system was maintained at <55 ºC. The initial iron had a maximum mean diameter of 10 µm and it was dispersed in a water suspension at 30% of iron by weight. In order to stabilize the suspension, dispersants were used in a concentration of 1-2%, i.e.: sodium polymethacrylate or ammonia polymethacrylate. The pH, ORP and the degradation capacity of trichloroethylene, seems promising. Unfortunately, there is not a quantification of the remaining Fe(0) / iron oxides proportion after the milling process or after a certain storage time.

- *(Li et al., 2009)*. In this work, iron particles with diameters < 50 nm were obtained. The mill used was also an attritor mill (LabStar, Netzsch), filling the grinding chamber of 0.7 l up to 64% with steel beads of 250 µm in diameter. The milling time lasted up to 8 h at 2000 – 2500 rpm. The initial iron was a microscale ZVI with a d_{50} of 2 µm. Dispersants were not used and further details about the feeding concentrations are not provided. After the process an extensive characterization of the particles was performed, including: SEM, BET, HR-XPS, XRPD, pH – ORP profiles and reactivity towards chlorinated aliphatic hydrocarbons. HR-XPS showed that at least the outer layer of the milled particles was mainly composed by maghemite, magnetite

and wustite. On the other hand, XRPD diffractograms showed a clear peak of α-Iron but again a quantitative analysis of Fe(0) / iron oxides proportion is not provided.

Recently, a new milling method using non-aqueous media Mono Ethylene Glycol (MEG) has been reported *(Köber et al. 2014)* and commercialized. The obtained suspensions showed a negligible loss of Fe(0) and a high specific surface area (18 $m^2 \cdot g^{-1}$). Nevertheless, milled particles had a flaky morphology of several microns in length with a thickness of less than 100 nm.

5.2.2 Materials and methods

The feed iron was a pure iron powder (99.9%) (Höganäs, Sweden) sieved at 45 µm for all tests except for milling time dependence experiments where it was switched to Carbonyl Iron Powder (CIP-SM, BASF SE), with an iron content >99% and a mean particle diameter of 2.77 µm by volume. In all the cases a 15 $g \cdot l^{-1}$ concentration on wet medium was used, meaning 1.5 g in the vial. The milling tests were carried out in a planetary ball mill (P-5, Fritsch GmbH), *Fig. 5.4*, using SAE 304 stainless steel vials with a capacity of 250 ml. 250g of grinding medium was used in all the tests but different sizes and chemical compositions were tested with the following mean diameters, *Table 5.2*. These grinding media are spherical shots used for shot peening or blast cleaning operations. They were chosen because of its low price meeting the goal for an economical method also a broad catalogue with different size distributions was a plus.

Fig. 5.4 Planetary ball mill (P-5, Fritsch GmbH). Curtesy of (Fritsch GmbH).

Table 5.2 Chemical composition of the grinding media used.

Ref.	Diameter	C	Mn	Cr	Ni	Si	S	P
	mm	%	%	%	%	%	%	%
S330	1----	0.85 - 1.2	0.6 - 1.2	---	---	> 0.4	< 0.05	< 0.05
S550	1.4--	0.85 - 1.2	0.6 - 1.2	---	---	> 0.4	< 0.05	< 0.05
S660	2----	0.85 - 1.2	0.6 - 1.2	---	---	> 0.4	< 0.05	< 0.05
G18	1.15	0.80 - 1.2	0.6 - 1.2	---	---	> 0.4	< 0.05	< 0.05
Cr/Ni 60	1----	0.15 - 0.25	0.7 - 1.3	16.0 - 20.0	7.0 - 9.0	1.5 - 2.5	---	---

Knowing the load of grinding medium (250 g) and the feed iron powder (1.5 g), Ball to Powder Ratio (BPR) can be obtained, which in this case is 166. This value is very large, in the high range of previously reported values *(Suryanarayana, 2001)*.

In all cases the vials were filled with 100 ml of wet medium. Different liquids were used for this purpose. The first experiments in this research were carried out in water medium but soon the need to use an inert medium concerning iron reactivity arose. Besides the requirement for the wet medium of being chemically inert against the Fe(0) and its oxides, there were other requirements to be met (some of the considered media *Table 5.3*):

- High water solubility. If the generated product could be injected in the field as it comes out from the milling process, it would represent a major simplification in the overall method. In order to be able to do this, the wet medium must be very soluble in water, diluting easily once the particles are in the aquifer matrix and not hindering. This way, inert medium is not an obstacle for the interaction of nZVI particles with pollutants. It is important because it is reported that organic coatings on the nZVI particles reduce nZVI reactivity *(Velimirovic et al., 2015)*.

- Environmentally friendly - Biodegradable. As it is intended to inject the particles in field suspended in this same wet medium used during grinding, it must be compatible with the environmental regulations and not suppose a treat to the environment or humans. Highly biodegradable substances should be a valid approach.

- High flash point. For safety considerations on working with pyrophoric material, flammability is a major concern. The wet medium must not be inflammable in the working temperature range, providing an extra layer of security during milling, besides the inert atmosphere used.

- Low dynamic viscosity. Viscosity of the wet medium has a dramatic effect on the milling performance, since it hiders the grinding because there is more drag force to overcome between the grinding medium and the particles to be milled, *(Lameck et al., 2006)*. It is interesting to note that viscosity decreases as temperature increases, i.e.: MEG has a dynamic viscosity of 16.2 cP at 20 ºC but it drops to 5.2cP at 60 ºC *(DOW, 2016)*.

- Cost. The aim of this research is to find a new economical and straightforward method for the nZVI production, cost must be as low as possible.

Table 5.3 Shows a fists screening of the considered wet media and properties, none of them fulfilling all the requirements.

Liquid	Density (20ºC) $g \cdot cm^{-3}$	Dynamic viscosity (20ºC) cP	Boiling point (1 bar) ºC	Flash point (O.C.) ºC	Solubility in water
Water[1]	1.000	0.9	100	---	---
Ethanol[1]	0.789	1.1	78	16.6	miscible
Mono Ethylene Glycol (MEG)[2]	1.113	16.2	197	111	miscible
Propylene glycol[3]	1.036	42	188	130	miscible
Polyethylene glycol MW200[4]	1.124	43 - 57	>250	180	miscible
Perfluoroheptane (FC-84)[5]	1.730	0.6	80	none	<5 $mg \cdot l^{-1}$
Perfluorooctane (FC-77)[6]	1.766	1.3	103	none	<5 $mg \cdot l^{-1}$

O.C.: Open Cup; [1] *(Mackay et al., 2006)*; [2] *(Sigma-Aldrich, 2016a)*; [3] *(Sigma-Aldrich, 2016b)*; [4] *(Sigma-Aldrich, 2016c)*; [5] *(3M, 2016a)*; [6] *(3M, 2016b)*.

After some initial test with absolute ethanol (Scharlau) and poly ethylene glycol M200 (Sigma-Aldrich Co. LLC.), MEG (Scharlau). MEG was selected mainly because of safety considerations (high flash point) and precedents of its use in the literature *(Köber et al., 2014)*. MEG has other interesting advantages such as: high solubility in water, high biodegradability *(Mrklas et al., 2004)* and its high viscosity drops quickly as temperature increases *(Bohne et al., 1984)*.

The vials were load with the desired: grinding medium, wet medium and 1.5g of iron. Then vials were purged with argon gas until a protective atmosphere was created inside the vials. The rotating speed was 400 rpm and the milling cycle consisted of 20 min of attrition followed by 20 min of stand-by periods to minimize the rise of temperature. The cycle was repeated until the desired total milling time was reached.

After milling, all the slurries were initially sieved with a stainless steel sieve of 180 µm to remove the grinding balls.

The particle size distribution was determined in an absolute ethanol solution by Laser Diffraction particle size analysis (LD) (LS 13320, Beckman Coulter). All the results obtained by this method were processed using the Fraunhofer method in particle volume mode. Total iron (Fe(0) and iron oxides) concentration was assessed, firstly, digesting the suspensions with 2:1 HNO_3:H_2O_2 and then analysing it by Inductively Coupled Plasma Atomic Emission Spectroscopy (ICP-AES), (Optima 3200, Perkin-Elmer). The content of Fe(0) was determined in triplicate by the hydrogen production method *(Liu et al. 2005a)* where the iron reacts with sulfuric acid added to the slurry and the volume of produced hydrogen is measured and Fe(0) is stoichiometrically found, *Eq. 5.1*.

$$Fe + H_2SO_4 \rightarrow FeSO_4 + H_2 \quad \textbf{Eq. 5.1}$$

The morphology of milled particles was studied by Scanning Electron Microscopy (SEM) (Gemini, Zeiss). pH and Oxidation Reduction Potential (ORP) of the obtained suspensions were determined with a multimeter (MM 41, Crison). ORP values were normalized to Standard Hydrogen Electrode (SHE) adding +209 mV (25ºC).

5.2.3 Results and discussion of wet milling in water media

Milling conditions and main characterization results of the completed tests with water are exposed in *Table 5.4*. As can be seen, in all the tests nanoscale particles were produced, for example:

In A1 test in which the particles were milled for 8 h, LD showed that 96% of the particles were < 1 µm with a mean particle diameter of 212 nm, *Table 5.4 and Fig. 5.5*. However in SEM images, *Fig. 5.6 (Left)* manual counting was carried out and the average diameter obtained was 23.4 nm. The discrepancy between SEM manual counting and LD is explainable because LD does not discriminate between aggregates and particles, there is a shift to higher values if aggregation is produced.

In A3 test the particles were milled for 24 h laser diffraction showed that 100% of the particles were < 1 µm with mean particle diameter of 382 nm, *Table 5.4 and Fig. 5.5*. However, an average diameter of 16.0 nm was found through manual counting in SEM images, *Fig. 5.6 (Right)*.

Table 5.4 Milling test in water media, grinding conditions and main characterization parameters. Shaded rows are blanks without feed iron.

Ref.	Feed Iron		Grinding media		Milling	LD (by vol.)		ZVI
	Mean Ø	Load	Ref.	Ø	Time	Mean Ø	< 1 µm	
	µm	$g \cdot l^{-1}$		mm	h	nm	%	%
A1	43.2	15	S110	0.5	8	212	96	< 2%
A5A	43.2	15	S110	0.5	8	396	84	
A5B	43.2	15	S110	0.5	8	122	100	
A6	43.2	15	S110	0.5	8	133	100	
A2		0.0	S110	0.5	8	279	91	< 2%
A3	43.2	15	S110	0.5	24	382	85	< 2%
A4		0.0	S110	0.5	24	142	100	< 2%

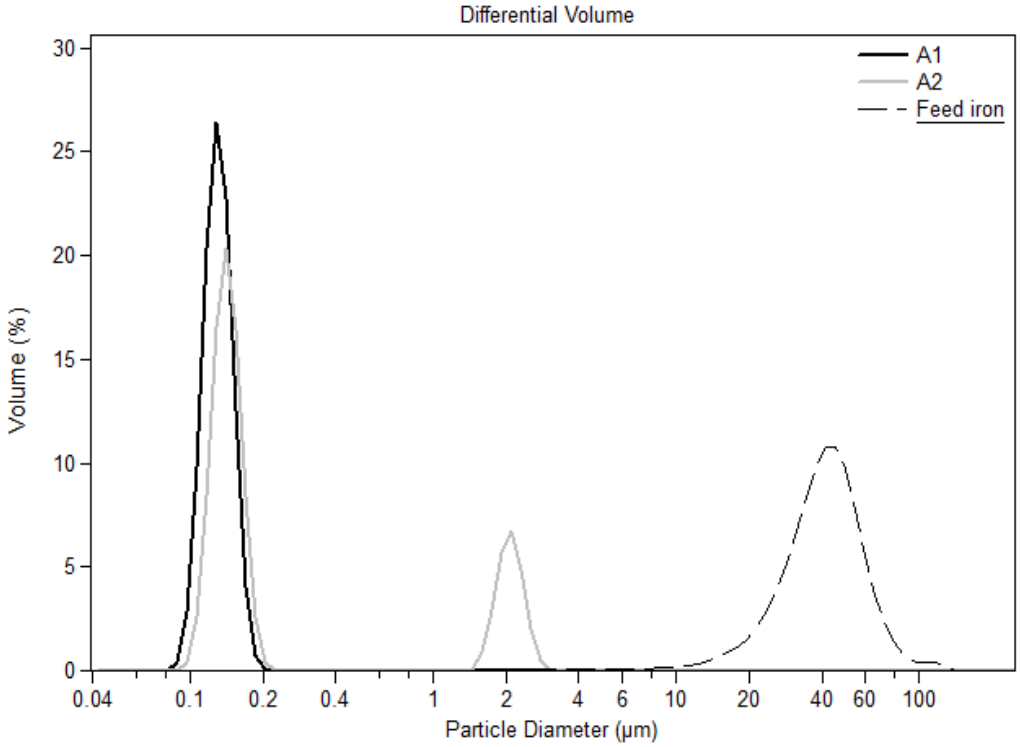

Fix. 5.5 Laser diffraction size distribution of A1, A2 tests and feed iron.

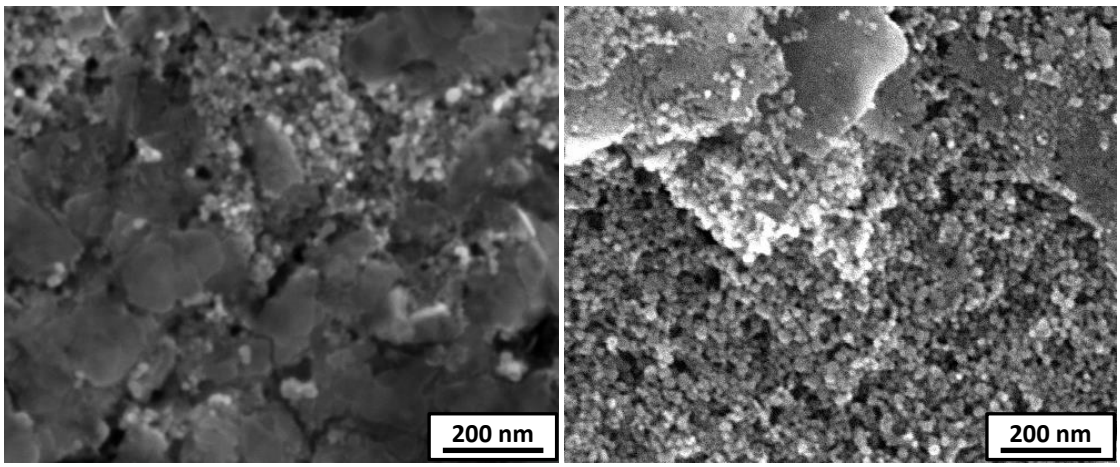

Fig. 5.6 *(Left) SEM image of A1 test 8 h of milling. (Right) SEM image of A3 test 24 h of milling.*

The SEM pictures, *Fig. 5.6*, show how the genesis of the nanoparticles is driven, firstly big flat disks or flakes are obtained by plastic deformation of the initial iron powder in a first step and after that, small particles from the flakes are detached. This sudden change in the ductile behaviour (from very ductile flakes to brittle nanoparticles), leaded to the suspicion that a generalized oxidation was going on. The iron oxides are very brittle, and their generation would help to explain the easy production of nanoparticles from the flakes. This latter point was confirmed by hydrogen measurement tests. As shown in *Table 5.4*, the obtained nanoparticles were formed mainly by iron oxides with a portion of Fe(0) < 2% regarding total iron. A Pourbaix diagram for iron was modelled (20ºC and a $[Fe^{2+}]$ = 0.1M was assumed), the model output was in agreement with the literature *(Beverskog and Puigdomenech, 1996; Chivot, 2004).*

The measured pH and ORP of the obtained suspensions were interpolated in the generated Pourbaix diagram, *Fig. 5.7*. It is clear that at the present conditions Fe(0) is not stable in water suspension and Fe(0) will irremediably trend to oxidize.

The results on particle size were very encouraging but the Fe(0) content determined by hydrogen measurements was very low, sometimes undetectable. New tests with the same milling conditions but decreasing milling time with the aim to reduce the oxidation at 6, 4 and 2 hours were performed. These showed that independently of the used milling time, the nanoparticles were formed only after the iron oxidation took place. Consequently, all the nanoparticles observed were in fact formed by iron oxide.

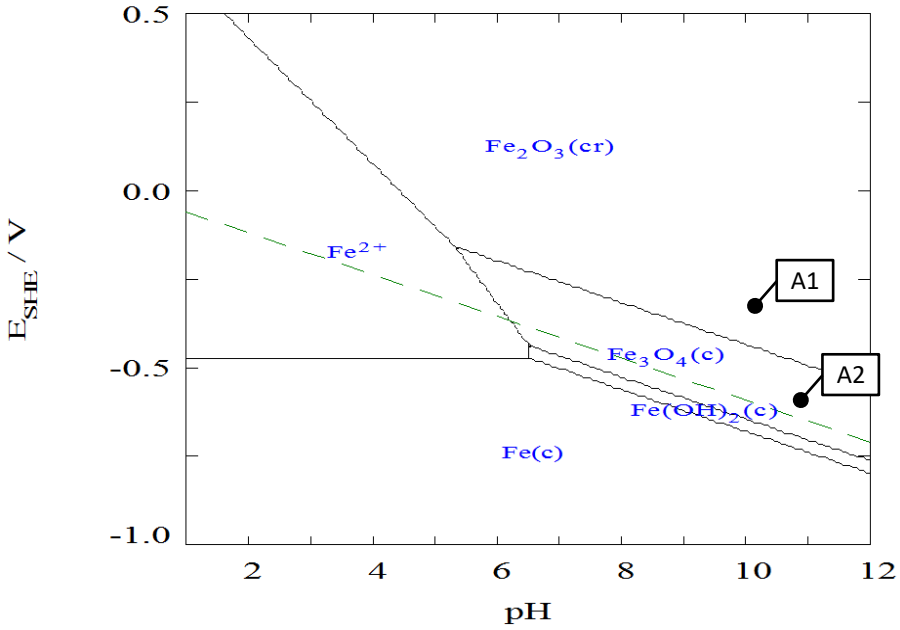

Fig. 5.7 Pourbaix diagram in which the obtained iron suspensions are overlaid.

5.2.4 Results and discussion of wet milling in a non-aqueous media

It was decided to continue the research looking for organic solvents that avoid oxidation of iron during milling. Some organic solvents supposed to be inert against iron were studied, *Table 5.3*.

Ethanol

Intended for a first approach ethanol was selected because of its low viscosity, relative high boiling point compared to other solvents with similar viscosities (i.e.: methanol and hexane), low toxicity and low price. Ethanol in terms of viscosity and density is very similar to water and considering that these are the governing properties in milling regarding to the wet medium, the only difference between water and ethanol would be their chemical behaviour.

In *Table 5.5*, some of the most representatives milling conditions and results are exposed. In general, the iron solutions were stable and no intense oxidation of iron was detected as can be seen through the Fe(0) analysis.

Concerning particle size, it is interesting to note that without oxidation, fragility and size reduction of iron particles were suppressed, *Table 5.5, Fig. 5.8 and Fig. 5.9*. As a consequence of the very large plastic deformations produced in the iron particles, there were substantial changes in their morphology, *Fig. 5.8*. The *Fig. 5.9* shows the large flakes formed, in which lengths of several µm were measured together with thickness of only 100 - 50 nm. Therefore, these flakes had a large aspect ratio although not being in all dimensions into the nanoscale range.

The main problem of milling with ethanol is that once the flakes are formed, no evolution to smaller particles was observed. The results in *Table 5.5* show that the milled material had a scarce fraction < 1µm.

Table 5.5 milling test in ethanol media, grinding conditions and main characterization parameters.

Ref.	Feed Iron		Grinding media		Milling	LD (by vol.)		Total Fe	Fe(0)
	Mean Ø	Load	Ref.	Ø	Time	Mean Ø	< 1 µm		
	µm	g·l^{-1}		mm	h	µm	%	g·l^{-1}	%
NA 1	43.2	15	S110	0.5	8	35.1	0.2	17.8	84
NA 2	43.2	15	S110	0.5	24	40.4	0.1	18.0	87

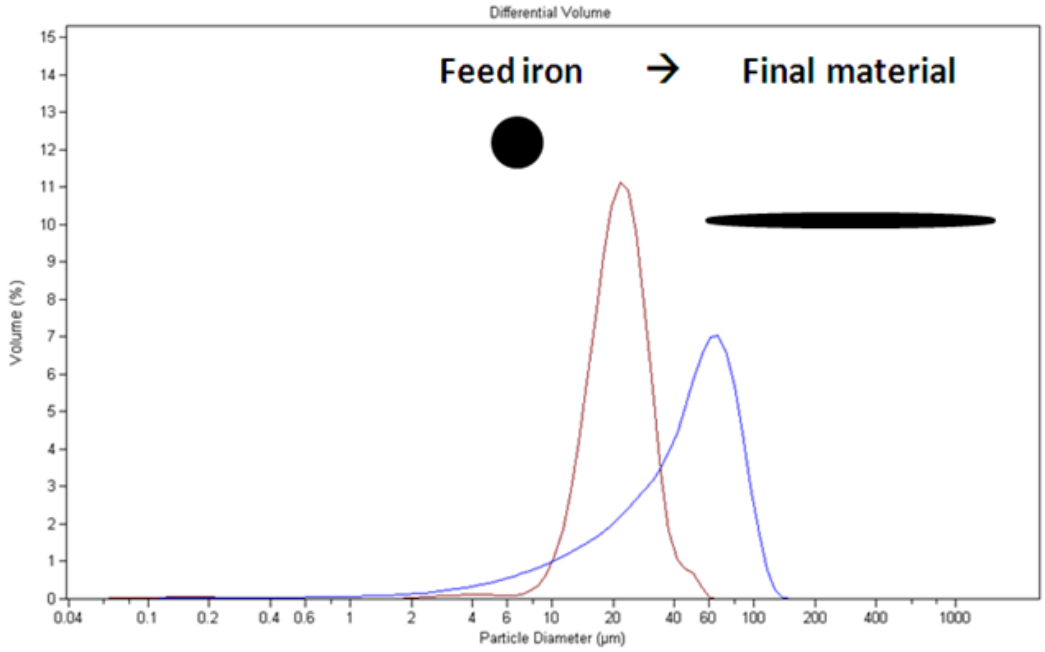

Fix. 5.8 Laser diffraction size distribution of NA 2 and conceptual particle morphology evolution.

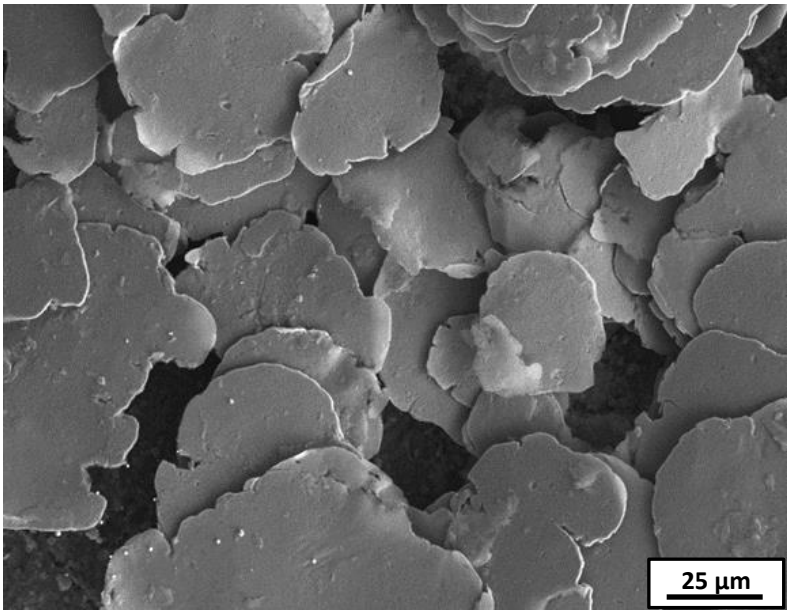

Fig. 5.9 SEM image of NA 2, flakes formed during milling.

Ethanol, thus, was abandoned due to the combination of no outstanding results, together with its inherent risks: a very flammable liquid that was in contact with pyrophoric iron and a pressure build up during milling. It was thought that scaling up under these conditions would be very complex.

Glycols

In order to continue with the research, besides ethanol other media were tested: ethylene glycol (MEG), propylene glycol and polyethylene glycol (PEG) MW200. Viscosity was the key factor to consider; as the viscosity was increased, the size reduction of the very ductile iron powder decreased. In *Fig. 5.10*, the effect of a very viscous medium (PEG) in the final flake thickness can be observed (PEG media).

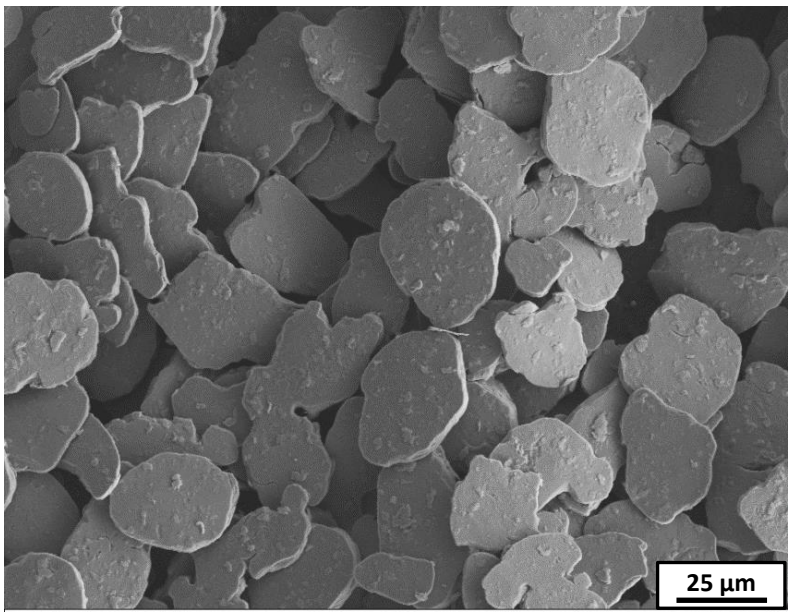

Fig. 5.10 SEM image of particles obtained using PEG media, flakes formed during milling.

Finally, MEG was chosen to continue with the experiments. It was selected because it has the lower viscosity of all feasible candidates and in addition its viscosity drop quickly with temperature. Considering this tendency in viscosity, planetary ball mill was allowed to reach a temperature of approximately 65ºC.

Milling time - size dependence was studied. 1.5g of iron powder (BASF CIP-SM) with a mean particle diameter of 2.77 µm by volume was milled for 24, 48, 72 and 96h with 250g of S660 media. The changes in morphology of the iron particles at different milling times can be observed in the SEM images in *Fig. 5.11*. After 24h of milling, the initial spherical iron particles evolved to a flaky morphology with a high reduction of thickness. With longer milling times, no changes in the aspect of the milled particles were observed. *Fig. 5.11e* shows a detailed view of some flakes in which thickness is less than 100 nm.

This evolution of iron powder with milling in MEG is fully in line with previous studies and literature *(Köber et al. 2014)* confirming that in the absence of embrittlement, iron behaves like a soft and ductile metal and it flattens plastically under the effect of the grinding media forming the observed flakes.

Fig. 5.12 shows the evolution with the milling time of the mean equivalent diameter of the particles by volume and the percentage of particles that are <1 µm as determined by LD. The change to a flaky morphology after milling for 24h led to an increase in the particle diameter and a reduction of the material <1 µm. As the milling time increases to 72h, a slight reduction of the mean particle size, together with a moderate increase of the material <1 µm up to 3.8% was observed. These changes were not detected in the SEM images of the dry particles in *Fig. 5.11*, but they could be related to a partial breakage of the thinner flakes that would create a certain number of smaller isolated particles in solution. Lastly, after 96h, no significant changes were observed neither in the mean particle diameter nor in the material <1 µm. In the light of these results, it seems that the current process is not able to break the flakes even at long milling times and consequently, particle size reduction is

stopped. The final flaky product has a very slight thickness less than 100 nm, an interesting SSA, good reactivity against some pollutants and even good mobility *(Köber et al. 2014)*, although agglomeration and settling of this type of milled particles has been considered to be a major problem for mobility *(Velimirovic et al. 2015)*.

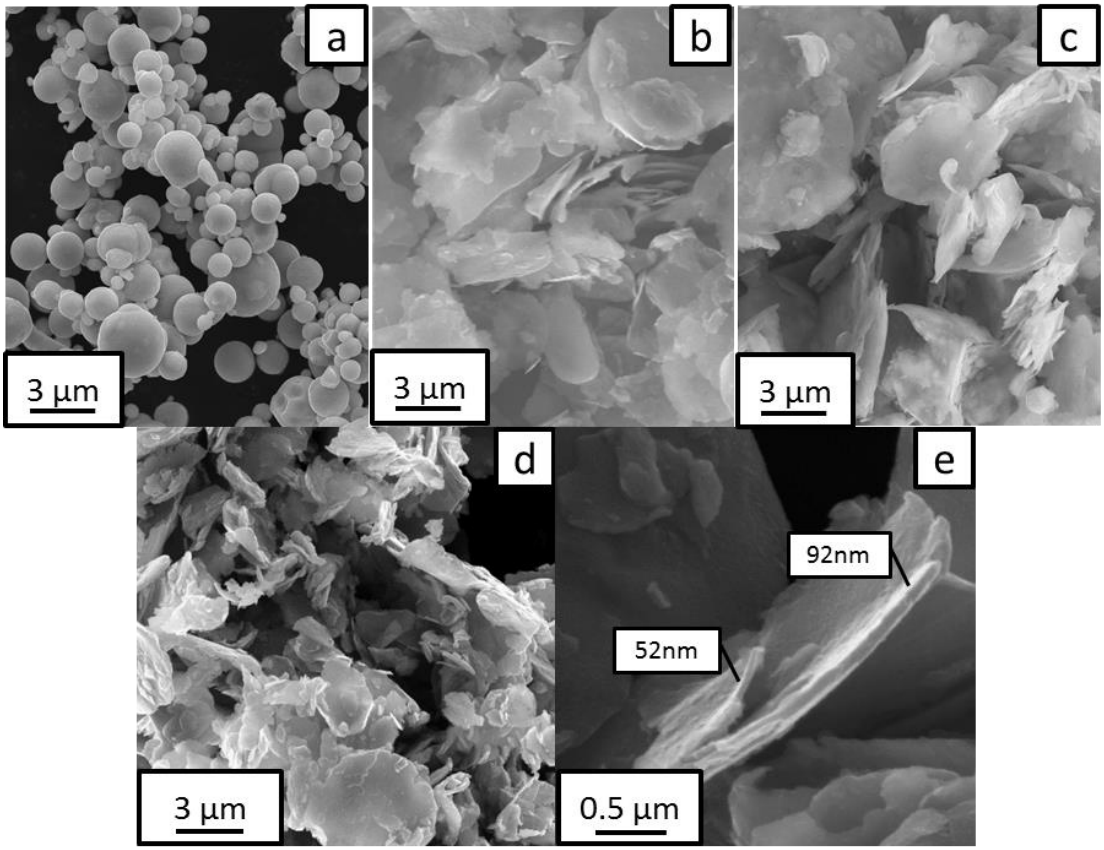

Fig. 5.11 SEM images of the milled particles without alumina. a) Initial iron powder, b) after 24 h, c) after 72 h, d) after 96 h and e) detail of one flake of a 72 h milled iron particle.

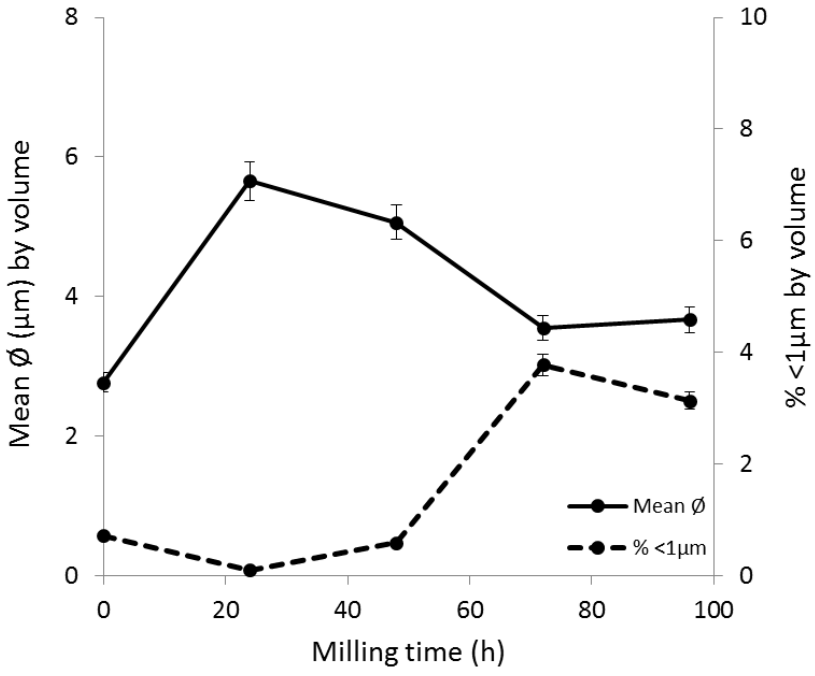

Fig. 5.12 Evolution of mean particle diameter and percentage of particles below 1µm with milling time without alumina.

Embrittlement trough alloying

Exceptions in the final particle size distribution were found during the milling tests with ethanol, some batches showed an important reduction in particle size. A reduction from the initial feed iron mean diameter of 22.2 µm to values between 5.3 and 3.8 µm was observed in three tests. It was the first progress since ball millings in inert wet media have started, being an accidental but at the same time a huge improvement comparing to the previous obtained values which ranged from 27.4 to 56.8 µm, *Table 5.6*.

This size reduction was only observed in tests where a stainless steel grinding media was present (Cr/Ni60). For example comparing the test NA 15 to the NA 18 a very similar grinding conditions were used: grinding media with a diameter of ≈ 1mm and the same milling running time of 24 h. However, the final mean particle size was very different, the NA 15 28.7 µm had a fraction of 0.0 % <1 µm contrasting to 4.7 µm and 22.9% <1 µm for the NA 18, *Fig. 5.13.*

Table 5.6 milling test in ethanol media, grinding conditions and main characterization parameters.

Ref.	Feed Iron		Grinding media		Milling	LD (by vol.)	
	Mean Ø	Load	Ref.	Ø	Time	Mean Ø	< 1 µm
	µm	g·l^{-1}		mm	h	µm	%
NA 7	22.2	15	S330	1	8	54.9	0.0
NA 9	22.2	15	S330	1	16	56.8	0.0
NA 14	22.2	15	S550	1.4	24	27.4	0.3
NA 15	22.2	15	G18	1.15	24	28.7	0.0
NA 19	22.2	15	S660	2	24	48.4	0.0
NA 16	22.2	15	Cr/Ni 60	1	24	4.9	17.8
NA 17	22.2	15	Cr/Ni 60	1	20	5.3	14.0
NA 18	22.2	15	Cr/Ni 60	1	24	3.8	22.9

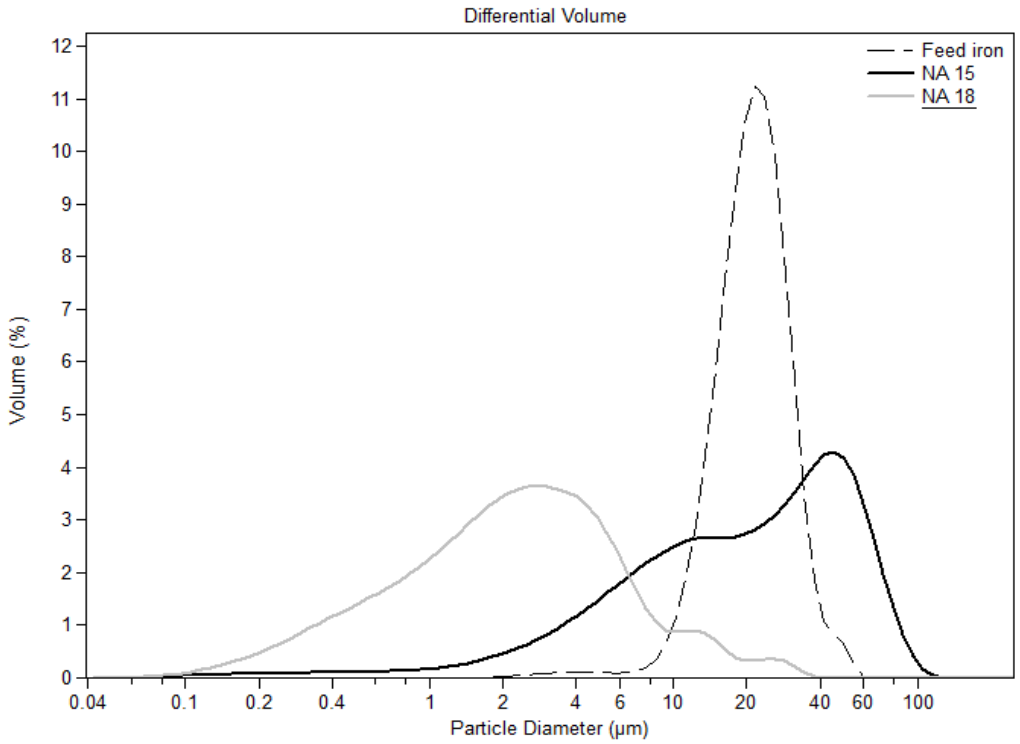

Fig. 5.13 Laser diffraction size distribution of NA 15, NA 18 (Cr/Ni 60) tests and feed iron.

The size reduction observed in the cases in which stainless steel grinding balls were used, can be related with the effect of chromium and nickel in the iron powder. Chromium has a large affinity for carbon and oxygen which are known to be present in the iron powder *(Casas et al., 2015)*, so it is possible that chromium could form precipitates in the form of hard oxides or carbides. This precipitates would be small and widely dispersed through the particles and thus creating a strong hardening effect, *(Roberts et al., 1998)*. The formed flakes in this condition could be then more prone to break than the former iron powder and the production of smaller particles would be favoured. On the other hand, nickel has not a large trend to form precipitates, and it is more likely that it will be dissolved forming a solid solution with iron with a less effect on hardness and brittleness of the flakes than chromium, *(Roberts et al., 1998)*.

The mechanical alloying mechanism was demonstrated through SEM-EDX where chromium and nickel were observed, i.e.: the test NA 18, *Fig. 5.14*. A semi-quantitative assessment of the elemental analysis was performed, *Table 5.7*, chromium was the most abundant alloying element with a 13.4% of the total particle composition and nickel accounted a 4.4%. Interestingly, these proportion fitted with the grinding media (Cr/Ni 60) composition used in this test, *Table 5.2*. Finally, in test where a chromium and nickel free grinding media was used these were not observed, i.e.: NA 14 *Fig. 5.15*.

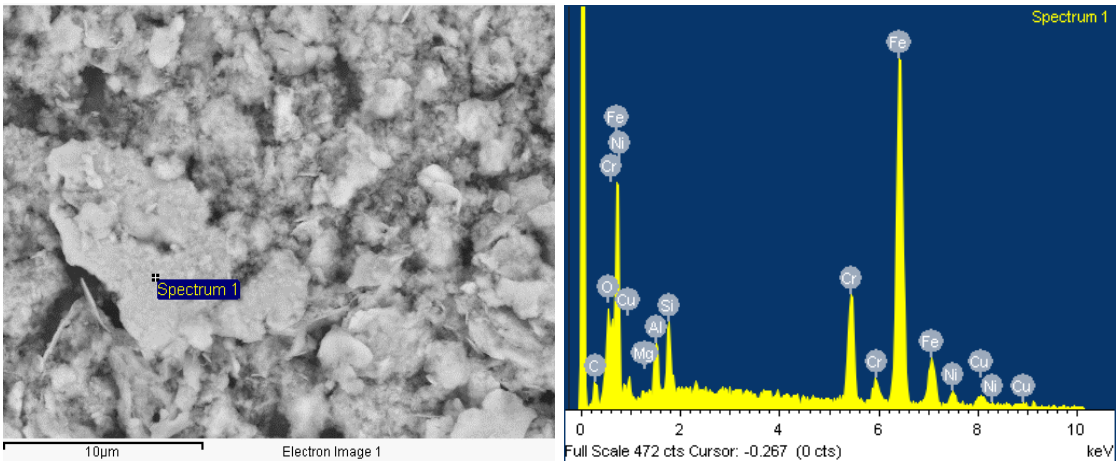

Fig. 5.14 (Left) SEM image of one of the analysed regions. (Right) SEM-EDX spectrum of the NA 18 sample.

Table 5.7 Semi-quantification of the SEM-EDX spectrum of the NA 18 sample.

	O	Mg	Al	Si	Cr	Fe	Ni	Cu
% by weight	2.5	0.2	2.1	2.3	13.4	72.0	4.4	3.2

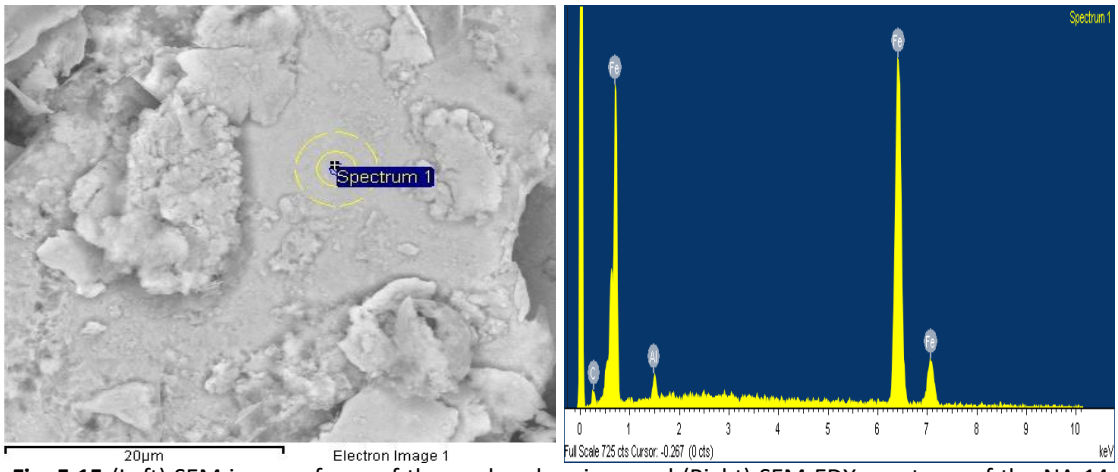

Fig. 5.15 (Left) SEM image of one of the analysed regions and (Right) SEM-EDX spectrum of the NA 14 sample.

Similar examples with phosphorus, boron or carbon were reported but all were discarded because of environmental concerns or a decrease in iron reactivity, *(Velimirovic et al., 2013a; Velimirovic et al., 2013b)*. Iron – silicon alloys (ferrosilicon) were taken into account, silicon adds strength and reduces ductility to iron, it is comparable to the effect of carbon but silicon solubility into iron is much higher *(Kubaschewski, 2013)* thus these effects could be maximized. The production of fine material by milling (undesired) is reported *(Guéneau et al., 1995)*. In addition the hydrogen production of ferrosilicon in contact with water *(Horn et al., 1998)* could increase the reactivity towards some pollutants *(Gu et al., 1999)*. Unfortunately, it was not possible to obtain a suitable feeding ferrosilicon material.

In spite of being a promising mechanism it was discarded and contamination was avoided discontinuing the usage of grinding media and milling vials containing chromium – nickel.

5.2.5 Conclusions

- First approaches with water as a wet media produced nanoscale particles under 25 nm but the iron was almost complete oxidized as it was show by the hydrogen analysis method and models with Pourbaix diagrams.

- The substitution of water to inert wet media such as: ethanol, MEG, propylene glycol and PEG avoided the oxidation.

- Ductile behaviour of the metallic iron arose when milling with inert media, the feed iron evolved to a flaky particles of several microns in diameter but just tents of nanometres in thickness. No improvements in particle reduction was observed increasing the milling time even with extremely long milling times.

- The viscosity of the used fluid had a dramatic effect in the thickness of the flakes, MEG was selected as a compromise solution because of having: relative low viscosity, high boiling point, inertness regarding Fe(0) and being environmentally acceptable.

- The accidental particle alloying with chromium and nickel showed a size reduction but this approach was discarded due to environmental concerns and the small improvements accomplished.

- Finally, the need to find a new strategies to decrease iron ductility is stated.

5.2.6 References

3M (2016a). Product information: Fluorinert™ electronic Liquid FC-84.

3M (2016b). Product information: Fluorinert™ electronic Liquid FC-77.

Beverskog, B., & Puigdomenech, I. (1996). Revised Pourbaix diagrams for iron at 25–300 C. Corrosion Science, 38(12), 2121-2135.

Bohne, D., Fischer, S., & Obermeier, E. (1984). Thermal, Conductivity, Density, Viscosity, and Prandtl-Numbers of Ethylene Glycol-Water Mixtures. Berichte der Bunsengesellschaft für physikalische Chemie, 88(8), 739-742.

Casas, C., Tejedor, R., Rodríguez-Baracaldo, R., Benito, J. A., & Cabrera, J. M. (2015). The effect of oxide particles on the strength and ductility of bulk iron with a bimodal grain size distribution. Materials Science and Engineering: A, 627, 205-216.

Chivot, J. (2004). Thermodynamique des produits de corrosion. Sciences et Techniques Series, ANDRA, 4.

Crane, R. A., & Scott, T. B. (2012). Nanoscale zero-valent iron: future prospects for an emerging water treatment technology. Journal of hazardous materials, 211, 112-125.

DOW (accessed 2016). DOW Ethylene Glycols Physical Properties.

Gu, B., Phelps, T. J., Liang, L., Dickey, M. J., Roh, Y., Kinsall, B. L., ... & Jacobs, G. K. (1999). Biogeochemical dynamics in zero-valent iron columns: implications for permeable reactive barriers. Environmental Science & Technology, 33(13), 2170-2177.

Guéneau, G., Servant, C., & Manier, F. (1995). Relationships between the grinding behaviour and the microstructure of ferro-silicon alloys with 65 wt. % silicon. INFACON 7, Norway.

Horn, Q. C., Heckel, R. W., & Nassaralla, C. L. (1998). Reactive phosphide inclusions in commercial ferrosilicon. Metallurgical and Materials Transactions B, 29(2), 325-329.

Klimkova, S., Cernik, M., Lacinova, L., Filip, J., Jancik, D., & Zboril, R. (2011). Zero-valent iron nanoparticles in treatment of acid mine water from in situ uranium leaching. Chemosphere, 82(8), 1178-1184.

Köber, R., Hollert, H., Hornbruch, G., Jekel, M., Kamptner, A., Klaas, N., ... & Braun, J. (2014). nanoscale zero-valent iron flakes for groundwater treatment. Environmental Earth Sciences, 72(9), 3339-3352.

Lameck, N. N. S. (2006). Effects of grinding media shapes on ball mill performance (Doctoral dissertation).

Li, S., Yan, W., & Zhang, W. X. (2009). Solvent-free production of nanoscale zero-valent iron (nZVI) with precision milling. Green Chemistry, 11(10), 1618-1626.

Liu, Y., Choi, H., Dionysiou, D., & Lowry, G. V. (2005a). Trichloroethene hydrodechlorination in water by highly disordered monometallic nanoiron. Chemistry of Materials, 17(21), 5315-5322.

Mackay, D., Shiu, W. Y., Ma, K. C., & Lee, S. C. (2006). Handbook of physical-chemical properties and environmental fate for organic chemicals. CRC press.

Mrklas, O., Chu, A., Lunn, S., & Bentley, L. R. (2004). Biodegradation of monoethanolamine, ethylene glycol and triethylene glycol in laboratory bioreactors. Water, Air, and Soil Pollution, 159(1), 249-263.

Mueller, N. C., Braun, J., Bruns, J., Černík, M., Rissing, P., Rickerby, D., & Nowack, B. (2012). Application of nanoscale zero valent iron (NZVI) for groundwater remediation in Europe. Environmental Science and Pollution Research, 19(2), 550-558. O'Carroll D, Sleep B, Krol M, Boparai H, Kocur C (2013) nanoscale Zero Valent iron and bimetallic particles for contaminated site remediation. Advances in Water Resources, 51:104-122.

Phenrat, T., Saleh, N., Sirk, K., Tilton, R. D., & Lowry, G. V. (2007). Aggregation and sedimentation of aqueous nanoscale zerovalent iron dispersions. Environmental Science & Technology, 41(1), 284-290.

Roberts, G. A., Kennedy, R., & Krauss, G. (1998). Tool steels. ASM international.

Sigma-Aldrich (2016a). Product information sheet, Ethylene glycol.

Sigma-Aldrich (2016b). Product information sheet, Polyethylene glycol M200.

Sigma-Aldrich (2016c). Product information sheet, Propylene glycol.

Suryanarayana, C. (2001). Mechanical alloying and milling. Progress in Materials Science, 46(1), 1-184.

Uegami, M., Kawano, J., Okita, T., Fujii, Y., Okinaka, K., Kayuka, K., & Yatagi, S. (2006). Iron particles for purifying contaminated soil or groundwater, US Patent No. 7,022,256.

Velimirovic, M., Larsson, P. O., Simons, Q., & Bastiaens, L. (2013a). Impact of carbon, oxygen and sulfur content of microscale zerovalent iron particles on its reactivity towards chlorinated aliphatic hydrocarbons. Chemosphere, 93(9), 2040-2045.

Velimirovic, M., Larsson, P. O., Simons, Q., & Bastiaens, L. (2013b). Reactivity screening of microscale Zero Valent irons and iron sulfides towards different CAHs under standardized experimental conditions. Journal of Hazardous Materials, 252, 204-212.

Velimirovic, M., Schmid, D., Wagner, S., Micić, V., von der Kammer, F., & Hofmann, T. (2016). Agar agar-stabilized milled zerovalent iron particles for in situ groundwater remediation. Science of The Total Environment, 563, 713-723.

Wang, C. B., & Zhang, W. X. (1997). Synthesizing nanoscale iron particles for rapid and complete dechlorination of TCE and PCBs. Environmental science & technology, 31(7), 2154-2156.

Yan, W., Lien, H. L., Koel, B. E., & Zhang, W. X. (2013). Iron nanoparticles for environmental clean-up: recent developments and future outlook. Environmental Science: Processes & Impacts, 15(1), 63-77.

Zhang W.X. (2006). Dispersed zero-valent iron colloids, US patent No. 7,128,841 B2.

5.3 Study of the cryomilling technique for the production of nano zero-valent iron particles

It is suspected that the main issue to reduce the iron particle size in nano Zero Valent Iron (nZVI) production trough ball milling is the high iron ductility. In this chapter, a method to overcome iron ductility is presented although not being cost – effective, states the performance increase once iron ductility is reduced.

Cryomilling takes advantage of the drop in ductile and elastic proprieties of materials at cryogenic temperatures. Four milling times were chosen: 20, 40, 60 and 90 minutes and samples were studied by SEM and Laser Diffraction (LD).

SEM images showed a pronounced diminution of particle size through time, moreover no flakes were formed entailing a fragile behaviour. Moreover, LD disclosed that the bonding in the aggregated particles was reversible and an important percentage of small particles come off from the surface after an ultrasonic pre-treatment. The smaller particle distribution was obtained at the longer time (90 min) with 36.2% of the material < 1µm and a mean diameter of 2.3 µm (all results expressed by particle volume).

The satisfactory results reducing particle size stated the need to develop new strategies to reduce the iron ductility in the ball milling production approach since ductility is the main handicap to overcome.

5.3.1 Introduction

As stated in the previous chapter *(Chapter 5.2)* particle size reduction is still an important challenge in order to obtain nano Zero Valent Iron (nZVI) particles suitable for the application in subsurface water remediation. To date, conventional milling has been limited possibly by the high iron ductility and the cold welding of particles which limit the achievable minimum particle size. Typically iron milling at room temperature produces large flakes of several microns in width and a thickness of tens of nanometres *(Köber et al., 2014)* without any significant improvement with time or energy, e.g.: *Fig. 5.16*. However, at cryogenic temperatures the iron ductility is dramatically reduced *(Petch, 1958)* leading to the production of finer particles very fast. Grinding very ductile or elastic materials thanks to the weakening of its proprieties at cryogenic temperatures is a common method, i.e.: as alternative strategy for the recycling of tires *(Smith et al., 2001)*, food *(Balasubramanian et al., 2012)* and aluminium powder *(El-Danaf et al., 2013)*.

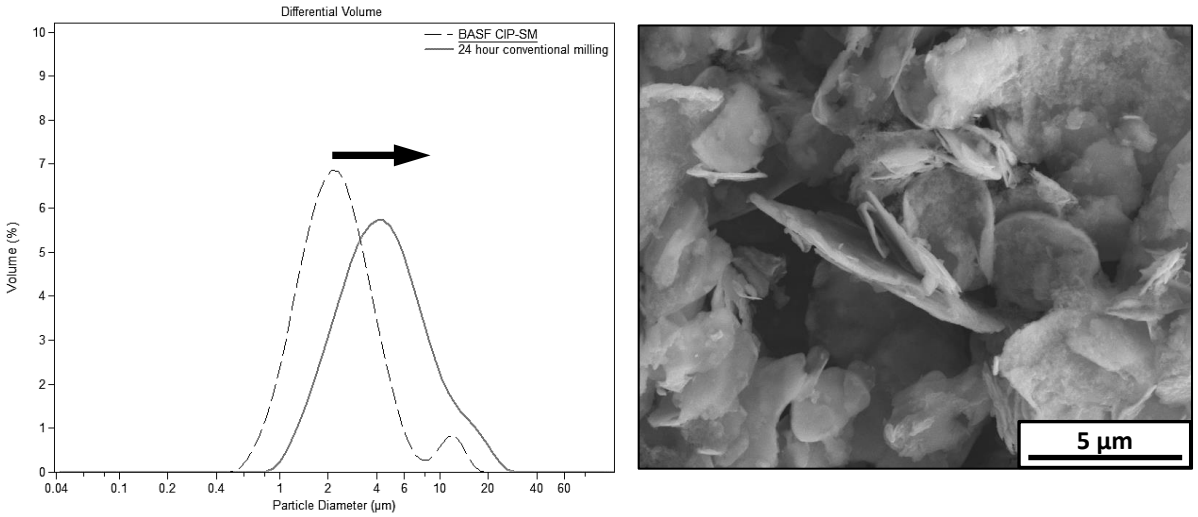

Fig. 5.16 (Left) Size distribution of initial iron powder (BASF CIP-SM) and these iron powder milled. (Right) SEM image of the 24h conventionally milled particles.

Powder evolution during conventional milling process involves five stages: particle flattening as a result of plastic deformation, particle welding, equiaxed particle formation, random welding of powder particles and steady-state deformation, during which a balance between fracture and cold welding is established, *(Lavernia et al., 2008)*. It is hypostatized that using cryomilling the plastic deformation stage will be reduced because of the ductility drop at cryogenic temperatures. Cryogenic millings up to different total times were performed to assess the power evolution trough time.

Although of being a very performing technique. The high costs of cryomilling which are in the range of few hundred dollars per processed kilogram *(Ye et al., 2004)* would be an insurmountable drawback for up scaling in nZVI remediation application since the present manufacturing cost are lower *(Stefaniuk et al., 2016)*. Cryomilling could only find its marketplace in a very specific and valuable products such as: highly specific alloys *(Newbery et al., 2006)* or pharmaceutics *(Loh et al., 2015)*. Despite of this, the present research would enable to test the real influence of iron ductility in particle size reduction.

5.3.2 Materials and methods

Experimental

In order to figure out the evolution of the material through the process, four milling times were chosen: 20, 40, 60 and 90 minutes, respectively. 3 g of Iron powder were used in each assay. The temperature was maintained cryogenic (77 K) during all the milling.

Feeding iron

Carbonyl Iron Powder was selected (CIP-SM, BASF SE). The initial size characteristics, by volume: a mean diameter of 2.77 µm and a 4.7% of the material <1 µm and the chemical composition: Fe ≥ 99.0%, C ≤ 0.1%, N ≤ 0.1% and O ≤ 0.55%, respectively.

Cryogenic mill

A bath cryogenic mill was used (6870 Freezer/Mill, SPEX SamplePrep). The grinding action is achieved thanks to a magnetic coil which moves a cylinder from face to face of the vial, smashing the sample. The main advantage of this specific model is the complete immersion of the vial into liquid nitrogen, theorically ensuring during all the process a cryogenic temperature and an inert atmosphere, *Fig. 5.17.* The vial wall is made from polycarbonate enclosed with a 440 stainless steel caps, the smashing cylinder is also made from 440 stainless steel, *Fig. 5.18*. Finally, working conditions were: running cycles of 10 min at 15 Hz with cooling down intervals of 1 min.

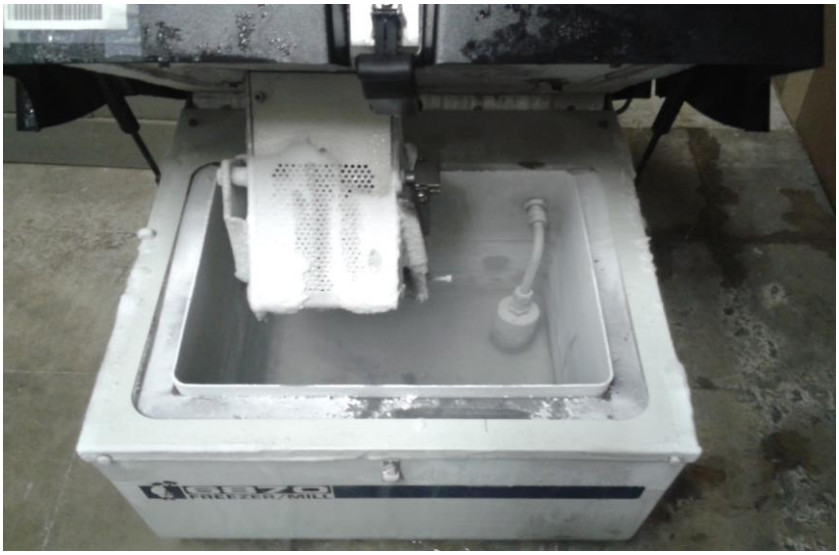

Fig. 5.17 Magnetic coil surrounding the Vial (Top), Vial container (Bottom).

Fig. 5.18 Polycarbonate vial, caps and smashing cylinder.

Particle characterization

All milled samples were manipulated in a glove box under nitrogen atmosphere (2P, Jacomex), then samples were stored in sealed vials in which a suitable solvent (absolute ethanol) was added.

For the Scanning Electron Microscope (SEM) studies, the samples were deposited and led to evaporate into the glove box over standard pins.

For size characterization, Laser Diffraction particle size analysis (LD) (LS 13320, Beckman Coulter) was chosen. Samples were previously mixed in an ultrasonic bath and then immediately analysed directly in ethanol. Finally, data was post processed with the Fraunhofer optical model.

5.3.3 Results and discussion

As SEM images show, a diminution of particle size through time can be observed, but signs of aggregation were detected especially for the longest milling times. Interestingly, no flakes were formed entailing a fragile behaviour, which represents a positive note for this technique, *Fig. 5.19.* Non-milled spherical particles could be identified in all the micrographs, it could have two explanations: problems of the milling system (i.e.: temperature increases during milling) or that there too much powder in the vials. This was not considered as a major issue because the presence of the non-milled particles is dramatically reduced as milling time is increased.

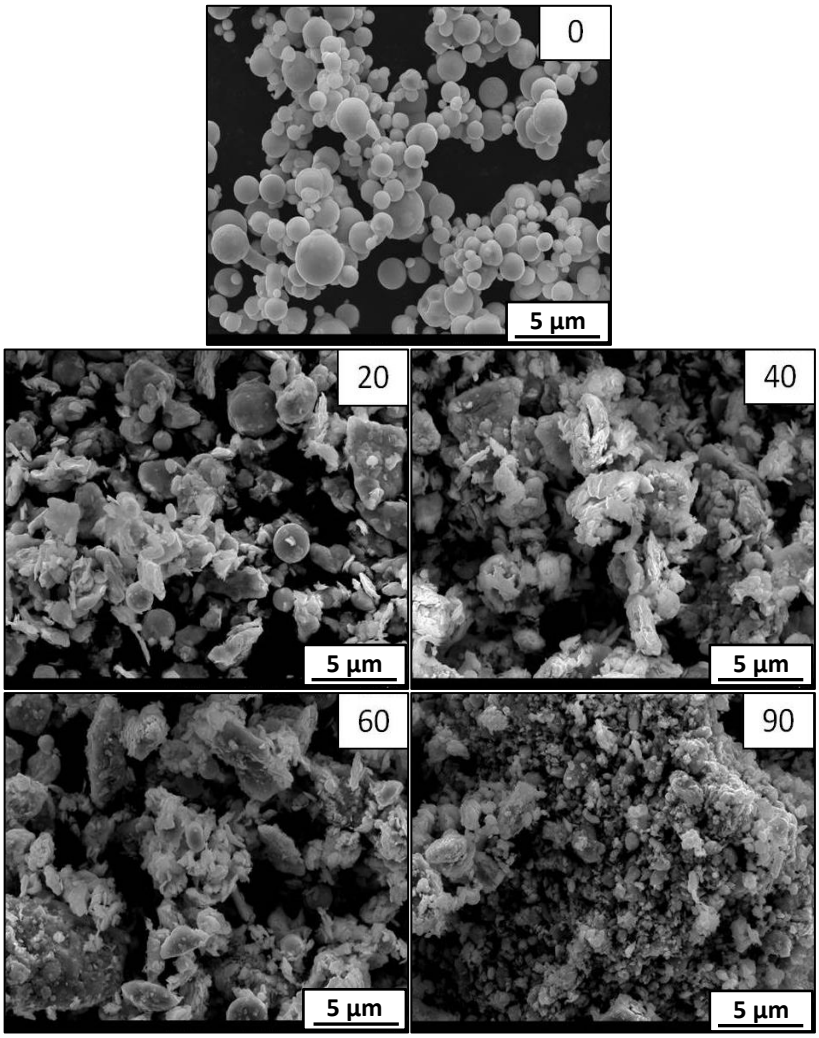

Fig. 5.19 SEM images: 0 (initial powder), 20, 40, 60 and 90 min milling.

By volume, *Fig. 5.20 (Left)*, there was an initial period in which a raise in mean particle size was observed but an increase in particle fraction of <1 µm started to grow at 40 min. Finally, increasing the milling time, the overall particle size decreased and a growth in sub-micron fraction was incremented, with a value of 36.2% and a mean of 2.3 µm at 90 min. The initial tale of big particles is maintained in all the tests, so it is feasible that the milling conditions were not enough energetic or perhaps aggregation was present in all the tests. When the results are analysed by the number of particles within a specific particle size, *(Fig. 5.20 (Left)),* the trend was similar but the 90 min sample had a very narrow distribution and interestingly the biggest particles decreased sharply compared to other tests. However, the minimum size reached (100 nm) did not decreased in the 90 min test meaning that the steady stage between fracture and cold welding was reached avoiding any further improvement.

Comparing with SEM images (*Fig. 5.19*), analysis by LD, *Fig. 5.20*, stated that the bonding in the aggregated particles was reversible and an important percentage of small particles come off after ultrasonic pre-treatment.

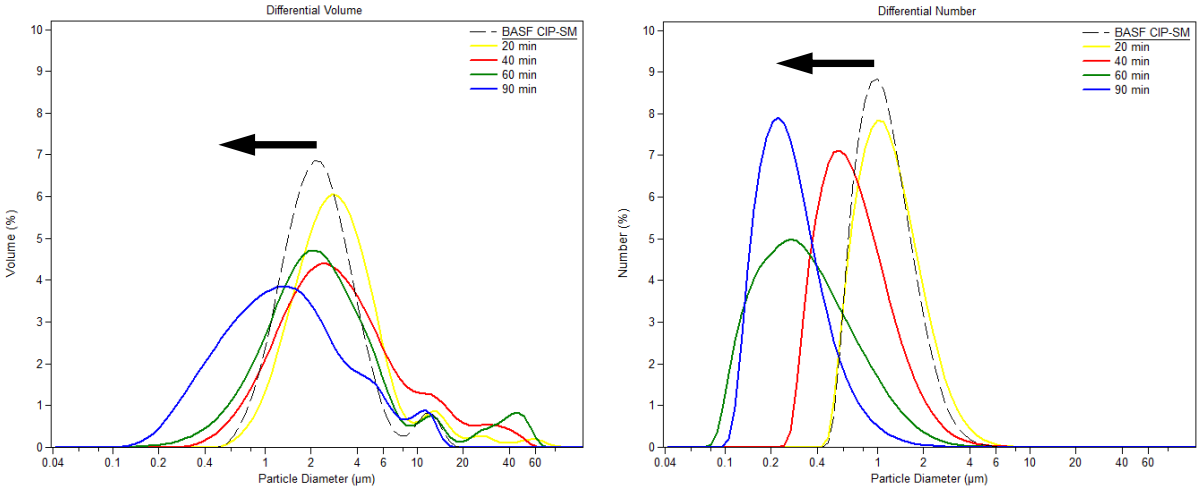

Fig. 5.20 Particle size distribution by volume (Left) and by number (Right).

5.3.4 Conclusions

- As a general conclusion, the use of cryomilling allows to obtain dry milled powder with a substantial amount of material <1µm which is ready to get into solution using the desired solvent.

- The use of cryomilling allows obtaining dry milled powder with a clear reduction of the particle size due to the brittle behaviour of iron at cryogenic temperatures. In comparison to room temperature milling in organic solvents *(Chapter 5.2)*, the final particle size is highly improved taking into account the small running times.

- These results highlights the need to develop new strategies to reduce the iron ductility at room temperature, since this work states that ductility is the main factor causing poor performance in conventional milling. At the same time cryomilling is not applicable due to its high costs and also the top possible performance in size reduction, reached between 60 - 90 min at 100 nm, is still insufficient.

5.3.5 References

Balasubramanian, S., Gupta, M. K., & Singh, K. K. (2012). Cryogenics and its application with reference to spice grinding: a review. Critical Reviews in Food Science and Nutrition, 52(9), 781-794.

El-Danaf, E. A., Soliman, M. S., Almajid, A. A., & Khalil, K. A. (2013). Mechanical characterization of cryomilled Al powder consolidated by high-frequency induction heat sintering. Advances in Materials Science and Engineering, 2013.

Köber, R., Hollert, H., Hornbruch, G., Jekel, M., Kamptner, A., Klaas, N., ... & Braun, J. (2014). nanoscale zero-valent iron flakes for groundwater treatment. Environmental Earth Sciences, 72(9), 3339-3352.

Lavernia, E. J., Han, B. Q., & Schoenung, J. M. (2008). Cryomilled nanostructured materials: Processing and properties. Materials Science and Engineering: A, 493(1), 207-214.

Loh, Z. H., Samanta, A. K., & Heng, P. W. S. (2015). Overview of milling techniques for improving the solubility of poorly water-soluble drugs. Asian Journal of Pharmaceutical Sciences, 10(4), 255-274.

Newbery, A. P., Nutt, S. R., & Lavernia, E. J. (2006). Multi-scale Al 5083 for military vehicles with improved performance. The Journal of The Minerals, Metals & Materials Society, 58(4), 56-61.

Petch, N. J. (1958). The ductile-brittle transition in the fracture of α-iron: I. Philosophical Magazine, 3(34), 1089-1097.

Smith, A. P., Ade, H., Koch, C. C., & Spontak, R. J. (2001). Cryogenic mechanical alloying as an alternative strategy for the recycling of tires. Polymer, 42(9), 4453-4457.

Stefaniuk, M., Oleszczuk, P., & Ok, Y. S. (2016). Review on nano zerovalent iron (nZVI): From synthesis to environmental applications. Chemical Engineering Journal, 287, 618-632.

Ye, J. I. C. H. U. N., & Schoenung, J. M. (2004). Technical cost modeling for the mechanical milling at cryogenic temperature (cryomilling). Advanced Engineering Materials, 6(8), 656-664.

5.4 Embrittlement approaches of iron in nanoscale zero-valent iron production by wet milling

The completed previous research stated the need to find a new method to reduce the iron ductility or to break the flakes formed during the milling process. The high ductile behaviour of iron have been up to now an insurmountable obstacle to reduce the particle size of the iron particles.

Different approaches have been considered: hydrogen embrittlement and the addition of micrometric abrasives that could help to break the flakes. All of them showed improvement in the final size distribution, thanks to the brakeage of the flakes.

Hydrogen embrittlement produced little improvement despite the extreme pressure and temperature used. It would not be cost – effective to scale up this method taking into consideration the complexity, expensive hardware and the little advance obtained.

Finally, the addition of micrometric alumina made a step forward progress producing a 20% of the particles below 1 µm. Considering this results and the nature of alumina which is a cheap and environmental friendly material it was selected for further research.

From the previous experiments *(Chapter 5.2 & 5.3),* the need to embrittle the iron particles or find an alternative milling system was stated. In the following chapter two different approaches are presented.

5.4.1 Hydrogen embrittlement

Embrittlement of certain metals once exposed to hydrogen gas or liquid phases is a common problem in the industry, i.e.: electrolytic process, absorption into pipelines carrying gas or liquid hydrogen, humid or contaminated hydrocarbons, contaminants in the melting and welding processes or hydrogen uptake in electroplating *(Barnoush, 2011)*. This problem affects a large number or metals and alloys including pure iron *(Telitchev and Vinogradov, 2008; Escobar et al., 2011)* also in single iron crystals *(Wang, 2000)*. The exact mechanism of hydrogen embrittlement remains unclear, numerous models have been proposed: internal pressure, hydrogen induced decohesion, surface energy, adsorption induced localised slip, hydrogen enhanced localized plasticity, corrosion enhanced plasticity and hydrogen rich phases. Attaining this research, illustratively it can be simplified as follows for hydrogen gas phases, *(Ćwiek, 2010; Barnoush, 2011)*:

1. - Adsorption of the hydrogen into the metal surface: $H_{2\,(g)} = H_{2\,(ads)}$
2. - Disassociation of the hydrogen molecule into an atomic hydrogen: $H_{2\,(ads)} = 2H_{(ads)}$
3. - Absorption into the metal: $H_{(ads)} = H_{(abs)}$
4. - Solid state diffusion, thanks to the small size of the hydrogen atom
5. - Hydrogen interaction with metal lattice, embrittlement:
    - Point defects: vacancy in metal lattice
    - Solutes and solute-defect complexes
    - Dislocations
    - Internal boundaries
    - Hydride formation

Because milling generates a great amount of lattice defects theoretically the hydrogen embrittlement effect should be magnified. It was already used at experimental scale assisting the milling to obtain AlCuFe nanoparticles *(Patiño-Carachure et al., 2009)*. Considering this antecedents, five different methods were considered for doping feed iron powder with hydrogen:

- Electrochemically. Since this method needs an aqueous phase and electric potentials, feed iron would be subjected to a high corrosive media thus oxidizing the iron. This approach was excluded.

- Milling in hydrogen atmosphere. It was tested with very poor results, the leak of improvement was attributed to an insufficient intake of hydrogen into the iron possibly due to the weak conditions used (hydrogen atmosphere at 1 atm and room temperature).

- Wet milling using fluorocarbons as a grinding media. Hydrogen is very soluble in fluorocarbons, this is an uncommon property because usually hydrogen is largely insoluble in liquids, i.e.: in water is 19 Nml $H_2 \cdot l^{-1}$ whereas fluorocarbons such as perfluoroheptane or perfluorooctane have a hydrogen solubility of 150 Nml $H_2 \cdot l^{-1}$ (all solubilities are expressed at 25ºC, 1 atm), *(Bonneau, 2002)*. Therefore, fluorocarbons give the chance to provide a high amount of hydrogen and additionally it is provided right into the shock zone. Finally, it was excluded due to the prohibitive prices of fluorocarbons in an up scaling context.

- Hydrogen plasma. This is a very interesting approach because hydrogen molecule is already disassociated aiding the intake into iron. Additionally, iron powder can be connected to the cathode, incrementing the hydrogen delivery in a similar way to plasma nitriding process. This method was not tested.

- High pressure and temperature hydrogen atmosphere. As reported, hydrogen intake in pure iron depends on the pressure and temperature *(Ćwiek, 2010)*, *Fig. 5.21.* Feed iron powder can be initially exposed to a hydrogen atmosphere with high pressure and temperature and then milled. Additionally, iron in powder form favours hydrogen intake because it has a higher surface area.

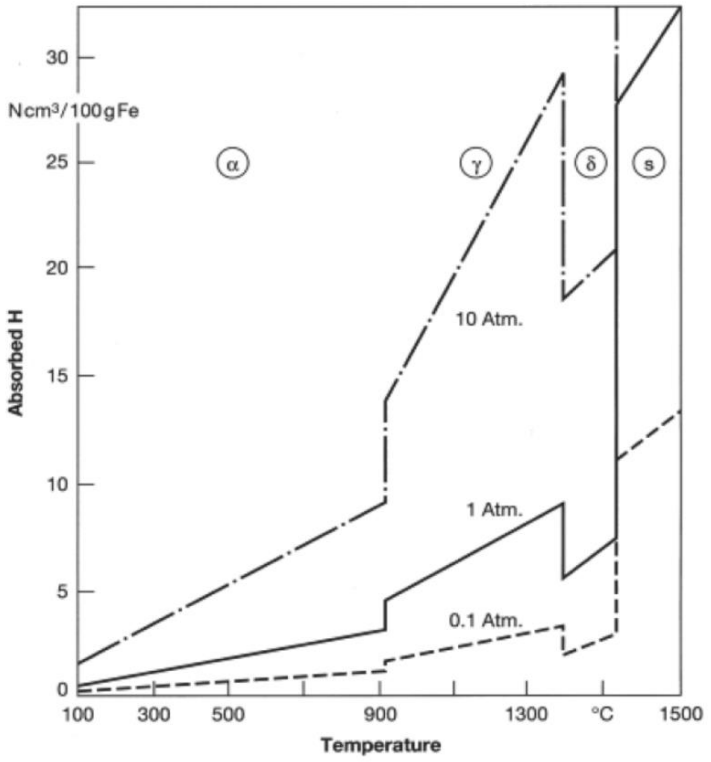

Fig. 5.21 temperature – pressure hydrogen intake dependence, *(Ćwiek, 2010).*

5.4.2 Hydrogen embrittlement: Materials and methods

Tests were carried out in a planetary ball mill (Pulverisette 5, Fritsch). Stainless steel vials were replaced by an own developed AISI 1085 steel vials with the same previous capacity of 250 ml and shape, *Fig. 5.22* and the chemical composition of the AISI 1085, *Table 5.8*. The new steel vials were developed to avoid chromium and nickel cross contamination. Vials were filled with 100 ml of Mono Ethylene Glycol (MEG) (Scharlab S.L.), 1.5 g of feed iron powder and 250 g of grinding media. Feed iron powder was Carbonyl Iron Powder (CIP-SM, BASF SE), with an iron content >99% and a mean particle diameter of 2.77 µm by volume. In all the cases, the grinding media was a medium-carbon steel balls with a diameter of ≈2 mm (ref. S660, Pometon). The vials were purged with argon gas for the control tests and with hydrogen for all the experimental tests. The rotating speed was 400 rpm and the milling cycle consisted of 20 min of attrition followed by 20 min of stand-by periods, it was repeated until the desired total milling time was achieved.

The feed iron powder was exposed to a high pressure (40 atm) and temperature (150 ºC) atmosphere for 1 week in order to maximise the hydrogen intake into the iron matrix. Assuming linearity from *(Ćwiek, 2010),* these conditions theoretically lead to a hydrogen content of 7 Ncm^3 per each 100 g of iron. A lab scale chemical reactor was used (500ml Zipperclave, Autoclave engineers Inc.) equipped with a proportional–integral–derivative fine temperature controller, *Fig. 5.23*. It was feed with a high purity hydrogen >99.9996% (Abelló Linde, S.A.) through a high pressure gas regulator (7902-1, Gloor S.L.). Before the hydrogen loading into the reactor vessel, all the system was subjected several times to argon purging and vacuum cycles to avoid an explosive atmosphere.

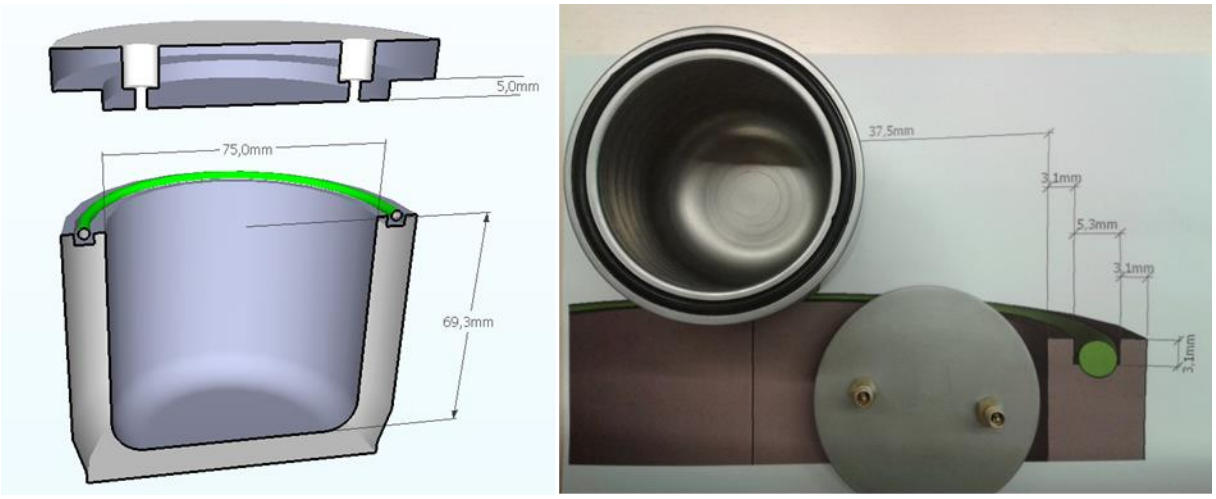

Fig. 5.22 (Left) design of the new vial made from AISI 1085 and (Right) the vial.

Table 5.8 Chemical composition of the AISI 1085 steel.

	C	Mn	Si	S	P
	%	%	%	%	%
AISI 1085	0.80 – 0.93	0.70 - 1.00	0.10 – 0.35	< 0.050	< 0.040

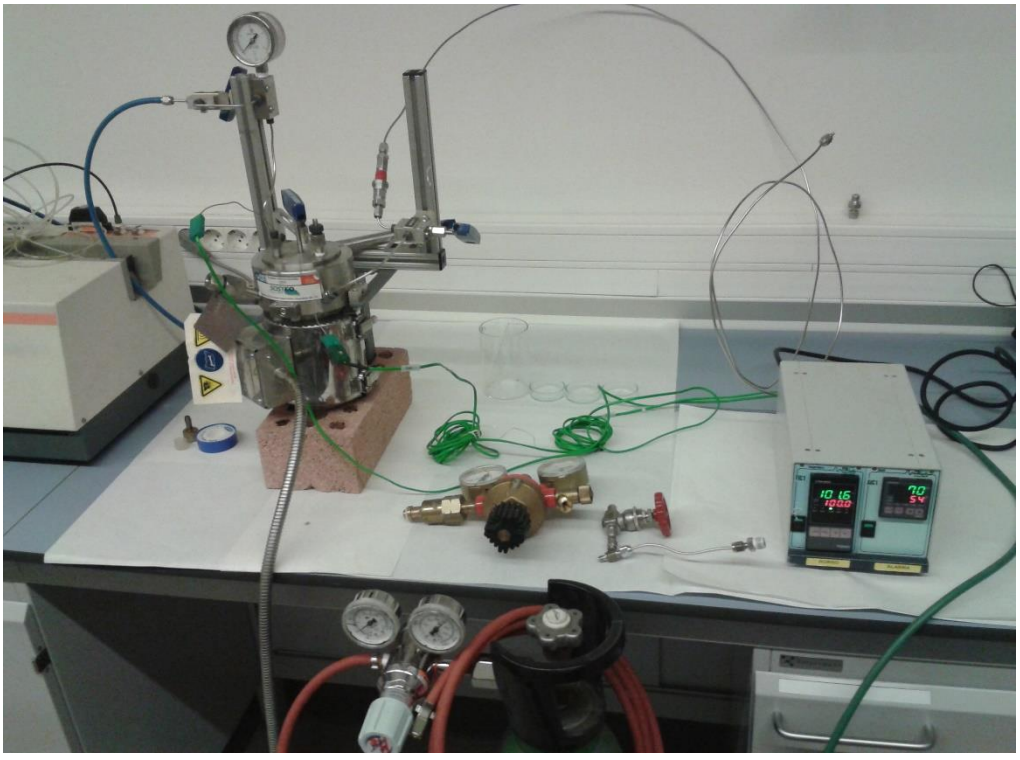

Fig. 5.23 Reactor vessel, temperature controller, hydrogen bottle and gas regulator.

Milled material handling and particle characterization

After milling, all the slurries were initially sieved to remove the steel grinding balls and poured into MEG up to a final volume of 500 ml. For particle characterization, the milled Fe(0) particles were separated from alumina powder by the use of a magnetic field. The slurry was placed next to powerful permanent magnet (720 g of NdFeB, Grade N42) to concentrate iron particles on the wall, supernatant was poured off and Fe(0) particles were dispersed in absolute ethanol. This procedure was repeated five times.

The particle size distribution was determined in an absolute ethanol solution by Laser Diffraction Particle size analysis (LD) (LS 13320, Beckman Coulter) by volume. The morphology of milled particles was studied by Scanning Electron Microscopy (SEM) (Gemini, Zeiss) equipped with an Energy-Dispersive X-ray spectroscopy elemental analyser (SEM-EDX). A drop of the ethanol suspension was placed into a copper support and then dried in a protective atmosphere inside a glove box.

5.4.3 Hydrogen embrittlement: Results and discussion

Improvements thanks to hydrogen embrittlement were poor and difficult to reproduce. Results from tests in which hydrogen pressure and temperature treatment were used showed little improvement. For example: *Table 5.9 and Fig. 5.24* shows the results for a hydrogen embrittlement test compared to control test. In the case of hydrogen embrittlement test a reduction in mean particle diameter and also an increase of particles below 1 µm compared with the control can be observed. It is an interesting usage of hydrogen embrittlement for particle reduction through milling and it has not been reported before for pure iron. However taking into account the extreme conditions used for the introduction of hydrogen into the iron powder: 150 ºC and 40 atm for 1 week and the expensive equipment required to accomplish these small improvements this approach cannot be commercially justified.

Table 5.9 Milling test, grinding conditions and main characterization parameters.

Ref.	Feed Iron		Grinding media		Milling	LD (by vol.)	
	Mean Ø	Load	Ref.	Ø	Time	Mean Ø	< 1 µm
	µm	$g \cdot l^{-1}$		mm	h	µm	%
Hydrogen	2.8	15	S660	2	48	3.5	9.1
Control	2.8	15	S660	2	48	5.1	0.6

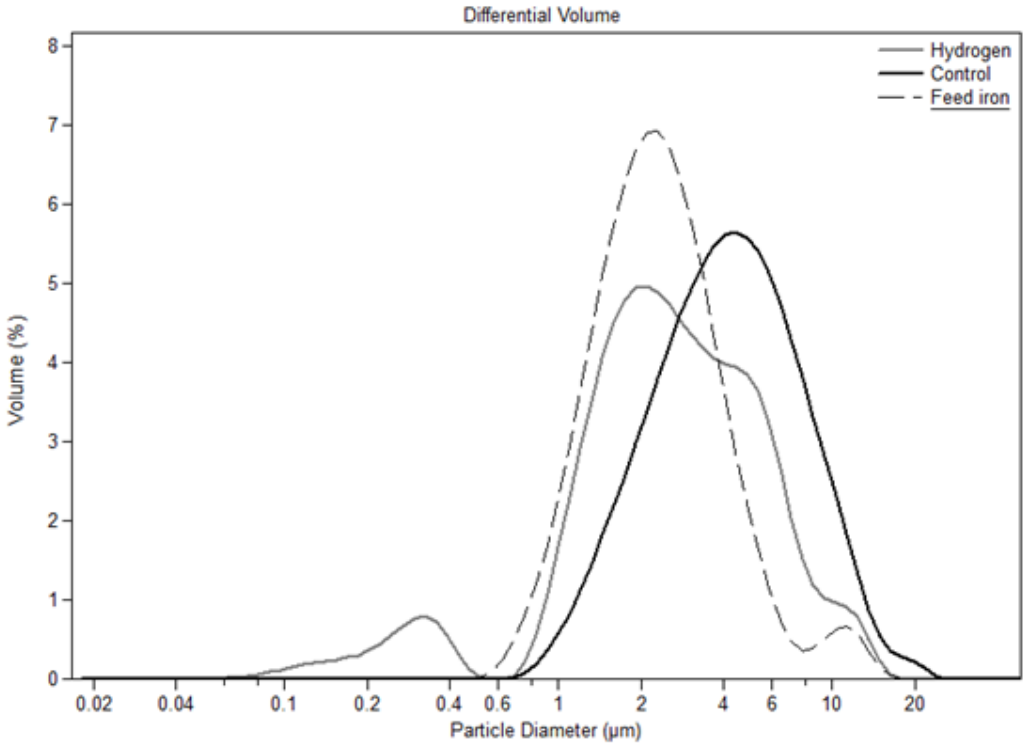

Fix. 5.24 Laser diffraction size distribution of the: hydrogen tests, control tests and feed iron.

5.4.4 Abrasive addition

This approach arose from the need to grind the iron flakes which did not breakdown regardless of the milling time and energy used *(Chapter 5.2)*. The addition of micronized abrasives was intended to behave as a micro grinding media. The abrasive particles would act as a small irregularities coating the grinding balls thus being a pressure spots between the grinding balls and the flakes, *Fig. 5.25*.

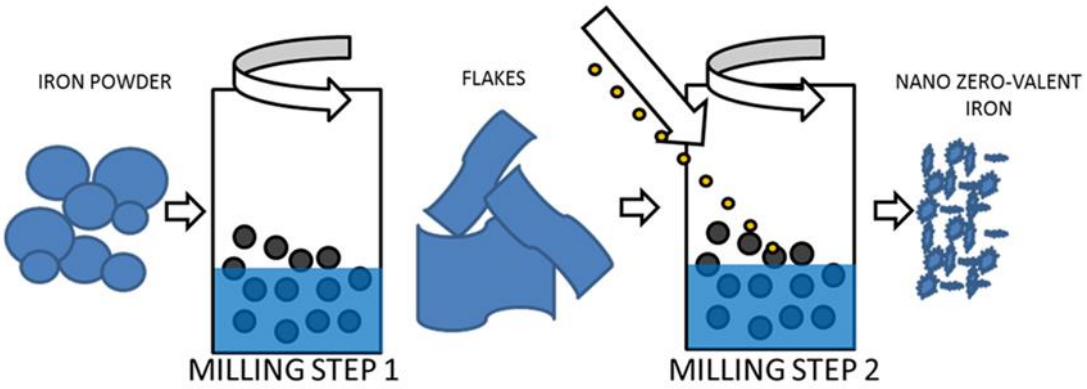

Fig. 5.25 conceptual diagram of the abrasive working mechanism.

Abrasives, in this case alumina (aluminium oxide, Al_2O_3) and silica (silicon dioxide, SiO_2) were selected over other materials for being extremely hard, inelastic, unexpansive, inert, environmentally friendly and available in micrometric sizes. *Table 5.10*, summarizes the most relevant properties, regarding milling of alumina and silica.

In addition to the breakdown of the flakes thanks to the pressure spots crated by the abrasive particles, direct formation of iron nanoparticles from the wear action must be considered. *(McMahon et al., 2014),* used a wear process on the grinding media to produce: aluminium, iron, and copper nanoparticles this process should increase if abrasives are used.

Table 5.10 Properties of alumina and silica, *(Callister, 2001)*.

	Knoop hardness ($kg \cdot mm^{-2}$)	**Mechanical strength** (MPa)	**Density** (kg/m^3)
Alumina	2100	275-700	3980
Silica	800	110	2200

5.4.5 Abrasive addition: Materials and methods

Tests were carried out in a planetary ball mill (Pulverisette 5, Fritsch). The new AISI 1085 steel vials with a capacity of 250 ml were used in all the tests, *Fig. 5.22*, chemical composition *Table 5.8*. The new steel vials were developed to avoid chromium and nickel leaching due to abrasion. Vials were filled with 100 ml of Mono Ethylene Glycol (MEG) (Scharlab S.L.), 1.5 g of feed iron powder and 250 g of grinding media. Feed iron powder was Carbonyl Iron Powder (CIP-SM, BASF SE), with an iron content >99% and a mean particle diameter of 2.77 µm by volume. As a grinding media medium-carbon steel balls with a diameter of ≈2 mm (ref. S660, Pometon) were used. The vials were purged with argon gas to create a protective atmosphere inside the vials. The rotating speed was 400 rpm and the milling cycle consisted of 20 min of attrition followed by 20 min of stand-by periods, it was repeated until the desired total milling time was achieved.

These tests were divided in two steps. In the first one, the iron was milled during 24 h. Once the vials were cooled, they were opened in a glove box with an N_2 protective atmosphere and the desired

abrasive was introduced: irregular alumina powder 5 µm (PRESI - Métallographie) or silica powder 1-5 µm (Sigma-Aldrich Co.). The vials were purged again with argon gas and they were placed in the planetary ball mill for a second milling step. In this case, the milling was extended for 24 h following the same standard procedure described above.

The methodologies and procedures applied into the handling of the milled material for its characterization were the same as is the previous section *(5.4.2 Hydrogen embrittlement, Materials and methods)*.

5.4.6 Abrasive addition: Results and discussion

First tests with abrasives had a very different performance depending on the abrasive used. Silica test showed no improvement comparing to the control but on the other hand alumina test produced a final very small particle mean diameter of 0.91 µm and a fraction <1 µm of 20.6%, *Table 5.11 and Fig. 5.26*, a huge steps forward comparing to the previous exposed results. It is hypothesized that the different performance between silica and alumina was due to the density or hardness difference between both, summarized in *Table 5.10*.

Table 5.11 milling test with abrasives, grinding conditions and main characterization parameters.

Ref.	Feed Iron		Abrasive		Grinding media		Milling	LD (by vol.)	
	Mean Ø	Load	Ref.	Load	Ref.	Ø	Time	Mean Ø	< 1 µm
	µm	$g \cdot l^{-1}$		$g \cdot l^{-1}$		mm	h	µm	%
Silica	2.8	15	SiO_2	17	S660	2	48	5.7	1.1
Alumina	2.8	15	Al_2O_3	17	S660	2	48	0.91	20.6
Control	2.8	15	---		S660	2	48	5.1	0.6
Feed iron								2.77	4.7

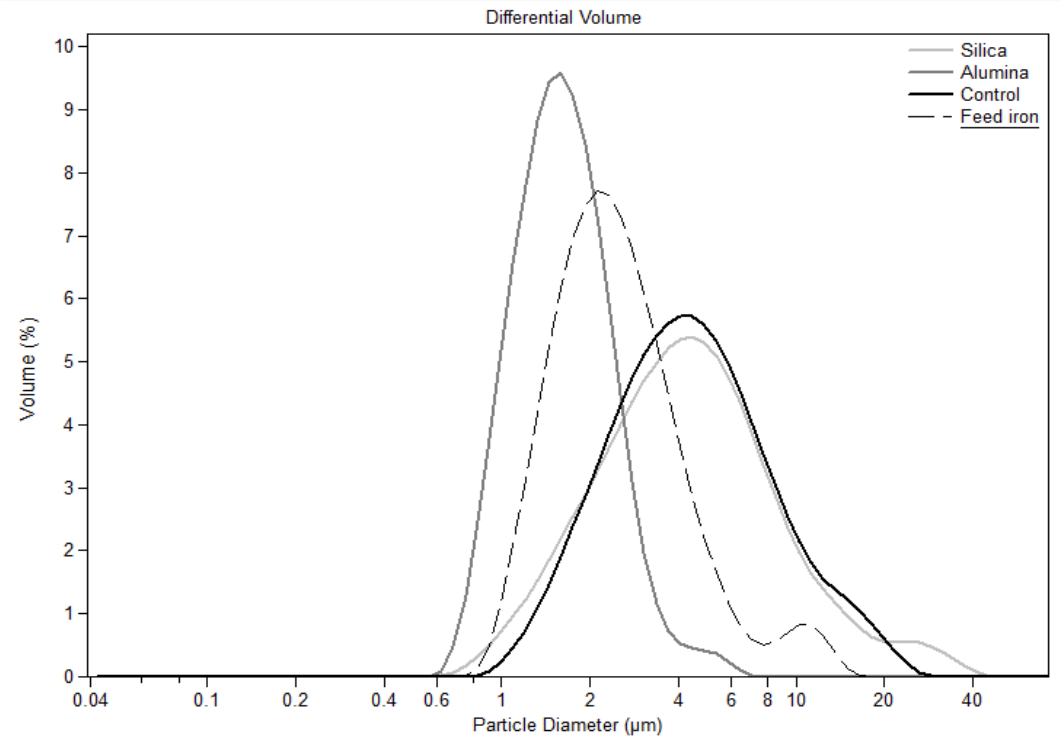

Fig. 5.26 Laser diffraction size distribution of the: silica tests, alumina tests, control and feed iron.

5.4.4 Conclusions

- Hydrogen embrittlement produced a little improvement not justifying the complexity and costs of this technique.

- Finally, alumina addition had a dramatic influence in both: mean particle diameter and the fraction below 1 μm reaching a 20%. Clearly, this is the most promising approach because of the simplicity and the huge improvement obtained comparing to all previous tests.

5.4.5 References

Barnoush, A. (2011). Hydrogen embrittlement. Saarland University.

Bonneau, P. (2002). Solubility of gases in fluorocarbons. CERN Detector Cooling Section. (accessed 06/2016) http://detector-cooling.web.cern.ch/Detector-Cooling/data/Fluoro_Solubility.htm

Callister, W. D., & Rethwisch, D. G. (2013). Fundamentals of materials science and engineering (Vol. 21). New York: Wiley.

Ćwiek, J. (2010). Prevention methods against hydrogen degradation of steel. Manufacturing Engineering, 43(1), 214-221.

Escobar, D. P., Minambres, C., Duprez, L., Verbeken, K., & Verhaege, M. (2011). Internal and surface damage of multiphase steels and pure iron after electrochemical hydrogen charging. Corrosion Science, 53(10), 3166-3176.

Kubaschewski, O. (2013). Iron—Binary phase diagrams. Springer Science & Business Media.

McMahon, B. W., Perez, J. P. L., Yu, J., Boatz, J. A., & Anderson, S. L. (2014). Synthesis of nanoparticles from Malleable and Ductile Metals Using Powder-Free, Reactant-Assisted Mechanical Attrition. ACS Applied Materials & Interfaces, 6(22), 19579-19591.

Patiño-Carachure, C., García-De León, E., Angeles-Chávez, C., Esparza, R., & Rosas-Trejo, G. (2009). Hydrogen embrittlement assisted by ball-milling to obtain AlCuFe nanoparticles. Journal of Non-Crystalline Solids, 355(34), 1713-1718.

Patnaik, P. (2003). Handbook of Inorganic Chemicals (Vol. 28). New York: McGraw-Hill, pp 11-12

Smallman, R. E., & Bishop, R. J. (1999). Modern physical metallurgy and materials engineering. Butterworth-Heinemann, pp 323-325.

Telitchev, I. Y., & Vinogradov, O. (2008). Modeling of hydrogen-assisted cracking in iron crystal using a quasi-Newton method. Journal of Molecular Modeling, 14(7), 621-630.

Wang, J. S. (2000). Internal hydrogen-induced embrittlement in iron single crystals. In Multiscale deformation and fracture in materials and structures (pp. 31-47). Springer Netherlands.

5.5 Improvements in nanoscale zero-valent iron production by milling through the addition of alumina

A new milling procedure for a cost-effective production of nano Zero-Valent Iron (nZVI) for environmental remediation is presented. Conventional ball milling of iron in an organic solvent produces flattened iron particles that are unlikely to break even after very long milling times.

With the aim of breaking down these iron flakes, in this new procedure further milling is carried out adding an amount of fine alumina powder to the previously milled solution. As the amount of added alumina increases from 9 $g \cdot l^{-1}$ to 54 $g \cdot l^{-1}$, a progressive decrease of the presence of flakes is observed. In the latter case, the appearance of the particles formed by fragments of former flakes is rather homogeneous, with most of the final nanoparticles having an equivalent diameter well below 1 μm and with an average particle size in solution around 400 nm. An additional increase of alumina content results in a highly viscous solution showing worse particle size distribution.

Milled particles, in the case of alumina concentrations of 54 $g \cdot l^{-1}$, have a fairly large specific surface area and high Fe(0) content. These new particles show a very good Cr (VI) removal efficiency compared with other commercial products available. This good reactivity is related to the absence of an oxide layer, the large amount of superficial irregularities generated by the repetitive fracture process during milling and the presence of a fine nanostructure within the iron nanoparticles.

The work described in this chapter has been published in:

Ribas, D., Cernik, M., Martí, V., & Benito, J. A. (2016). Improvements in nanoscale zero-valent iron production by milling through the addition of alumina. Journal of Nanoparticle Research, 18(7), 1-11.

5.5.1 Introduction

Following the conclusions from *(Chapter 5.2 & 5.3)* where the need to embrittle the iron flakes formed during the milling process in non-aqueous media was stated and the promising results obtained with the addition of alumina *(Chapter 5.4)*. This work is focused on exploring a new milling procedure capable of breaking down the iron flakes produced by milling in organic solvents thanks to the addition of micrometric alumina.

With this aim, the study extensively studied the effect of adding alumina during the milling process to produce nZVI. Alumina (Al_2O_3) is a chemically inert and biocompatible material used in medical devices and which is very abundant in nature, *(Smallman et al. 1999; Patnaik, 2003)*. At the same time, alumina has high mechanical strength and hardness and therefore, has the capacity to deform commercial iron powder. In this sense, the use of alumina balls during the milling of iron powder enabled to form thin iron films all around the smooth surface of alumina balls, *(Hao et al. 2012)*. It is thought that the use of irregular alumina during the milling in non-aqueous media of iron can help to break the previously described very thin flakes and then to reduce the size of the milled iron particles. Finally, it is important to note that the chemical reaction of alumina with iron can be neglected because it has only been described in dry high energy mechanical milling processes, *(Paesano et al. 2004)*.

Since the main use of these particles is to remove contaminants from groundwater, the reactivity of new milled particles has been investigated through their capacity to reduce Cr (VI), *(Crane et al. 2012; O'Carroll et al. 2013)*. Hexavalent chromium Cr (VI) is a heavy metal used in many industrial applications e.g. chromium production and leather tanning. Its reduction to trivalent chromium Cr (III) is a common mitigation approach in contaminated waters since a mobile and very toxic chromium species is converted to a less mobile and less toxic form, *(Bagchi et al. 2002)*. nZVI is widely studied as a remediation method for Cr (VI), *(Gheju 2011; Tang et al. 2013)*. Although it has been extensively studied, there is a great diversity of proposed pathways to describe chromium reduction and precipitation, *(Mystrioti et al. 2014)*. Eq.1 describes the reaction between nZVI and Cr(VI), *(Melitas et al. 2001)*.

$$Fe^0_{(s)} + CrO^{2-}_{4\,(aq)} + 4H_2O_{(l)} \rightarrow Fe(OH)_{3\,(s)} + Cr(OH)_{3\,(s)} + 2OH^- \quad \textbf{Eq. 5.2}$$

5.5.2 Materials and methods

The initial iron powder was Carbonyl Iron Powder (BASF CIP-SM), with an iron content of >99%, a mean particle diameter of 2.77 µm by volume and a Superficial Surface Area (SSA) of 0.7 ± 0.1 $m^2 \cdot g^{-1}$. The milling tests were carried out in a planetary ball mill (P-5, Fritsch) using AISI 1085 steel vials with a capacity of 250 ml. In all cases the vials were filled with 100 ml of Mono Ethylene Glycol (MEG, Scharlab S.L.), 3 g of iron powder and 250 g of medium-carbon steel balls with a diameter of ≈2 mm (ref. S660, Pometon). The vials were purged with argon gas until a protective atmosphere was created inside them. The rotating speed was 400 rpm and the milling cycle consisted of 30 min of attrition followed by 30 min of stand-by periods to minimize the temperature rise.

These new tests were divided into two steps. In the first, the iron was milled for 24 h following the standard procedure described above. Once the vials have cooled, they were opened in a glove box with an N_2 protective atmosphere and varying amounts of irregular Al_2O_3 powder (9, 18, 27, 54 and 108 $g \cdot l^{-1}$) with an average diameter of 5 µm added to them (PRESI - Métallographie). The vials were once again purged with argon gas and placed in the planetary ball mill for a second milling step. In this case, milling lasted 24h and followed the standard procedure described above.

After the milling process, all the slurries were sieved to remove the steel grinding balls. Milled Fe(0) particles were separated from the alumina powder using a magnetic field so as to carry out a particle

characterization. The slurry was placed over a powerful permanent magnet (720g of NdFeB, Grade N42) in order to concentrate iron particles in the bottom, supernatant was poured over it and iron particles were dispersed in absolute ethanol. This procedure was repeated five times.

The particle size distribution was determined in an absolute ethanol solution by Laser Diffraction Particle Size Analysis (LD) (LS 13320, Beckman Coulter). All the results obtained by this method were obtained using the volume of particles mode. The Specific Surface Area (SSA) was analysed by BET gas adsorption drying the ethanol suspension with a maximum degassing temperature of 100 ºC (ASAP 2020, Micromeritics). The Fe(0) content was determined in triplicate by the hydrogen production method *(Liu et al. 2005a)* where iron reacts with sulphuric acid added to the slurry and the volume of produced hydrogen was measured. Total iron concentration was assessed, firstly, digesting the suspensions with 2:1 HNO3:H2O2 and then analysing it by Inductively Coupled Plasma Atomic Emission Spectroscopy (ICP-AES), (Optima 3200, Perkin-Elmer). The morphology of the milled particles was studied by Scanning Electron Microscopy (SEM) (Gemini, Zeiss). A drop of the ethanol suspension was placed on a copper support and then dried in a protective atmosphere inside a glove box. A very small presence of Al_2O_3 was confirmed by secondary electron images and Energy-dispersive X-ray Spectroscopy (EDS). For Transmission electron Microscopy (TEM) (Philips CM30) observation, a droplet of the ethanol suspension was placed on a 300 copper mesh grid with a supporting film made of holey carbon and then transferred to a microscope over a liquid nitrogen flask to reduce oxygen contact.

Reduction of Cr (VI) to Cr (III) was used to quantify the reactivity of the selected iron nanoparticles in batch mode. Batches were set in 250 ml hermetic borosilicate glass bottles with an initial Cr (VI) concentration of 50 $mg \cdot l^{-1}$ prepared from dried potassium chromate (K_2CrO_4, p.A., AppliChem GmbH). In order to simulate ions interferences and ionic strength in real water, tap water was used in all the experiments after leaving it overnight to eliminate the chlorine. By way of comparison, apart from the milled nZVI obtained in the present work, two nZVI commercial products were also tested:

(I) Commercial NANOFER 25P (NANOIRON s.r.o), named “N25P”. The particles are obtained by gas reduction at high temperature, being extremely reactive and pyrophoric with an SSA of 25 $m^2 \cdot g^{-1}$ and an average particle size of 50 nm, forming aggregates of a few microns in water, *(Soukupova et al. 2015)*. The particles’ Fe(0) content is 87 ±1%. For the experiments, a 20% w/w iron water slurry was prepared and immediately used.

(II) Novel nZVI milled flakes supplied by (UVR-FIA GmbH), named “A01”. The particles are produced by wet milling in MEG and they are supplied in this MEG slurry. A01 is composed mainly of iron flakes with a lateral size of several micrometers and a thickness of <200 nm forming agglomerates of different sizes ranging from 200 nm to 45 µm, *(Köber et al. 2015)*. The SSA is 18 $m^2 \cdot g^{-1}$ and Fe(0) content is 74 ±1%.

Seven reaction batches were prepared for each type of nZVI, spiking each sample to a final iron concentration of 0.1, 0.25, 0.5, 1.0, 2.0, 2.5 and 4.0 $g \cdot l^{-1}$. The different types of nZVI were used as received or produced in the reactivity tests, and the Al_2O_3 and MEG were not separated from the slurries, emulating a commercial application. So as to observe the effect of alumina and MEG, a blank with the used amount of both products was prepared. Finally, it must be noted that the solutions were not buffered in order to mimic field conditions.

After nZVI addition, the solutions were put into a rotating shaker with a bottom-up rotation step every 60 s to keep nanoparticles in suspension avoiding particle settling. The batch reactors were not stirred to prevent an increase of reactivity of nanoparticles with water. Batches were allowed to react for 24h after being analysed. The reference batches were analysed repeatedly over 2 months with no significant changes in Cr (VI) concentration. Cr (VI) concentration was determined colorimetrically (DR3900 Spectrometer, Hach Lange GmbH) by diphenylcarbazide reaction in acid solution (US EPA method 7196A).

5.5.3 Results

The final shape of iron particles after milling with steel balls and different amounts of alumina following the two-step process described above is show in, *Fig. 5.27*. The evolution of the mean particle size and the percentage of the material <1 µm analysed by LD with Al_2O_3 content is plotted in, *Fig. 5.28*. The first step was prepared so as to transform the initial rounded iron particles into flakes and it corresponds exactly to the first 24h of the process, in which only steel balls were used, *Fig. 5.27a*. This sample was named "M24h-step1". The second step, in which small and hard alumina was added, was designed with the aim of breaking the flakes. The SEM image of dry milled particles with an addition of 9 $g \cdot l^{-1}$, *Fig. 5.27b,* shows that this goal was achieved, since a great number of small, flat fragments were originated. It must be noted that a great variability between the different trials was observed as well as numerous remains of former large flakes. However, the breaking of flakes was reflected in a significant decrease on the mean particle diameter and an increase of particles <1 µm. With higher alumina additions, as in the case of 27 $g \cdot l^{-1}$ *(Fig. 5.27c)*, the remains of large flakes disappeared and milled particles became more homogeneous. It resulted in a large reduction of the mean particle size, but in many cases the particles still maintained a flat form. When the amount of Al_2O_3 added was 54 $g \cdot l^{-1}$, an improvement in milled particles was observed, *Fig. 5.27d*. Firstly, the variability between the different tests was reduced and the morphology of milled particles changed from flat to more irregular as a result of bonding between the very small fragments. On the other hand, a slight particle size reduction was observed compared with 27 $g \cdot l^{-1}$: the mean diameter was reduced to 1.1 µm and the material *<1* µm was above 30%. Finally, with large Al_2O_3 concentrations (108 $g \cdot l^{-1}$) the tests were difficult to carry out due to a significant increase of pressure and temperature inside vials that resulted in leaks. As the particle size distributions were also worse, these large concentrations were discarded.

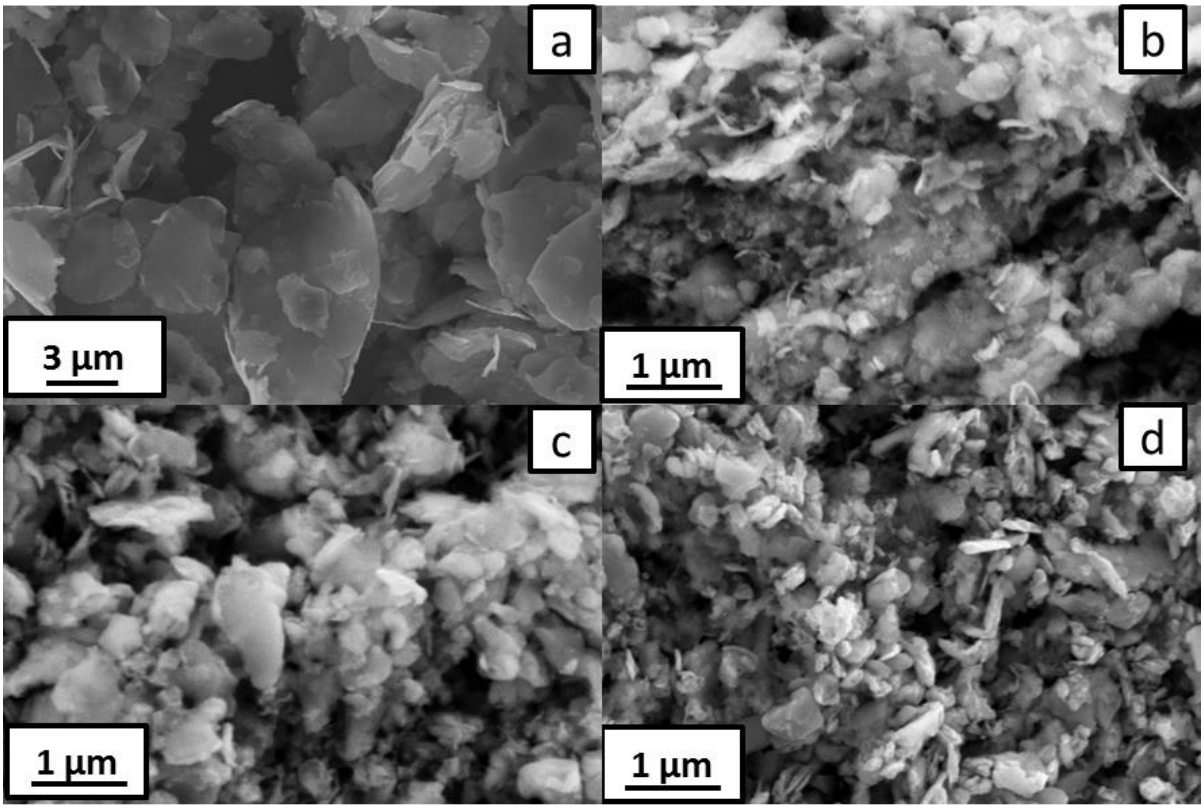

Fig. 5.27 SEM images of the milled particles after the two-steps process adding different amounts of alumina. a) After first steps (M24h-steps1), b) 9 $g \cdot l^{-1}$, c) 27 $g \cdot l^{-1}$, d) 54 $g \cdot l^{-1}$.

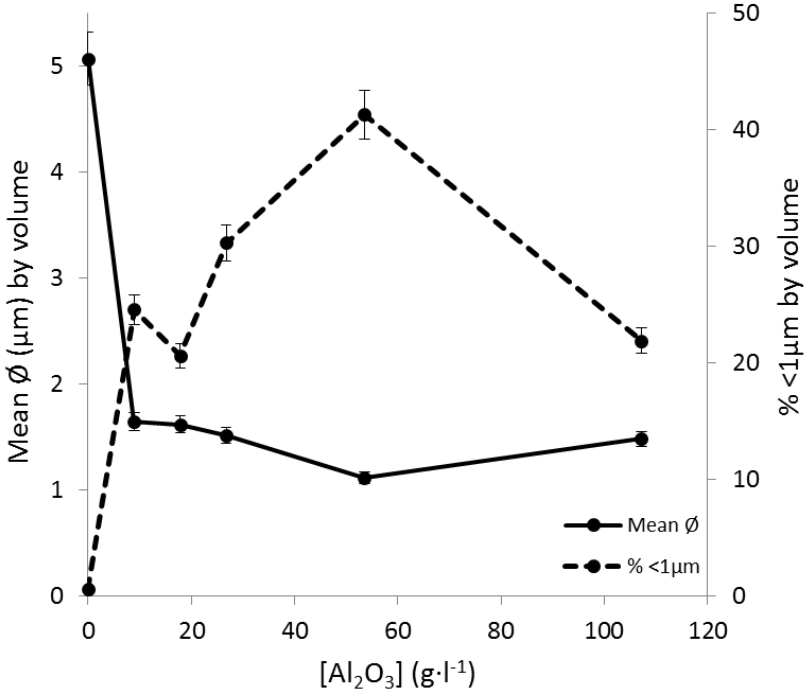

Fig. 5.28 Evolution of mean particle diameter and percentage of particles <1µm with alumina concentration after additional 24 h milling from M24h-step1.

In the light of these results, the milling process with 54 $g \cdot l^{-1}$ of Al_2O_3 was chosen for further characterization and reactivity tests. This sample was named "M48h-Al_2O_3"; TEM images for this sample are shown in, *Fig. 5.29*. At low magnifications *(Fig. 5.29a)*, the irregular and fragmented shapes of milled particles created by the fracture of former flakes can be observed. At higher magnifications, it can be noted that many of the particles have been formed by the joining of smaller fragments, *Fig. 5.29c*. The dark field image in, *Fig. 5.29c,* shows that these iron particles have a nanocrystalline structure, with grains of only a few nanometres, *Fig. 29d*. This type of structure is frequent after ball milling of iron *(Liu et al. 2001; Rodriguez et al. 2007)*. The analysis of the diffraction rings included in the Selected-Area Diffraction (SAD) of *Fig. 5.29c* confirmed that the particles were composed entirely of α-Fe grains with a random orientation. It must be noted that there were few points in the SAD that suggest a residual presence of Al_2O_3. Unlike other air-stabilized or water aged nZVI particles *(Kim et al. 2010)*, there was an absence of an oxide layer on the outside of the particles *(Fig. 5.29b)*, which can be explained by the protective coating of MEG and argon atmosphere during milling *(Köber et al. 2014)*. The lack of oxide layer is consistent with the high Fe(0) content of the M48h-Al_2O_3 suspension which was 92% ± 1.

Fig. 5.30, shows the comparison of the mean particle diameter in a solution as determined by LD for the initial material; the milled particles after the first and second step (M24h-step1 and M48h-Al_2O_3 respectively) and the two nZVI commercial products used in the reactivity tests (N25P and A01). Regarding milled materials, the particle size distribution of M24h-step1 moved to higher equivalent diameters than those of the initial powder due to the change from spherical to flaky morphology. After the second milling step, the fracture process of flakes moved the particle size distribution to lower values, with a mean equivalent diameter of 1.1 µm. The diameter of the milled particles in the present case is higher than the particle size of typical nZVI particles produced by gas reduction, as is the case of N25P, which are in the range of 50-150 nm *(Soukupova et al. 2015; nanoIron 2016)*. However, when compared with M48h-Al_2O_3, a significant shift in the average particle size toward larger values was detected for N25P, which means a higher degree of agglomeration. The other milled iron chosen for comparison (A01) has a better particle size distribution than M24-step1, but is larger than N25P and M48h-Al_2O_3.

As mentioned above, the Fe(0) content of the M48h-Al_2O_3 suspension was 92% ±1. It was found that the other reference products also had high Fe(0) content: N25P had an 87% ±1 and A01 a 74% ±1. On the contrary, the SSA value for milled M48h-Al_2O_3 was 14.0 ±0.1 $m^2 \cdot g^{-1}$, slightly below the value reported for A01 (18 $m^2 \cdot g^{-1}$) *(Köber et al. 2014)* and clearly lower than the one for N25P (25 $m^2 \cdot g^{-1}$) *(Soukupova et al. 2015)*.

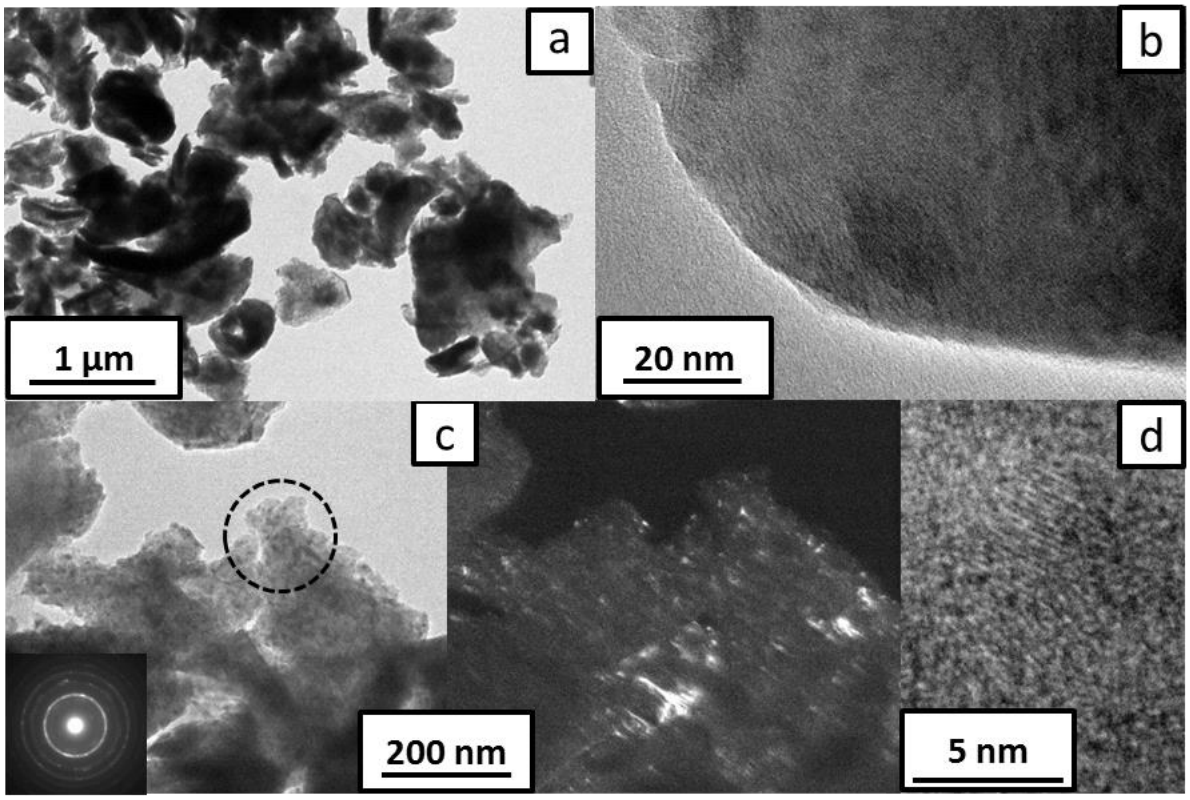

Fig. 5.29 TEM images of M48h-Al_2O_3. (a) General view. (b) Details of the surface of nanoparticles. (c) Bright (left) and dark (right) field image and Selected Area Diffraction (SAD) of milled particles. (d) Detail of nanostructure in an iron nanoparticle.

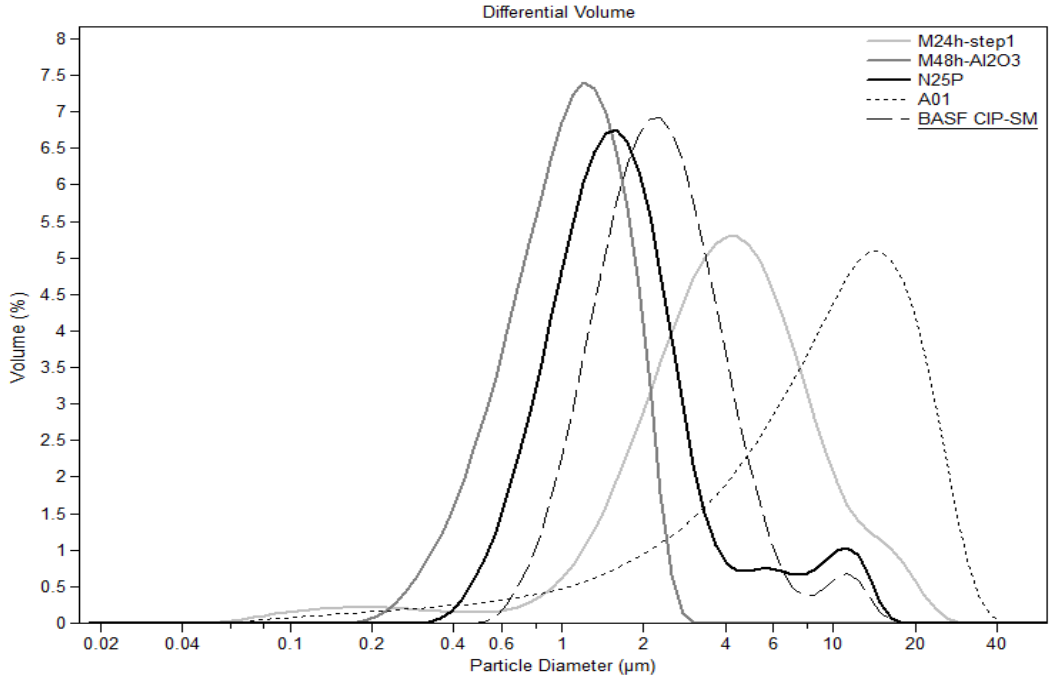

Fig. 5.30 Particle size distribution of: as-received iron powder (BASF CIP-SM), milled iron after the first step of milling (M24h-step1), iron after milling with alumina (M48h-Al_2O_3) and commercial reference irons N25P and A01.

Reactivity of the developed iron

Fig. 5.31 shows the depletion of Cr(VI) in a solution with the amount of nZVI used in the reactivity tests, whereas *Table 5.12* shows the slope of the depletion curve of Cr(VI), the Cr(VI) removal efficiency as weight of Cr(VI) removed by weight of Fe(0) and finally, this Cr(VI) removal efficiency normalized by SSA. As it can be observed in *Fig. 5.31*, the blank with alumina powder in MEG had no effect on the Cr (VI) concentration, which indicates that alumina is not active in the reduction or sorption of Cr (VI). At the same time, the activity of nZVI suspensions had a good performance in all the cases, considering that the reactivity tests were done without stirring and buffering of pH *(Buerge et al. 1997)*. The oxidation of Fe(0) leads to a high pH in solution (≈9-10) and iron passivation, which reduces the electron transfer from iron nanoparticles *(Song et al. 2005; O'Carroll et al. 2013)*. This behaviour can be observed in *Fig. 5.32*, where the evolution of Cr(VI) content with time is shown for the case of N25P nanoparticles. In all cases the Cr(VI) depletion took place mainly within the first 2 hours, and subsequent analysis for 2 months did not show significant changes in Cr(VI) concentration. Passivation of nZVI is a frequently reported problem *(Li et al. 2008; Liu et al. 2006; Kim et al. 2012; Xie et al. 2012)* and in the specific case of Cr (VI) reduction, it seems to be related to the growth of Fe-Cr compounds on the particle surface *(Kerkar et al. 1990)*.

As can be seen in *Fig. 5.31*, the Cr (VI) removal efficiency of M48h-Al_2O_3 is very high in comparison with the other tested particles, being significantly higher when it is normalized with SSA. M48h-Al_2O_3 Cr (VI) removal efficiency is within the range of the values reported for nZVI obtained from borohydride method (Fe^{BH}) at similar pH *(Li et al. 2008; Xie et al. 2012; Yu et al. 2014)*. This can be considered as a good result: first, because Fe^{BH} is known to have a higher reactivity than other commercial nZVI products *(Kim et al. 2012)* and second, due to the fact that in the present case the batches were not stirred during reaction.

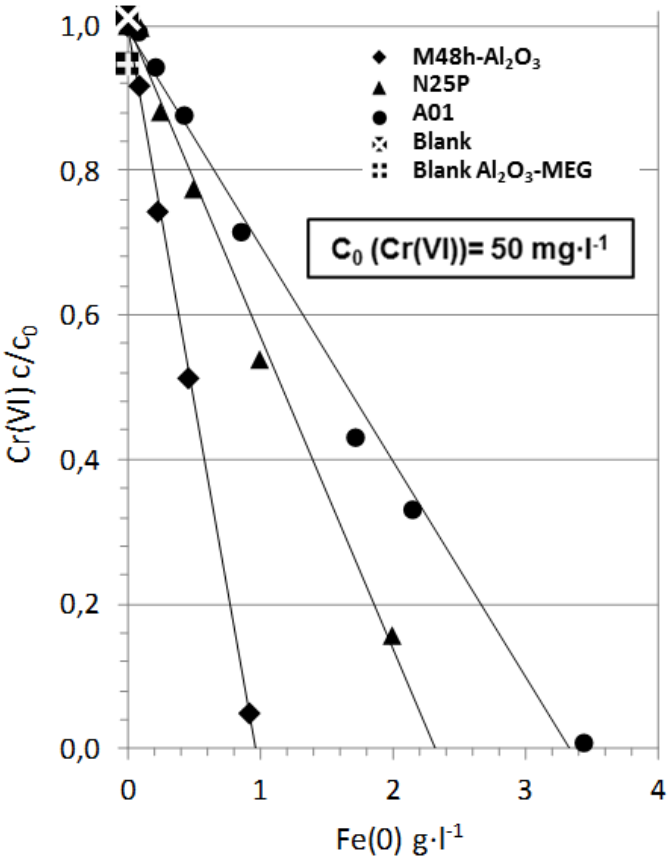

Fig. 5.31 Depletion curves of Cr(VI) for the milled iron with alumina (M48h-Al_2O_3) and commercial reference irons N25P and A01.

Table 5.12 Slope (*S*) of the depletion curve of Cr(VI), Cr(VI) removal capacity and normalized Cr(VI) removal capacity by SSA for the three nZVI tested.

	$S = \frac{\Delta\, c/c_0}{\Delta\, [Fe]}$	Cr(VI) removal capacity	Normalized Cr(VI) removal capacity by SSA
		mg Cr(VI)·g Fe(0)$^{-1}$	mg Cr(VI)·g Fe(0)$^{-1}$·m^{-2}
M48h-Al_2O_3	-1.035	-51.75	-3.70
N25P	-0.432	-21.92	-0.84
A01	-0.298	-15.88	-0.88

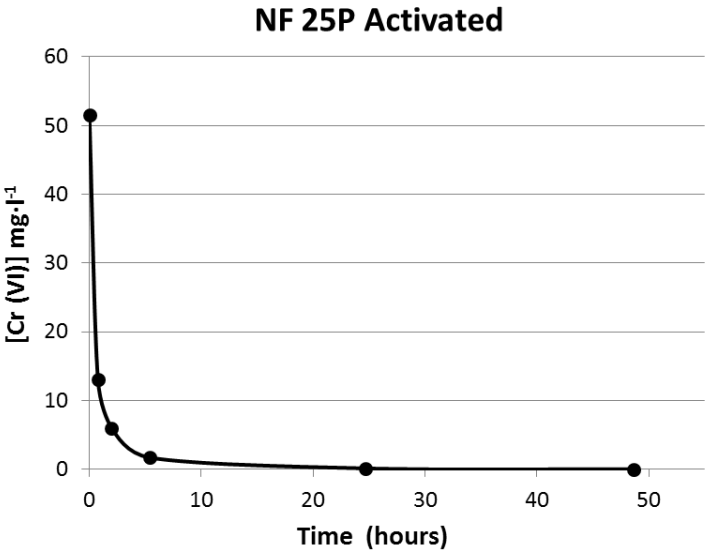

Fig. 5.32 Depletion curve of Cr(VI) with time.

The high Cr (VI) removal capacity of M48h-Al_2O_3 observed can be attributed to different reasons. As described in literature, the main Cr (VI) removal mechanism is the reduction to Cr (III) *(Li et al. 2008; O'Carroll et al. 2013)*. In this process, the electron transfer from Fe(0) is a critical point and consequently the presence of a thick oxide layer can cause a reduction of reactivity *(Kim et al. 2010; O'Carroll et al. 2013)*. In the light of the images in *Fig. 5.29* and taking into account the high Fe(0) content of M48h-Al_2O_3 particles, no signs of an oxide layer were observed. It is interesting to note that this absence is also applicable to A01 particles *(Köber et al. 2014)* and N25P *(Soukupova et al. 2015; nanoIron 2016)*. Concerning the milled 48h-Al_2O_3 particles, the reason for the absence of an oxide layer can be mainly attributed to the use of MEG in the processes of milling and storing particles, which results in a very efficient protection against iron corrosion *(Köber et al. 2014)*. Another important point for a high Cr (VI) removal capacity is a high SSA, because then a larger number of reactive sites are provided by the particles *(O'Carroll et al. 2013)*. But in this case, the SSA for M48h-Al_2O_3 is lower than that for the other nZVI, which should result in lower reactivity.

Since the oxide layer and SSA values do not account for the high Cr (VI) removal capacity of M48h-Al_2O_3, this high efficiency must be more related to two other factors: the first would be an enhanced density of reactive sites in the surface *(Lapuerta et al. 2006)*, the second would be the internal structure of the nanoparticles *(Liu et al. 2005a)*. In the first point, it has been suggested that the new surfaces created by the fracture of the former particles and the presence of a great amount of irregularities offer a large number of reaction sites, which causes an increase of reactivity *(Li et al. 2009; Köber et al. 2014)*. According to this, the milling process of M48h-Al_2O_3 has the capacity to break up the iron flakes, which means a large number of fractured surfaces and new and very irregular nanoparticles are formed by the joining of small fragments. Consequently, the reactivity of M48h-Al_2O_3 particles must then be larger than in the cases where no alumina is used during milling *(Li et al. 2009; Köber et al. 2014)* or where the particles are not milled, as is the case of N25P *(Crane et al. 2012)*. Here it should

be added that during milling there is a breakdown of the initial oxide layer of former particles which causes a number of the oxides to become finely dispersed throughout the new welded particles, giving rise to new surfaces with less oxygen content *(Li et al. 2009; Casas et al. 2015)*.

The second point is related to the improvement in reactivity associated with an increase in defects in the crystalline structure of iron particles. In this respect, better reactivity has been reported to highly disordered Fe^{BH} compared with crystalline nZVI obtained by H_2 reduction of iron oxides *(Liu et al. 2005a)* or by vacuum annealed Fe^{BH} *(Liu et al. 2005b)*, although in the latter case the reactivity against some pollutants seems to be unaffected by crystallization during annealing *(Dickinson et al. 2011)*. In the case of M48h-Al_2O_3 *(Fig. 5.29c & d)* it is composed by nanostructured ferrite obtained by a severe plastic deformation process *(Rodriguez et al. 2007)*. It is possible to think that this structure is more disordered than that obtained in A01 and N25P. In the first case due to the absence of breakage of the flakes during milling and in the second case by the clear presence of α-Fe in X-ray measurements with an average grain size of around 50-100 nm *(nanoIron 2016; Soukupova et al. 2015)*.

5.5.4 Conclusions

- The introduction of fine alumina powder during ball milling of iron in an organic solvent as MEG allows the breakage of the iron flakes obtained after a conventional milling process. Low alumina concentrations (9-27 $g \cdot l^{-1}$) render clearly inhomogeneous distributions that are a mixture of remaining former flakes and smaller fragments, whereas high concentrations (108 $g \cdot l^{-1}$) are difficult to handle due to excessive heating and viscosity of the slurry.

- When an alumina content of 54 $g \cdot l^{-1}$is added, a homogeneous distribution of irregular particles formed from the fragments of the former iron flakes is observed. Particles present an equivalent diameter of 1.1 μm. However, due to the little tendency to aggregation of milled particles, the particle size distribution in solution is clearly finer than that for other commercial nZVI suspensions even for the smaller ones. In addition, milled particles have high Fe(0) content (92 ±1 %) and fairly good specific surface area (14.0 ± 0.1 $m^2 \cdot g^{-1}$).

- The Cr (VI) removal efficiency is -51.75 mg Cr(VI) g $Fe(0)^{-1}$, that is higher than the observed in the other commercial nZVI solutions tested in this paper. The reactivity is better when the Cr(VI) removal capacity is normalized by the specific surface area (-3.70 mg Cr(VI) per g $Fe(0)^{-1}$ m^{-2}). This good reactivity comes first from an absence of an oxide layer, but it is thought that the great amount of superficial irregularities that form a great number of reactive sites and the presence of a very fine nanostructure inside the milled particles also play a key role. As a final thought, this procedure is expected to offer a cost-effective way of producing nZVI for large-scale environmental remediation.

5.5.5 References

Bagchi, D., Stohs, S.J., Downs, B.W., Bagchi, M., & Preuss, H.G. (2002). Cytotoxicity and oxidative mechanisms of different forms of chromium. Toxicology 180(1):5-22.

Buerge, I.J., & Hug, S.J. (1997). Kinetics and pH dependence of chromium (VI) reduction by iron (II). Environmental Science & Technology, 31(5):1426-1432.

Casas, C., Tejedor, R., Rodriguez-Baracaldo, R., Benito, J.A., & Cabrera, J.M. (2015). The effect of oxide particles on the strength and ductility of bulk iron with a bimodal grain size distribution. Materials Science and Engineering: A 627:205-216.

Crane, R.A., & Scott, T.B. (2012). nanoscale zero-valent iron: future prospects for an emerging water treatment technology. Journal of Hazardous Materials, 211:112-125.

Dickinson, M., & Scott, T.B. (2011). The effect of vacuum annealing on the remediation abilities of iron and iron–nickel nanoparticles. Journal of Nanoparticle Research, 13(9):3699-3711.

Gheju, M. (2011). Hexavalent chromium reduction with zero-valent iron (ZVI) in aquatic systems. Water, Air, & Soil Pollution, 222(1-4):103-148.

Hao, L., Lu, Y., Asanuma, H., & Guo, J. (2012). The influence of the processing parameters on the formation of iron thin films on alumina balls by mechanical coating technique. Journal of Materials Processing Technology, 212(5): 1169-1176.

Kerkar, M., Robinson, J., & Forty, A.J. (1990). In situ structural studies of the passive film on iron and iron/chromium alloys using X-ray absorption spectroscopy. Faraday Discussions Chemical Society, 89(P001): 1-20.

Kim, H.S., Ahn J.Y., Hwang K.Y., Kim, I.K., & Hwang, I. (2010). Atmospherically stable nanoscale zero-valent iron particles formed under controlled air contact: characteristics and reactivity. Environmental Science & Technology, 44(5): 1760-1766.

Kim, H.S., Kim, T., Ahn, J.Y., Hwang, K.Y., Park, J.Y., Lim T.T., & Hwang, I. (2012). Aging characteristics and reactivity of two types of nanoscale zero-valent iron particles (Fe BH and Fe H2) in nitrate reduction. Chemical Engineering Journal, 197: 16-23.

Köber, R., Hollert, H., Hornbruch, G., Jekel, M., Kamptner, A., Klaas, N., ... & Paar, H. (2014). Nanoscale zero-valent iron flakes for groundwater treatment. Environmental earth sciences, 72(9), 3339-3352.

Lapuerta, S., Moncoffre, N., Millard-Pinard, N., Jaffrézic, H., Bérerd, N., & Crusset, D. (2006). Role of proton irradiation and relative air humidity on iron corrosion. Journal of nuclear materials, 352(1), 174-181..

Li S, Yan W, & Zhang, W.X. (2009). Solvent-free production of nanoscale zero-valent iron (nZVI) with precision milling. Green Chemistry, 11(10):1618-1626.

Li, X. Q., Cao, J., & Zhang, W. X. (2008). Stoichiometry of Cr (VI) immobilization using nanoscale zerovalent iron (nZVI): a study with high-resolution X-ray photoelectron spectroscopy (HR-XPS). Industrial & Engineering Chemistry Research, 47(7), 2131-2139.

Liu, Y., & Lowry, G.V. (2006). Effect of particle age (Fe0 content) and solution pH on NZVI reactivity: H2 evolution and TCE dechlorination. Environmental Science & Technology, 40(19):6085-6090.

Liu, Y., Choi, H., Dionysiou, D., & Lowry, G.V. (2005a). Trichloroethene hydrodechlorination in water by highly disordered monometallic nanoiron. Chemistry of Materials, 17(21):5315-5322.

Liu, Y., Majetich, S.A., Tilton, R.D., Sholl, D.S., & Lowry, G.V. (2005b). TCE dechlorination rates, pathways, and efficiency of nanoscale iron particles with different properties. Environmental Science & Technology, 39(5): 1338-1345.

Liu, Z.G., Hao, X.J., Masuyama, K., Tsuchiya, K., Umemoto, M., & Hao, S.M. (2001). nanocrystal formation in a ball milled eutectoid steel. Scripta Materialia, 44(8):1775-1779.

Melitas, N., Chuffe-Moscoso, O., & Farrell, J. (2001). Kinetics of soluble chromium removal from contaminated water by zerovalent iron media: corrosion inhibition and passive oxide effects. Environmental Science & Technology, 35(19):3948-3953.

Mystrioti, C., Xenidis, A., & Papassiopi, N. (2014). Application of Iron nanoparticles Synthesized by Green Tea for the Removal of Hexavalent Chromium in Column Tests. Journal of Geoscience and Environment Protection, 2(04):28.

NANORION s.r.o. nanofer 25P (2016) http://www.nanoiron.cz/en/nanofer-25p (accessed 04.03.16).

O'Carroll, D., Sleep, B., Krol, M., Boparai, H., & Kocur, C. (2013). nanoscale Zero Valent iron and bimetallic particles for contaminated site remediation. Advances in Water Resources, 51:104-122.

Paesano Junior, A., Matsuda, C. K., Cótica, L. F., Medeiros, S. N. D., Cunha, J. B. M. D., Hallouche, B., & Silva, S. L. (2004). Structural and Mössbauer characterization of the ball-milled Fe/sub x/(Al/sub 2/O/sub 3)/sub 100-x/system. Journal of applied physics. Vol. 96, no. 5 (Sept. 2004), p. 2540-2546.Patnaik P (2003) Handbook of inorganic chemicals. New York: McGraw-Hill 28:11-12.

Rodríguez-Baracaldo, R., Benito, J. A., Cabrera, J. M., & Prado, J. M. (2007). Mechanical response of nanocrystalline steel obtained by mechanical attrition. Journal of materials science, 42(5), 1757-1764.

Smallman, R.E., & Bishop, R.J. (1999). Modern physical metallurgy and materials engineering. Butterworth-Heinemann. 323-325.

Song, H., & Carraway, E.R. (2005). Reduction of chlorinated ethanes by nanosized zero-valent iron: kinetics, pathways, and effects of reaction conditions. Environmental Science & Technology, 39(16):6237-6245.

Soukupova, J., Zboril, R., Medrik, I., Filip, J., Safarova, K., Ledl, R., ... & Cernik, M. (2015). Highly concentrated, reactive and stable dispersion of zero-valent iron nanoparticles: Direct surface modification and site application. Chemical Engineering Journal, 262, 813-822.

Tang, S. C., & Lo, I. M. (2013). Magnetic nanoparticles: essential factors for sustainable environmental applications. Water research, 47(8), 2613-2632.

Xie, Y., & Cwiertny, D. M. (2012). Influence of anionic cosolutes and pH on nanoscale zerovalent iron longevity: time scales and mechanisms of reactivity loss toward 1, 1, 1, 2-tetrachloroethane and Cr (VI). Environmental science & technology, 46(15), 8365-8373.

Yu, R. F., Chi, F. H., Cheng, W. P., & Chang, J. C. (2014). Application of pH, ORP, and DO monitoring to evaluate chromium (VI) removal from wastewater by the nanoscale zero-valent iron (nZVI) process. Chemical Engineering Journal, 255, 568-576.

5.6 Extended studies of nano Zero Valent Iron produced by milling through the addition of alumina

A promising cost-effective new milling method for nano Zero Valent Iron production was developed thanks to the addition of alumina, as previously reported. Optimising the milling parameters such as: alumina concentration, grinding media load, chemical composition and diameter is an important challenge with a key effect on nZVI throughput and properties.

After a long period of further testing, two milling configurations were selected to perform a deep characterization of the produced nZVI compared with other commercial products. On all the samples granulometry, morphology, chemical composition, sedimentation rates (suspension stability) and reactivity against: Cr (VI), TCE and PCE, was determined.

The developed particles showed excellent properties in all studied parameters, highlighting reactivity and suspension stability. Reactivity for both samples was several times higher than the commercial nZVIs also when reactivity is normalized to specific surface area and Fe(0).

In addition, the mechanism of nanoparticle formation thanks to the addition of alumina is successfully explained. Abrasion of the grinding media is the main responsible of nanoparticles production besides grinding action of alumina.

The work described in this chapter appears or it is intended to be published in:

Ribas, D., Cernik, M., Martí, V., & Benito, J. A. (2016). Improvements in nanoscale zero-valent iron production by milling through the addition of alumina. Journal of Nanoparticle Research, 18(7), 1-11.

Ribas, D., Cernik, M., Martí, V., & Benito, J. A. High performance nanoscale zero-valent iron production by milling through the addition of alumina.

5.6.1 Introduction

As discussed in the Introduction *(Chapter 1)* and in the previous section *(Chapter 5.5)*, new and reliable methods for large-scale and cost-effective nano Zero Valent Iron (nZVI) production are crucial for the success of this remediation technology, *(Müller and Nowack, 2010)*.

This chapter is the extension of the research performed in *Chapter 5.5* where an optimal milling time of 24h for the step 1 without alumina followed by a second step of 24h with alumina was found. Moreover, finest alumina concentration was restricted to be equal or over 54 $g \cdot l^{-1}$ but lower than 108 $g \cdot l^{-1}$. Once these two parameters were stablished an extensive testing with different grinding media diameters and steel compositions was completed. In addition, other alumina concentrations and grinding media load within the optimal range were tested. Finally, the two best configurations were selected and a deep characterization was performed over these samples.

The ultimate aim of this work is to unveil the properties of a new developed nZVI using alumina which would merge the advantages of the milling approach (low cost and high throughput) with the advantages of ZVI within the nanometric size (high reactivity and mobility). This study will reveal the performance of the developed nZVI in terms of granulometry, reactivity and suspension stability compared to the commercialized nZVI products. In addition, the mechanism of nanoparticle formation thanks to the addition of alumina is disclosed.

5.6.2 Materials and methods

Commercial zero-valent iron nanoparticles

Commercial particles obtained by gas reduction of iron oxides (STAR 197 and 25P) were supplied by (NANORION s.r.o.). STAR 197 nanoparticles are air stable because of a process based on building a protective oxide layer thanks to a progressive and controlled oxidation. This oxide layer reduces its reactivity but it is removable, thus in this way re-activating the particles, *(Chapter 6)*. The activation was carried out under nitrogen atmosphere in a glove box (2P, Jocomex SAS) preparing a 0.2 w/w iron to water suspension and dispersing it with an energetic mixer (MICCRA D-9 ART Prozess & Labortechnik) at 11,000 rpm following a sequence of: 60s on - 60 off - 60s on. Immediately it was stored for 36 h at 5ºC and re-suspended again and introduced into the reaction batches.

25P nanoparticles are pyrophoric and very reactive. These have been used in several full scale field remediations, i.e.: *(Soukupova et al., 2015)*. 25P was also dispersed in a 0.2 suspension into the glove box following the above protocol but without the 36h incubation and immediately used.

STAR 197 and 25P were extensively characterized in terms of size, SSA and Fe(0) content. All results were in agreement with previous literature, *(Filip et al., 2014)*.

A novel commercial milled ZVI flakes (named A01) supplied by (UVR-FIA GmbH), were also tested. The particles are produced by wet milling in MEG and supplied in this MEG slurry. It is composed mainly of iron flakes with a lateral size of several micrometres, previous characterization was in concordance with the available literature *(Köber et al., 2015)*. In order to precisely dose these product for reactivity test and characterization analysis, it was separated from MEG by absolute ethanol rinses and dried in a glovebox.

nZVI production through wet milling

The initial iron powder was Carbonyl Iron Powder, with an iron content >99% a carbon content ≤ 0.1% and a narrow size distribution with a mean particle diameter of 2.77 µm by volume (CIP-SM, BASF SE). The millings were performed in a planetary ball mill (P-5, Fritsch) using a self-designed and manufactured hermetic steel vials (AISI 1085) in order to minimize cross metallic contamination from the vials with a capacity of 250 ml *(Chapter 5.4)*. The tests were divided in two 24h steps. Firstly, the flattened iron particles or flakes were produced and secondly, these flakes were broken and smaller iron particles were obtained:

(I) In the first step, the vials were filled with 100 ml of Mono Ethylene Glycol (MEG), 1.5 g of iron powder and a grinding media load of 230 g. The vials were purged with Argon gas until a protective atmosphere was created inside the vials. The rotating speed was 400 rpm and the milling cycle consisted of 30 min of attrition followed by 30 min of stand-by periods to let the vial cool down. The effective milling time was 24 hours.

(II) The vials were opened in a glove box and irregular alumina powder (PRESI - Métallographie) with an average diameter of 5 µm was introduced. The vials were purged again and the milling was extended for 24 hours under the same conditions described in the first step. Following the milling process, the slurry was sieved at 150 µm to remove the steel grinding balls. For particle characterization, the milled particles were separated from alumina powder using a magnet as explained below.

After a long period tuning the milling process, two different samples were selected for a further characterization:

The NA 64, where a grinding media with Ø 5mm ball made from a low carbon steel AISI 1010 (0.08-0.13%) (Luis Aparicio S.L.) and an alumina a concentration of 53.6 $g \cdot l^{-1}$.

The NA 84, using a Ø 0.5mm shots composed of high carbon steel (0.80-1.20% C) (Ref. S110, Pometon) and an alumina concentration of 80.4 $g \cdot l^{-1}$.

General particle characterization

The following analysis required to isolate the particles from MEG and alumina unless otherwise indicated. It was done placing the slurry near a powerful permanent magnet (720 g of NdFeB, Grade N42) to concentrate iron particles. Supernatant was poured off and particles were re-suspended in pure ethanol. This procedure was repeated five times and its reliability was check by an elemental analysis where only traces of aluminium were found.

The particle size distribution was determined using two different techniques. By Laser Diffraction Particle Size Analysis (LD) (LS 13320, Beckman Coulter) in an absolute ethanol solution and by Size Measurements on Disc Centrifuge (CPS Disc Centrifuge, CPS Instruments). All the results obtained by this methods were expressed by particle volume. Nitrogen Brunauer-Emmett-Teller Specific Surface Area (SSA) was measured (ASAP 2020, Micromeritics), degassing was carried out for several hours at a maximum temperature of 100ºC.

For electronic microscopy characterization, samples were prepared in a glove box, keeping oxygen concentration below 5 ppm. Samples were re-suspended mixing it vigorously in absolute ethanol. The samples were transferred to microscopes over a surface of liquid nitrogen contained in box to reduce contact with oxygen. The morphology of the particles and elemental composition was

studied by Scanning Electron Microscopy (SEM) (Gemini ultra plus, Zeiss) equipped with Energy-Dispersive X-ray Spectroscopy (EDS) (X-MAX 50 mm^2, Oxford Instruments), samples were deposited and led to evaporate over cooper pins in a glove box.

Regarding particles composition, carbon content was analysed by combustion infrared analysis a (CS-200, LECO). To avoid a premature combustion the dried sample was enclosed in an aluminium foil in a glovebox. Total iron and Fe(0) determination did not require particle isolation from suspension. Total iron concentration was assessed, firstly, digesting the suspensions with 2:1 HNO_3:H_2O_2 and then analysing it by Inductively Coupled Plasma Atomic Emission Spectroscopy (ICP-AES), (Optima 3200, Perkin-Elmer). The content of Fe(0) was analysed by triplicate through the hydrogen production method *(Liu et al., 2005)* where the iron reacts with sulfuric acid added to the slurry and the volume of produced hydrogen is measured using an specific hardware (nZVI Tester, NANOIRON).

Reactivity characterization

In order to assess the reactivity of the developed particles compared with the commercial ones, dose (different nZVI concentrations) – response (contaminant depletion) tests were set in batch mode using deionized water. Hermetic bottles of 250 ml with a very small head space were used, they were vertically rotated at 2 rpm (Reax 20, Heidolph) in order to avoid particles to settle and stick on the glass. For these experiments, three harmful substances extensively reported for nZVI remediation were selected. Batches were sampled firstly isolating the sample from the particles to avoid further interferences thanks to the magnet technic, described above.

Reduction of Cr(VI) to Cr(III), with an initial Cr(VI) concentration of 50 $mg \cdot l^{-1}$ prepared from dried potassium chromate (≥99,5%, Panreac AppliChem). Tests were set, spiking each iron sample to a final concentration of: 0.1, 0.25, 0.5, 2.0, 2.5, 4.0 and 8.0 $g \cdot l^{-1}$ (total weight iron + oxides). Batches were afterwards analysed after 24h, preliminary Cr(VI) batch tests showed that Cr(VI) depletion took place mainly within the first hours. The Cr(VI) concentration was determined colorimetrically (DR3900 Spectrometer, Hach Lange) by diphenylcarbazide reaction in acid solution (US EPA method 7196A).

Trichloroethylene (TCE) and Tetrachloroethylene (PCE) reduction were tested as representatives of Chlorinated Aliphatic Hydrocarbons (CAHs) compounds. Simulating a real polluted site initial TCE (≥99.5% Sigma Aldrich) and PCE (≥99.97% Scharlab) at 2.0 $mg \cdot l^{-1}$ and 4.5 $mg \cdot l^{-1}$ were set. Each iron sample was spiked to a final iron concentration of: 0.25, 1.0, 2.0, 4.0 and 6.0 $g \cdot l^{-1}$ (total weight: iron + oxides), all the tests were duplicated together with some blanks. CAHs batches were let to react for 14 days, ensuring that the major part of the reaction has taken place. Developed nZVI particles were injected without removing the MEG or alumina as it is intended to be used in field applications. To refuse MEG or alumina side effects such as an advantageous dispersant action, controls with commercial irons at the same MEG and alumina concentrations were performed and additionally with Guar Gum (Sigma Aldrich) at 1 $g \cdot l^{-1}$. The results of these control tests with MEG and Guar Gum over the commercial particles showed an important drop in reactivity due to particle shielding that prevents pollutant interaction as stated by literature, i.e.: *(Velimirovic et al., 2015; Dong et al., 2016)*. Concerning analytes volatilization, batches were sampled at 4ºC by a 1 ml gastight micro-syringe and introduced into the bottom of a 20 ml vial containing 10 ml of cold water and immediately vial were sealed with a PTFE/rubber septum. TCE, PCE and its chlorinated transformation products (1,1-Dichloroethylene, cis-1,2-Dichloroethylene, trans-1,2-Dichloroethene and Vinyl Chloride) in aqueous phase were quantified by Head Space (HS 7694E, Agilent) - Gas Chromatography (HP6890, Hewlett Packard) – Electron Capture Detector (μECD G2397A, Agilent). The GC was equipped with a split/splitless injector operated at 1:200 ratio and the column (DB-624, Agilent) (25 m × 0.2 mm × 1.12 μm). The system was calibrated

using a volatile halocarbons mix (48001, Sigma-Aldrich) with all the analytes included. Dibromomethane (41097, Sigma-Aldrich) was used as internal standard for all the analysis.

Besides Cr(VI) and CAHs, pH and ORP were determined in all batches at the same experimental times with a multimeter (MM 41, Crison). ORP values were normalized to Standard Hydrogen Electrode (SHE) adding +209 mV (25ºC).

Stability

Suspensions stability was measured through the sedimentation rates using a (TurbiScan LAB, Quantachrome) at 1 $g \cdot l^{-1}$ in water and extracting the alumina.

5.6.3 Results and discussion

nZVI production, flake breakage and abrasion of the grinding media

The addition of micronized alumina was intended to behave as a micro grinding media. The abrasive particles would act as a small irregularities coating the grinding balls, being a pressure spots between the grinding balls and the flakes. Previous results showed that, after the addition of alumina, iron flakes from the initial iron powder disappeared *(Chapter 5.5)* meaning that the proposed mechanism was working.

However, further analysis stated that the main responsible for the nanoparticle production was the alumina abrasion onto the grinding steel balls. *Table 5.13*, shows the expected total iron concentration according to the initial iron powder supplied into the vials and the real recovered iron concentration. As can be seen, final total iron concentration was several times higher than the expected concentration in both tests (NA 64 and NA 84). These results demonstrates a large iron abrasion from the grinding media. Graphically, in *Fig. 5.33* micro alumina particles had iron residues adhered on the edges, possibly due to shear action which can explain the working mechanism.

Table 5.13 Expected and real iron concentrations in MEG at the end of the milling (expressed in $g \cdot l^{-1}$).

	NA 64	NA 84
Expected [Fe]	15.0	15.0
Real [Fe]	96.7	148.3

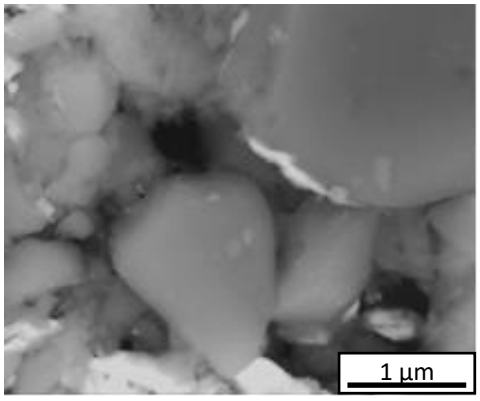

Fig. 5.33 Alumina (pale) and Iron (bright) SEM image in backscattering mode.

General particle characterization

Size characterization is a key feature since mobility and reactivity are largely dependent on particle size, *(O'Carroll et al., 2013)*. However, nano granulometry is still a challenging subject and results are strong dependent on the methods used. Therefore, particle granulometry was carefully assessed using different methods in order to have a representative view, *Table 5.14*. SEM particle counts showed an average size for NA 64 of 0.47 µm with a maximum particle diameter of 2.89 µm, for NA 84 the average particle size was 0.16 µm with a maximum particle diameter of 0.54 µm, *Table 5.14 and Fig. 5.34*. On the other hand 25P and STAR 197 were smaller and A01 was clearly within the micrometric range.

The analysis by LD for NA 64 evidences higher mean diameter sizes by volume and by number being 0.47 µm by number and 1.01 µm by volume. In the case of NA 84 were 0.39 µm by number and 0.52 µm by volume with the 100% of the material <1 µm. *Table 5.14; Fig. 5.34; Fig. 5.35.*

This discrepancy is produced because LD cannot discern agglomerated particles thus the size reported corresponds to the NP aggregates. In the same way, DCS measures also presents some degree of agglomeration, *Table 5.14*, possibly due to a mechanical separation produced by the advance of the NP through the medium. Comparing NA 64 and NA 84 results with the commercial nZVI 25P and STAR 197, *Table 5.14; Fig. 5.34; Fig. 5.35*, it can be established that the commercial nZVI had a smaller particle size. This can be easily verified in SEM images, *Fig. 5.36*. Nevertheless, 25P and STAR 197 form bigger agglomerates than NA 64 and NA 84 as stated by LD and DCS analysis, *Table 5.14*. Otherwise, A01 sample had the bigger values among all granulometric methods which is in concordance by the multi micron sized observed flakes, *Fig. 5.36*.

Comparing size measurements *(Table 5.14)* with SSA *(Table 5.15)* results, some conflicts arises. Firstly, NA 84 had the highest SSA with 29.6 $m^2 \cdot g^{-1}$ and NA 64 the third one with 20.0 $m^2 \cdot g^{-1}$ after 25P (26.1 $m^2 \cdot g^{-1}$) in spite of having higher mean particle diameter than 25P and STAR 197. This is possibly produced thanks to a great amount of defects produced by the milling action, such as: cracks, folds, wrinkles and internal voids. Other interesting detail is the pronounced difference between 25P and STAR 197, (26.1 versus 14.6 $m^2 \cdot g^{-1}$), taking into account the similar granulometry, perhaps the cause of this is the welding between aggregates during the passivation process of STAR 197. Finally, the SSA of A01 is surprisingly high 18 $m^2 \cdot g^{-1}$ taking into account their size *(Köber et al., 2014)*, this can be caused by the flake morphology which confers a high aspect ratio.

Table 5.14 Size parameters using different techniques. By V (by Volume); by No. (by number) all results are show in µm; * length measurements by SEM.

	NA 64	NA 84	25P	STAR 197	A01
SEM Mean Ø (by No.)	0.46	0.16	0.11	0.11	7.35*
Max Ø (by No.)	2.89	0.54	0.28	0.30	34.17*
LD Mean Ø (by No.)	0.47	0.39	0.83	0.75	1.68
LD mean Ø (by V)	1.01	0.52	2.35	3.31	10.9
LD % <1 µm (by V)	53.6	100	17.7	21.4	5.7
DCS Mean Ø (by V)	0.76	0.62	0.81	0.81	1.04

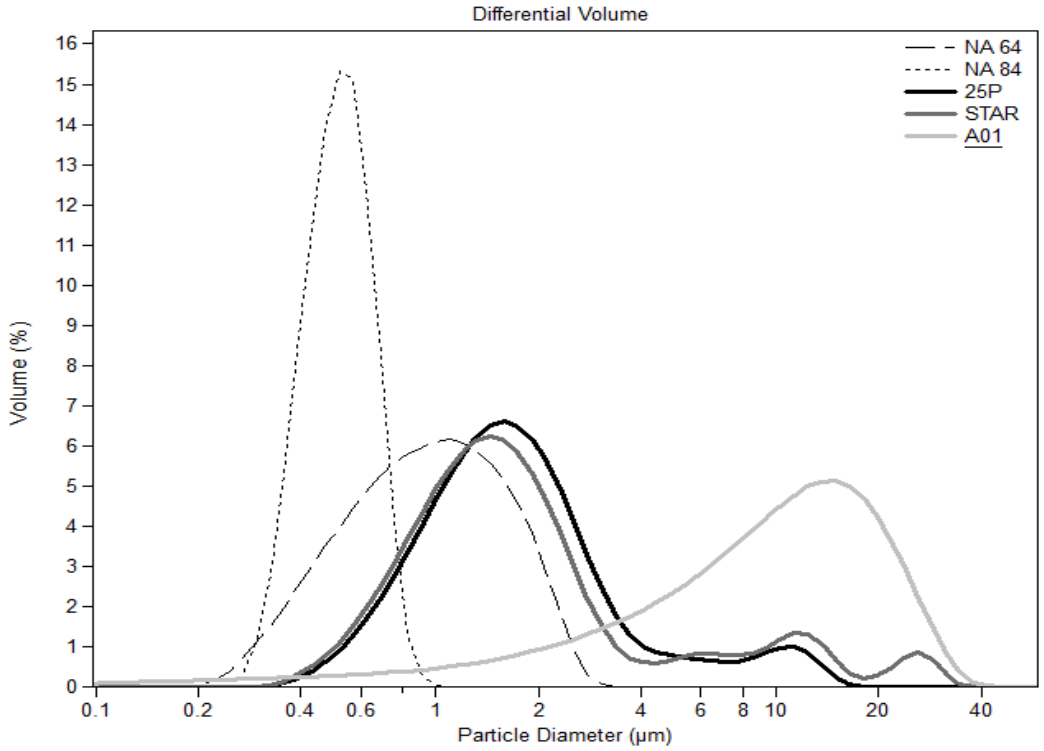

Fig. 5.34 LD particle size distribution by volume of: NA 64, NA 84, 25P, STAR 197 and A01.

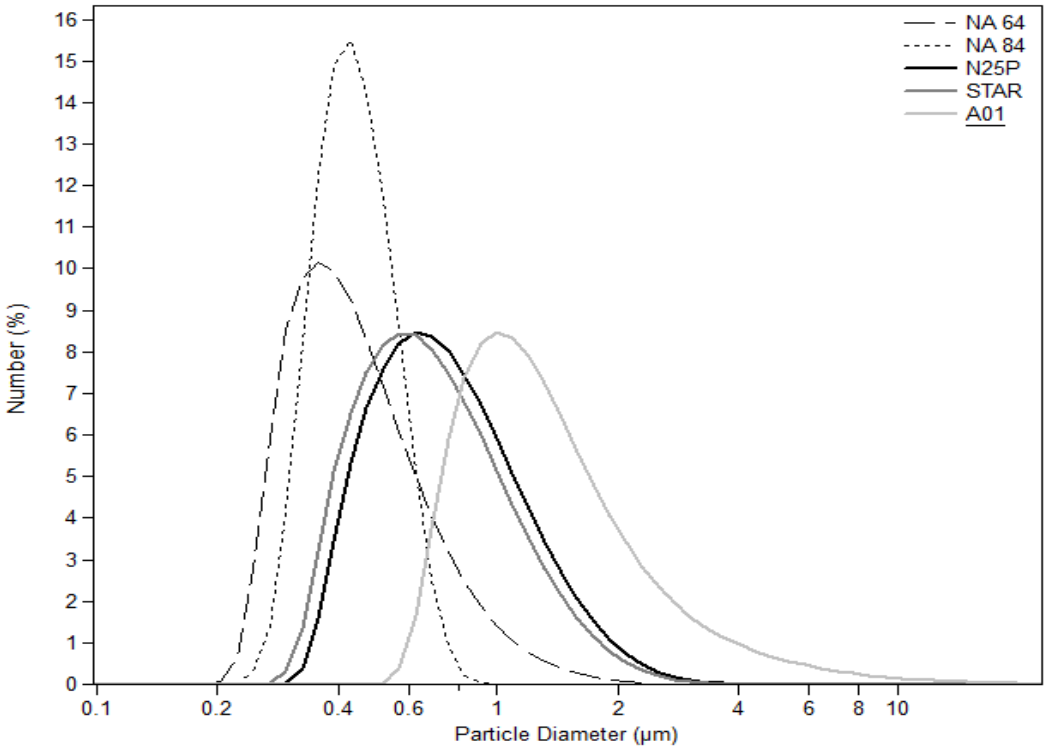

Fig. 5.35 LD particle size distribution by number of: NA 64, NA 84, 25P, STAR 197 and A01.

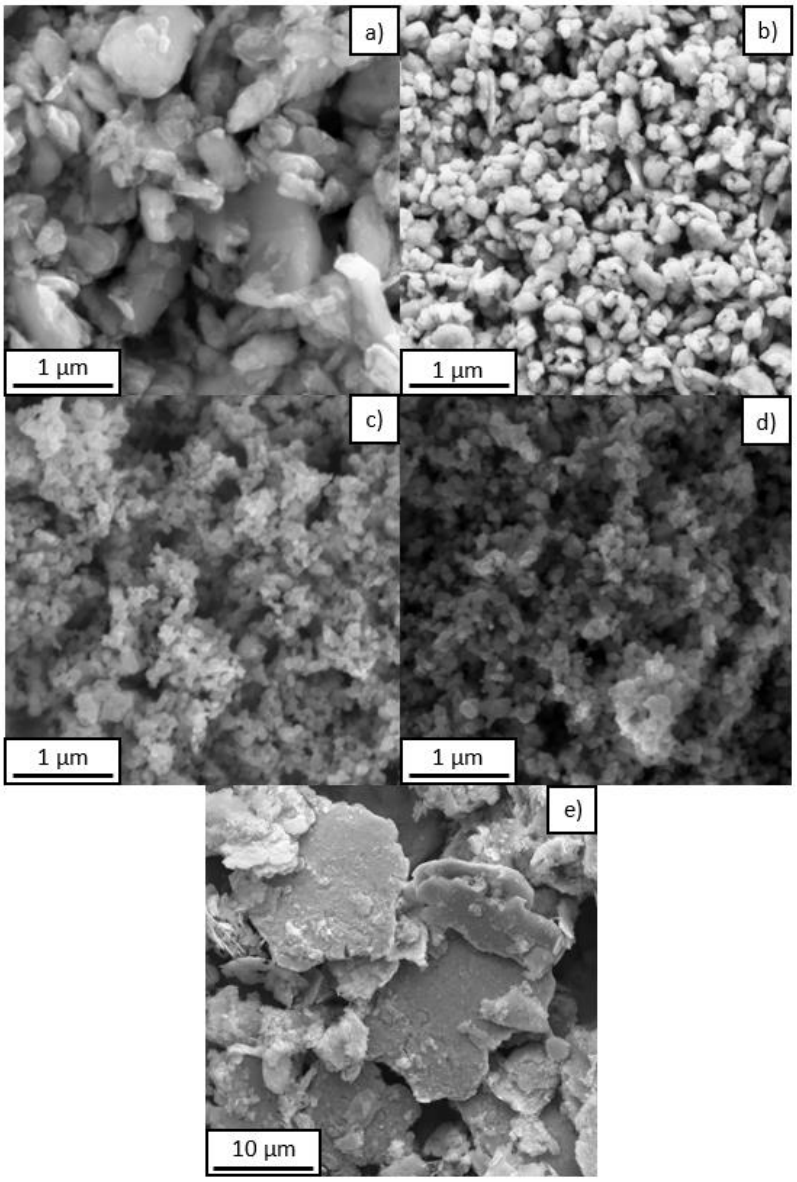

Fig. 5.36 SEM images: a) NA 64, b) NA 84, c) 25P, d) STAR 197 and e) A01. NA 64 and NA 84 nZVI isolated from the alumina particles.

Table 5.15 BET specific surface area Results are expressed in $m^2 \cdot g^{-1}$. **(Köber et al., 2014)*.

	NA 64	NA 84	25P	STAR 197	A01
BET	20.0 ±0.1	29.6 ±0.1	26.1 ±0.1	14.6 ±0.1	18 *

Chemical and Reactivity characterization

The relative content of Fe(0) was analysed *(Table 5.16)* since oxidation of Fe(0) is the driving force of nZVI remediation. As can be seen, in *Table 5.16* all samples had a Fe(0) content above 70%, NA 64, NA 84, STAR 197 and A01 were similar but 25P had a superior concentration reaching a Fe(0) content of 93%. In addition carbon relative content of NA 64 and NA 84 was analysed because these particles were produced from carbon steel and it is known that carbon can interfere with the reactivity of organic pollutants due to adsorption *(Velimirovic et al., 2013)*. As show in *Table 5.16* an important concentration of carbon was present in both samples. NA 84 had a higher concentration with a 2.69% C this is in agreement with the high carbon steel used whereas for NA

64 with a 2.01% C a low carbon steel (AISI 1010) was chosen. The carbon content of NA 64 and in some degree the content of the NA 84 cannot be explained by their steel composition alone (0.1% C for AISI 1010 and 0.80-1.20% C for the high carbon steel) or by a cross transference from the vial (0.45% C AISI 1045). It can be hypothesized that some MEG was trapped inside the particles due to the successive plastic deformations during the milling. It is doubtful that this trapped carbon could act as an adsorber.

Table 5.16 Relative Fe(0) and C content of the iron particles. Results are expressed in weight percentages.

	NA 64	NA 84	25P	STAR 197	A01
Fe(0)	78 ±1	74 ±1	93 ±1	78 ±1	74 ±1
C %	2.10	2.69	---	---	---

The Cr(VI) removal capacity *(Fig. 5.37 and Table 5.17)* of NA 64 and NA 84 was very high compared with the other tested particles. The superior removal capacity of NA 64 and NA 84 is maintained when it is normalized to SSA and Fe(0) whereas 25P, STAR 197 and A01 equalized they performances *(Table 5.17)* meaning that for example: composition, crystallographic or surface factor is playing a role in this improvement further than the particle size effect. As discussed in *(Chapter 5.5)*. Blanks with MEG alone did not show any Cr (VI) depletion (not plot on *Fig. 5.37*).

Comparing the normalized reactivity by SSA and Fe(0) against Cr (VI) of the particles: NA 84 (-1.41 mg Cr(VI)·g $Fe(0)^{-1}\cdot m^{-2}$) with M48h-Al2O3 (-3.70 mg Cr(VI)·g $Fe(0)^{-1}\cdot m^{-2}$) from *(Chapter 5.6)* it can be seen that the latter had a much superior performance. Since the grinding media and the initial iron powder had a very similar chemical composition and also the milling conditions were very similar at the moment a satisfactory explanation for this discrepancy cannot be found.

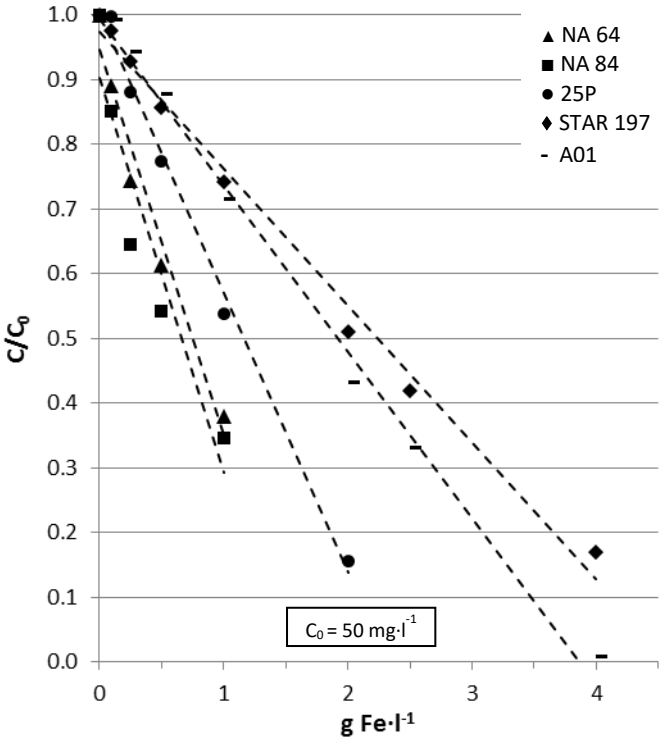

Fig. 5.37 Depletion curves of Cr(VI) for the produced nanoparticles NA 64, NA 84 and the commercial reference irons 25P, STAR 197 and A01.

Table 5.17 Slope, R^2 of regressions from Cr(VI) tests and removal capacity by weight and SSA.

	$S = \frac{\Delta\, c/c_0}{\Delta\, [Fe]}$	R^2	Cr(VI) removal capacity	Cr(VI) removal capacity by SSA and Fe(0)
			mg Cr(VI)·g Fe^{-1}	mg Cr(VI)·g $Fe(0)^{-1}$·m^{-2}
NA 64	-0.596	0.97	-30.10	-1.93
NA 84	-0.611	0.90	-30.86	-1.41
25P	-0.432	0.99	-20.39	-0.84
STAR 197	-0.212	0.99	-10.00	-0.88
A01	-0.257	0.99	-11.75	-0.88

The results of the reactivity tests with chlorinated compounds (TCE and PCE) are shown in *Fig. 5.38 and Table 5.18; 5.19*. The observed performances were in accordance with the above presented reduction performances for Cr(VI), the most reactive particles by weight and normalized by SSA and Fe(0) were NA 84 and NA 64. In addition, NA 84 TCE and PCE elimination performance was much higher than NA 64, contrasting to Cr(VI) reduction where the difference by weigh was narrower and normalized by SSA and Fe(0) NA 64 exceeded NA 84. Dechlorinating products (1,1-Dichloroethylene, cis-1,2-Dichloroethylene, trans-1,2-Dichloroethene and Vinyl Chloride) were under the quantification level in all samples (25 µg·l^{-1}), this is in agreement with literature where it is stated that β-elimination prevails over α-elimination because of being 10-100 times faster *(Hara et al., 2005)*.

The reactivity of NA 64 and NA 84 against TCE and PCE (easily adsorbable) compared with to the similar results with Cr(VI) (non adsorbable) can confirm that the role of carbon content if present was secondary.

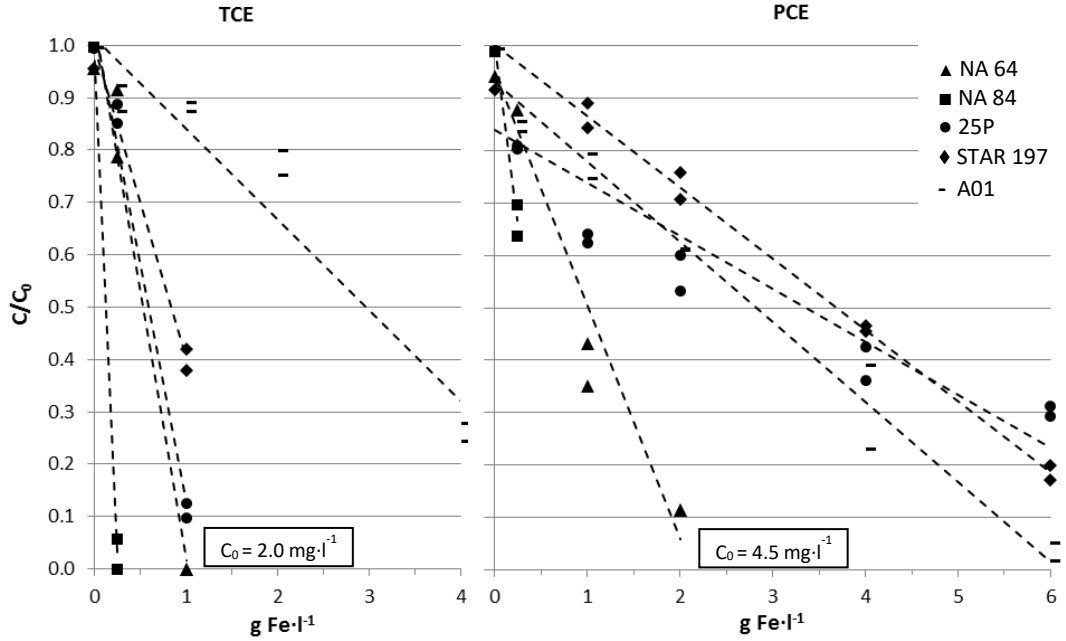

Fig. 5.38 Depletion curves of CAH for the produced nanoparticles NA 64, NA 84 and the commercial reference irons 25P, STAR 197 and A01.

These experiments stated that the developed particles were effective removing a wide range of different pollutants and in all the present cases (Cr (VI), TCE and PCE) performed better than all commercial tested products.

Table 5.18 Slope, R^2 of regressions from TCE tests and removal capacity by weight and SSA.

	$S = \frac{\Delta\, c/c_0}{\Delta\, [Fe]}$	R^2	TCE removal capacity	TCE removal capacity by SSA and Fe(0)
			mg TCE·g Fe^{-1}	mg TCE·g Fe^{-1}·m^{-2}
NA 64	-1.031	0.98	-2.55	-0.13
NA 84	-3.884	1.00	-11.76	-0.40
25P	-0.917	0.99	-2.20	-0.08
STAR 197	-0.600	0.99	-1.47	-0.10
A01	-0.174	0.93	-0.56	-0.03

Table 5.19 Slope, R^2 of regressions from PCE tests and removal capacity by weight and SSA.

	$S = \frac{\Delta\, c/c_0}{\Delta\, [Fe]}$	R^2	PCE removal capacity	PCE removal capacity by SSA and Fe(0)
			mg TCE·g Fe^{-1}	mg TCE·g Fe^{-1}·m^{-2}
NA 64	-0.446	0.95	-2.26	-0.11
NA 84	-1.331	0.98	-8.25	-0.28
25P	-0.101	0.85	-0.54	-0.02
STAR 197	-0.136	0.98	-0.62	-0.04
A01	-0.153	0.98	-1.04	-0.06

Stability

Sedimentation rates showed that milled particles had a much higher resistance to settle comparing to STAR 197 and even further with the milled micro particles A01, *Table 5.20*. A01 sedimentation rate could be explained due to the superior particle diameter. There is not a straightforward explanation for these good results, but it is preliminary hypothesized that can be caused by:

(I) Reduced magnetic susceptibility due to the high carbon content of the NA 64 and NA 84 which avoids agglomeration *(see Chapter 7.2)*.

(II) Some residual interference from the alumina although the analysis were performed after the alumina separation process.

Table 5.20 Sedimentation Rates (SR) results expressed in mm·h^{-1}.

	NA 64	NA 84	25P	STAR 197	A01
SR	5.64	1.39	-	42-89[1]	1116[2]

[1] Kindly provided by Dr. Micic Batka, V (University of Vienna), [2] *(Velimirovic et al., 2015)*.

5.6.4 Conclusions

- Abrasion is the main responsible mechanism of a new high throughput nZVI manufacture method by milling thanks to the addition of micronized alumina. Although, flake breakage of the initial iron powder due to the mechanical action of alumina is also produced.

- The produced particles had an excellent reactivity against chromium, TCE and PCE. being several times superior (2-5X) regarding the commercial ones. Furthermore, the Fe(0) content was fairly good. When smaller grinding media was used (NA 84) the particles had the highest specific surface area and granulometry was within nanoscale with a very narrow distribution. In addition, if the agglomeration of the commercial particles is taken into account, the results are then much superior.

- Stability of the new particles was much higher than the commercial ones, further research to know the reasons is required. These results points out to a very promising mobility.

5.6.5 References

Dong, H., He, Q., Zeng, G., Tang, L., Zhang, C., Xie, Y., ... & Wu, Y. (2016). Chromate removal by surface-modified nanoscale zero-valent iron: Effect of different surface coatings and water chemistry. Journal of Colloid and Interface Science, 471, 7-13.

Filip, J., Karlický, F., Marušák, Z., Lazar, P., Černík, M., Otyepka, M., & Zbořil, R. (2014). Anaerobic reaction of nanoscale zerovalent iron with water: mechanism and kinetics. The Journal of Physical Chemistry C, 118(25), 13817-13825.

Hara, J., Ito, H., Suto, K., Inoue, C., & Chida, T. (2005). Kinetics of trichloroethene dechlorination with iron powder. Water Research, 39(6), 1165-1173.

Köber, R., Hollert, H., Hornbruch, G., Jekel, M., Kamptner, A., Klaas, N., ... & Braun, J. (2014). Nanoscale zero-valent iron flakes for groundwater treatment. Environmental Earth Sciences, 72(9), 3339-3352.

Liu, Y., Choi, H., Dionysiou, D., & Lowry, G. V. (2005). Trichloroethene hydrodechlorination in water by highly disordered monometallic nanoiron. Chemistry of Materials, 17(21), 5315-5322.

Müller, N. C., & Nowack, B. (2010). Nano zero valent iron—The solution for water and soil remediation. Report of the ObservatoryNANO, 1-34.

O'Carroll, D., Sleep, B., Krol, M., Boparai, H., & Kocur, C. (2013). Nanoscale zero valent iron and bimetallic particles for contaminated site remediation. Advances in Water Resources, 51, 104-122.

Soukupova, J., Zboril, R., Medrik, I., Filip, J., Safarova, K., Ledl, R., ... & Cernik, M. (2015). Highly concentrated, reactive and stable dispersion of zero-valent iron nanoparticles: Direct surface modification and site application. Chemical Engineering Journal, 262, 813-822.

Velimirovic, M., Larsson, P. O., Simons, Q., & Bastiaens, L. (2013). Impact of carbon, oxygen and sulfur content of microscale zerovalent iron particles on its reactivity towards chlorinated aliphatic hydrocarbons. Chemosphere, 93(9), 2040-2045.

Velimirovic, M., Schmid, D., Wagner, S., Micić, V., von der Kammer, F., & Hofmann, T. (2016). Agar agar-stabilized milled zerovalent iron particles for in situ groundwater remediation. Science of The Total Environment, 563, 713-723.

6 Oxide surface characterization and activation of air stable nano Zero Valent Iron

In this chapter the surface of a passivated (air stable, meaning non-pyrophoric) nano Zero Valent Iron (nZVI) is extensively characterized regarding composition and structure. The ultimate objective is to develop a method to depassivate the air stable nZVI once in the field to improve its reactivity.

Besides depassivating procedure, the correlation of the oxide layer thickness with a certain reactivity drop allows to advise to the manufacturers an optimum passivating layer thickness limiting the effect on reactivity.

6.1 Activation process of air stable nano Zero Valent Iron particles

nano Zero Valent Iron (nZVI) represents a promising material for subsurface water remediation technology. However, dry, bare nZVI particles are highly reactive, being pyrophoric when they are in contact with air. The current trends of nZVI manufacturing lead to the surface passivation of dry nZVI particles with a thin oxide layer, which entails a decrease in their reactivity.

In this work an activation procedure tries to recover the reactivity of air-stable nZVI particles is presented. The method consists of exposing nZVI to water for 36 hours just before the reaction with the pollutants. To assess the increase in nZVI reactivity with the activation procedure three types of nZVI particles with different oxide shell thicknesses have been tested for Cr(VI) removal. The two types of air-stable nZVI particles with an oxide shell thickness of around 3.4 and 6.5 nm increased their reactivity by a factor of 4.7 and 3.4 after activation, respectively. However, the pyrophoric nZVI particles displayed no significant improvement in reactivity.

The improvement in reactivity is related mainly to the degradation of the oxide shell, which enhances electron transfer and leads secondarily to an increase in the specific surface area of the nZVI after the activation process. In order to validate the activation process, additional tests with selected chlorinated compounds demonstrated an increase in the degradation rate by activated nZVI particles.

The work described in this chapter is intended to be published as:

Ribas, D., Černík, M., Benito, J., Filip, J. & and Marti, V. (). Activation process of air stable nanoscale zero-valent iron particles.

6.1.1 Introduction

nano Zero Valent Iron (nZVI) particles have been extensively studied and used to degrade a wide range of contaminants, such as: chlorinated organic compounds (e.g.: Tetrachloroethylene, Trichloroethylene, Trichloroethane, 1,2-Dichloroethylene, Vinyl Chloride, γ-Hexachlorocyclohexane), and nitroaromatic compounds (e.g.: Nitrobenzene, 2,4,6-Trinitrotoluene) *(Fu et al., 2014)*. Besides organic (halogenated) compounds, nZVI can reduce and/or immobilize harmful metals and metalloids like: Ag, Ba, Cd, Co, Cr, Cu, Hg, Ni, Pb, Pd, U and Zn *(O'Caroll et al., 2013; Almeelbi and Bezbaruah, 2012)* and other ions: PO_4^{3-} NO_3^-, NO_2^- *(Lin et al., 2008)*. Depending on the nature of the contaminant, there are many proposed mechanisms and pathways of iron action: reduction, adsorption, reduction and adsorption, adsorption and precipitation or oxidation *(Tang and Lo, 2013; Ji, 2014)*. It seems clear that the chemical energy is mandatorily supplied by iron corrosion *(Crane and Scott, 2012)*, *Eq. 6.1 and 6.2.*

$$2Fe^0_{(s)} + 2H_2O \rightarrow 2Fe^{2+}{}_{(aq)} + H_{2\,(g)} + 2OH^-_{(aq)} \quad E^0 = -0.39\,V \qquad \textbf{Eq. 6.1}$$

$$2Fe^{2+}_{(s)} + 2H_2O \rightarrow 2Fe^{3+}{}_{(aq)} + H_{2\,(g)} + 2OH^-_{(aq)} \quad E^0 = -1.60\,V \qquad \textbf{Eq. 6.2}$$

One of the most important features of nZVI is its high specific surface area, boosting its reactivity by several orders of magnitude compared to micrometric ZVI, which results in faster degradation rates of pollutants *(Zhang, 2003).* It is geometrically demonstrable that particles with a *d* of 0.5 mm and 50 nm have a specific surface area of 1.5 and 15,250 $m^2 \cdot kg^{-1}$, respectively, *(Macé et al. 2006)*. The increased reactivity of nanosized ZVI presents new challenges at different levels, among which are the possible environmental toxicology and pyrophoricity *(Grieger et al., 2010)*. With regard to the second point, dry, bare nZVI particles undergo a fast but not explosive exothermic reaction when exposed to the free air-atmosphere *(Sohn et al., 2006; nano Iron s.r.o)*. This behaviour entails a handling, safety and logistic problem. Many different approaches have been adopted to desensitize nZVI *(Tiehm et al., 2009).* The two most common commercial methods are faced with important drawbacks:

(I) Transport in a water-slurry form could partially solve safety problems but implies an increase in shipping costs and a loss of reactivity caused by aging *(Liu and Lowry, 2006)*.

(II) Surface passivation of iron powder by the formation of an oxide shell allows storage in air and lower transportation costs but also significantly decreases the reactivity of the product.

Surface passivation is performed leaving the free atmosphere become slowly and progressively in contact with pristine particles. As a result of this process, a superficial oxide layer is generated giving long-term air stability *(Shafranovsky and Petrov, 2004; Sohn et al., 2006)*. The thickness of the oxide shell ranges from 1 to 25 nm depending on the oxidation conditions, and this thickness is nearly independent of the diameter of the nanoparticles *(Martin et al., 2008)*. The nature of this oxide shell is being extensively studied since it hinders the electron flow from the metallic iron *(Signorini et al., 2003)*. As a result, it has been reported that the increase in shell thickness negatively affects the reactivity of nZVI *(Liu et al., 2005a; Kim et al., 2010)*. Oxide shells compositions have been analysed by many authors with different results summarized in *Table 6.1*.

During the immersion of non-passivated nZVI particles into water, transformations of the particle surface are significantly slower. It has been clearly demonstrated that long-term water exposure decreases the reactivity of nZVI against a wide range of pollutants *(Liu and Lowry, 2006; Sohn et al., 2006; Liu et al., 2007; Kim et al., 2010; Xiu et al., 2010; Xie and Cwiertny, 2012; Kim et al., 2012; Woo et al., 2014)* due to the growing of the oxide/hydroxide shell, which leads to a passivation of the particles *(Filip et al. 2014)*. However, there are certain disparities about the effect on the reactivity of short immersion times. On the one hand, an increase in reactivity after 1-2 days of water immersion has been reported for carbon tetrachloride, trichloroethane and 1,1,1,2-tetrachloroethane *(Sarathy et*

al., 2008; Kim et al., 2010; Xie and Cwiertny, 2012) but other studies have shown little changes on reactivity during the first days of aging *(Liu and Lowry 2006; Liu et al., 2005b)*.

Table 6.1 Components found into air crated protective oxide shell by different authors, nanoparticles synthesis method. *Table 6.2* shows the equivalences between chemical formulas to compound names.

	FeO	Fe_3O_4	γ -Fe_2O_3	α-Fe_2O_3	?-Fe_2O_3	FeOOH	$Fe(OH)_2$	amorphous
Signorini et al., 2003[IGC]		X	X					
Kim et al., 2010[H2]	X	X	X	X				
Kim et al., 2012[BH]		X	X					
Kim et al, 2012[H2]		X						
Liu and Zhang, 2014[BH]	X	X	X			X	X	X
Ji, 2014[BH]	X	X			X			

[BH]: BoroHydride precipitation
[CBD]: Cluster Beam Deposition
[H2]: H2 iron oxides reduction
[IGC]: Inert Gas Condensation synthesis

In the cases in which an increase of reactivity was detected, different mechanisms were proposed to explain reactivity recovery:

(I) The dissolution of the anionic hydroxo species from a spontaneously-formed oxide/hydroxide shell, such as $Fe(OH)_y^{2-y}$ and $Fe(OH)_x^{3-x}$ known to be soluble and unstable in alkaline media *(Sohn et al., 2006)*. This process is supported by evidence of the formation of new iron oxide particles in the vicinity of the nZVI particles *(Sohn et al., 2006; Kim et al., 2012; Xie and Cwiertny, 2012)*.

(II) The volumetric expansion of the nZVI core and the intermediate oxides formed during corrosion, which leads the oxide layers to flake off and expose metallic iron to the contaminants *(Sarathy et al 2008; Kim et al., 2010)*. The expansion of the corrosion products is being studied due to expected clogging problems in the aquifer matrix during nZVI treatment *(Noubactep et al., 2012)*. In general, theoretical calculations for the different iron oxides formed in nZVI reactions show that the volume of oxides is 2-4 times greater than the volume of iron, which demonstrates a pronounced change in shell volume *(Lide, 2004; Cornell and Schwertmann, 2006; Schwertmann and Cornell, 2000)*. Expansion can be theoretically calculated using the molecular volume V_M according to $V_M=M/\rho$, where: M the molecular weight and ρ the specific weight. Therefore, the quotient V_{rust}/V_{Fe} provides the theoretical expansion coefficients *Table 6.2*. These calculated expansion coefficients are only approximated because the exactly composition and hydration of rust products is not well known *(Caré et al., 2008)* but demonstrates a pronounced change in shell volume.

The aim of this work is to introduce an activation process to recover the reactivity of air stable nZVI and to describe the main mechanisms of this activation. Three types of nZVI particles, differing in the oxide shell thickness, were selected and subjected to an activation process based on their aging in water in the form of a dense nZVI slurry over a short period of time. The particles were characterized by Transmission Electron Microscopy (TEM), Scanning Electron Microscopy (SEM), and X-Ray Diffraction (XRD) before and after the activation process. In addition, the specific surface area (SSA), the particle size distribution and the Fe(0) content were determined. The reduction of hexavalent chromium has been chosen as a simple method of evaluating changes in nZVI reactivity after the activation process since the reduction of Cr(VI) to trivalent chromium is a common mitigation approach in contaminated waters where nZVI is widely studied as a remedial method in this case. Additional

tests for degradation of chlorinated compounds have been included to demonstrate the ability of the nZVI activation process to be applicable also for efficient removal of organic pollutants.

Table 6.2 Major iron oxides, ρ specific weight, (Fe S) stoichiometry in oxide regarding iron, V_M molecular volume and V_{rust}/V_{Fe} volumetric expansion.

Fe species	ρ ($kg \cdot m^{-3}$)	(Fe S)·V_M ($m^3 \cdot mol^{-1}$)	V_{Rust}/V_{Fe}
α-Fe, Iron	7874 [1]	(1) · $7.09 \cdot 10^{6}$	1.00
FeO, Wüstite	5900 [2]	(1) · $1.22 \cdot 10^{-5}$	1.72
α-Fe_3O_4,Magnetite	5180 [2]	(⅓) · $4.47 \cdot 10^{-5}$	2.10
α-Fe_2O_3, Hematite	5260 [2]	(½) · $3.04 \cdot 10^{-5}$	2.14
γ-Fe_2O_3, Maghemite	4870 [2]	(½) · $3.28 \cdot 10^{-5}$	2.31
α-FeOOH, Goethite	4260 [2]	(1) · $2.09 \cdot 10^{-5}$	2.94
β-FeOOH, Akaganéite	3560 [3]	(1) · $2.50 \cdot 10^{-5}$	3.52
γ-FeOOH, Lepidocrocite	4090 [2]	(1) · $2.17 \cdot 10^{-5}$	3.06
δ'-FeOOH, Feroxyhyte	4200 [2]	(1) · $2.12 \cdot 10^{-5}$	2.98
$Fe_5HO_8 \cdot 4H_2O$, Ferrihydrite	3960 [3]	(⅕) · $1.21 \cdot 10^{-4}$	3.42
$Fe(OH)_2$, Ferrous hydroxide	3400 [1]	(1) · $2.64 \cdot 10^{-5}$	3.73
$Fe(OH)_3$, Bernalite	3320 [2]	(1) · $3.22 \cdot 10^{-5}$	4.54

[1] *(Lide, 2004);* [2] *(Cornell and Schwertmann, 2006);* [3] *(Schwertmann and Cornell, 2000).*

6.1.2 Materials and methods

Iron nanoparticles and suspensions

Iron nanoparticles with a different thickness of shielding oxide layer and Fe(0) to Fe-oxide ratio (labelled here as 25P, STAR 197 and STAR 400) were prepared according to a previously published procedure, *(Zboril et al.2012)*. These nZVI particles were obtained by the thermal reduction of Fe oxides by H_2 at high temperature. Samples STAR 197 and STAR 400 were surface-stabilized by protective oxide layers of different thicknesses. In contrast, 25P had no tailored surface modification. For this reason, 25P nZVI particles remain pyrophoric whereas both types of STAR nanoparticles are air stable.

To prepare the nZVI slurries, 20 g of nZVI particles were added to 80 ml of deionised water, so the final w/w iron to water ratio was 0.2. The non-pyrophoric iron nanoparticles (STAR 197 and 400) were dispersed with an ultra-disperser (MICCRA D-9 ART, Prozess & Labortechnik GmbH & Co. KG) at 11,000 rpm, following the sequence: 60s on – 60s off – 60s on. Suspensions of pyrophoric iron (25P) nanoparticles were prepared using a laboratory dispersing unit LD 05 (NANOIRON, s.r.o.) under a nitrogen atmosphere to prevent nZVI oxidation. The Fe(0) content was determined based on the volume of produced hydrogen gas when iron nanoparticles react with sulphuric acid added to the nZVI slurry, *(Liu et al. 2005b)*. The volume of evolved hydrogen is directly proportional to the amount of metallic iron. The presence of iron oxides has no effect on the volume of generated hydrogen, although they can slow down the rate of the reaction, *(Liu and Lowry, 2006)*.

Activation process

To enhance the reactivity of surface-passivated nZVI particles prior to their application, a simple activation procedure was investigated. The nZVI slurry was aged for a period of 36 hours in deionised water at room temperature followed by re-suspension and dilution to the final nZVI concentration. During the course of the activation process, pH and oxidation redox potential (ORP) data were logged every 2 minutes (Multi 3430, WTW GmbH). ORP values were normalized to a standard hydrogen electrode (SHE) adding +209 mV (for 25°C). The activated samples (labelled as "A" samples) were

characterized in detail by the procedure described above and compared to un-activated samples (labelled as "UA" samples), which were prepared in the same way but without the 36 hours of aging in a concentrated slurry and immediately introduced into the reaction batches.

Reactivity evaluation

Batch experiments with two types of model contaminants, Cr(VI) and Chlorinated Aliphatic Hydrocarbons (CAHs), were designed to determine the reactivity of the selected nZVI samples in the un-activated and the activated states. In the case of Cr(VI) removal, the experiments were conducted in 250 ml hermetically-closed glass bottles with an initial Cr(VI) concentration of 50 $mg \cdot l^{-1}$ prepared from dried potassium chromate (K_2CrO_4, p.a., AppliChem GmbH). To simulate the ion interference and the ionic strength of real groundwater, tap water was used with an electric conductivity of 210 $\mu S \cdot cm^{-1}$ (after leaving the tap water exposed to air overnight to eliminate the chlorine content). Seven reaction batches were prepared in the same way for each type of nZVI in both states. To initiate the experiments, a different amount of nZVI suspension was spiked into each batch to get a final concentration of 0.1, 0.25, 0.5, 2.0, 2.5, 4.0 and 8.0 $g \cdot l^{-1}$. The solutions were allowed to react for 24 h without agitation except for a vertical rotation every 60 s to avoid particles settling down or sticking to the glass walls. The batch pH was not buffered in order to simulate real conditions, consequently pH reached values of around 9 in all cases. After the 24 h reaction time, the Cr(VI) depletion was quantified using the colorimetric test EPA METHOD 7196A. ORP and pH values were also determined following the same procedures as described above. The 24 h reaction time was chosen since preliminary Cr(VI) batch tests showed that Cr(VI) depletion mainly took place within the first 2 h. Finally, it is important to note that selected batches were periodically analysed during a 2 month period.In the case of the Chlorinated Aliphatic Hydrocarbons (CAH), the batch reactors contained real polluted water from an industrial site to imitate real conditions. In this case, the experiments were performed with only one type of nZVI particles, i.e., STAR 197, in both the un-activated and activated state. The particular amount of nZVI suspension was spiked into each batch to get a final concentration of 2.9 $g \cdot l^{-1}$ of nZVI. Due to the slower degradation rates of CAH compared to Cr(VI), the batches were vertically rotated every 60 s for 10 days. After the reaction time, the presence of the different chlorinated species was determined by sampling the batch water phase and analysed by GC-MS (CP-3800 coupled to Saturn 2200 MS, Varian).

Nanoparticle characterization

The BET specific surface area (SSA) was determined from N_2 adsorption using a BET surface area and porosity analyser (ASAP 2020 Micromeritics). Degassing was carried out at a maximum temperature of 100 °C. In addition, the particle size distribution was determined by the laser diffraction technique using a particle size analyser (Beckman coulter LS 13 320) to investigate the degree of agglomeration. The particles were suspended in ethanol and sonicated for ten minutes before each measurement.

For electron microscopy characterization, samples were prepared in a glove box under a nitrogen atmosphere with air locks (2P, Jacomex), keeping the oxygen concentration below 5ppm. The samples were suspended by mixing vigorously in absolute ethanol. For the SEM studies (Gemini ultra plus, Zeiss) the samples were deposited and left to evaporate on standard SEM discs. For the TEM studies (Philips CM30, operating at 300 kV) a droplet was placed on a 300 copper mesh grid with a supporting film made of holey carbon (S147-3, Agar Scientific). Pyrophoric samples were transferred to the microscope using a liquid nitrogen flask to avoid any contact with oxygen. Detailed nZVI surface observations were performed using a High-Resolution Transmission Electron Microscopy image (HRTEM) (Titan 60-300, FEI) microscope with an X-FEG type emission gun, operating at 80 kV.

X-Ray powder diffraction (XRD) was performed on a q/q Bragg-Brentano powder diffractometer (X'Pert PRO MPD, PANalytical) using Cu-$K\alpha$ radiation. Continuous scans from 12 to 120° 2θ were collected with a steps size of 0.017° and a scan speed of $3.4 \cdot 10^{-3}$ °·min^{-1}.

6.1.3 Results and Discussion

Characterization of the initial nanoparticles.

The as-prepared particles were initially characterized prior to the activation process. The morphology and particle size obtained by FE-SEM for the three types of un-activated nanoparticles are shown in *Fig. 6.1*. In all cases, the particles had a roughly spherical morphology with a particle size of between 50 and 150 nm. The particle size distribution in water solution carried out by laser diffraction techniques showed the presence of aggregates with a size ranging from hundreds of nanometers to some microns, especially in the case of the UA STAR 197 and UA STAR 400 samples. The specific surface area (BET) was 26.1 ± 0.1 $m^2 \cdot g^{-1}$ for UA 25P nanoparticles, whereas for the surface stabilized samples (UA STAR 197 and UA STAR 400), the surface area decreased to 14.6 ± 0.1 $m^2 \cdot g^{-1}$ and 16.1 ± 0.1 $m^2 \cdot g^{-1}$, respectively. The observed decrease in the specific surface area of UA STAR 197 and UA STAR 400 nanoparticles together with the increase in the size of the aggregates could be related to an increase in the level of sintering during the surface passivation process. During the passivation process, the growth of the protective oxide layer may cause intergrowth of individual nanoparticles promoting a significant increase in the size of the agglomerates. A decrease in the specific surface area for shell-modified nZVI particles obtained by similar methods has been already observed by *(Kim et al. 2010)*.

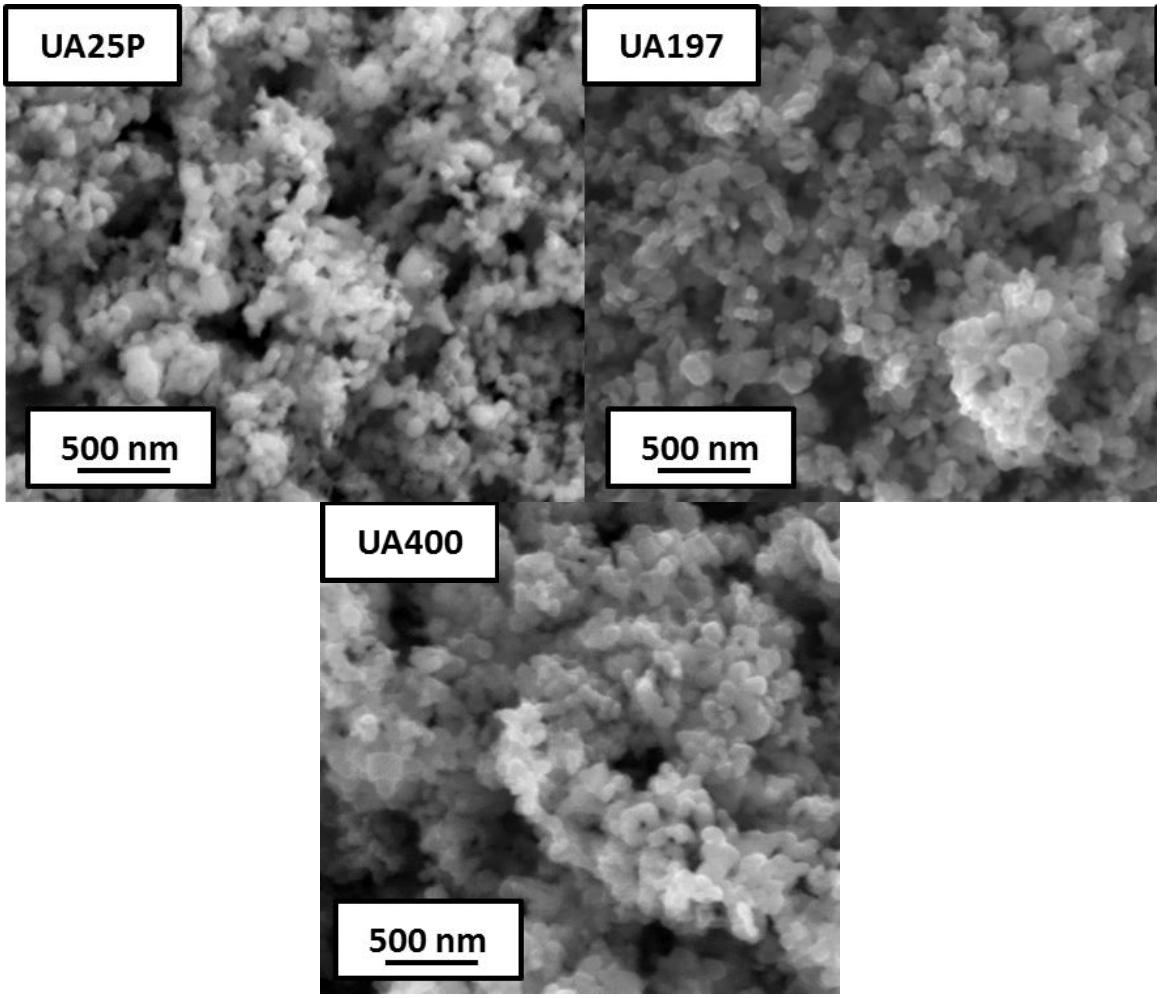

Fig. 6.1 FE-SEM image of the as-received particles in the un-activated state.

Activation Process

Fig. 6.2, shows the evolution of pH and ORP for the three types of suspensions during the activation process: the pH of all the solutions increased up to the value of around 10 in all cases. This behaviour is consistent with the expected iron corrosion in water according to *Eq. 6.1 and 6.2* or in the presence of oxygen *(O'Carroll et al., 2013; Zhang, 2009)* and with previously described conditions of high concentrated slurries *(Liu and Lowry, 2006)*. On the other hand, the ORP decreased in all cases to below -500 mV. However, there are clear differences in the evolution rates. The UA 25P nanoparticles caused a faster decrease n ORP than the STAR nanoparticles (pH and ORP were stabilized in less than 4 hours). In the UA STAR 197 suspension, the pH and ORP values reached constant values after 12 hours, and the UA STAR 400 suspension caused even slower changes in pH and ORP as it reached stabile values after 36 hours. These differences in the evolution rates are proportional to the degree of shielding of each type of particle.

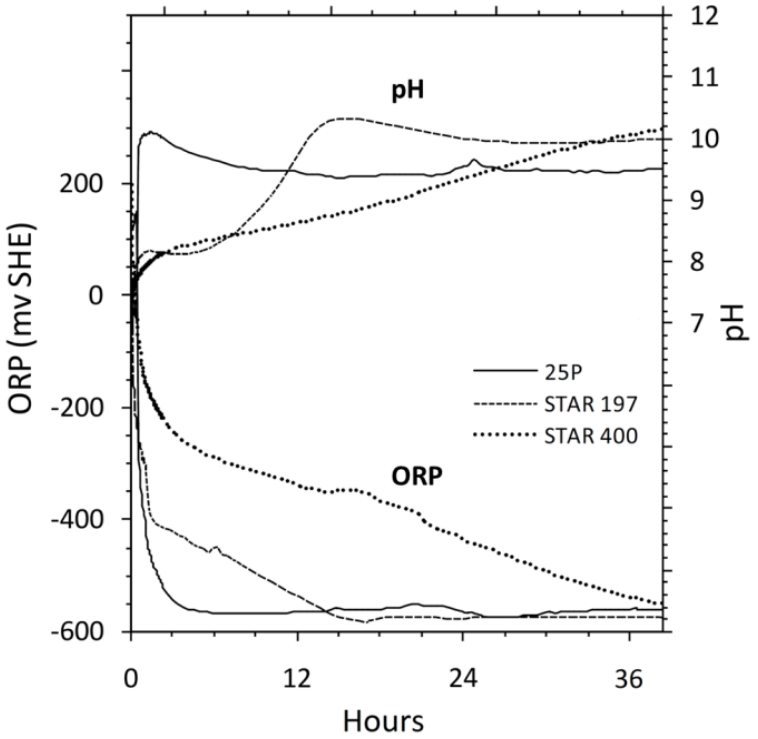

Fig. 6.2 pH and ORP development during the activation process.

Characterization of un-activated and activated particles

Fig. 6.3, presents the TEM images of the three types of nanoparticles in the un-activated and the activated states. The average thickness of the oxide layers, as determined from TEM images, is presented in *Table 6.3*. For UA 25P nanoparticles, a very thin oxide layer (around 1.8 nm) was observed, which is typical for iron nanoparticles without shell modification *(Kim et al, 2012; Martin et al., 2008)*. The shell-modified nanoparticles showed a uniform layer with a thickness of 3.4 nm and 6.5 nm for UA STAR 197 and UA STAR 400, respectively. For the UA 25P nanoparticles the absence of a protective shell promotes the rapid reaction of iron with water or dissolved oxygen. Moreover, UA 25P showed a high specific surface area. These facts explain the fast reaction of UA 25P with water during the activation process as shown in *Fig. 6.2*. On the contrary, the shell-modified species showed slower rates than the UA25P nanoparticles. As it has been described elsewhere *(Sohn et al, 2006; Kim et al. 2010)*, the presence of an oxide layer of about 5 nm thick implies a clear decrease in reactivity. For UA STAR 197, the stabilization of pH and ORP was clearly delayed with respect to UA 25P, but for UA STAR 400 with an even thicker layer, the reaction with water and oxygen was much slower. Unlike previously performed experiments *(Kim et al. 2010)*, in this case the specific surface area was very similar between both shell modified species and the changes in reactivity seem not to be influenced by this factor.

The activated A 25P nanoparticles displayed only slight changes compared to their un-activated counterparts, *Fig. 6.3*. However, substantial changes in the oxide shell morphology were found for the A STAR 197 nanoparticles. The surface reveals numerous irregularities caused by partial dissolution of the compact oxide shell. The detail of shell morphology for STAR 197 nanoparticles before and after activation process is shown in *Fig. 6.4*. This shell detachment was already observed after one-day reaction with deionized water *(Sarathy et al, 2008; Kim et al. 2010)*. There was very little evidence of oxides forming during water aging. Some acicular crystals were observed especially in the case of the A STAR 197 sample, which were previously identified as lepidocrocite *(Liu and Zhang, 2014)* or goethite *(Kim et al 2012)*, similarly to hexagonal plates of ferrous hydroxide *(Filip et al. 2014)* or secondary magnetite/maghemite *(Sohn et al. 2006, Kim et al. 2012)*. Another important aspect is that unlike the UA STAR 197 nanoparticles, the activated A STAR 197 nanoparticles showed pyrophoricity when dried in an argon atmosphere and subsequently exposed to air. This is clear evidence of the successful recovery of nZVI reactivity after the dissolution of the passivating oxide layer. On the other hand, after following the same treatment, the A STAR 400 nanoparticles still contained a uniform shell with just a few discontinuities, but with a clear reduction in the oxide-shell thickness. However, this change was not sufficient to cause pyrophoricity of the dried A STAR 400 samples when exposed to air.

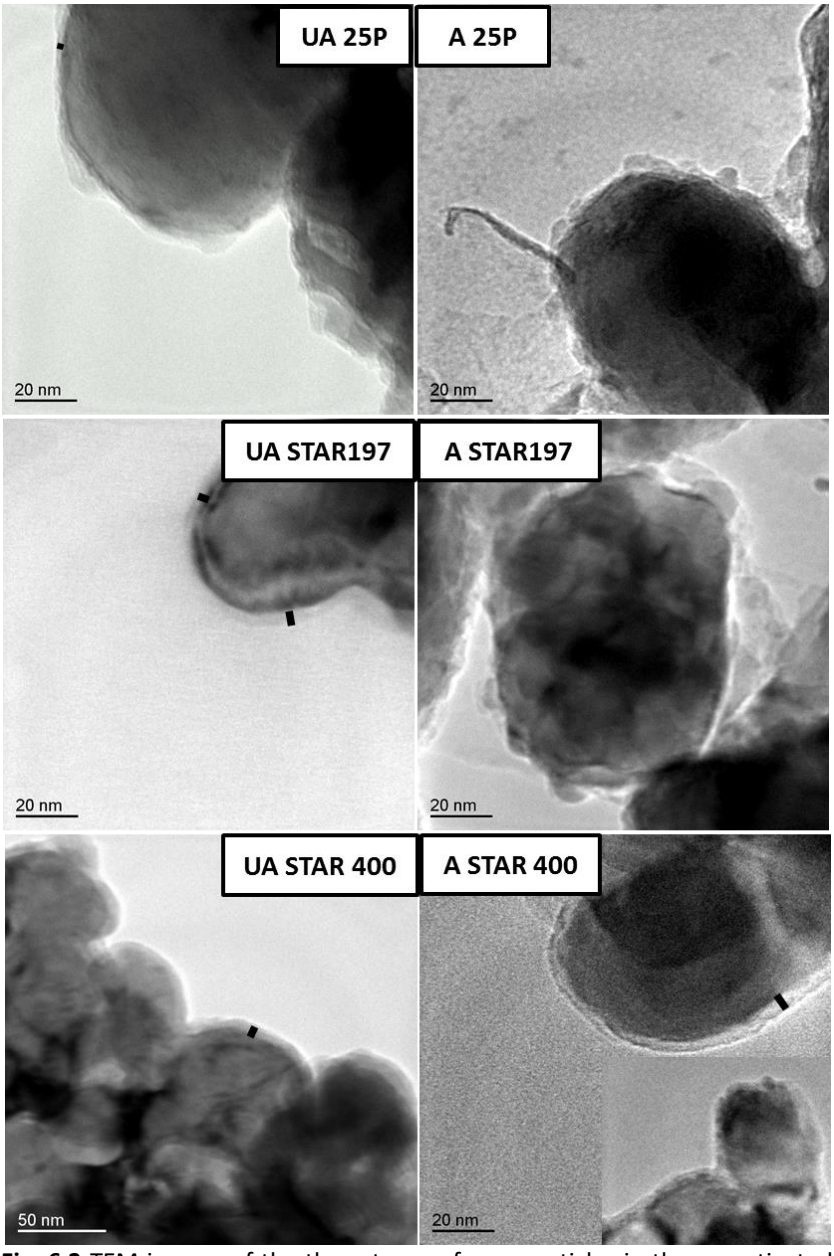

Fig. 6.3 TEM images of the three types of nanoparticles in the un-activated and activated states. The black bars show the thickness of the oxide layer.

Table 6.3 Mean thickness of the oxide layer in nm, 95% confidence interval, (n) = number of measurements.

	25P	STAR 197	STAR 400
Un-activated	1.8 ±1.0 (10)	3.4 ±1.5 (12)	6.5 ±1.2 (12)
Activated	Discontinuous	Discontinuous	4.4 ±1.3 (12)

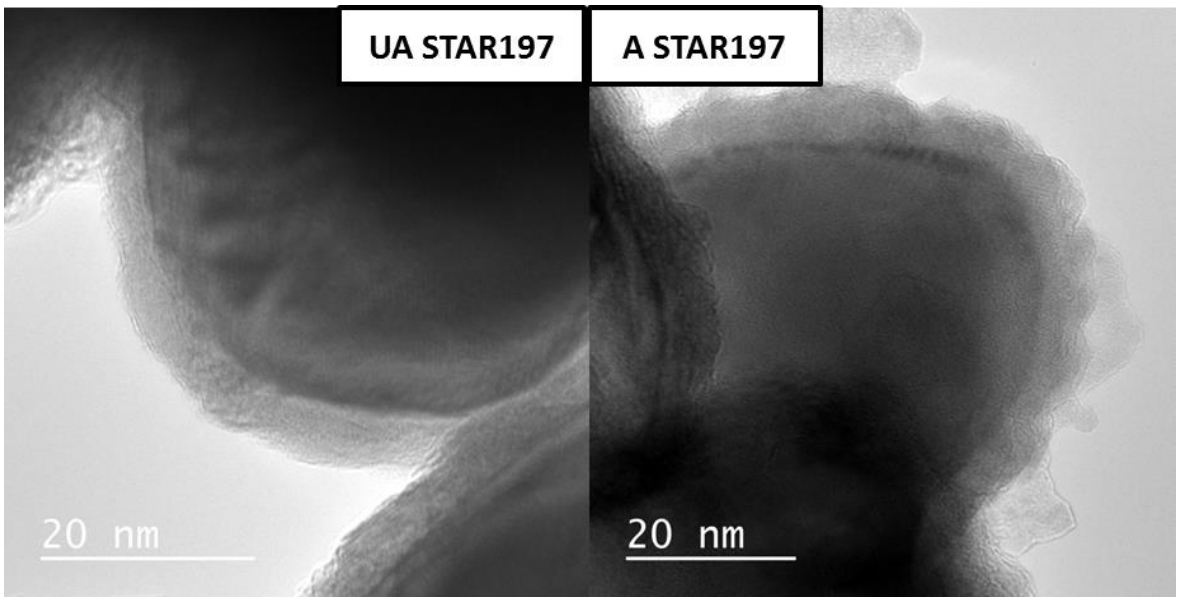

Fig. 6.4 Detail of the surface layer on STAR 197 nanoparticles before (UA STAR 197) and after activation (A STAR 197).

The changes in the Fe(0) content during the activation process are summarized in *Table 6.4* demonstrating the minimal effect of the activation process on the content of metallic iron. This is consistent with the negligible presence of secondary oxides/hydroxides observed by TEM. Similarly, highly concentrated slurries (300 ZVI $g \cdot l^{-1}$) with or without a very low stirring speed together with a high pH have shown similar behaviour *(Sarathy, 2008; Liu and Lowry, 2006)*. In contrast, if the slurry is diluted, buffered to low pH, with significant stirring speed or with a significant presence of oxygen, the loss of Fe(0) is much more dramatic at similar aging times *(Kim et al., 2010; Xie and Cwiertny, 2012; Liu and Zhang 2014; Liu et al., 2015)*. These results thus indicate that the nZVI core (i.e., metallic iron) is not significantly affected during the activation process.

Table 6.4 Relative Fe(0) content of the selected iron nanoparticles, before and after activation. Results are expressed in weight percentages.

	25P	STAR 197	STAR 400
Un-activated	87 ±1	78 ±1	57 ±1
Activated	86 ±1	77 ±1	57 ±1

Another important aspect is the change in specific surface area (SSA) during the activation process. The results of BET measurements for the three kinds of nanoparticles in both states are presented in *Table 6.5*. It is known that water aging under aerobic conditions, as in the present case, leads to an increase in the SSA *(Woo et al., 2014)* and that the SSA could increase during interaction with pollutants *(Sohn et al., 2006; Huang et al., 2013)*. It must be taken into account that nZVI obtained by the gas reduction process has a different reaction mechanism to nZVI particles obtained by borohydride reduction and a smaller increase in SSA would be expected *(Kim et al, 2012; Liu et al, 2015)*. As can be seen, the SSA increased with the activation process in all cases: this increase was small for A 25P, in accordance with a previous study on similarly-prepared nZVI particles *(Sarathy et al. 2008)*. This

increase could be attributed to partial iron dissolution followed by overgrowing of nZVI particles by sheet-like iron hydroxides *(Woo et al, 2014; Filip et al. 2014)*. On the other hand, changes in the SSA are much more pronounced in the case of the STAR 197 nanoparticles (see *Table 6.5*) due to the high degree of detachment of the oxide shell. In the case of A STAR 400 the increase was less significant, reflecting less incidences of oxide shell loosening. Another mechanism the can explain an increase in the SSA during the activation process of surface-passivated nZVI particles could be the partial breakdown of aggregates accompanying the dissolution of the oxide shell.

Table 6.5 BET specific surface area of nZVI particles before and after activation. Results are expressed in $m^2 \cdot g^{-1}$.

	SSA ($m^2 \cdot g^{-1}$)
UA 400	16.1 ±0.1
A 400	23.4 ±0.1
UA 197	14.6 ±0.1
A 197	30.0 ±0.1
UA 25P	26.1 ±0.1
A 25P	28.7 ±0.1

The XRD patterns measured on the nanoparticles in the un-activated and activated state are shown in *Fig. 6.5.* No significant differences were found between nanoparticles in the un-activated and activated states. This is in line with the fact that very little changes were observed in the Fe(0) content after the activation process. Along with dominant α-Fe peaks, the presence of magnetite (Fe_3O_4) and Würstite (FeO) was also confirmed. The highest oxide content was found in the un-activated and activated STAR 400 nanoparticles, where the relative content was 27% for magnetite and 15% for Wüstite based on Rietveld refinement. Both iron oxide phases have been previously identified as possible oxides forming the shell on nZVI prepared by thermal reduction of iron oxide precursors in hydrogen *(Kim et al., 2010; Liu et al., 2014; Ji, 2014)*. Although XRD patterns of magnetite and maghemite (γ-Fe_2O_3) are very similar *(Kim et al., 2010)*, the absence of any secondary peaks of maghemite excludes its presence, *(Sohn et al., 2006)*.

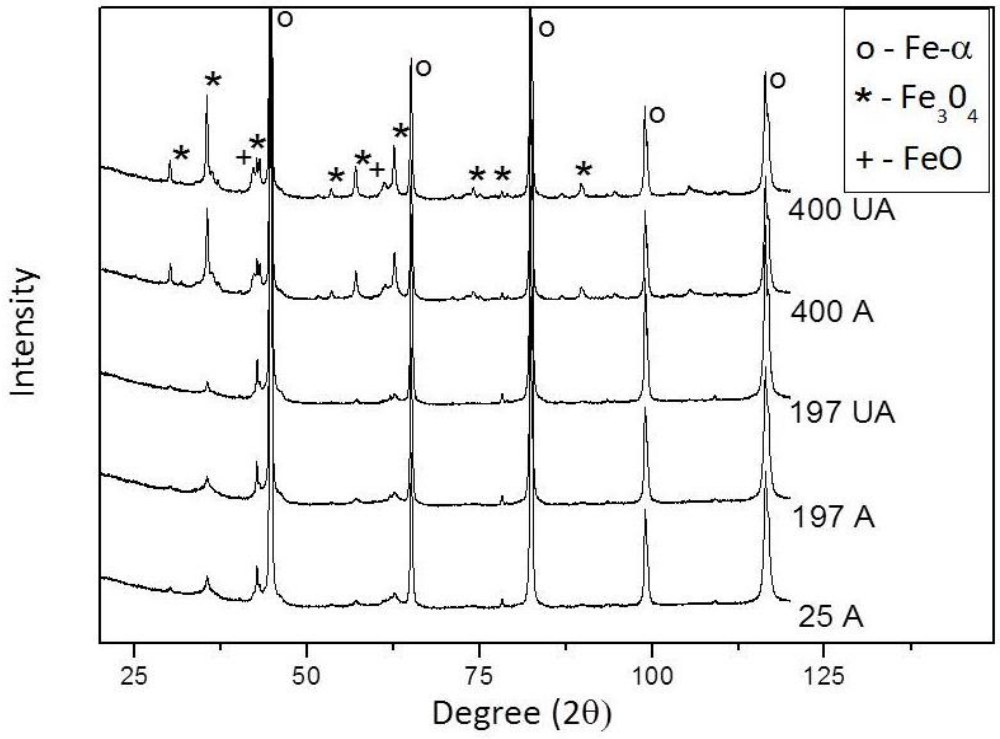

Fig. 6.5 XRD patterns of: UA (Un-Activated) and A (Activated) samples.

Evaluation of particle reactivity

Reduction of Cr(VI)

The concentration trends of Cr(VI) as a function of the nZVI concentration and the calculated Cr(VI) removal capacities as mg of Cr(VI) removed by g of Fe(0) for the studied nanoparticles are shown in *Fig. 6.6 and Table 6.6*, respectively. Evidently, the Cr(VI) removal capacity varied with the type of nZVI and with the activation state. The highest reaction rate corresponds to the 25P nanoparticles, with negligible differences between the un-activated and activated particles (i.e., higher for the A 25P nanoparticles with a removal capacity of 25.8 mg Cr(VI)/gFe(0)). Even higher reaction rates have been reported in the literature for experiments where the batches were stirred *(Yu et al., 2014)*, the solutions were buffered to a lower pH *(Xie and Cwiertny, 2012; Petala et al., 2013)* or the nZVI were obtained by the borohydride reduction method *(Li et al, 2008)*. The stabilized nanoparticles in the un-activated state, UA STAR 197 and UA STAR 400, showed very low reactivity compared to the 25P nanoparticles. However, when activated, these nanoparticles experienced a significant increase in the reaction rate. In the case of A STAR 197, the Cr(VI) removal capacity increased nearly five times more than UA STAR 197 and the values reached slightly above half the reactivity of the 25P nanoparticles. For A STAR 400 the growth was also considerable since the improvement in reactivity over three times more than for UA STAR 400.

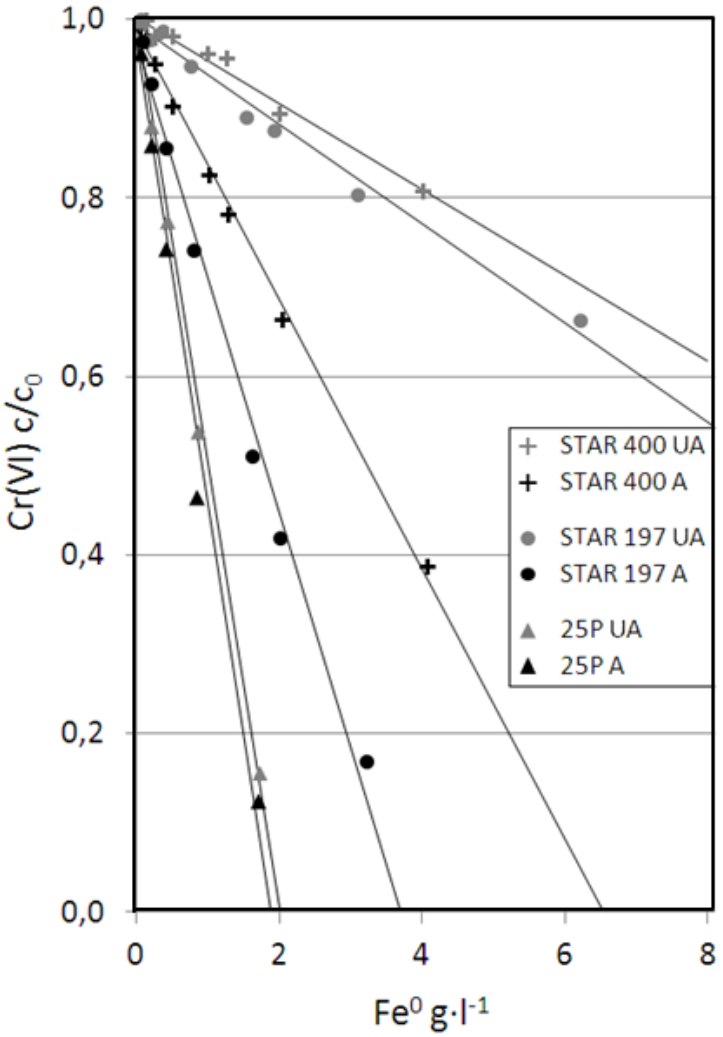

Fig. 6.6 Cr(VI) removal by various concentrations of nZVI particles (STAR 400, STAR 197 and 25P) in the activated and un-activated states.

Table 6.6 Slope, relative slope increment after the activation process (**Δ),** R^2 of regressions from concentration iron tests and Cr(VI) removal capacity.

	$\frac{\Delta\, c/c_0}{\Delta\, [Fe]}$	Δ	R^2	$\frac{mg\ Cr(VI)}{g\ Fe(0)}$
STAR 400 UA	-0.048		0.98	2.4
STAR 400 A	-0.151	3.15	0.99	7.5
STAR 197 UA	-0.056		0.99	2.8
STAR 197 A	-0.263	4.70	0.99	13.2
25P UA	-0.495		0.99	24.8
25PA	-0.516	1.04	0.99	25.8

In full accordance with the activation process described in Section 3.2, these differences in reactivity can be explained mainly by the nature of the oxide layer of the un-activated samples and the changes observed in this oxide shell with the activation process. The main removal mechanism of Cr(VI) is the reduction to Cr(III) *(Mystrioti et al. 2014, Li et al, 2008)* and *Eq. 6.3* illustrates the reduction reaction *(Melitas et al. 2001)*.

$$Fe^0_{(s)} + CrO^{2-}_{4\,(aq)} + 4H_2O_{(l)} \rightarrow Fe(OH)_{3\,(s)} + Cr(OH)_{3\,(s)} + 2OH^- \quad \textbf{Eq. 6.3}$$

In this process, the transfer of electrons from Fe(0) (i.e., from the core of nZVI) to the outer surface is a crucial point and it can be produced basically through defects in the oxide layer or via the oxide conduction band *(O'Carroll et al. 2013)*. Therefore, the morphology and thickness of the oxide layer play a key role. On the one hand, irregularities in the oxide layer such as pinholes, detached zones, etc., would promote reaction sites and enhance reactivity. On the other hand, the thickening of the uniform oxide layer would reduce reactivity. Numerous studies suggest that a thickness of around 5 nm prevents reactivity in the air and therefore leads to lower performance in water remediation *(Kim et al., 2010, Sohn et al., 2006. Nurmi et al., 2005)*.

At this point it is also important to note that although the batches were allowed to react for 24 hours, the reaction mainly took place within the first 2 hours followed by a dramatic decrease in reactivity which persisted for at least 2 months. Since Fe(0) was not completely consumed, such sudden retardation of reactivity could be directly related to the removal mechanism of Cr(VI): the reaction of nZVI with Cr(VI) in an aqueous solution leads to the reduction of Cr(III) forming Cr-Fe hydroxides being incorporated into the outer layers of the oxide shell *(Kerkar et al, 1990; Li et al, 2008)*. At a pH of above 8, the reaction with water slows down, and CrO_4^{2-} receive the electrons from Fe(0) and the precipitation of Cr-Fe compounds at the reaction sites creates a passive layer that hinders further Cr(VI) reduction *(Xie and Cwiertny, 2012)*. In order to simulate real groundwater conditions, the batch pH was not buffered and therefore the pH reached a value of ≈9. This condition allowed the formation of a passivation layer and could explain the observed sudden drop in nZVI reactivity *(Liu et al, 2007; Li et al 2008)*. Thus, it can be deduced that the removal capacity of any type of nZVI will depend mainly on the initial sites disposed to electron transfer, either by defects or by zones of thin oxide layers, which allow higher conductivity. In this sense, the specific surface area will also play a significant role allowing more reduction sites prior to passivation.

Considering the above arguments, we will now discuss the reactivity of nZVI with various extents of surface passivation. In the case of the UA 25P nanoparticles with an initial thin non-uniform oxide layer *(Fig. 6.3 and Table 6.3)* and with a high SSA, one could expect that the electrons move easily outwards by the oxide conduction band or due to the great number of defect points in the oxide layer *(Li et al, 2006)*. This is then reflected in the high reaction rate. For UA STAR 197 and UA STAR 400 nanoparticles, the drop in the Cr(VI) removal capacity can be linked to an initial thicker oxide layer *(Fig. 6.3, 6.4 and*

Table 6.3) and with the UA 25P nanoparticles and the lower specific surface area. The differences in thickness of the oxide shell between both types of nZVI seem to have a minor effect on Cr(VI) reactivity.

The increase in nZVI reactivity against some pollutants after aging in water for 1-2 days *(Sarathy et al., 2008; Kim et al., 2010; Xie and Cwiertny, 2012; Liu et al., 2007)* is related to the removal of oxide layer, either by dissolution *(Sohn et al., 2006; Kim et al., 2012; Xie and Cwiertny, 2012)* or by detachment *(Sarathy et al., 2008; Kim et al., 2010)*. There is no a clear increase in the removal capacity of the A 25P nanoparticles compared to the UA 25P nanoparticles because the changes in the oxide layer after the activation process are negligible and are accompanied by just a small increase in the SSA. However, this observation is not in accordance with the results obtained after 1-2 days of aging similar bare nanoparticles in water *(Sarathy et al., 2008)*. In that study, aging led to a large increase in the removal of carbon tetrachlorine. Despite the similarities in synthetic procedure, particle size, Fe(0) content, SSA and aging conditions, the TEM images of the as-received particles revealed a rather uniform and 4-5 nm thick oxide layer, which indicates that the particles were probably passivated spontaneously during handling.

A completely different development has been observed for the A STAR 197 and A STAR 400 nanoparticles, where a significant improvement in the removal of Cr(VI) occurred. In the case of A STAR 197, this increase can be related to the partial removal of the compact shell *(Fig. 6.3, 6.4 and Table 6.3)* enhancing electron transfer. In the case of the A STAR 400 nanoparticles, the activation process created less defect points on the surface of the nanoparticle than in the case of the A STAR 197 sample: many places were observed where the oxide shell remains uniform *(Fig. 6.3)*, although with a reduction in thickness. This helps to explain the lower increase in the Cr(VI) removal capacity of the A STAR 400 nanoparticles.

Finally, the role of the SSA in the enhanced reactivity of A STAR 197 and A STAR 400 should be taken into account. In the work of Sarathy et al. *(Sarathy et al., 2008)* no significant increase in the SSA related to the process of nZVI aging in water was described, and no other references to an increase in the SSA can be found in published works in which nZVI aging in water for short periods of time was studied *(Kim et al, 2010; Liu and Lowry, 2006)*. As mentioned above, a partial breakdown of nanoparticle aggregates is considered to be the main reason for the increase in the SSA in A STAR 197 and A STAR 400, along with nZVI overgrowing by very small secondary phases. The key parameter influencing the improvement of reactivity of the surface stabilized nZVI particles during the activation process is the increase in the density of defects in the oxide shell *(Lapuerta et al. 2006)*. Therefore, if the density of defects is constant, the increase of new surfaces is significant for the reactivity *(Kim et al, 2010)* and therefore an increase in the SSA would result in an increase in the capacity of Cr(VI) removal. In this particular case, the increase in the SSA has a minor effect on the overall increase in the capacity of Cr(VI) removal. This is elucidated by a comparison of the reactivity of A 25P and A STAR 197 nanoparticles, although both nZVI particles have a comparable SSA the A 25P sample has twice the Cr (VI) removal capacity as A STAR 197.

Removal of CAH

The results of the reactivity tests of UA STAR 197 and A STAR 197 samples with different types of chlorinated compounds are shown in *Table 6.5*. Following the activation process, there was a significant improvement in the activity against the different CAHs tested. This enhancement of reactivity with a short period of water aging has also previously been reported for carbon tetrachloride, trichloroethylene and 1,1,1,2-tetrachloroethane *(Sarathy et al., 2008; Kim et al., 2010; Xie and Cwiertny, 2012)* and it is in full accordance with the above-presented reduction of Cr(VI). These experiments confirm that the described process, employed here for the activation of initially dry, surface-passivated nZVI particles, can be further applied for the effective removal of a wide range of different pollutants that are usually treatable by nZVI particles.

Table 6.5 Final concentrations of contaminants in blanks and their relative final content in un-activated and activated batches. Trichloromethane (TCM), Tetrachloromethane (PCM), *cis*-1,2-Dichloroethene (cis-DCE), Trichloroethylene (TCE), Tetrachloroethylene (PCE). (n) number of replicates.

	TCM	**PCM**	***cis*-DCE**	**TCE**	**PCE**
Blank ($\mu g \cdot l^{-1}$) (3)	553	1187	276	420	7308
UA STAR 197 (2)	0.89	1.01	0.92	0.98	1.07
A STAR 197 (2)	0.00	0.00	0.00	0.06	0.26

6.1.4 Conclusions

- The thick and compact oxide shield of surface-passivated nZVI particles significantly decreases their performance in the reduction of Cr(VI) compared to non-stabilized nZVI particles. The introduction of a simple activation process consisting of an aging of dense nZVI slurry in water for less than 48 hours led to a partial recovery of the nZVI reactivity.

- The increase in the reactivity is explained by partial dissolution of the oxide layers, which allows an improvement in the transfer of electrons from the inside of the particles to the surface, as well as a partial breakdown of aggregates leading to an increase in the SSA. The recovery of reactivity is higher the thinner the initial thickness of the oxide shell, since it seems to be more favourable for breaking the uniform oxide shell and creating a high density of defects.

- At the same time, the activation process does not decrease Fe(0) content. The clear improvement in the degradation of chlorinated organic compounds after the activation process confirms that the proposed procedure is suitable for nZVI-based treatment of a wide range of contaminants.

- Therefore, the described activation process is an important new procedure, which can be applied before the injection of nZVI into the treated subsurface area and could represent an easy way of increasing the effectiveness of the remediation and simplifying the overall handling of nZVI.

- Besides previous exposed conclusions, the thickness of oxide shield on the passivated particles governs the degree of reactivity recovery. STAR 400 with a mean oxide thickness of 6.5 nm had a much lower reactivity recovery comparing to STAR 197 (3.4 nm) after the activation process. It is strongly recommended to passivated nZVI manufacturers to keep as low as possible within safety limits the oxide shied thickness.

6.1.5 References

Almeelbi, T., & Bezbaruah, A. (2012). Aqueous phosphate removal using nanoscale zero-valent iron. Journal of nanoparticle Research, 14(7), 1-14.

Caré, S., Nguyen, Q. T., L'Hostis, V., & Berthaud, Y. (2008). Mechanical properties of the rust layer induced by impressed current method in reinforced mortar. Cement and Concrete Research, 38(8), 1079-1091.

Cornell, R. M., & Schwertmann, U. (2006). The iron oxides: structure, properties, reactions, occurrences and uses. John Wiley & Sons. Ch. 1, pp. 4-5.

Crane, R. A., & Scott, T. B. (2012). nanoscale zero-valent iron: future prospects for an emerging water treatment technology. Journal of Hazardous Materials, 211, 112-125.

Filip, J., Karlický, F., Marušák, Z., Černík, M., Otyepka, M. & Zbořil, R. (2014): Anaerobic Reaction of nanoscale Zerovalent Iron with Water: Mechanism and Kinetics. Journal of Physical Chemistry C, 118, 13817-13825.

Fu, F., Dionysiou, D. D., & Liu, H. (2014). The use of zero-valent iron for groundwater remediation and wastewater treatment: a review. Journal of Hazardous Materials, 267, 194-205.

Grieger, K. D., Fjordbøge, A., Hartmann, N. B., Eriksson, E., Bjerg, P. L., & Baun, A. (2010). Environmental benefits and risks of zero-valent iron nanoparticles (nZVI) for in situ remediation: Risk mitigation or trade-off? Journal of Contaminant Hydrology, 118(3), 165-183.

Huang, P., Ye, Z., Xie, W., Chen, Q., Li, J., Xu, Z., & Yao, M. (2013). Rapid magnetic removal of aqueous heavy metals and their relevant mechanisms using nanoscale Zero Valent iron (nZVI) particles. Water Research, 47(12), 4050-4058.

Ji, Y. (2014). Ions removal by iron nanoparticles: a study on solid–water interface with zeta potential. Colloids and Surfaces A: Physicochemical and Engineering Aspects, 444, 1-8.

Kerkar, M., Robinson, J., & Forty, A. J. (1990). In situ structural studies of the passive film on iron and iron/chromium alloys using X-ray absorption spectroscopy. Faraday Discussions of the Chemical Society, 89(P001), 1-20.

Kim, H. S., Ahn, J. Y., Hwang, K. Y., Kim, I. K., & Hwang, I. (2010). Atmospherically stable nanoscale zero-valent iron particles formed under controlled air contact: characteristics and reactivity. Environmental Science & Technology, 44(5), 1760-1766.

Kim, H. S., Kim, T., Ahn, J. Y., Hwang, K. Y., Park, J. Y., Lim, T. T., & Hwang, I. (2012). Aging characteristics and reactivity of two types of nanoscale zero-valent iron particles (Fe^{BH} and Fe^{H2}) in nitrate reduction. Chemical Engineering Journal, 197, 16-23.

Lapuerta, S., Moncoffre, N., Millard-Pinard, N., Jaffrézic H., Bérerd, N., & Crusset, D. (2006) Role of proton irradiation and relative air humidity on iron corrosion. Journal of Nuclear Materials. 352, 174-179.

Li, X. Q., Cao, J., & Zhang, W. X. (2008). Stoichiometry of Cr (VI) immobilization using nanoscale zerovalent iron (nZVI): a study with high-resolution X-ray photoelectron spectroscopy (HR-XPS). Industrial & Engineering Chemistry Research, 47(7), 2131-2139.

Li, XQ., Elliot DW., & Zhang W-X. (2006), Zero-valent iron nanoparticles for abatement of environmental pollutants: materials and engineering aspects. Critical Reviews in Solid State, 31, 111-22.

Lide, D. R. (Ed.). (2004). CRC handbook of chemistry and physics. CRC press. Ch. 4, pp. 16.

Lin, K. S., Chang, N. B., & Chuang, T. D. (2008). Fine structure characterization of zero-valent iron nanoparticles for decontamination of nitrites and nitrates in wastewater and groundwater. Science and Technology of Advanced Materials, 9(2), 025015.

Liu, A., & Zhang, W. X. (2014). Fine structural features of nanoscale zero-valent iron characterized by spherical aberration corrected scanning transmission electron microscopy (Cs-STEM). Analyst, 139(18), 4512-4518.

Liu, A., Liu, J., & Zhang, W. X. (2015). Transformation and composition evolution of nanoscale Zero Valent iron (nZVI) synthesized by borohydride reduction in static water. Chemosphere, 119, 1068-1074.

Liu, A., Liu, J., Pan, B., & Zhang, W. (2014). Formation of lepidocrocite (γ-FeOOH) from oxidation of nanoscale zero-valent iron (nZVI) in oxygenated wáter. RSC Advances, 4, 57377.

Liu, Y., & Lowry, G. V. (2006). Effect of particle age (Fe0 content) and solution pH on NZVI reactivity: H2 evolution and TCE dechlorination. Environmental Science & Technology, 40(19), 6085-6090.

Liu, Y., Choi, H., Dionysiou, D., & Lowry, G. V. (2005b). Trichloroethene hydrodechlorination in water by highly disordered monometallic nanoiron. Chemistry of Materials, 17(21), 5315-5322.

Liu, Y., Majetich, S. A., Tilton, R. D., Sholl, D. S., & Lowry, G. V. (2005a). TCE dechlorination rates, pathways, and efficiency of nanoscale iron particles with different properties. Environmental Science & Technology, 39(5), 1338-1345.

Liu, Y., Phenrat, T., & Lowry, G. V. (2007). Effect of TCE concentration and dissolved groundwater solutes on NZVI-promoted TCE dechlorination and H2 evolution. Environmental Science & Technology, 41(22), 7881-7887.

Macé, C., Desrocher, S., Gheorghiu, F., Kane, A., Pupeza, M., Cernik, M., ... & Zhang, W. X. (2006). Nanotechnology and groundwater remediation: a step forward in technology understanding. Remediation Journal, 16(2), 23-33.

Martin, J. E., Herzing, A. A., Yan, W., Li, X. Q., Koel, B. E., Kiely, C. J., & Zhang, W. X. (2008). Determination of the oxide layer thickness in core-shell zerovalent iron nanoparticles. Langmuir, 24(8), 4329-4334.

Melitas, N., Chuffe-Moscoso, O., & Farrell, J. (2001). Kinetics of soluble chromium removal from contaminated water by zerovalent iron media: corrosion inhibition and passive oxide effects. Environmental Science & Technology, 35(19), 3948-3953.

Mystrioti, C., Xenidis, A., & Papassiopi, N. (2014). Application of Iron nanoparticles Synthesized by Green Tea for the Removal of Hexavalent Chromium in Column Tests. Journal of Geoscience and Environment Protection, 2(04), 28.

Noubactep, C., Caré, S., & Crane, R. (2012). nanoscale metallic iron for environmental remediation: prospects and limitations. Water, Air, & Soil Pollution, 223(3), 1363-1382.

Nurmi, J. T., Tratnyek, P. G., Sarathy, V., Baer, D. R., Amonette, J. E., Pecher, K., ... & Driessen, M. D. (2005). Characterization and properties of metallic iron nanoparticles: spectroscopy, electrochemistry, and kinetics. Environmental Science & Technology, 39(5), 1221-1230.

O'Carroll, D., Sleep, B., Krol, M., Boparai, H., & Kocur, C. (2013). nanoscale Zero Valent iron and bimetallic particles for contaminated site remediation. Advances in Water Resources, 51, 104-122.

Petala, E., Dimos, K., Douvalis, A., Bakas, T., Tucek, J., Zbořil, R., & Karakassides, M. A. (2013). nanoscale zero-valent iron supported on mesoporous silica: Characterization and reactivity for Cr (VI) removal from aqueous solution. Journal of Hazardous Materials, 261, 295-306.

Sarathy, V., Tratnyek, P. G., Nurmi, J. T., Baer, D. R., Amonette, J. E., Chun, C. L., ... & Reardon, E. J. (2008). Aging of iron nanoparticles in aqueous solution: effects on structure and reactivity. The Journal of Physical Chemistry C, 112(7), 2286-2293.

Schwertmann, U., & Cornell, R. M. (2000). Iron oxides in the laboratory: preparation and characterization. John Wiley & Sons. Ch. 1, pp. 12.

Shafranovsky, E. A., & Petrov, Y. I. (2004). Aerosol Fe nanoparticles with the passivating oxide shell. Journal of nanoparticle Research, 6(1), 71-90.

Signorini, L., Pasquini, L., Savini, L., Carboni, R., Boscherini, F., Bonetti, E., ... & Nannarone, S. (2003). Size-dependent oxidation in iron/iron oxide core-shell nanoparticles. Physical Review B, 68(19), 195423.

Sohn, K., Kang, S. W., Ahn, S., Woo, M., & Yang, S. K. (2006). Fe(0) nanoparticles for nitrate reduction: stability, reactivity, and transformation. Environmental Science & Technology, 40(17), 5514-5519.

Tang, S. C., & Lo, I. (2013). Magnetic nanoparticles: essential factors for sustainable environmental applications. Water Research, 47(8), 2613-2632.

Tiehm, A., Kraßnitzer, S., Koltypin, Y., & Gedanken, A. (2009). Chloroethene dehalogenation with ultrasonically produced air-stable nano iron. Ultrasonics Sonochemistry, 16(5), 617-621.

Woo, H., Park, J., Lee, S., & Lee, S. (2014). Effects of washing solution and drying condition on reactivity of nano-scale Zero Valent irons (nZVIs) synthesized by borohydride reduction. Chemosphere, 97, 146-152.

Xie, Y., & Cwiertny, D. M. (2012). Influence of anionic cosolutes and pH on nanoscale zerovalent iron longevity: time scales and mechanisms of reactivity loss toward 1, 1, 1, 2-tetrachloroethane and Cr (VI). Environmental Science & Technology, 46(15), 8365-8373.

Xiu, Z. M., Jin, Z. H., Li, T. L., Mahendra, S., Lowry, G. V., & Alvarez, P. J. (2010). Effects of nano-scale zero-valent iron particles on a mixed culture dechlorinating trichloroethylene. Bioresource Technology, 101(4), 1141-1146.

Yu, R. F., Chi, F. H., Cheng, W. P., & Chang, J. C. (2014). Application of pH, ORP, and DO monitoring to evaluate chromium (VI) removal from wastewater by the nanoscale zero-valent iron (nZVI) process. Chemical Engineering Journal, 255, 568-576.

Zboril, R., Andrle, M., Oplustil, F., Machala, L., Tucek, J., Filip, J. & Sharma, V.K. (2012): Treatment of chemical warfare agents by zero-valent iron nanoparticles and Fe(VI)/Fe(III) composite. Journal of Hazardous Materials, 211-212, 126-130.

Zhang, W. X. (2003). nanoscale iron particles for environmental remediation: an overview. Journal of nanoparticle Research, 5(3-4), 323-332.

7 nano Zero Valent Iron: aggregation driving factors

In the following chapter the main mechanisms of nano Zero Valent Iron (nZVI) aggregation are studied. The aggregation problem was considered following two different interparticle phenomena, electrostatic attraction - repulsion and magnetic attraction:

- ζ-potential of some nZVI aging products were determined to disclose the effect of iron aging products over this parameter. In addition, the effect of the activation process described in *(Chapter 6.1)* over the ζ-potential was determined.

- Aggregation studies were extended to magnetism as a first effort to understand and explore methods to reduce interparticle magnetic attraction.

7.1 ζ-Potential characterization of activated, unactivated nano Zero Valent Iron and some of its aging oxides

Agglomeration of nano Zero Valent Iron (nZVI) suspensions is a key factor that has a dramatic impact on the availability of nZVI technology for its application on the field. Agglomeration produces large nanoparticles clusters of several microns which reduces reactivity and ultimately clogs the aquifer pores, reducing the nZVI mobility and thus the performance in the interception of pollutants.

Some common iron oxides generated by nZVI aging, such as goethite and magnetite, presents very different ζ-potential – pH titration profiles. These observed differences should be taken into account when designing nZVI dispersions. The dispersants chosen and its concentrations tailored for nZVI would not work for the generated iron oxides, jeopardizing the long term stability and mobility.

The consequences of the activation process on the ζ-potential of the NF STAR 197 nanoparticles are studied. No significant changes were observed meaning that similar performance should be expected and in addition the same dispersants could be used.

7.1.1 Introduction

In spite of the nano Zero Valent Iron (nZVI) capability to degrade a broad range of pollutants *(Crane and Scott, 2012)*, the high chemical reactivity of nZVI is not the only parameter that drives the effectiveness of remediation in a full-scale applications. One of the present main challenges is to minimize the aggregation of the nanoparticles. Through the aggregation processes large aggregates of several microns are produced, clogging the aquifer pores thus reducing dramatically the nZVI mobility into the porous media and reactivity due to the decrease of surface area, *Johnson et al., 2013; Tosco et al., 2014*.

Since the diameter of commercial nZVI is deep into the colloidal size, the aggregation would not be expected because Brownian motion usually prevails over the other forces. However, since iron is an easy magnetisable material, strong magnetic attractive forces arises among particles producing large aggregates, *He and Zhao, 2005*. This mechanism is treated in *Chapter 7.2*.

A common approach to mitigate the aggregation is the use of dispersants. The anti-agglomeration effect of dispersants is given thanks to at least one of the following mechanisms: increasing the surrounding charge of nanoparticles (electrostatic stabilization), preventing physically colloids from approaching at close distances (steric stabilization) and increasing the viscosity of the liquid reducing the Brownian motion thus reducing the probability of the particles to collide (shear-thinning stabilization), *(Comba and Sethi, 2009)*. Usually, a simultaneous combination of these mechanisms is used, i.e.: electrosteric stabilization whit polyelectrolytes, *(Sun et al., 2007)*. Some considered dispersants in the literature includes: guar gum *(Comba and Sethi, 2009; Tiraferri and Sethi, 2009)*, sodium polyaspartate *(Sun et al., 2007; Phenrat et al., 2008)*, polyacrylic acid *(Ponder et al., 2000; Ponder et al., 2001; Schrick et al., 2002; Cirtiu et al., 2011)*, polyethylene glycol *(Ghauch et al., 2009)*, potato starch *(Kim et al., 2009)*, sodium alginate *(Kim et al., 2009; Phenrat et al., 2009)*, xanthan gum *(Comba and Sethi, 2009; Vecchia et al., 2009; Tosco and Sethi, 2010)*, poly(vinyl alcohol-co-vinyl acetate-co-itaconic acid) *(Cantrell et al., 1997; Sun et al., 2007; Comba and Sethi, 2009)*, among others.

Electrostatic repulsion is achieved by increasing the surrounding charge of the nZVI particles through dispersants. It is defined by the ζ-potential which is the electric potential difference between the dispersion medium and the last stationary layer attached to the dispersed particle. From a practical point of view, ζ-potential governs interparticle interaction (attraction repulsion), *Fig. 7.1*. Generally, it is considered that ζ-potential values > ±30 mV produce stable dispersions because of the strong repulsion achieved between particles with the same charge, *(Morrison and Ross, 2002)* although it cannot directly be applied to nZVI suspensions due to the intrinsic particle magnetism, *(He and Zhao, 2005)*. Another important property of the particles is the isoelectric point which is the pH where ζ-potential reach a zero value, at that point the particles show the highest propensity to aggregate.

On the other hand, steric stabilization is attained through the adsorption of long-chain organic molecules onto the particle surface. Adsorption of these long-chain molecules is also governed by the surface charge of the nZVI particles. ζ-potential can be used as an indicator to choose the suitable dispersant, optimize the formulations and aid in predicting long-term particles stability. It is important to know that pH has a dramatic effect on ζ-potential, therefore it must be considered when designing dispersions. Literature shows a typical pH of 8–10 of ∼1 g/L iron nanoparticles suspensions, *(Zhang, 2003)*.

In the following research the ζ-potential over a wide range of pH was determined for activated, and unactivated NANOFER STAR 197 nZVI. The results would assess if the activation process described in *(Chapter 6.1)* had any repercussion over the ζ-potential and consequently on the suspensions stability. If important variations are observed, this new ζ-potential value will have to be considered on future dispersant selection otherwise present methodology will continue to be suitable.

Besides the activation process effect on the ζ-potential, ζ-potentials of the expected oxides due to the aging of the nZVI were studied. The present selection of the dispersants was based only on the pristine nZVI although aging is known to be a fast process once particles come in contact with water. Different aging products of nZVI are reported in literature: lepidocrocite *(Liu and Zhang, 2014)*, goethite *(Kim et al. 2012a; Kim et al., 2012b)*, ferrous hydroxide *(Filip et al. 2014)* and secondary magnetite/maghemite *(Sohn et al., 2006; Kim et al. 2012)*. This research pretends to report the ζ-potentials of these oxides, aiding on the prediction of aged nZVI suspension stability and mobility. Additionally, it will assist the selection of dispersants in which the aging products of the nZVI can be taken into account. Since the particle size influences the ζ-potential *(Hyam et al., 2008)* different oxide nanoparticles were studied emulating an aged nZVI.

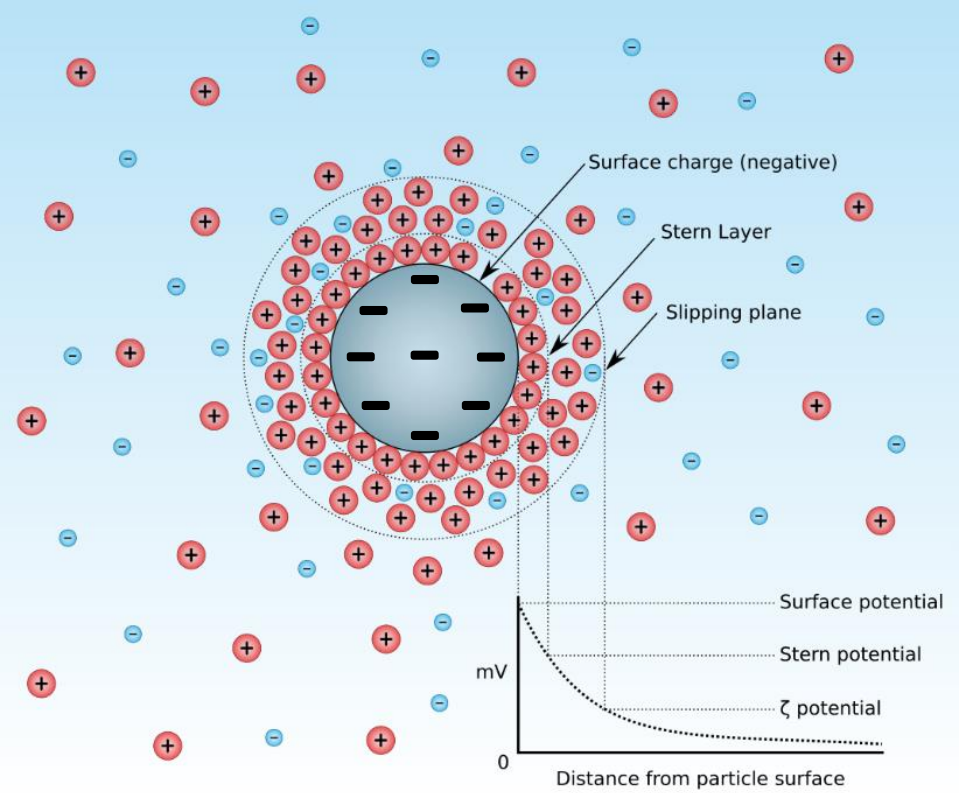

Fig. 7.1 Diagram showing the layers of electric charges surrounding a particle and the ζ-potential location (for a positive particle all charges would be inverted), *(Mjones 1984)*.

7.1.2 Materials and methods

All the samples were kindly provided by CXI-TUL (The institute for nanomaterials, advanced technology and innovation, Liberec). STAR 197 is a nZVI a commercial batch produced by (NANORION s.r.o.), these particles were air-stable thanks to a passivation process. In order to study the aging effects on the ζ-potential, three different oxide nanoparticles were also provided: nano goethite, nano hematite and nano magnetite. These were produced by synthesis. To prepare the nanoparticles slurries, 10 g of nZVI particles were added to 40 ml of deionised water, being the final w/w iron to water ratio 0.2. Finally, slurries were dispersed using a high-power mixer at 11,000 rpm, following the sequence: 60s on – 60s off – 60s on. Dispersants were not use in order to avoid interferences with the ζ-potential of the particles.

The activation process consisted on the aging of the nZVI slurry for a period of 36 hours at room temperature followed by re-suspension using the same dispersion procedure as described above. Hereafter activated (STAR 197 A) and unactivated (STAR 197 UA) samples were studied.

Size characterization of the initial nanoparticles was carried out by Scaning Electron Microscopy (SEM) (Gemini ultra plus, Zeiss). Samples were suspended mixing it vigorously in absolute ethanol, deposited and let to evaporate over standard pins.

ζ-potential – pH titrations were measured using dynamic light scattering and electrophoretic light scattering (Z-Sizer nano ZS, Malvern). The experiment started with the preparation of 1.0 $g \cdot l^{-1}$ suspensions of the nZVI and iron oxides with water at 0.01M (NaCl) ionic stretch. All procedure was done under nitrogen atmosphere that also served as agitation. Before an initial stabilization period of 30 min, pH was modified by the addition of NaOH (0.01M) and HCl (0.01M) as required. Samples were analysed every 0.5-1 pH intervals.

7.1.3 Results

SEM images showed that STAR 197 UA, hematite and magnetite presents a particle size clearly under 1 µm and a spherical - globular morphology. In the opposite hand, goethite is characterized by an acicular morphology with crystals of approximately 1 µm and a thickness of few hundred manometers, *Fig. 7.2*. Observed morphologies are in agreement with the literature, contrasting to other oxides, goethite is frequently reported as acicular, *(Kim et al., 2010; Kim et al., 2012a; Kim et al., 2012b)*.

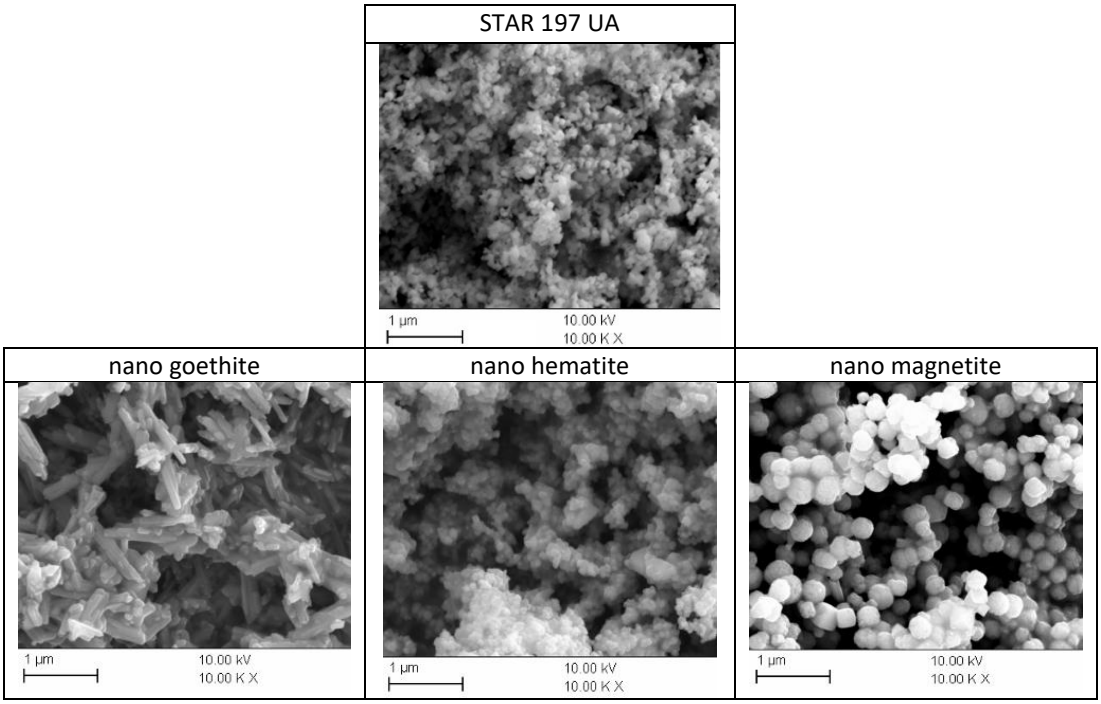

Fig. 7.2 SEM image of the as-received particles.

Activation process effect on ζ-potential

The activation process performed to STAR 197 had a very small repercussion over the ζ-potential, *Fig. 7.3*. This minor change on the ζ-potential means little affection on suspension stability and mobility performance but allowing a high reactivity improvement provided by the activation process. It also states that the same dispersants and concentrations can be used without affecting the performance. ζ-potential values of the particles are consistent with the previous ones reported in the literature for similar nZVI *(Honetschlägerová et al., 2012)*.

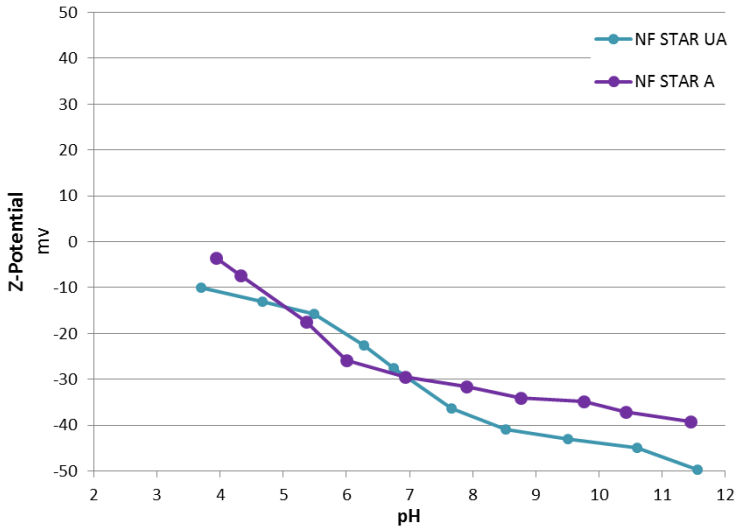

Fig. 7.3 Z potential – pH titrations of activated and unactivated NF STAR.

Particle oxidation (aging) effect on ζ-potential

The results from experiments with iron oxide particles can be seen in the *Fig. 7.4*, the nZVI STAR 197 UA and some of the oxide nanoparticles behaved very different. At the pH range of interest 8–10 in which the particles slurries should be expected to be, hematite and STAR 197 UA presented similar ζ-potential values. On the other hand, goethite and magnetite compared to STAR 197 UA showed a different ζ-potential trend, especially in the low pH range of interest. At ≈ 8 pH goethite had ζ-potential where close to the isoelectric point, magnetite -20 mV and NF STAR 197 – 40 mV, respectively. Isoelectric points of magnetite (≈7.3 pH) and goethite (≈8.5 pH) were similar to literature values, being 6.3 - 7.1 for magnetite and 7.5 - 9.5 for goethite, respectively *(Cornell et al, 2003)*.

On goethite and magnetite cases the observed disparity compared to STAR 197 UA has strong implications into the evolution of the aggregation behaviour during the aging, and consequently, in long term stability. When choosing dispersants for nZVI this must be considered, the aging products would present very different ζ-potentials in a broad pH range. In the light of the results, a new approach in the dispersant selecting process taking into account the ζ-potentials of the aging compounds is strongly recommended.

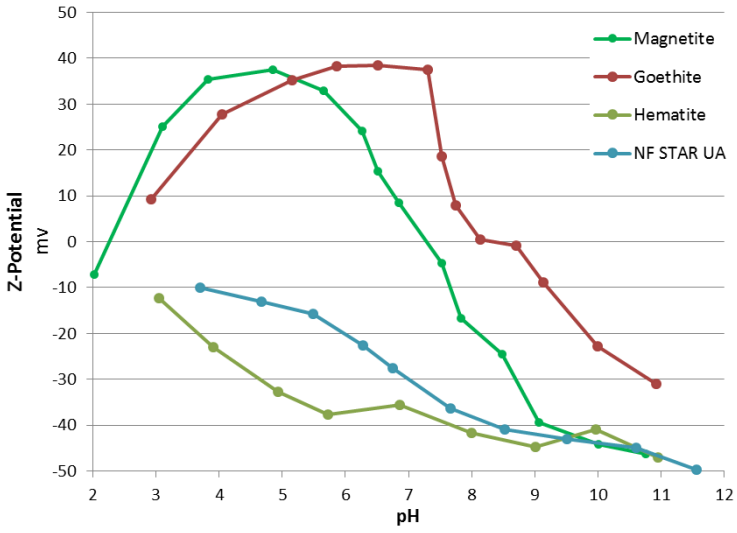

Fig. 7.4 ζ-potential – pH titrations unactivated NF STAR and iron oxide nanoparticles.

7.1.4 Conclusions

- The activation process on nZVI NF STAR 197 particles did not affect ζ-potential significantly. It implies that activation process had little effect on activated NF STAR 197 suspension stability and possible over mobility. Moreover results state the suitability to use the same previous dispersants at the same concentrations.

- Concerning aging, goethite and magnetite presented remarkable different ζ-potential values which indicate that ζ-potentials of the aging products must be taken into account when assessing the long term stability suspensions and the dispersant selection.

7.1.5 References

Cantrell, K. J., Kaplan, D. I., & Gilmore, T. J. (1997). Injection of colloidal Fe0 particles in sand with shear-thinning fluids. Journal of Environmental Engineering, 123(8), 786-791.

Cirtiu, C. M., Raychoudhury, T., Ghoshal, S., & Moores, A. (2011). Systematic comparison of the size, surface characteristics and colloidal stability of Zero Valent iron nanoparticles pre-and post-grafted with common polymers. Colloids and Surfaces A: Physicochemical and Engineering Aspects, 390(1), 95-104.

Comba, S., & Sethi, R. (2009). Stabilization of highly concentrated suspensions of iron nanoparticles using shear-thinning gels of xanthan gum. Water Research, 43(15), 3717-3726.

Cornell, R. M., & Schwertmann, U. (2006). The iron oxides: structure, properties, reactions, occurrences and uses. John Wiley & Sons. Ch. 1.

Crane, R. A., & Scott, T. B. (2012). nanoscale zero-valent iron: future prospects for an emerging water treatment technology. Journal of Hazardous Materials, 211, 112-125.

Filip, J., Karlický, F., Marušák, Z., Černík, M., Otyepka, M. & Zbořil, R. (2014): Anaerobic Reaction of nanoscale Zerovalent Iron with Water: Mechanism and Kinetics. Journal of Physical Chemistry C, 118, 13817-13825.

Ghauch, A., Tuqan, A., & Assi, H. A. (2009). Antibiotic removal from water: elimination of amoxicillin and ampicillin by microscale and nanoscale iron particles. Environmental Pollution, 157(5), 1626-1635.

He, F., & Zhao, D. (2005). Preparation and characterization of a new class of starch-stabilized bimetallic nanoparticles for degradation of Chlorinated Aliphatic Hydrocarbons in water. Environmental Science & Technology, 39(9), 3314-3320.

Honetschlägerová, I., Janouškovcová, P., & Soffer, Z. (2012). nanoscale zero valent iron coating for subsurface application. In Presented at the Proceedings of the 4th international conference NANOCAN 2012,"NANOCAN 2012" Proceedings of the 4th international conference, Brno, Czech Republic.

Hyam, R. S., Subhedar, K. M., & Pawar, S. H. (2008). Effect of particle size distribution and zeta potential on the electrophoretic deposition of boron films. Colloids and Surfaces A: Physicochemical and Engineering Aspects, 315(1), 61-65.

Johnson, R. L., Nurmi, J. T., O'Brien Johnson, G. S., Fan, D., O'Brien Johnson, R. L., Shi, Z., ... & Lowry, G. V. (2013). Field-scale transport and transformation of carboxymethylcellulose-stabilized nano zero-valent iron. Environmental Science & Technology, 47(3), 1573-1580.

Kim, H. J., Phenrat, T., Tilton, R. D., & Lowry, G. V. (2009). Fe0 nanoparticles remain mobile in porous media after aging due to slow desorption of polymeric surface modifiers. Environmental Science & Technology, 43(10), 3824-3830.

Kim, H. S., Ahn, J. Y., Hwang, K. Y., Kim, I. K., & Hwang, I. (2010). Atmospherically stable nanoscale zero-valent iron particles formed under controlled air contact: characteristics and reactivity. Environmental Science & Technology, 44(5), 1760-1766.

Kim, H. S., Kim, T., Ahn, J. Y., Hwang, K. Y., Park, J. Y., Lim, T. T., & Hwang, I. (2012a). Aging characteristics and reactivity of two types of nanoscale zero-valent iron particles (Fe BH and Fe H2) in nitrate reduction. Chemical Engineering Journal, 197, 16-23.

Kim, K. R., Lee, B. T., & Kim, K. W. (201b2). Arsenic stabilization in mine tailings using nano-sized magnetite and Zero Valent iron with the enhancement of mobility by surface coating. Journal of Geochemical Exploration, 113, 124-129.

Liu, A., & Zhang, W. X. (2014). Fine structural features of nanoscale zero-valent iron characterized by spherical aberration corrected scanning transmission electron microscopy (Cs-STEM). Analyst, 139(18), 4512-4518.

Mjones 1984, Origional work by Larryisgood. Creative Commons BY-SA 3.0, https://commons.wikimedia.org/w/index.php?curid=18238739.

Morrison, I. D., & Ross, S. (2002). Colloidal dispersions: suspensions, emulsions, and foams. Wiley-Interscience.

Phenrat, T., Long, T. C., Lowry, G. V., & Veronesi, B. (2008). Partial oxidation ("aging") and surface modification decrease the toxicity of nanosized zerovalent iron. Environmental Science & Technology, 43(1), 195-200.

Phenrat, T., Saleh, N., Sirk, K., Kim, H. J., Tilton, R. D., & Lowry, G. V. (2008). Stabilization of aqueous nanoscale zerovalent iron dispersions by anionic polyelectrolytes: adsorbed anionic polyelectrolyte layer properties and their effect on aggregation and sedimentation. Journal of nanoparticle Research, 10(5), 795-814.

Ponder, S. M., Darab, J. G., & Mallouk, T. E. (2000). Remediation of Cr (VI) and Pb (II) aqueous solutions using supported, nanoscale zero-valent iron. Environmental Science & Technology, 34(12), 2564-2569.

Ponder, S. M., Darab, J. G., Bucher, J., Caulder, D., Craig, I., Davis, L., ... & Shuh, D. K. (2001). Surface chemistry and electrochemistry of supported zerovalent iron nanoparticles in the remediation of aqueous metal contaminants. Chemistry of Materials, 13(2), 479-486.

Schrick, B., Blough, J. L., Jones, A. D., & Mallouk, T. E. (2002). Hydrodechlorination of trichloroethylene to hydrocarbons using bimetallic nickel-iron nanoparticles. Chemistry of Materials, 14(12), 5140-5147.

Sohn, K., Kang, S. W., Ahn, S., Woo, M., & Yang, S. K. (2006). Fe(0) nanoparticles for nitrate reduction: stability, reactivity, and transformation. Environmental Science & Technology, 40(17), 5514-5519.

Sun, Y. P., Li, X. Q., Zhang, W. X., & Wang, H. P. (2007). A method for the preparation of stable dispersion of zero-valent iron nanoparticles. Colloids and Surfaces A: Physicochemical and Engineering Aspects, 308(1), 60-66.

Tiraferri, A., & Sethi, R. (2009). Enhanced transport of zerovalent iron nanoparticles in saturated porous media by guar gum. Journal of nanoparticle Research, 11(3), 635-645.

Tosco, T., & Sethi, R. (2010). Transport of non-Newtonian suspensions of highly concentrated micro-and nanoscale iron particles in porous media: a modeling approach. Environmental Science & Technology, 44(23), 9062-9068.

Tosco, T., Papini, M. P., Viggi, C. C., & Sethi, R. (2014). nanoscale zerovalent iron particles for groundwater remediation: a review. Journal of Cleaner Production, 77, 10-21.

Vecchia, E. D., Luna, M., & Sethi, R. (2009). Transport in porous media of highly concentrated iron micro-and nanoparticles in the presence of xanthan gum. Environmental Science & Technology, 43(23), 8942-8947.

Zhang, W. (2003) nanoscale iron particles for environmental remediation: An overview. Journal of nanoparticles Research, vol. 5, pp. 323 – 332.

7.2 Magnetic properties of zero-valent iron particles and its influence on sedimentation rate and mobility

The nano Zero Valent Iron suspension stability and mobility is limited by the spontaneous tendency of the particles to aggregate and form large flogs when in suspension. The main reason of this behaviour could be the magnetic interparticle attraction, since iron is a ferromagnetic material. A screening over possible strategies to reduce iron magnetism was performed.

Furthermore, demagnetization using an oscillating magnetic field was tested. Four identic iron particle suspensions were set and pre-conditioned: initial iron, initial iron demagnetized, initial iron magnetized and finally an initial iron magnetized and then demagnetized. Afterwards a qualitative sedimentation tests was run over all samples.

Results showed that magnetization dramatically increased the sedimentation rate. Demagnetization process worked but an improvement over the initial iron could not be accomplished. It is hypothesized that the magnetic field of Earth or spontaneous magnetization of the iron nanoparticles were an insurmountable barrier. Further research is need to confirm this hypothesis, in a positive case alloying iron with non-magnetic materials could be explored.

7.2.1 Introduction

nano Zero Valent Iron (nZVI) remediation technology is seriously limited by the spontaneous tendency of the particles to aggregate. nZVI particles forms aggregates when in suspension, firstly primary clusters are produced and secondly these clusters forms large network structures usually of several microns with a dendritic morphology, afterwards forming flocs. The formed microscale nZVI structures clog the pore media, reducing its mobility. In addition, reactivity decreases because of the specific surface area loss. *(He and Zhao, 2005; Dalla Vecchia et al., 2009; Tosco et al., 2014)*.

The aggregate formation of colloids is usually governed by a balance of repulsive and attractive forces acting between particles. According to the DLVO (Derjaguin, Landau, Verwey and Overbeek) theory, the net force between interacting charged surfaces derives from the combined effect of Van der Waals attraction and the electrostatic double layer repulsion, *(Dalla Vecchia et al., 2009)*. However, in the case of nZVI attractive magnetic forces must be taken into account. Despite the favourable ζ-potential and nanoscale size observed on nZVI samples, aggregation occurs quickly, *(Sun et al., 2007; Comba and Sethi, 2009).* Sedimentation rates of $min \cdot m^{-1}$ are observed whereas theoretically particles of these characteristics should be in the range of $day \cdot m^{-1}$ as stated by Stokes law. It is consequence of attractive magnetic forces *(Phenrat et al., 2007; Dalla Vecchia et al., 2009)* which prevails over the repulsive ones, causing colloid instability. Once interparticle forces are defined, aggregation is just a probabilistic process where Brownian motion and particle concentration rules the rate between particle interactions.

The purpose of this chapter is to bring a very initial exploration of methods to reduce the nZVI magnetism. Two different approaches have been considered:

- Demagnetization
    - Through temperature. Heating up the particles over Curie temperature of iron 770ºC *(Lide et al., 2004)* would remove the remanent magnetization of the particles. Although it seems and straightforward method there are important complications: (I) it requires an inert atmosphere to avoid oxidation at high temperatures, (II) negative side effects could be produced i.e.: changes into crystal lattice affecting reactivity and agglomeration due to sintering.
    - Through a magnetic field. This aproach is based on the application of a decreasing oscillating magnetic field which eliminates the previous magnetism. It is a common industrial process also applied to particles. It was chosen because of being a simple and scalable process.
- nZVI alloying, pure iron has a particularly high magnetic permeability and remanence but low reluctance (because it is difficult to find reluctance data, it is assumed that reluctance equals to coercivity). Iron properties specifically implies:
    - Permeability. Iron develops easily a temporal magnetization as a response to an applied magnetic field. In the worst-case scenario, if the nZVI is enough sensitive, earth magnetic field could be sufficient to magnetize nZVI particles.
    - Remanence. Once iron is exposed to an external magnetic field iron keeps a high degree of magnetization even after the external magnetic field is removed. It could have some implications over the nZVI manufacture and handling.
    - Reluctance. Low iron values of this magnetic property implies a low ability to withstand an external magnetic field without becoming permanently magnetized. Low reluctance

together with high permeability highlights the iron vulnerability to external magnetic fields.

- Superparamagnetism. It is a property which arises at nanoscale on ferromagnetic or ferrimagnetic particles leading to an extreme susceptibility to magnetization by external magnetic fields. Literature here shows different results, possibly depending on the degree of agglomeration because agglomerated particles behave as a macroscopic system. Some authors detected this property in non-agglomerated nZVI *(de Caro et al., 1996)* whereas *(Dalla Vecchia et al., 2009)* did not observe superparamagnetism because the single domain condition of the nanoparticles was cancelled by aggregation.

- Spontaneous magnetization. It is the appearance of an ordered spin state, choosing magnetization direction by the spins, at zero applied magnetic field in a ferromagnetic or ferrimagnetic material below the Curie temperature, *(Crangle and Goodman, 1971)*.

All of these properties are strongly modified if iron is alloyed, *Table 7.1.* An interesting strategy could be to find an alloying element which does not interfere with the positive characteristics of nZVI such as reactivity and environmental compatibility, but at the same time may degrade the magnetic properties.

Table 7.1 Magnetic properties of different iron grades and alloys.

	Relative permeability (μ/μ_0)	**Coercivity Hc** (Oe)	**Remanence Mr** (Gs)
Iron (99.95% pure Fe annealed in H)[1]	200000	0.05	13000
Iron (99.8% pure)[1]	5000	1.0	13000
Ferrite (manganese, zinc)	600	0.04	---
Steel (0.9% C)[1]	100	70	10300
Martensitic stainless steel	65	7.54	---
Austenitic stainless steel	5	0.01	---

[1] *(Rod Nave of Georgia State University, 2016)*.

From a production point of view, the alloying approach is feasible because as stated in the *(Chapter 5.6.)* the nZVI was produced thanks to the abrasion of the grinding medium. In this sense, using different medium materials the particle composition could be tailored. Actually, because the grinding medium used in the *(Chapter 5.6)* was a high carbon steel and consequently particles produced had a high carbon content, the magnetic properties would be weaker than the commercial products obtained by iron oxide reduction through hydrogen, *Table 7.1*. It could explain the superior mobility results obtained with alumina milled nZVI but in order to confirm this theory further experiments must be performed.

Another key aspect to consider is the aging in water of nZVI which includes oxidation products being ferrimagnetic such as magnetite, *Table 7.2*. Magnetite is frequently reported as iron oxide produced from nZVI aging, *(Kim et al., 2012)*, whereas common antiferromagnetic oxides have also been found, such as: goetite, maghemite and lepidocrocite, *(Liu et al., 2015)*.

The fact that some aging oxides of nZVI are ferrimagnetic must be considered because it could reduce the effectiveness of the demagnetization efforts. Further research is needed, there are important questions to solve, i.e.: do aging products occur when the main process of nZVI migration is already produced? Because magnetite generation over other oxides depends on the environmental parameters, could an additive avoid the magnetite pathway?

Table 7.2 Magnetic properties of different iron oxides. Adapted from *(Cornell and Schwertmann, 2006)*.

	Temperature (K)	**Magnetic structure**
Goethite	400 T_N	Antiferromagnetic
Lepidocrocite	77 T_N	Antiferromagnetic
Akaganéite	290 T_N	Antiferromagnetic
δ-FeOOH	440-460 T_N	Ferrimagnetic
Feroxyhyte	455 T_C	Ferrimagnetic
HP-FeOOH	470 T_N	Antiferromagnetic
Ferrihydrite	~350 T_N	Speromagnetic
Bernalite	~427 T_N	Weakly ferromagnetic
Hematite	956 T_C 260 T_M	Weakly ferromagnetic
Magnetite	850 T_C	Ferrimagnetic
Maghemite	820-986 T_C	Antiferromagnetic
ε-Fe_2O_3	1026 T_N	Planar Antiferromagnetic
$Fe(OH)_2$	34 T_N	
Wüstite	203-211 T_N	Antiferromagnetic

T_N: Néel temperature; T_C: Curie temperature; T_M Morin transition temperature.

7.2.2 Materials and methods

In order to explore if magnetization has a direct effect over aggregation and if this effect can be reverted, qualitative sedimentation test were performed under different magnetic pre-conditionings. A Zero Valent Iron (ZVI) suspension in ethanol at 10 $g \cdot l^{-1}$ was prepared using Carbonyl Iron Powder (CIP-SM, BASF SE) with an iron content > 99.0% and a mean particle diameter of 2.77 µm by volume. Ethanol was selected as sedimentation media instead of water to avoid the formation of oxides. Four 10 ml aliquots were poured into test tubes and pre-conditioned with the following treatments:

- I: Initial iron without modification
- I-D: Initial iron Demagnetized
- M: Magnetized iron
- M-D: Magnetized iron and then Demagnetized

Magnetization was performed leaving the suspension next to powerful permanent magnet (720g of NdFeB, Grade N42) during 5.0 min. Magnetization was confirmed comparatively through a magnetic field hall effect detector.

On the other hand, demagnetization was accomplished thanks to a decreasing oscillating magnetic field. A standard transformer 230 V was modified to work as a demagnetizer, cutting the transformer core. The primary coil was connected, in the course of the demagnetization, to the grid (230 V 50 Hz) whereas the secondary was unloaded. During the demagnetization, the sample was initially placed into the former transformer core and extracted slowly up to a distance of 100 cm. This process was repeated 3 times over a total demagnetization time of 30 s. As stated by *(Smith, 1961)*, it is important to immobilize the suspensions to avoid a coupled spinning of the particles whit the oscillating field which would avoid the demagnetization, consequently, suspensions were frozen submerging the sample tubes into liquid nitrogen. All the set up parts can be seen into *Fig. 7.5*.

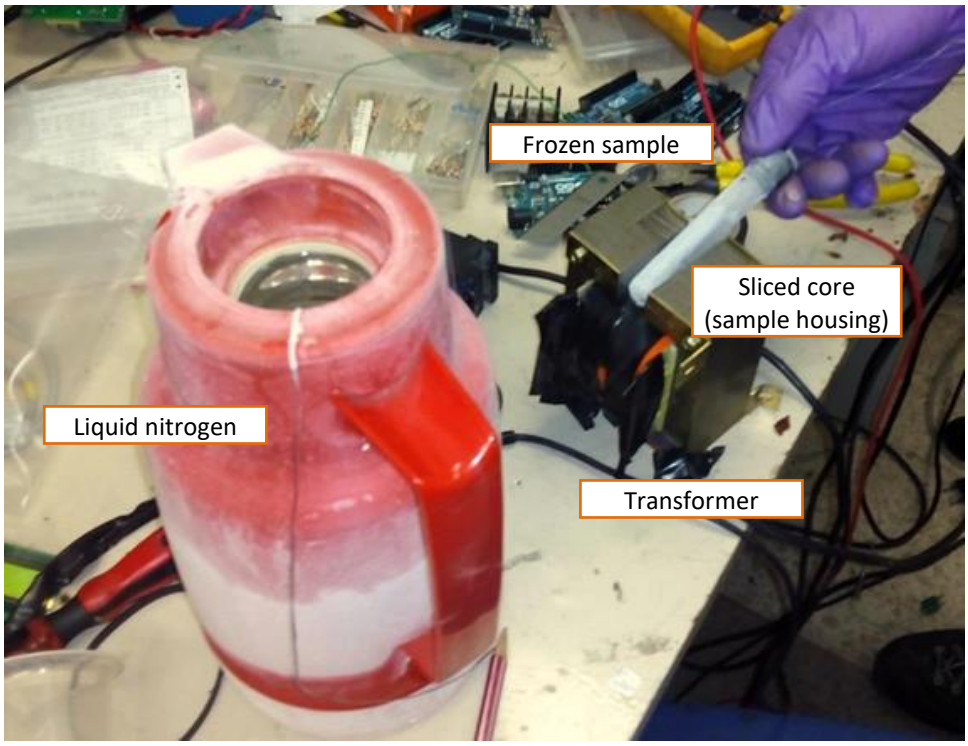

Fig. 7.5 Demagnetization setup parts.

Once the samples were magnetically pre-conditioned, these were strongly agitated and placed on a holder at the same time to perform the sedimentation tests. Sedimentation was followed recording the process with a video camera for 1 hour.

7.2.3 Results and discussion

The most evident statement from the sedimentation test *(Fig. 7.6)* is that M had so far the fastest sedimentation rate whereas the other samples behaved similarly. Differences between the samples: I, I-D and M-D cannot be disclosed because of the qualitative nature of the experiment but at less it can be stated that no important dissimilarities could be observed compared to M.

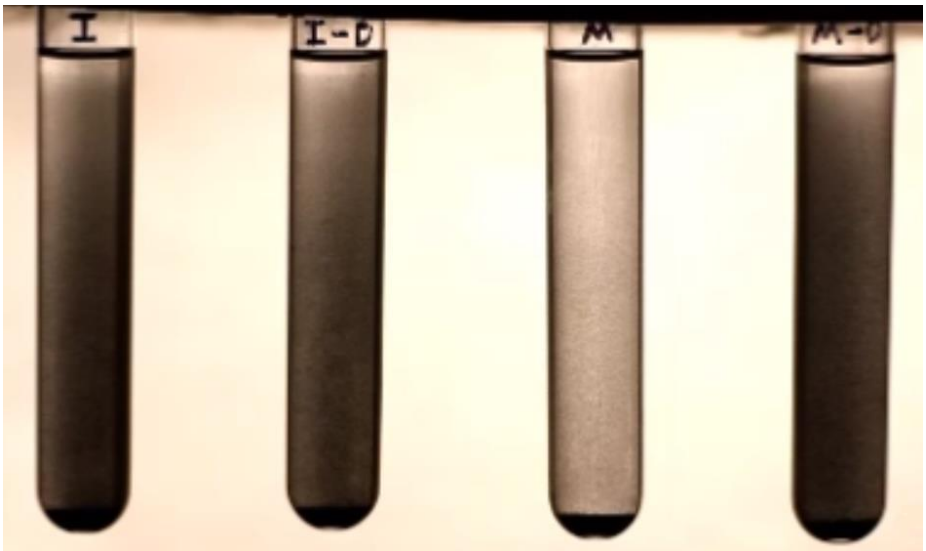

Fig. 7.6 Sedimentation tests after 15 minutes, Initial (I), Initial-Demagnetized (I-D), Initial-Magnetized (M), Initial-Magnetized-Demagnetized (M-D)

Aggregation due to magnetic attractive forces is the most plausible reason for the faster sedimentation rate of the M sample. The aggregates can be appreciated in the, *Fig. 7.7*.

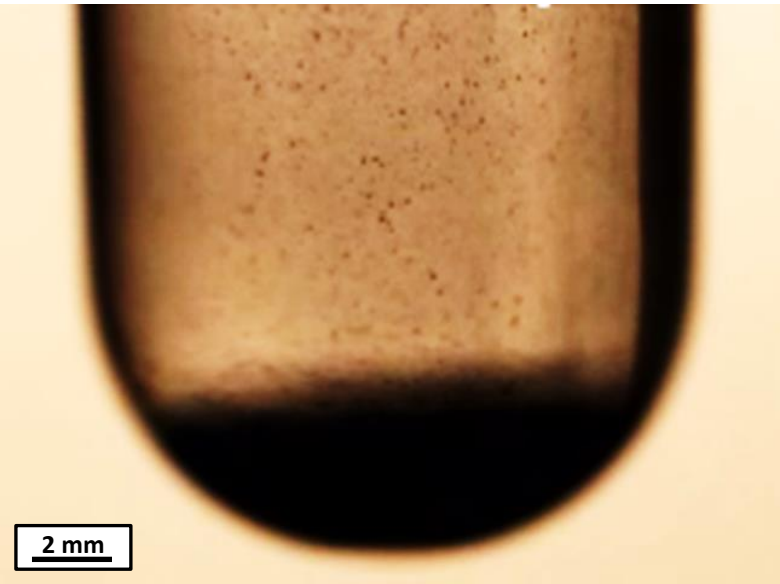

Fig. 7.7 Aggregates sedimenting on the magnetized sample.

Demagnetization process worked at less up to the initial level, unfortunately a further improvement could not be seen, possibly because one or the combination of the following hypothesis:

- Earth magnetic field or spontaneous magnetization, magnetizes the iron particles being impossible to demagnetize them completely.
- Demagnetizer performance is poor. It is possible, but demagnetizer already demagnetized the magnetized sample (M-D) up to the initial level (I).
- The lack of a quantitative technique avoids the observation of the different sedimentation rates of I, I-D and M-D samples. Although, certainly differences between these samples must exist the sedimentation rates were still too fast to represent a real improvement.

7.2.4 Conclusions

- Magnetism could have a dramatic effect on the sedimentation rate.
- Previously magnetized iron particles slurries were demagnetized successfully close to the initial level.
- There is a sedimentation rate baseline which cannot be overcome it is hypothesised that the magnetic field of Earth or spontaneous magnetization sets a base magnetism to the iron particles.

7.2.5 Proposed further experiments

After this first exploratory research a second step using quantitative techniques is mandatory. The following experiments should elucidate if the magnetic field of earth is playing a role.

- It would be interesting to repeat the experiment inside a Helmholtz coil which is able to cancel the magnetic field of the earth. If the demagnetized iron suspension does not settle under these conditions it would mean unequivocally that earth's magnetic field is magnetizing the iron particles. Alloying approach would be the only remaining option.

- Repeat the experiments using a magnetometer to measure the remaining magnetic field. It would be very useful in order to see the performance of the demagnetization. Moreover, it would be very interesting to establish a correlation between sedimentation rates and the magnetism of the particles. A quantitative method to determine the sedimentation rates is also required for example using a (TurbiScan LAB, Quantachrome).

Experiments using real nZVI in water media should be performed in order to elucidate the weight in the aggregation due to magnetism interparticle forces of the magnetic oxides generated during aging.

7.2.6 References

Comba, S., & Sethi, R. (2009). Stabilization of highly concentrated suspensions of iron nanoparticles using shear-thinning gels of xanthan gum. Water Research, 43(15), 3717-3726.

Cornell, R. M., & Schwertmann, U. (2006). The iron oxides: structure, properties, reactions, occurrences and uses. John Wiley & Sons. Ch. 6, pp. 123.

Crangle, J., & Goodman, G. M. (1971, March). The magnetization of pure iron and nickel. In Proceedings of the Royal Society of London A: Mathematical, Physical and Engineering Sciences (Vol. 321, No. 1547, pp. 477-491). The Royal Society.

Dalla Vecchia, E., Coisson, M., Appino, C., Vinai, F., & Sethi, R. (2009). Magnetic characterization and interaction modeling of zerovalent iron nanoparticles for the remediation of contaminated aquifers. Journal of nanoscience and nanotechnology, 9(5), 3210-3218.

de Caro, D., Ely, T. O., Mari, A., Chaudret, B., Snoeck, E., Respaud, M., ... & Fert, A. (1996). Synthesis, characterization, and magnetic studies of nonagglomerated zerovalent iron particles. Unexpected size dependence of the structure. Chemistry of materials, 8(8), 1987-1991.

He, F., & Zhao, D. (2005). Preparation and characterization of a new class of starch-stabilized bimetallic nanoparticles for degradation of Chlorinated Aliphatic Hydrocarbons in water. Environmental Science & Technology, 39(9), 3314-3320.

Kim, H. S., Kim, T., Ahn, J. Y., Hwang, K. Y., Park, J. Y., Lim, T. T., & Hwang, I. (2012). Aging characteristics and reactivity of two types of nanoscale zero-valent iron particles (Fe BH and Fe H2) in nitrate reduction. Chemical Engineering Journal, 197, 16-23.

Lide, D. R. (Ed.). (2004). CRC handbook of chemistry and physics. CRC press. Ch. 29, pp. 120.

Liu, A., Liu, J., & Zhang, W. X. (2015). Transformation and composition evolution of nanoscale Zero Valent iron (nZVI) synthesized by borohydride reduction in static water. Chemosphere, 119, 1068-1074.

Phenrat, T., Saleh, N., Sirk, K., Tilton, R. D., & Lowry, G. V. (2007). Aggregation and sedimentation of aqueous nanoscale zerovalent iron dispersions. Environmental Science & Technology, 41(1), 284-290.

Rod Nave of Georgia State University. (accessed 2016). http://hyperphysics.phy-astr.gsu.edu/hbase/tables/magprop.html#c2

Smith, F. (1961). Demagnetization of ferromagnetic particles. British Journal of Applied Physics, 12(4), 155.

Sun, Y. P., Li, X. Q., Zhang, W. X., & Wang, H. P. (2007). A method for the preparation of stable dispersion of zero-valent iron nanoparticles. Colloids and Surfaces A: Physicochemical and Engineering Aspects, 308(1), 60-66.

Tosco, T., Papini, M. P., Viggi, C. C., & Sethi, R. (2014). nanoscale zero valent iron particles for groundwater remediation: a review. Journal of Cleaner Production, 77, 10-21.

8 General conclusions

8.1 Denitrification chapter general conclusions

Denitrification showed to be a sensitive process regarding different environmental parameters. These parameters must be carefully studied and quantified in order to set a performing nitrate and nitrite remediation.

In the first experimental phase, repercussions of seasonal changes (temperature variations, a drought period and a freeze-thaw event) on nitrate reduction were assessed. The following behaviours were observed:

- Nitrate reduction is an Arrhenius temperature dependant process. In addition, when studying denitrification using an Arrhenius model, mass transfer limitations must be considered. It is suspected that mass transfer constrains have a greater impact on activation energy than the denitrification kinetics itself.

- Heterotrophic denitrification was the most important process in nitrate reduction during the experiments but the importance of Dissimilatory Nitrate Reduction to Ammonium (DNRA) arose in dried and frozen soils. DNRA must be taken into account because the DNRA-produced ammonia will be reconverted into nitrite or nitrate through nitrification. Furthermore, a nitrite increase was observed in dried and frosted soils produced by an incomplete denitrification or DNRA.

- In spite of the former conclusions, denitrification is a very resilient process regarding seasonal variations. Nitrate was eliminated through denitrification in percentages in less of 60% of all anoxic experiments under the different seasonal conditionings.

The aim the second experimental phase was to reveal the effects that the characteristics of the soil have on nitrate reduction by comparing two wetlands: the restored Brynemade and the natural Evi sites. It was determined that soil composition has a dramatic impact over the nitrate reduction, as it is stated by the following conclusions:

- Subsurface nitrate reduction under these riparian zones took place in a very narrow superficial zone. In deeper samples, nitrate reduction decreased to undetectable levels.

- Dissolved Organic Carbon (DOC) and Lost On Ignition (LOI) cannot express by themselves an absolute correlation with nitrate reduction potential. However, high amounts of DOC in Brynemade during the time of the experiment ensured enough quantity and quality of organic matter for nitrate reduction. Evi site presented a low nitrate reduction potential and a high concentration of LOI but a scarce abundance of DOC, showing organic matter that was not usable for nitrate reduction. Quality over quantity must be considered, closer related analytics than DOC and organic matter have to be used.

- DNRA was important only in the very superficial samples where an excessive content of organic matter could trigger this process.

- The Brynemade wetland was satisfactorily restored with a superior performance than the evidenced at Evi site with a similar geology and climate. Demonstrating in this way the viability of re-establishing functional wetlands.

In the light of these results, some guidelines for denitrification can be stated: a correct amount of labile organic matter is essential for denitrification, wetlands that are permanently flooded with low freezing periods exhibit better denitrification potentials.

8.2 nano Zero Valent iron general conclusions

This section is divided in three main parts, the conclusions drawn from the search for a new method for nano Zero Valent Iron (nZVI) production and the study of nZVI particle surface which included reactivity and agglomeration studies.

The manufacture of nZVI through wet milling is the logical choice for nZVI production in an economical and straightforward way, but after replicating the previous methods serious drawbacks were observed:

- A large oxidation of the nZVI when using water as a medium during milling.

- On the other hand, when inert media is used, the obtained final product is composed of large flakes of several micrometres in length despite the application of large milling times and energies. This is a consequence of the ductility of metallic iron which arises when the oxidation is avoided thanks to the use of an inert media.

The iron ductility was an insurmountable barrier to obtain nZVI, thus the need to break the iron flakes or to reduce the iron ductility was stated. Different approaches were tested (cryomilling, hydrogen embrittlement, alloying and addition of abrasives). Finally, the addition of alumina during milling was able to produce nanoscale particles.

- After a long process tuning the milling parameters, best results regarding granulometry were obtained using Ø 0.5 mm high carbon steel shots and an alumina concentration of 80.4 $g \cdot l^{-1}$ in the wet medium (mono ethylene glycol).

- The physicochemical properties of the obtained particles are: a mean particle diameter of 0.16 µm with a maximum size of 0.54 µm (determined by number through SEM images) and a mean particle diameter of 0.52 µm with all the particles under 1 µm (using laser diffraction by volume). The specific surface area of this material is 29.6 $m^2 \cdot g^{-1}$. Finally, the Fe(0) content is 74%.

- Abrasion of the grinding media by the addition of micronized alumina is the main responsible mechanism of the nZVI production. Therefore, the grinding media is the main source of material for the nZVI. Besides abrasion, flake breakage of the initial iron powder due to the mechanical action of alumina acting as a pressure spots over the grinding media surface is also produced.

- The reactivity towards Cr (VI), trichloroethylene and tetrachloroethylene is several times (2-5X) higher than commercial nZVIs. This high reactivity could be consequence of three factors: (I) absence of an oxide layer possibly due to the abrasion, (II) a high amount of superficial irregularities forming a great number of reactive sites thanks to a severe plastic deformation during milling and (III) the presence of a very fine nanostructure inside the milled particles because of nanoparticles re-welding and plastic deformation.

Concerning the work performed assessing the effect of a passivation oxide layer of a commercial nZVI (NANOFER STAR, NANORION s.r.o.), it was concluded that:

- Oxide shield of surface-passivated nZVI particles significantly decrease reactivity against pollutants. The degree of reactivity loss is positively related to the oxide layer thickness and its regularity - continuity.

- The process used to weaken the oxide shield is successful, increasing the reactivity against Cr (VI) several times. It consists of exposing the passivated nZVI to water for 36 hours at w iron / w water concentration of 0.2, just before the reaction with the pollutants. The activation process does not decrease the Fe(0) content.

- The increase in the reactivity is thought to be produced by: (I) a partial dissolution of the oxide layer, (II) a flake off of the oxide shell due to the expansion of the oxide and (III) a partial breakdown of the nZVI aggregates leading to an increase in the specific surface area.

- This activation process is an important new procedure, which can be applied before the injection of nZVI and could represent an easy way of increasing the effectiveness of the remediation and simplifying the overall handling of nZVI.

Electrical interparticle interactions are strongly related to the nZVI suspension stability and afterwards to the mobility. ζ-potential determinations at different pHs of the nZVI and its aging oxides leaded to two important conclusions:

- The activation process on nZVI NF STAR 197 particles does not affect ζ-potential significantly. It implies the suitability to use the same previous dispersants at the same concentrations to obtain an equal performance.

- Concerning nZVI oxidation products, goethite and magnetite presented remarkable different ζ-potential values and isoelectric points, which indicates that aging products must be taken into account when assessing the long term stability of nZVI suspensions and the dispersant selection.

Previous research of ζ-potential brought to consider the interparticle magnetic attraction because nZVI suspensions with favourable ζ-potentials still had very poor performances. It was decided to carry out an initial exploratory research in this field, the first results stated:

- Magnetized particles showed a much faster sedimentation compared to non-magnetized particles, meaning that magnetism could play an important role in the sedimentation rate.

- Previously magnetized iron particles slurries were successfully demagnetized up to the initial level, but there was a sedimentation rate baseline which could not be overcome. It is hypothesised that the magnetic field of the Earth or spontaneous magnetization sets a base magnetism to the iron particles.

9 Future perspectives

- As stated in the Denitrification chapters, quality over quantity of organic matter has a paramount effect over the heterotrophic denitrification potential. Characterization and speciation of organic matter must be performed to assess the key components that feed the denitrification.

- nano Zero Valent Iron (nZVI) abrasive milling production method is intended to be scaled up. At the moment, all process parameters are being transferred to the milling company UVR-FIA GmbH under an agreement on exploitation within the nanoRem FP7 project. The scale up process is set in the following steps:

    - The first stage will consist of carrying out some milling tests in a 10 kg grinding media capacity horizontal ball mill. Particle size vs time-energy and particle throughput vs time-energy will be studied. In order to do so, an extended characterization of the obtained particles will be performed, including: particle size analysis, Fe(0) and total iron content, scanning electron microscopy and specific surface area.

    - The second goal is the production of sufficient amount of nZVI (10 – 30 kg) to be tested in a real site. Thanks to a collaboration with UVR-FIA GmbH (nZVI producer) and TUL – CXI (site provider and monitoring). The site would probably be the Spolchemie, Czech Republic location, which is contaminated with chlorinated aliphatic hydrocarbons.

    - If the previous steps are satisfactory, the new production method would be tested in a several hundred kilograms horizontal ball mill.

- nZVI further research:

    - Regarding nZVI magnetic properties, it is essential to extend the experiments using quantitative techniques and specific hardware. This is a new and very promising path which can lead to the enhancement of the agglomeration and the mobility features of nZVI.

    - Toxicity test, TUL–CXI is assessing the toxicity of the newly produced nZVI by abrasive milling in this thesis. Specifically, the particles NA84 are being dosed in a real water and the effects on the bacterial community are being determined, the first results show very little effect on bacteria.

- Due to the fact that the new nZVI abrasive milling method could be used for the production of nanoparticles from other ductile metals besides nZVI, further applications are being studied. Catalysis is an interesting option, abrasive milled nZVI samples were given to Centre Tecnològic de la Química de Catalunya where catalytic tests are being performed. Contrasting to other nanoparticles production methods, the fact that nZVI produced by abrasive milling lacks an oxide shell seems very promising. If the results are positive, nickel and copper could be the next target metals. In addition, the knowledge of this thesis has been applied to mill minerals such as: iron oxides (hematite) and calcium carbonate.

- Approaches to improve and bring new features to the developed abrasive milling method are being studied, such as: production of multimetallic nanoparticles, increase size reduction using dispersants, increase size reduction using smaller alumina particles and other wet media.